ISSN
2712-8172

Magazine of Civil Engineering

109(1), 2022

Федеральное государственное автономное образовательное учреждение
высшего образования
Санкт-Петербургский политехнический университет Петра Великого

ПОЛИТЕХ
Санкт-Петербургский
политехнический университет
Петра Великого

Инженерно-строительный институт
Центр дополнительных профессиональных программ

195251, г. Санкт-Петербург, Политехническая ул., 29,
тел/факс: 552-94-60, www.stroikursi.spbstu.ru,
stroikursi@mail.ru

Приглашает специалистов организаций, вступающих в СРО, на курсы повышения квалификации (72 часа)

Код	Наименование программы	Виды работ*
	Курсы по строительству	
БС-01-04	«Безопасность и качество выполнения общестроительных работ»	**п.1,2, 3, 5, 6, 7, 9, 10, 11, 12, 13, 14**
БС-01	«Безопасность и качество выполнения геодезических, подготовительных и земляных работ, устройства оснований и фундаментов»	**1,2,3,5**
БС-02	«Безопасность и качество возведения бетонных и железобетонных конструкций»	**6,7**
БС-03	«Безопасность и качество возведения металлических, каменных и деревянных конструкций»	**9,10,11**
БС-04	«Безопасность и качество выполнения фасадных работ, устройства кровель, защиты строительных конструкций, трубопроводов и оборудования»	**12,13,14**
БС-05	«Безопасность и качество устройства инженерных сетей и систем»	**15,16,17,18,19**
БС-06	«Безопасность и качество устройства электрических сетей и линий связи»	**20,21**
БС-08	«Безопасность и качество выполнения монтажных и пусконаладочных работ»	**23,24**
БС-12	«Безопасность и качество устройства мостов, эстакад и путепроводов»	**29**
БС-13	«Безопасность и качество выполнения гидротехнических, водолазных работ»	**30**
БС-14	«Безопасность и качество устройства промышленных печей и дымовых труб»	**31**
БС-15	«Осуществление строительного контроля»	**32**
БС-16	«Организация строительства, реконструкции и капитального ремонта. Выполнение функций технического заказчика и генерального подрядчика»	**33**
	Курсы по проектированию	
БП-01	«Разработка схемы планировочной организации земельного участка, архитектурных решений, мероприятий по обеспечению доступа маломобильных групп населения»	**1,2,11**
БП-02	«Разработка конструктивных и объемно-планировочных решений зданий и сооружений»	**3**
БП-03	«Проектирование внутренних сетей инженерно-технического обеспечения»	**4**
БП-04	«Проектирование наружных сетей инженерно-технического обеспечения»	**5**
БП-05	«Разработка технологических решений при проектировании зданий и сооружений»	**6**
БП-06	«Разработка специальных разделов проектной документации»	**7**
БП-07	«Разработка проектов организации строительства»	**8**
БП-08	«Проектные решения по охране окружающей среды»	**9**
БП-09	«Проектные решения по обеспечению пожарной безопасности»	**10**
БП-10	«Обследование строительных конструкций и грунтов основания зданий и сооружений»	**12**
БП-11	«Организация проектных работ. Выполнение функций генерального проектировщика»	**13**
Э-01	«Проведение энергетических обследований с целью повышения энергетической эффективности и энергосбережения»	
	Курсы по инженерным изысканиям	
И-01	«Инженерно-геодезические изыскания в строительстве»	**1**
И-02	«Инженерно-геологические изыскания в строительстве»	**2,5**
И-03	«Инженерно-гидрометеорологические изыскания в строительстве»	**3**
И-04	«Инженерно-экологические изыскания в строительстве»	**4**
И-05	«Организация работ по инженерным изысканиям»	**7**

***(согласно приказам Минрегионразвития РФ N 624 от 30 декабря 2009 г.)**

По окончании курса слушателю выдается удостоверение о краткосрочном повышении квалификации установленного образца (72 ак. часа)

Для регистрации на курс необходимо выслать заявку на участие, и копию диплома об образовании по телефону/факсу: 8(812) 552-94-60, 535-79-92, , e-mail: stroikursi@mail.ru.

Magazine of Civil Engineering
SCHOLAR JOURNAL

ISSN 2712-8172

Свидетельство о государственной регистрации:
Эл № ФС77-77906 от 19.02.2020,
выдано Роскомнадзором

Специализированный научный журнал.

Выходит с 09.2008.

Включен в Перечень ВАК РФ

Индексируется в БД Scopus

Периодичность: 8 раз в год

Учредитель и издатель:

Санкт-Петербургский политехнический университет Петра Великого

Адрес редакции:

195251, СПб, ул. Политехническая, д. 29

Дата выхода: 14.02.2022

Magazine of Civil Engineering
SCHOLAR JOURNAL

ISSN 2712-8172

Peer-reviewed scientific journal

Start date: 2008/09

8 issues per year

Publisher:

Peter the Great St. Petersburg Polytechnic University

Indexing:

Scopus, Web of Sceince (ESCI, RSCI), Compendex, EBSCO, Google Academia, Index Copernicus, ProQuest, Ulrich's Serials Analysis System, CNKI

Corresponding address:

29 Polytechnicheskaya st., Saint-Petersburg, 195251, Russia

Date of issue: 14.02.2022

Contacts:
E-mail: mce@spbstu.ru
Web: http://www.engstroy.spbstu.ru

Contents

Magazine of Civil Engineering. 2022. 109(1). Article No. 10901

Magazine of Civil Engineering

ISSN 2712-8172

journal homepage: http://engstroy.spbstu.ru/

DOI: 10.34910/MCE.109.1

Effect of elastomer polymer on the moisture susceptibility of asphalt concrete

***A. Shabani*[a], *Gh.H. Hamedi*[b] ***

[a] *KTH Royal Institute of Technology, Stockholm, Sweden*

[b] *University of Guilan, Rasht, Guilan Province, Iran*

**E-mail: hamedi@guilan.ac.ir*

Keywords: experimental investigations, strength, moisture, cyclic loads, asphalt mixtures, asphalt pavements, polymers

Abstract. There are various experimental methods for improving the moisture strength of asphalt concrete, such that the most common one being the use of anti-stripping materials. In the present paper, the influences of polymer materials on\ asphalt binder were investigated using repetitive loading test in wet and dry conditions along with thermodynamic parameters based on the surface free energy (SFE) components of asphalt binder and aggregates. The obtained results of this investigation indicate that using styrene butadiene rubber (SBR) polymer has improved the asphalt concrete strength against the moisture damage, especially in the specimens made of granite aggregates. Also, SBR polymer increases the cohesion free energy and reduces the energy released by the system during the stripping event, which represents a decrease in the tendency for stripping. The stripping percentage index, which is obtained by combining the results of the repetitive loading test in wet and dry conditions along with the results of thermodynamic parameters, represents that the specimens made of controlled asphalt binder in the loading cycles under wet conditions have a higher stripping rate. Also, the modulus loss rate in control asphalt concrete is faster than the modified specimens.

1. Introduction

Aggregates and asphalt binder are two main components of asphalt concrete as a composite material [1]. Asphalt binder is absorbed on the surface of aggregates and forms the asphalt binder film. This film stickes aggregates to eachother and creates the strong structure of asphalt mixture [2]. Displacement of asphalt binder from the aggregate surface or failure in the asphalt binder film is defined as moisture damage. This type of damage occurs when the aggregates have a greater tendency to absorb water than being coated by the asphalt binder [3]. In addition to moisture damage, moisture causes different damages such as rutting, fatigue, shoving, bleeding, and pothole [4].

In order to compare the susceptibility and the effects of stripping additives and the moisture damage potential of asphalt concrete, a variety of experimental tests have been performed in wet and dry conditions [5]. The modified Lottman method (AASHTO T283) is a well-known experimental approach in this field which does not focus on the fundamental properties of materials that effects on damage event, and they cannot present the reason for the weakness or the strength of asphalt concrete [6]. Accordingly, in the last two decades, many studies have been conducted on using different methods based on the properties of materials that affect the asphalt binder cohesion and the asphalt binder-aggregate adhesion for determination of the moisture susceptibility of asphalt concrete.

Shabani, A., Hamedi, Gh.H. Effect of elastomer polymer on the moisture susceptibility of asphalt concrete. Magazine of Civil Engineering. 2022. 109(1). Article No. 10901. DOI: 10.34910/MCE.109.1

1.1. Previous studies

Free energy of asphalt mixture constituent elements play a significant role in mechanical properties of asphalt concrete [7]. The primary investigation was reported in Texas Transportation Institute by Elphingstone [8], which revealed that SFE measurements could be applied as an impressive tool to predict moisture damage and fatigue cracking in asphalt concrete. Cheng [9] examined the concepts of SFE and its application in asphalt concrete. The results of his study showed that thermodynamic changed in adhesion and cohesion of SFE were directly related to debonding in the asphalt binder aggregates' contact surface and cracks in the mastic. Abandansari and Modarres [10] investigated the influence of using nanomaterials on moisture strength of asphalt concrete by using mechanical and thermodynamic methods. Bhasin [11] initially developed the methods to measure the SFE components of asphalt binder and aggregate. Then, he investigated the relationship between the thermodynamic parameters, which were obtained by measuring the SFE components of asphalt binders and aggregates as well as the moisture susceptibility potential in the asphalt concrete. Following the previous studies, Howson [12] evaluated using SFE for identification of the resistance of asphalt concrete against moisture. The obtained experimental results of this investigation indicated that the modifications made on asphalt binder had negative or positive influences on their SFE components and adhesion energy. In the study reported by Moghadas Nejad and Hamedi [13], the relationship between moisture damage potential and thermodynamic parameters was evaluated using the susceptibility test results from different combinations of asphalt concrete. The results showed that the thermodynamic parameters were significantly associated with the event and severity of moisture damage [14].

In recent years polymer and nanomaterial have also been applied to investigate the moisture properties of asphalt concrete [15, 16]. The most important methods for improving the asphalt mixture's strength against moisture are changing the mixture design, materials, or using anti-stripping additives. Changes in the mix design can also slightly affect the asphalt mixture strength against moisture. Accordingly, using anti-stripping additives is the most optimal method to improve the asphalt mixture's strength against moisture [17]. Although studies have been carried out on an aggregate modification to improve asphalt mixture's strength against moisture, most of these studies have been limited to experimental studies [18, 19]. Hydrated lime [20], nano anti-stripping [21], and liquid anti-stripping [22] additives are the most common anti-stripping materials used in the experimental studies and executive projects.

1.2. SFE theory

SFE of the materials has been described in several theories according to the molecular structure. An acidic-basic theory is one of the most significant theories which is used extensively for the description of the SFE components of various materials [23].

By combining the mentioned components, the total SFE can be obtained as the following expression:

$$\Gamma = \Gamma^{LW} + \Gamma^{AB}. \tag{1}$$

Hitherto, Γ, Γ^{AB}, and Γ^{LW} denote the total SFE of the materials, the polar component of SFE, and the non-polar component of SFE, respectively. Γ^{AB} can be explained as Equation (2) which is a composition of Lewis acid $\left(\Gamma^{+}\right)$ and base components $\left(\Gamma^{-}\right)$.

$$\Gamma^{AB} = 2\sqrt{\Gamma^{+}\Gamma^{-}}. \tag{2}$$

From the thermodynamic perspective, the cohesion free energy $\left(\Delta G_i^c\right)$ can be explained as the amount of energy required for creating a crack in a material with the unit surface. Based on this definition, the total cohesion work is obtained for different materials as Equation (3):

$$W^{AC} = 2\Gamma_A, \tag{3}$$

where Γ_A denotes the total SFE of the desired material. Cohesion work of an asphalt binder is a significant factor applied in some fracture mechanics basic equations to determine the energy required to grow tiny cracks in the asphalt binder phase or the asphalt mixture mastic phase.

Adhesion free energy $\left(\Delta G_i^a\right)$ is defined based on two main components of non-polar or Lifshitz Van der Waals $\left(\Delta G_i^{aAB}\right)$ and Polar or acid-base $\left(\Delta G_i^{aLW}\right)$. Hence, Equation (4) is applied for the determination of the adhesion-free energy between aggregate and asphalt binder.

$$\Delta G_i^a = -W^a = \Delta G_i^{aLW} + \Delta G_i^{aAB} = -2\left[\left(\sqrt{\Gamma_2^{lw}\Gamma_1^{lw}}\right)+\left(\sqrt{\Gamma_2^{+}\Gamma_1^{-}}\right)+\left(\sqrt{\Gamma_2^{-}\Gamma_1^{+}}\right)\right], \tag{4}$$

where Γ_1^{lw}, Γ_1^{+} and Γ_1^{-} are the asphalt binder components' SFE and Γ_2^{lw}, Γ_2^{+} and Γ_2^{-} are the aggregate components' SFE. For a mixture of aggregate and asphalt binder, Equation (4) is used for the case when the SFE components of the mixture are measured.

From a thermodynamic point of view, the ΔG_i^c is the total work per unit area to form two new surfaces, the energy of which is equal to the sum of the surface energies of the two newly created surfaces. In addition, the W^a is the work required to separate two materials at their contact surface under vacuum conditions. The cohesion and adhesion works are shown in Fig. 1.

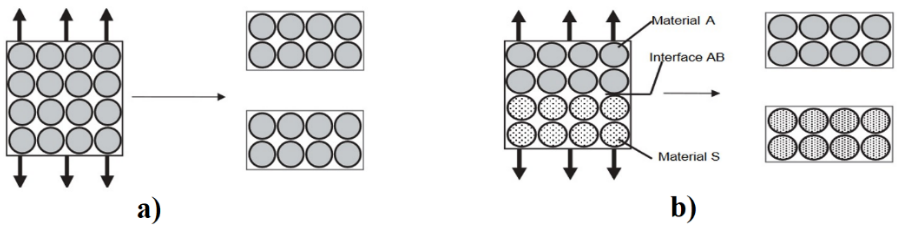

Figure 1. a – the cohesion, b – the adhesion work of energy.

Equation (5) is used to calculate aggregate and asphalt binder adhesion in the presence of water. In this equation, the subscripts of 1, 2, and 3 show the asphalt binder, aggregate, and water, respectively. It is noteworthy to mention that the negative values of adhesion free energy represent that the two materials tend to bond with each other. For the case when the ΔG_i^a value becomes more negative, this tendency increases.

$$\Delta G_{132}^a = \Gamma_{12} - \Gamma_{13} - \Gamma_{23} = -\left[\begin{array}{l} \left(2\Gamma_3^{LW}\right)+\left(4\sqrt{\Gamma_3^{+}\Gamma_3^{-}}\right)-\left(2\sqrt{\Gamma_1^{LW}\Gamma_3^{LW}}\right) \\ -\left(2\sqrt{\Gamma_3^{+}\Gamma_1^{-}}\right)-\left(2\sqrt{\Gamma_1^{+}\Gamma_3^{-}}\right)-\left(2\sqrt{\Gamma_2^{LW}\Gamma_3^{LW}}\right) \\ -\left(2\sqrt{\Gamma_3^{+}\Gamma_2^{-}}\right)-\left(2\sqrt{\Gamma_2^{+}\Gamma_3^{-}}\right)-\left(2\sqrt{\Gamma_1^{LW}\Gamma_2^{LW}}\right) \\ +\left(2\sqrt{\Gamma_1^{+}\Gamma_2^{-}}\right)+\left(2\sqrt{\Gamma_2^{+}\Gamma_2^{-}}\right) \end{array}\right]. \tag{5}$$

1.3. Problem statement and research objectives

Although the currently-used anti-stripping materials have reduced moisture damage in asphalt concrete, their use is associated with a series of executive or technical problems [23]. Therefore, this research has attempted to investigate the use of polymer modifiers. Also, despite the numerous studies conducted on the application of thermodynamic methods in detecting the susceptibility of asphalt concrete, it is worth mentioning that its use as a tool to determine the susceptibility of different asphalt concrete and its effects on the anti-stripping mechanism has not yet been widespread. Therefore, this study attempts to first obtain the SFE components of the controlled and modified asphalt binder and aggregateThe most significant objectives of the present study can be categorized as follows:

1. Studying the influence of SBR polymer on the controlled asphalt binder's SFE components

2. Studying the influence of SBR polymer on thermodynamic parameters including asphalt binder-aggregate adhesion free energy, asphalt binder cohesion free energy, and the system's free energy in the event of stripping

3. Studying the effects of using SBR polymer on the modulus ratio of wet to dry condition in the controlled and modified specimens

4. Comparing the results of the thermodynamic parameters and modulus ratio in wet to dry conditions

5. Combining the results of the thermodynamic parameters and repetitive loading to determine the process of stripping event in the controlled and modified specimens.

2. Methods

2.1. Designing an experimental program

Different experimental procedures used in this study include:

1. Modifying the controlled asphalt binder with SBR in two different percentages;

2. Mix design by AASHTO T245 method;

3. Implementing the repetitive loading test on specimens made of controlled and modified asphalt binders;

4. Determining the SFE components of the controlled and modified asphalt binders using Wilhelmy plate and Universal Sorption Device (USD);

5. Calculating thermodynamic parameters based on SFE components of asphalt binders, aggregates, and water for various compounds of asphalt concrete, and;

6. Calculating the percentage of asphalt concrete' aggregate surface stripping in different loading cycles by combining the results of repetitive loading test and thermodynamic parameters.

2.2. Materials

2.2.1. Aggregate

In the present paper, two different types of granite and limestone aggregates have been used, which are acidic and basic, respectively. The main reason for using these two different aggregates is the different structure of minerals constituting these two types of aggregates, which makes them different in their susceptibility to moisture damage. The structure of aggregate surface minerals is evaluated by the X-ray fluorescence (XRF) experiment. The results of these experiments are presented in Table 1.

Table 1. Structure of minerals forming aggregates used in this study.

Properties	Limestone	Granite
Calcium oxide, CaO (%)	72.47	31.75
Magnesium oxide, MgO (%)	2.24	2.92
Ferric oxide, Fe_2O_3 (%)	3.87	7.08
Aluminum oxide, Al_2O_3 (%)	4.84	1.74
Silicon dioxide, SiO_2 (%)	13.58	52.19

The gradation of aggregates used in the present investigation is the ASTM-standard medium grading to produce dense asphalt concrete. The rated size of the aggregates in this gradation is 19 mm [24]. The aggregate gradations of two used materials are illustrated in Fig. 2, whereas their physical properties are documented in Table 2.

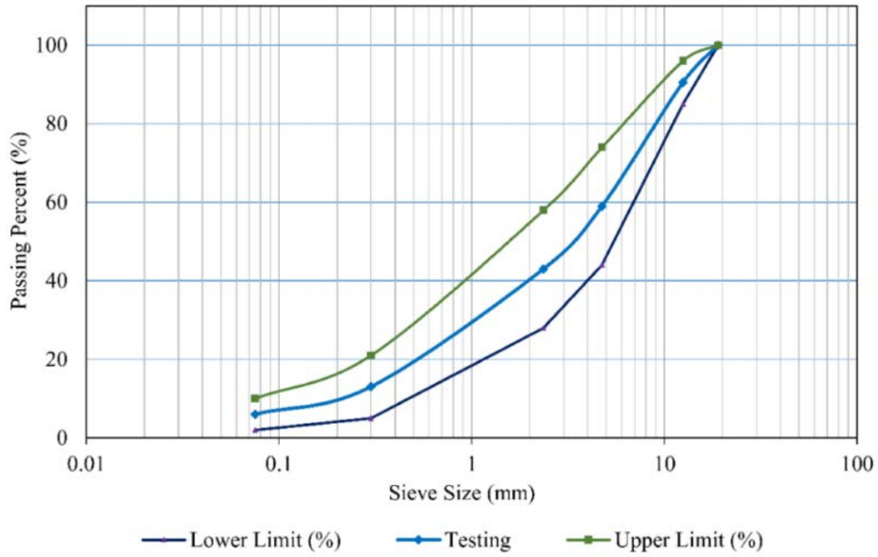

Figure 2. Gradation of aggregates used in this study.

Table 2. Physical properties of aggregates used in this study.

Properties	**Standard**	Limestone	Granite	Specification limit
Coarse aggregate				
Bulk specific gravity (g/cm^3)	ASTM C 127	2.63	2.61	–
SSD specific gravity (g/cm^3)		2.65	2.63	–
Apparent specific gravity (g/cm^3)		2.68	2.67	–
Fine aggregate				
Bulk specific gravity (g/cm^3)	ASTM C 128	2.62	2.60	–
SSD specific gravity (g/cm^3)		2.65	2.62	–
Apparent specific gravity (g/cm^3)		2.68	2.65	–
Specific gravity of filler (g/cm^3)	ASTM D 854	2.65	2.65	–
Los Angeles abrasion (%)	ASTM C 131	32	22	Max 45
Flat and elongated particles (%)	ASTM D 4791	9	6	Max 10
Sodium sulfate soundness (%)	ASTM C 88	7	9	Max 10–20
Fine aggregate angularity	ASTM C 1252	56.2	59.2	Min 40

2.2.2. Asphalt binder

The base asphalt binder used in the present paper has the penetration grade of 60–70 provided by the Isfahan refinery. Table 3 presents the characteristics of the asphalt binder. The asphalt binder is modified by SBR polymer materials in two different percentages. The next section will explain the anti-stripping materials used in this study and their properties.

Table 3. Properties of base asphalt binders used in this study.

Properties	Standard	Value
Penetration (mm/10)	ASTM D5-73	69
Softening point (°C)	ASTM D36-76	51
Ductility (cm)	ASTM D113-79	105
Flashpoint (°C)	ASTM D92-78	262
Loss of heating (%)	ASTM D1754-78	0.75
Trichloroethylene solubility, (%)	ASTM D2042-76	99.5

2.2.3. SBR polymer

SBR describes a family of synthetic rubbers that consist of styrene and butadiene. These materials have a suitable strength against wear and aging. SBR is defined as a common polymer with high efficiency, and it is considered to be the world's most consumed rubber, due to the availability of cheap and abundant raw materials. Therefore, it has the highest volume of production in the rubber industry [25]. The mechanical properties of the SBR polymer used in this study are presented in Table 4.

Table 4. Mechanical properties of the SBR polymer used in this study.

Properties	Value
Tensile Strength (MPa)	18
Elongation at tear (%)	544
Mooney Viscosity (100 °C)	49.2
Glass transition temperature (°C)	–60
Polydispersity	2.7
PH	9.5

2.3. Laboratory Studies

2.3.1. Asphalt binder modification

In this study, SBR polymer material is used as an anti-stripping asphalt binder modifier. This material is used at 2 and 4 % of asphalt binder weight. For the production of modified asphalt binders, the base asphalt binder is first heated to 160 °C, and then the additives are added at the intended percentage. Mixing operation is carried out in the mixer at the rate of 2000 rpm for 15 minutes. Since mixing procedure causes aging in asphalt binder [26], the base asphalt binder is placed in the mixer at the same conditions to experience the effect of aging similar to the modified asphalt binders.

2.3.2. Mix design

In the present investigation, the Marshall mix design has been applied according to the AASHTO T245 standard for the determination of the optimum asphalt binder content [27]. Also, the optimum asphalt binder content is determined based on the MS-2 guideline of the Asphalt Institute. The values of optimum asphalt binder were calculated based on the average asphalt binder content corresponding to the maximum unit weight, maximum marshal stability, and 4 % air void. The corresponding values of the five parameters of Marshall stability, flow, air void (AV), voids in mineral aggregate (VMA), and void fill with asphalt binder (VFA were then controlled by the specifications.

2.3.3. Repetitive loading test

The repetitive load test was used to determine the modulus of asphalt concrete in dry and wet conditions. The AASHTO T283 method is used to subject the specimens to wet conditions. The modified *AASHTO* T283 method is one of the most common methods used to determine moisture sensitivity of HMA. It should be considered that the percentage of existing air pores of the mixture should be 6.5–7.5 %. Three cases of prepared specimens are remained in dry conditions and the other 3 specimens should be conditioned in order to prepare wet specimens. First, the specimens should be saturated using relative vacuum conditions under absolute pressure of 13–67 kPa for 5 minutes. Samples are then kept submerged without vacuum conditions for 5–10 minutes, and in the following, specimens are withdrawn and weighted in order to achieve the saturation percent of 70–80 %. Then the specimens are kept into freezer at –18 °C for 16 h and after that the specimens are placed in warm water bath at 60 °C and they are allowed to remain at this temperature for 24 h. In this study, the indirect tensile modulus experiment is conducted at 25 °C and a frequency of 1 Hz under haversine loading with the stress level of 300 kPa. The value of the indirect tensile modulus for each mixture in a particular loading cycle can be measured by using Equation (6).

$$E^* = \frac{\sigma_{\max}}{\varepsilon_{\max}}, \tag{6}$$

where $\sigma_{\max}$ is the maximum stress for a particular cycle and $\varepsilon_{\max}$ is the corresponding stress in the same cycle.

Modulus ratio for each cycle is obtained according to Equation (7), which is considered as an indicator for moisture susceptibility in asphalt concrete [28]. The larger the parameter K is, according to

Equation (7), means that the asphalt mixture strength against the simultaneous effects of traffic and high moisture is higher.

$$K = \frac{E^*_{wet}}{E^*_{dry}} \times 100, \tag{7}$$

where, E^*_{wet} and E^*_{dry} indicate the indirect tensile modulus value in wet and dry conditions, respectively.

2.3.4. Measuring the SFE components of aggregate and asphalt binder

A variety of methods can be used to measure the SFE components of asphalt binder and aggregate. Due to the susceptibility of measurement in these experiments, the methods used here are the methods that were proven to have higher accuracy in the previous studies [29].

2.3.4.1. Measuring the SFE components of aggregates

Universal Sorption Device (USD) has been used to measure the aggregate's SFE indirectly using gas adsorption by three solvents. Hence, for the creation of a set of three equations and three unknowns (the three components of the solid matter's SFE), three equations are needed. Therefore, it could be noted that three research matters, whose SFE components should be specified, are required for calculation of the SFE components of a solid body.

The relationship between the vapor pressure of a vapor of the probe material and the mass of a vapor absorbed on the surface of an aggregate is an example of isothermal adsorption. Moreover, the relationship between the adhesion work and the square root of the SFE components (Equation 8) is linear. Therefore, three equations are required to create a set of three equations with three unknowns, with each equation needing a probe material. Thus, three probe materials are required to obtain the SFE components of a solid.

$$W^a_{S,V} = \pi_e + 2\Gamma^{total}_v = -2\left[\sqrt{\Gamma^{LW}_s \Gamma^{LW}_l} + \sqrt{\Gamma^+_s \Gamma^-_l} + \sqrt{\Gamma^-_s \Gamma^+_l}\right], \tag{8}$$

where $W^a_{S,V}$ is the work of adhesion between the surface aggregate (S) and vapor (V), Γ^{Total}_V is the total SFE of liquids tested, and π_e is the equilibrium pressure distribution of the liquid vapor over the aggregate surface.

USD is able to indirectly obtain the SFE components of the aggregate using three different probe liquids. Generally, the passing aggregates of 4.75 mm and the residue on sieve 2.36 mm are used. 40 g of these aggregates are washed and dried on a 2.36 mm sieve to remove dust and moisture completely. Finally, these aggregates are washed using water, methanol, hexane and again methanol. After washing is complete, these aggregates are brought to standard room temperature. Once the materials have reached room temperature (25 °C), they are placed inside the aluminum mesh sample holder of the USB device.

The equilibrium pressure distribution on the aggregate is obtained as Equation 9:

$$\pi_e = \frac{RT}{MA}\int_0^{Pn} \frac{n}{p}\, dp. \tag{9}$$

In which R is the gas constant, T is the test temperature (Kelvin), M is the molecular mass of the tested vapor-liquid, n is the mass of the absorbed vapor per unit mass of the aggregate at vapor pressure p, and A is the specific surface area of the aggregate, which is calculated as follows using the BET equation (Equation 10):

$$A = \left(\frac{n_m \times N_0}{M}\right) \times \alpha, \tag{10}$$

where N_0 is Avogadro's number, α is the imaged surface of one molecule, and n_m is single-layer capacity. The number of molecules required to cover the surface of the aggregate in one layer is referred to as the absorbable monolayer capacity on the aggregate surface, which can be obtained by Equation 11. In this equation, S and I denote the slope and intercept of the diagram between $p/n(p_0 - p)$ and

p/p_0, P stands for the partial vapor pressure, P_n indicates the saturated vapor pressure, and n represents the mass of the absorbed vapor relative to the aggregate mass.

$$n_m = \frac{1}{s+I}. \tag{11}$$

The SFE components for different used materials are reported in Table 5.

Table 5. SFE components of the research materials for measuring the SFE components of aggregates (ergs/cm²).

SFE components	SFE components (ergs/cm²)				
	Total SFE	Lifshitz Van der Waals	Polar	Acidic	Basic
n-Hexane	18.4	18.4	0	0	0
Methyl Propyl Ketone (MPK)	24.7	24.7	0	0	19.6
Water	72.8	21.8	51	25.5	25.5

2.3.4.2. Measuring SFE components of asphalt binder

In this section, the Wilhelmy plate technique is used to obtain the contact angle between the asphalt binder and a liquid which is a characteristic of the hydrophilicity or hydrophobicity of the surface [30].

The relationship between the vapor pressure of a vapor of the probe material and the mass of a vapor absorbed on the surface of an aggregate is an example of isothermal adsorption. Moreover, the relationship between the adhesion work and the square root of the SFE components (Equation 12) is linear. Therefore, three equations are required to create a set of three equations with three unknowns, with each equation needing a probe material. Thus, three probe materials are required to obtain the SFE components of a solid.

$$W_{S,V}^{a} = \pi_e + 2\Gamma_v^{total} = -2\left[\sqrt{\Gamma_s^{LW}\Gamma_l^{LW}} + \sqrt{\Gamma_s^{+}\Gamma_l^{-}} + \sqrt{\Gamma_s^{-}\Gamma_l^{+}}\right], \tag{12}$$

where $W_{S,V}^{a}$ is the work of adhesion between the surface aggregate (S) and vapor (V), Γ_v^{total} is the total SFE of liquids tested, and π_e is the equilibrium pressure distribution of the liquid vapor over the aggregate surface.

USD is able to indirectly obtain the SFE components of the aggregate using three different probe liquids. Generally, the passing aggregates of 4.75 mm and the residue on sieve 2.36 mm are used. 40 g of these aggregates are washed and dried on a 2.36 mm sieve to remove dust and moisture completely. Finally, these aggregates are washed using water, methanol, hexane and again methanol. After washing is complete, these aggregates are brought to standard room temperature. Once the materials have reached room temperature (25 °C), they are placed inside the aluminum mesh sample holder of the USB device.

The equilibrium pressure distribution on the aggregate is obtained as Equation 13:

$$\pi_e = \frac{RT}{MA}\int_0^{Pn} \frac{n}{p}\,dp, \tag{13}$$

where R is the gas constant, T is the test temperature (Kelvin), M is the molecular mass of the tested vapor-liquid, n is the mass of the absorbed vapor per unit mass of the aggregate at vapor pressure p, and A is the specific surface area of the aggregate, which is calculated as follows using the BET equation (Equation 14):

$$A = \left(\frac{n_m \times N_0}{M}\right) \times \alpha, \tag{14}$$

where N_0 is Avogadro's number, α is the imaged surface of one molecule, and nm is single-layer capacity. The number of molecules required to cover the surface of the aggregate in one layer is referred to as the absorbable monolayer capacity on the aggregate surface, which can be obtained by Equation 15.

In this equation, S and I denote the slope and intercept of the diagram between $p/n(p_0 - p)$ and p/p_0, P stands for the partial vapor pressure, P_n indicates the saturated vapor pressure, and n represents the mass of the absorbed vapor relative to the aggregate mass.

$$n_m = \frac{1}{s+1}. \tag{15}$$

To obtain the passive components, at least three fluids with specified surface energy components are required. In this paper, water, formamide, and glycerin have been used due to the relatively large amounts of SFE components, non-miscible with asphalt binder, and different amounts of SFE. Their surface energy components are provided in Table 6.

Table 6. SFE components of the research materials for measuring the SFE components of asphalt binder (ergs/cm^2).

SFE components	SFE components (ergs/cm^2)				
	Total SFE	Lifshitz Van der Waals	Polar	Acidic	Basic
Water	72.6	21.6	51	25.5	25.5
Glycerol	62.8	34	28.8	3.92	57.4
Formamide	58	39	19	2.28	39.6

3. Results and Discussion

3.1. Mix design

The optimum asphalt binder content in the specimens made of granite and limestone aggregates was 5.5 and 5.8 %, respectively. Due to their surface porosity, limestone aggregates absorb more asphalt binder. This process causes more optimum asphalt binder content to be absorbed compared to the granite aggregates with fewer pores.

It should be mentioned that the mix design is only carried out for specimens containing aggregates and base asphalt binders, because if different asphalt binder percentages are used in the specimens containing controlled and modified asphalt binders, the asphalt binder content variable is also an important factor affecting the modulus ratio in wet to dry condition which causes the results to face an error.

3.2. SFE tests

3.2.1. Measuring the SFE components of aggregates

Table 7 indicates the results of measuring the SFE components of aggregates used in the present paper. In all reported cases, the basic components of both aggregates are higher than their acidic components. However, as it is clear, the ratio of the acidic to the basic component of granite aggregate is higher than the limestone aggregate. The non-polar component of limestone and granite aggregates are close to each other, but the polar component of limestone aggregate is more than granite aggregate, which has led to a significant increase in the total SFE associated with limestone aggregate compared to granite aggregate.

Table 7. The SFE components of aggregates used in this study.

Aggregate type	SFE components (ergs/cm^2)				
	Basic	Acidic	Polar	Nonpolar	Total
Limestone	522.4	31.7	257.5	67.1	324.6
Granite	525.8	20.5	207.7	68.8	276.6

3.2.2. Measuring the SFE components of asphalt binders

Asphalt is a single-phase homogeneous mixture of many different molecules, which may be differentiated into two broad classes: polar and non-polar. The non-polar molecules serve as a matrix or solvent for the polar molecules, which form weak “networks” of polar-polar associations that give asphalt its elastic properties. The polar materials are uniformly distributed throughout the asphalt, and upon heating the weak interactions are broken to yield a Newtonian fluid. Asphalts that have too much polar material will be subject to fatigue cracking in thin pavements, brittleness, and thermal cracking. Asphalts that have too much non-polar material, or asphalts in which the non-polar materials are too low in molecular weight, will suffer from fatigue cracking in thick pavements, moisture sensitivity, and rutting. Asphalt binder is acidic in nature. Results related to the controlled and modified asphalt binder's SFE are presented in Table 8. As is clear from the table data, the base asphalt binder's acidic component is higher than its basic component. This causes the asphalt binder to have more acidic properties. Acidic properties of asphalt binder lead to the formation of stronger bonds with basic materials such as lime aggregates. The use of SBR polymer has increased both the acid and basic components of modified asphalt binders. The percentage of increase in the basic component is higher than the acidic component, which results in the formation of more basic properties in the SBR modified asphalt binders. An increase in the percentage of this material from 2 to 4 percent also increases the mentioned changes.

The results of Table 8 show that SBR polymer has increased the asphalt binder polar component. The positive or negative impact of this parameter on the asphalt binder-aggregate adhesion cannot be stated with certainty. The only thing to mention is that the increase in the polar properties of asphalt binders will increase their adhesion tendency to polar materials such as aggregate and water.

The results related to a non-polar component of asphalt binder's SFE in Table 8 show that using SBR polymer has increased the non-polar component of modified asphalt binders compared to the base asphalt binder. This leads to a formation with stronger non-polar bonds.

The total SFE results show that using SBR polymer has increased this parameter. The total SFE has a direct and linear relationship with cohesion free energy. The increase in the total SFE increases cohesion free energy. This means that higher energy is needed for the creation of a specific crack on the asphalt binder film. Increasing the energy needed for failure in the asphalt binder film reduces the probability of cohesion failure.

Table 8. SFE components of controlled and modified asphalt binders used in this study.

Asphalt binder type	SFE components (ergs/cm^2)				
	Basic	Acidic	Polar	Nonpolar	Total SFE
AC 60/70	0.45	2.69	2.20	11.36	13.56
AC 60/70 with 2 % SBR	0.79	2.98	3.07	12.28	15.35
AC 60/70 with 4 % SBR	1.03	3.27	3.67	13.84	17.51

3.2.3. Thermodynamic parameters

Results related to the cohesion free energy parameters, debonding energy, and adhesion free energy have been provided in Fig. 3–5.

A closer look in Fig. 3 shows that using SBR polymer has increased cohesion free energy value. This suggests that higher energy is required for cracking on the asphalt binder film which reduces the probability of cohesion failure.

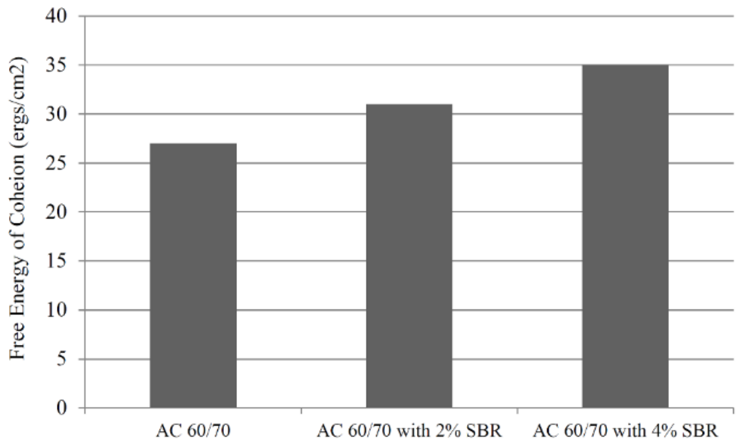

Figure 3. Cohesion free energy in controlled and modified asphalt binders.

Results related to the asphalt binder-aggregates adhesion free energy in dry conditions are shown in Fig. 4. This parameter presents the amount of energy required for creation of failure in asphalt binder-aggregate contact surface. It means that more energy is needed for separation of the asphalt binder from the aggregate surface. The amount of adhesion free energy in the specimens made of granite aggregate is more considerable than limestone aggregate. This suggests that more energy is required to separate the asphalt binder from the granite aggregate surface unit.

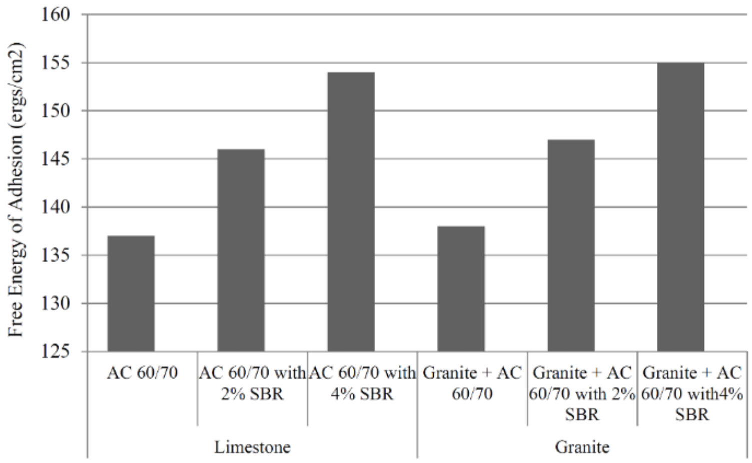

Figure 4. The asphalt binder-aggregate adhesion free energy under dry conditions.

According to the principles of thermodynamics, any energizer process is performed spontaneously. Therefore, when water enters into the binder-aggregate system, the asphalt binder debonding and the stripping event are expected to happen spontaneously. The important thing here is that greater amounts of released energy, lead to a higher stripping intensity. The results presented in Fig. 5 show that the use of SBR polymer in the specimens made of both types of aggregates has reduced the debonding energy. Increasing the percentage of these materials has reduced the value of this parameter. So, increasing the percentage of the polymer material has increased the tendency for stripping. As the data provided in the figure suggests, in the stripping of the compounds made of granite aggregates more energy is released, which indicates that stripping in the granite aggregate surface unit is more likely to occur.

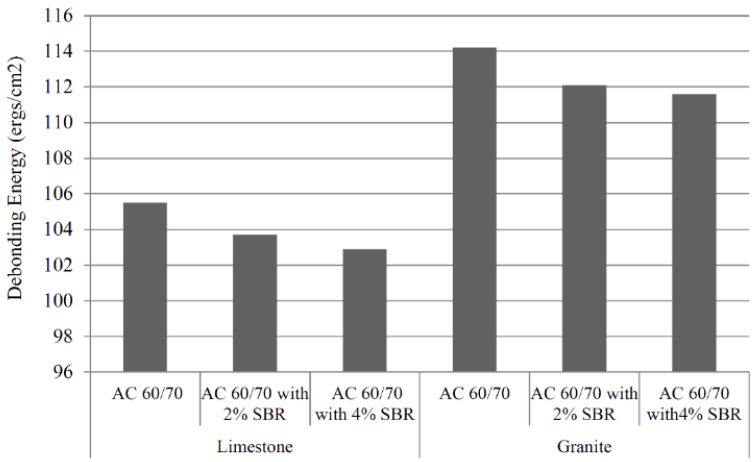

Figure 5. The asphalt binder-aggregate adhesion free energy under wet conditions.

3.3. Repetitive loading tests

Modulus ratio results for the specimens made of limestone and granite aggregates have been provided in Fig. 6, 7. The obtained results in Fig. 6, 7 shows the obvious effects of using the aggregates, asphalt binders and different additives on the moisture damage. Each of these components with mixed features can strengthen or weaken the asphalt mixture against moisture damage.

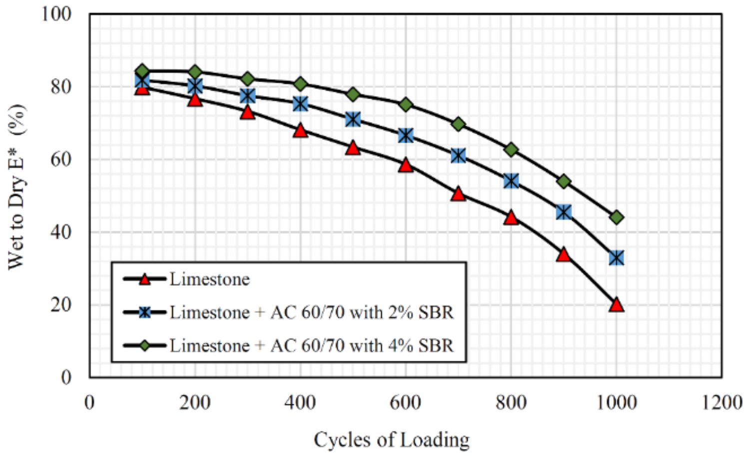

Figure 6. Indirect tensile modulus ratio in samples made of limestone aggregates.

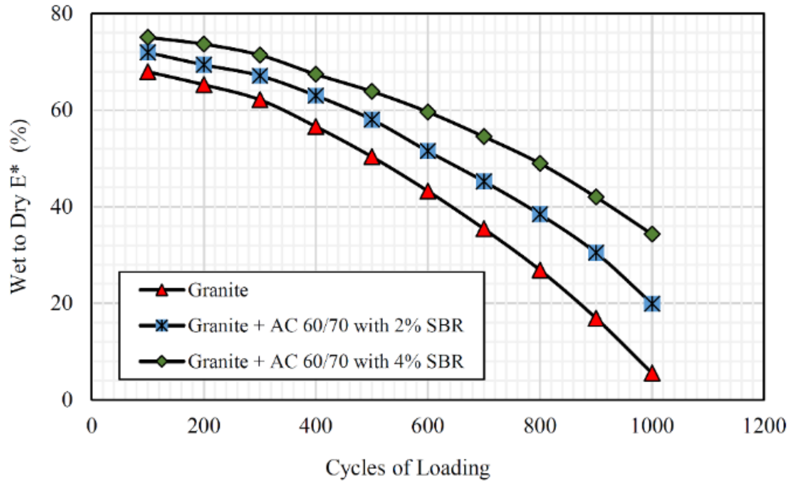

Figure 7. Indirect tensile modulus ratio in samples made of granite aggregates.

According to the results obtained in Fig. 6, the specimens made of controlled asphalt binder have the lowest modulus ratio in wet to dry conditions. The use of SBR polymer has increased the modulus ratio in these specimens. By increasing the percentage of the polymer additive, better performance of asphalt mixture against moisture has become more evident. The difference in the ratio of wet to dry modulus in the low loading cycle has become lower between the controlled and modified specimens. As the number of loading cycle increases, this difference also increases. In fact, it can be noted that the rate of decrease in the modulus (slope) in the controlled specimens is higher than the modified specimens.

The similar trend observed in specimens made of limestone aggregate can be seen in the specimens made of granite aggregate. The notable difference is that the use of SBR additives has made more improvements to the specimens made of granite aggregate.

As was observed in the analysis of the SFE method's results, the use of polymer materials increases cohesion and adhesion free energy in dry conditions. These two events reduce failure in the asphalt binder-aggregate contact surface and asphalt binder film, which increases the asphalt mixture's strength in loading conditions. As expected, placing the specimens under wet conditions has reduced asphalt mixture's strength against loading, because the influences of moisture reduce cohesion in asphalt binder and cause loss of adhesion in asphalt binder-aggregates. All of these factors reduce the asphalt mixture's strength.

3.4. Stripping percentage of the aggregates in loading cycles

Cheng [9] successfully used the continuous non-linear viscoelastic theory provided by Schapery for material damage for the description of the response of asphalt concrete under the strain and stress control loading. He applied the Schapery theory which mentioned that damage prediction was validated by repetitive loading tests based on diffusion theory. Thus, the moisture damage of asphalt concrete is obtained in repetitive loading by calculation of the aggregate surface percentage, which is subjected to stripping in different cycles. As can be observed in Equation (16), the strength ratio (modulus) in wet to dry conditions can be considered to be same as the adhesion ratio between aggregates-asphalt binder in wet and dry conditions [31].

$$\infty \frac{E_{*wet}}{E_{*dry}} = \frac{\left[\Delta G_{12} * (1-P) + \Delta G_{132} P\right]}{\left[\Delta G_{12}\right]}, \quad (16)$$

where ΔG_{12} denotes the asphalt binder-aggregate adhesion energy, ΔG_{132} denotes the asphalt binder-aggregate debonding or system energy in a saturated condition, and P is the percentage of the aggregate surface which is subjected to stripping.

For repetitive loading test of strain control, Equation (16) can be converted to Equation (17).

$$\circ \frac{E_{*wet}}{E_{*dry}} = \frac{\left(\frac{\sigma}{\varepsilon}\right)_{wet}}{\left(\frac{\sigma}{\varepsilon}\right)_{dry}} = \frac{\varepsilon_{wet}}{\varepsilon_{dry}} = \frac{\left[\Delta G_{12}(1-P) + \Delta G_{132} P\right]}{\left[\Delta G_{12}\right]}. \quad (17)$$

All parameters of Equation (17), except for index P, can be obtained from the thermodynamic concepts by measuring the SFE components of asphalt binders and aggregates (Tables 7, 8) and wet to dry modulus ratio (Fig. 6, 7). Knowing that P is the only thing missing from this equation, it can be calculated and used to determine the stripping trend of the aggregate surface from asphalt binders in different loading cycles for various asphalt concrete.

Results related to asphalt binder stripping percentage from the aggregate surface on the specimens made of granite and limestone aggregates are provided in Fig. 8, 9, respectively. As a consequence, using polymer additives has reduced the asphalt binder stripping percentage from the aggregate's surface in different loading cycles. Moreover, it can be observed that the slope in the stripping percentage against the loading cycles chart has an increasing trend. In fact, all aggregates in the primary cycles of loading are attached to the asphalt binder. Higher exposure of specimens to wet conditions and loading frequency leads to a higher percentage of aggregates to be stripped from the asphalt binder. This causes the adhesion reduction and the attached aggregate percentage reduction to intensify each other, and therefore, the asphalt binder stripping from the aggregate surface continues with a steeper slope.

It can be observed from Fig. 8, 9 that specimens made of limestone aggregates have higher strength compared to the specimens made of granite aggregates. Different factors are effective in the occurrence of moisture damage and the strength of asphalt concrete against it. The structure of minerals forming the aggregates used in asphalt concrete is one of the most significant parameters. Two minerals, SiO_2, and CaO (or $CaCO_3$) cause a significant change in the hydrophobic or hydrophilic properties of aggregates. A higher percentage of SiO_2 mineral indicates that the hydrophilic tendency of aggregates has increased and vice versa.

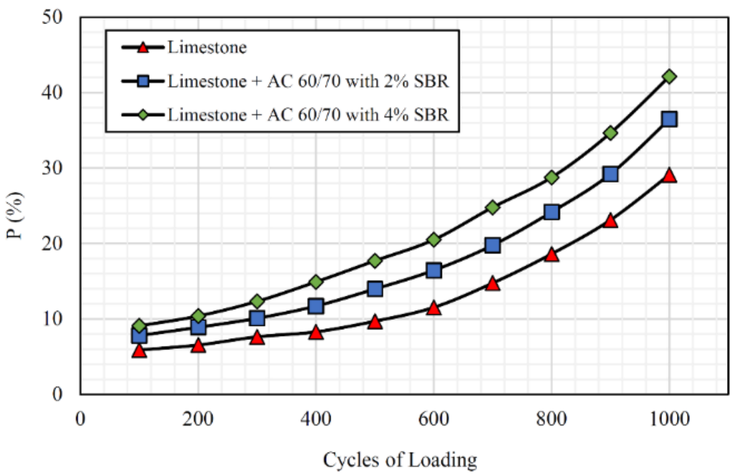

Figure 8. Stripping percentage of aggregate surface in samples made of limestone aggregates.

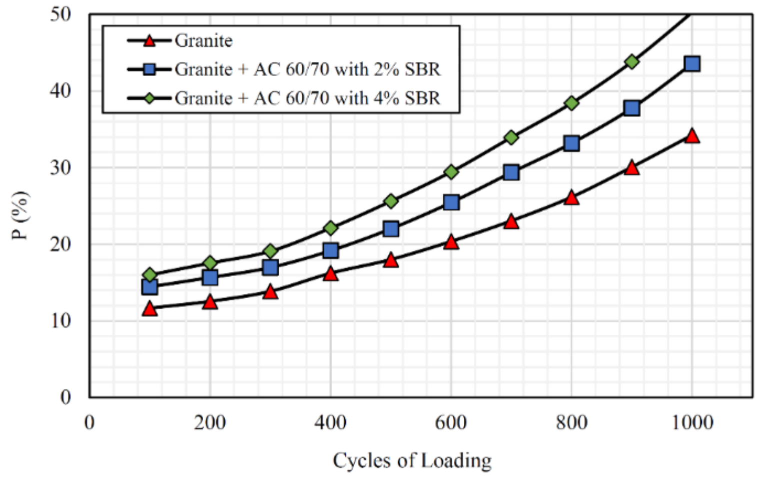

Figure 9. Stripping percentage of aggregate surface in samples made of granite aggregates.

Conversely, a higher percentage of the CaO mineral indicates that the hydrophobic tendency of aggregates has increased and vice versa [32]. It can be observed from Table 1 that a large part of granite aggregate is formed by silicon dioxide (SiO_2) which leads to strong acidic properties. The amount of strong basic parts such as calcium oxide (CaO) in this type of aggregate is much lower than the acidic part. There are hydroxyl groups (OH) on the surface of granite aggregate. These groups (SiOH) form hydrogen bonds with carboxylic acids, which are very effective in asphalt binder-aggregates adhesion. However, hydrogen bond easily breaks in the presence of water, and these two groups are separated, and each one produces a hydrogen bond with water molecules [33]. Conversely, in the case of limestone aggregates, it is observed that the SiO_2 mineral percentage is much lesser than the CaO mineral. In fact, the main reason for the high adhesion strength between limestone aggregates and asphalt binders is caused by the formation of insoluble bonds (covalent) in water that is formed due to the physical reaction between the calcium on the aggregate surface and some functional groups of asphalt binder.

4. Conclusions

There are various experimental methods for improving the moisture susceptibility in asphalt concrete, and the most common one is the use of anti-stripping additives. Technical and executive problems of the existing anti-stripping materials and the technical defects in the moisture susceptibility evaluation methods of asphalt concrete have led to the study of the SBR polymer effects using mechanical and thermodynamic techniques. The most important experimental results obtained in the present investigation are:

1. Using SBR polymer improved the strength of asphalt concrete against moisture damage, especially in specimens made of granite aggregates.

2. Adding SBR polymer increases the cohesion and adhesion free energy and reduces the debonding energy in stripping of specimens containing both types of aggregates, which indicates a decrease in the tendency of the system for stripping.

3. The stripping percentage index that is obtained by combining the results of the repetitive loading test in wet and dry conditions along with the results of the thermodynamic parameters indicate that the specimens made of controlled asphalt binders in loading cycles under wet conditions are subject to a higher rate of stripping, and the falling rate of the loading modulus in them is faster than the modified specimens.

4. The use of SBR polymer has increased both the basic and acidic components of asphalt binders. The percentage of increase in the basic component is higher than the acidic component, which results in the formation of more basic properties in the asphalt binders modified by this material.

5. Adding SBR polymer has increased the asphalt binder's polar component. The positive or negative impact of this parameter on the asphalt binder aggregates adhesion cannot be stated with certainty. The only thing to note is that the increase in the polar properties of asphalt binders increases the desire of its adhesion to polar materials such as aggregates and water.

6. The use of SBR polymer has increased the non-polar component of the modified asphalt binders compared to the base asphalt binder. This leads to the formation of stronger non-polar bonds.

References

1. Arabani, M., Shabani, A., Hamedi, G.H. Experimental Investigation of Effect of Ceramic Fibers on Mechanical Properties of Asphalt Mixtures. Journal of Materials in Civil Engineering. 2019. 31 (9). DOI: 10.1061/(ASCE)MT.1943-5533.0002821
2. Shekhovtsova, Sy., Korolev, E., Inozemtcev, S., Yu, J., Yu, H. Method of forecasting the strength and thermal sensitive asphalt concrete. Magazine of Civil Engineering. 2019. 89 (5). Pp. 129–140. DOI: 10.18720/MCE.89.11

3. Stuart, K. Moisture damage in asphalt mixtures-a state-of-the-art report. 1990. Pp. 125. URL: https://trid.trb.org/view/1175602 (date of application: 16.12.2019).
4. McGennis, R.B., Kennedy, T.W., Machemehl, R.B. Stripping and moisture damage in asphalt mixtures. Center For Transportation Research, The University Of Texas, Austin. 1984.
5. Hamedi, G.H. Evaluating the effect of asphalt binder modification using nanomaterials on the moisture damage of hot mix asphalt. Road Materials and Pavement Design. 2017. 18 (6). Pp. 1375–1394. DOI: 10.1080/14680629.2016.1220865
6. Al-Qadi, I.L., Abuawad, I.M., Dhasmana, H., Coenen, A.R., Trepanier, J.S. Effects of Various Asphalt Binder Additives/Modifiers on Moisture-Susceptible Asphaltic Mixtures. Illinois Center for Transportation. 2014.
7. Zavyalov, M.A., Kirillov, A.M. Evaluation methods of asphalt pavement service life. Magazine of Civil Engineering. 2017. 70 (2). Pp. 42–56. DOI: 10.18720/MCE.70.5
8. Elphingstone, G. Adhesion and cohesion in asphalt-aggregate systems. Texas A&M University, 1998.
9. Cheng, D. Surface free energy of asphalt-aggregate system and performance analysis of asphalt concrete based on surface free energy. Texas A&M University, 2003.
10. Fallahi Abandansari, H., Modarres, A. Investigating effects of using nanomaterial on moisture susceptibility of hot-mix asphalt using mechanical and thermodynamic methods. Construction and Building Materials. 2017. 131. Pp. 667–675. DOI: 10.1016/j.conbuildmat.2016.11.052
11. Bhasin, A. Development of methods to quantify bitumen-aggregate adhesion and loss of adhesion due to water. Texas A&M University, 2006.
12. Howson, J.E. Relationship between surface free energy and total work of fracture of asphalt binder and asphalt binder-aggregate interfaces. Texas A&M University, 2011.
13. Hamedi, G.H., Moghadas Nejad, F. Using energy parameters based on the surface free energy concept to evaluate the moisture susceptibility of hot mix asphalt. Road Materials and Pavement Design. 2015. 16 (2). Pp. 239–255. DOI: 10.1080/14680629.2014.990049
14. Hamedi, G.H., Moghadas Nejad, F. Evaluating the effect of mix design and thermodynamic parameters on moisture sensitivity of hot mix asphalt. Journal of Materials in Civil Engineering. 2017. 29 (2). DOI: 10.1061/(ASCE)MT.1943-5533.0001734
15. Cai, L., Shi, X., Xue, J. Laboratory evaluation of composed modified asphalt binder and mixture containing nano-silica/rock asphalt/SBS. Construction and Building Materials. 2018. 172. Pp. 204–211. DOI: 10.1016/j.conbuildmat.2018.03.187
16. Moghadas Nejad, F., Azarhoosh, A.R., Hamedi, G.H., Azarhoosh, M.J. Influence of using nonmaterial to reduce the moisture susceptibility of hot mix asphalt. Construction and Building Materials. 2012. 31. Pp. 384–388. DOI: 10.1016/j.conbuildmat.2012.01.004
17. Hamedi, G.H., Moghadas Nejad, F., Oveisi, K. Investigating the effects of using nanomaterials on moisture damage of HMA. Road Materials and Pavement Design. 2015. 16 (3). Pp. 536–552. DOI: 10.1080/14680629.2015.1020850
18. Hamedi, G.H., Moghadas Nejad, F. Use of aggregate nanocoating to decrease moisture damage of hot mix asphalt. Road Materials and Pavement Design. 2016. 17 (1). Pp. 32–51. DOI: 10.1080/14680629.2015.1056215
19. Moghadas Nejad, F., Arabani, M., Hamedi, G.H., Azarhoosh, A.R. Influence of using polymeric aggregate treatment on moisture damage in hot mix asphalt. Construction and Building Materials. 2013. 47. Pp. 1523–1527. DOI: 10.1016/j.conbuildmat.2013.06.060
20. Hesami, S., Roshani, H., Hamedi, G.H., Azarhoosh, A. Evaluate the mechanism of the effect of hydrated lime on moisture damage of warm mix asphalt. Construction and Building Materials. 2013. 47. Pp. 935–941. DOI: 10.1016/j.conbuild-mat.2013.05.079
21. Faramarzi, M., Golestani, B., Lee, K.W. Improving moisture sensitivity and mechanical properties of sulfur extended asphalt mixture by nano-antistripping agent. Construction and Building Materials. 2017. 133. Pp. 534–542. DOI: 10.1016/j.conbuildmat.2016.12.038
22. Park, D.W., Seo, W.J., Kim, J., Vo, H.V. Evaluation of moisture susceptibility of asphalt mixture using liquid anti-stripping agents. Construction and Building Materials. 2017. 144. Pp. 399–405. DOI: 10.1016/j.conbuildmat.2017.03.214
23. Souliman, M.I., Hajj, E.Y., Sebaaly, P.E. Impact of antistrip additives on the long-term aging rheological properties of asphalt binders. Journal of Materials in Civil Engineering. 2015. 27(8). DOI:10.1061/(ASCE)MT.1943-5533.0001111.
24. ASTM D7369. Standard test method for determining the resilient modulus of bituminous mixtures by indirect tension test.West Conshohocken, PA, 2011.
25. De, S.K., White, J.R. Rubber technologist's handbook. Smithers Rapra Technology. New York, 2001.
26. Arabani, M., Shabani, A. Evaluation of the ceramic fiber modified asphalt binder. Construction and Building Materials. 2019. 205. Pp. 377–386. DOI: 10.1016/J.CONBUILDMAT.2019.02.037
27. ASTM D1559. Test method for resistance of plastic flow of bituminous mixtures using marshall apparatus.West Conshohocken, PA, 1989.
28. Shah, B.D. Evaluation of moisture damage within asphalt concrete mixes. Texas A&M University, 2004.
29. Little, D.N., Bhasin, A. Using Surface Energy Measurements to Select Materials for Asphalt Pavement. National Cooperative Highway Research Program (NCHRP). 2006. 104.
30. Shekhovtsova, S.Y., Korotkov, A. V., Vysotskaya, M.A. Method of forecasting the effectiveness of cationic bitumen emulsions. Magazine of Civil Engineering. 2018. 78 (2). Pp. 91–100. DOI: 10.18720/MCE.78.7
31. Witczak, M., Kaloush, K., Pellinen, T., El-Basyouny, M. Appendix A–Test method for dynamic modulus of asphalt concrete mixtures for permanent deformation. National Cooperative Highway Research Program (NCHRP). 2002. 465.
32. Tarrer, A., Wagh, V. The effect of the physical and chemical characteristics of the aggregate on bonding. Strategic Highway Research Program (SHRP). 1991.
33. Hicks, R. Moisture damage in asphalt concrete, NCHRP synthesis of highway practice 175. Transportation Research Board. 1991.

Contacts:

Amir Shabani, amirsh@kth.se

Gholam Hossein Hamedi, hamedi@guilan.ac.ir

Magazine of Civil Engineering

journal homepage: http://engstroy.spbstu.ru/

ISSN 2712-8172

DOI: 10.34910/MCE.109.2

Deformation criteria for reinforced concrete frames under accidental actions

N.V. Fedorovaa, **N.T. Vu**b*

[a] *National Research Moscow State Civil Engineering University, Moscow, Russia*

[b] *Southwest State University, Kursk, Russia*

**E-mail: fenavit@mail.ru*

Keywords: reinforced concrete, capacity curve, column removal scenario, alternate load path, progressive collapse

Abstract. A review of scientific research on survivability and protection of buildings from progressive collapse showed that despite the researchers' increasing interest in the problem, many tasks in this area are waiting to be solved. The subject of the study in this work was the study of the parameters of the capacity curves of cross-sections of reinforced concrete elements of constructive systems of building frames under their static-dynamic loading conditions. This paper presents a methodology for determining the parameters of "load-deflection" curves and the deformation criterion for accidental limit state of a reinforced concrete element of statically indeterminate frame-rod constructive systems under an accidental action caused by removing one of the load-bearing elements from the constructive system. Two stages of loading such systems are considered: static loading to a specified design level and additional dynamic loading caused by a sudden structural rearrangement of the constructive system from the mentioned action. At the first stage of loading, the relative parametric load of cracking in an arbitrary cross-section of the reinforced concrete element of the constructive system and the sequence of formation of plastic hinges in this element is determined using an extraordinary version of the mixed method of structural mechanics of rod systems. At the second stage, the limit value of the relative parametric load is determined on an energy basis without using the structural dynamics apparatus. An algorithm for calculating parameters of the capacity curve of cross-sections of reinforced concrete elements of constructive systems under the considered actions and calculation results of the "relative parametric load-deflection" curve for the most stressed cross-section of the reinforced concrete frame when a middle column is removed from it are presented. The calculated values of the deforming cross-section parameters are compared with experimental data. It is shown that the use of parametric load in the proposed calculated dependencies for analyzing the sequence of formation of plastic hinges in the constructive system is in satisfactory agreement with the test results of such constructive systems under the considered loading regimes.

1. Introduction

Currently, in the regulatory documents of many countries, when designing constructive systems of buildings, an analysis must be performed to protect against progressive collapse, in particular, to check the criteria for an accidental limit state for elements of a constructive system when one of the supporting structures, for example, one of the columns of the first floor of a building, is suddenly removed from it. And despite the fact that scientific research in this area around the world has been intensively conducted since the end of the last century, after the well-known event with the Ronan Point tower in London [1], answers to many scientific questions about this problem have not yet been received. And if the term "progressive (disproportionate) collapse" is clearly understood by scientists in various countries as a sequential (chain) failure of load-bearing building structures, leading to the collapse of the entire structure or its parts due to

Fedorova, N.V., Vu, N.T. Deformation criteria for reinforced concrete frames under accidental actions. Magazine of Civil Engineering. 2022. 109(1). Article No. 10902. DOI: 10.34910/MCE.109.2

a sudden local failure [2–5], the criteria for protection against such failure are understood and accepted far from unambiguous. Moreover, even terminologically, these criteria are designated differently: limit state criteria [6–9], beyond limit state criteria [2, 3], accidental limit state criteria [10, 11]. In the most rapidly developing algorithms for numerical modeling of these processes, for example [12, 13], traditional physical models of material deformation are laid, without taking into account the specifics and mechanisms of the considered loading regime of structures, and despite the fact that such models are the most representative and can be relatively universal, the practical recommendations for designing that follow from these models are not confirmed experimentally are of a particular nature and are often questionable. Moreover, such models are very demanding in terms of computational capabilities (see, for example, [14]), which, taking into account the requirements for the qualification of the constructor, allows them to be used in design practice only in special cases.

There are also known alternative approaches to solving problems of considered class, focused on analytical and semi-analytical methods of analysis using the concept of the so-called " alternate load path" and structural level models for these problems [5, 15, 16]. In these solutions, the physical side of deformation is associated with the mechanisms of progressive collapse development, followed by the available experimental studies results. Assessment of dynamic forces arising in this case in cross-sections of constructive system elements is most often made on an energy basis, the idea of which was first expressed still a quarter of a century ago by prof. G.A. Geniev [17] and which is currently used in many researches, for example [16, 18, 19]. At the same time, the material stress–strain curves in these researches are accepted as for the regime of one-stage static loading, without taking into account the time of removal of the supporting structure and the features of cross–section deformation under high-speed loading (impact), see, for example, the research [6, 10, 20–22]. And this, as established by experimental studies [23–25], significantly affects the ultimate strains and strength properties of structural materials and, accordingly, the deformation or strength criteria of an accidental limit state accepted for analysis.

One of the criteria for the accidental limit state of reinforced concrete elements of statically indeterminate constructive systems of buildings in scientific publications [3, 7, 11, 20, 26] and current regulatory documents is the condition for limiting the ultimate deflections of the structure after removing one of the constructive elements, the excess of which is taken as the exhaustion of the load-bearing capacity of the constructive system. At the same time, the analysis of deflections of reinforced concrete elements of the considered structures using traditional "moment-curvature" curves, especially static capacity curves, can be performed to the load level, when the reinforced concrete element is crushed by compressed zone, divided into separate blocks and turns into a hanging system. Such a solution for the simplest structurally nonlinear statically indeterminate beam was considered, for example, in [27, 28]. But this solution is limited to the first two criteria of failure, defined by limiting the ultimate strains of concrete or rebar. There are very few works devoted to the study of deformation of reinforced concrete constructive systems during their transformation from rigid to flexible hanging systems, and the available solutions, even such detailed ones as [18–22], also use diagrams of static deformation of concrete and reinforcement.

This work aimed to determine the parameters of static-dynamic capacity curves and strain criteria for concrete frames with their structural rearrangement from rigid systems in hanging when the sudden removal of constructive systems of one of the bearing structures. The main investigated parameters were the relative load levels at which cracks and plastic hinges formed in the frame elements during static load increase and their subsequent dynamic additional loading after removal of one of the columns, and the deformation criteria for failure of the constructive system under the considered static-dynamic loading regime.

2. Methods

Consider the frame-rod constructive system of a reinforced concrete building, the beams of which are reinforced symmetrically with reinforcing bars in the upper and lower zones (Fig. 1). Such reinforcement and reliable anchoring of reinforcing bars of beams with their lead into the body of the column are aimed at ensuring the work of the loaded system under accidental limit state caused by removing one of the columns, and the sudden redistribution of force flows in the frame system.

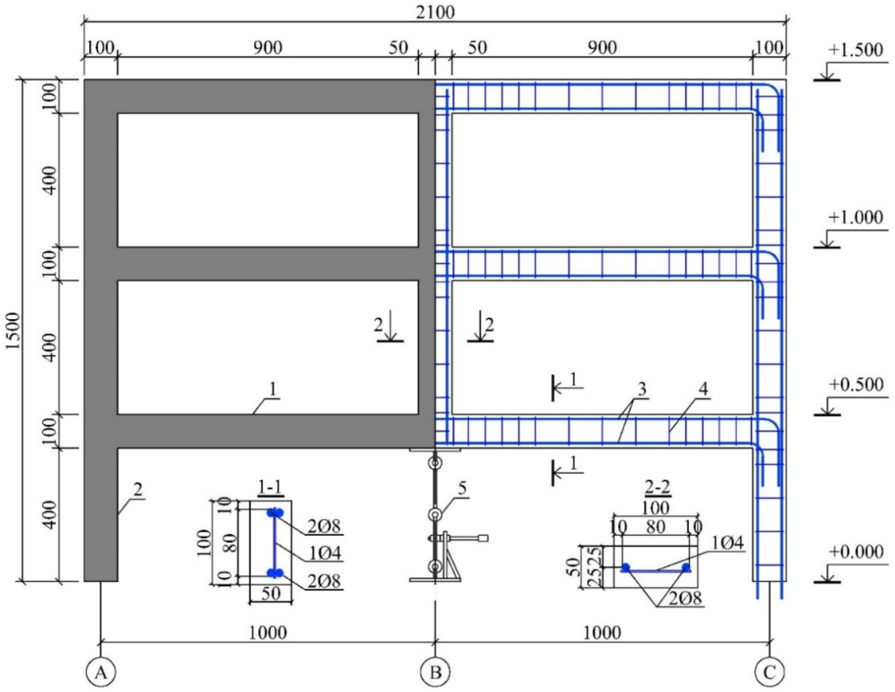

a b

Figure 1. The formwork scheme (a) and the reinforcement scheme (b) of the frame structure: 1 – beam; 2 – column; 3 – longitudinal reinforcement; 4 – transverse reinforcement; 5 – equipment modeling loss of column.

The “parametric load-deflection” curve $(\lambda_m - f)$ of the cross-section of the reinforced concrete element of a constructively non-linear system at all levels of its deformation under static and static-dynamic loading in a general form can be represented by graphs in Fig. 2.

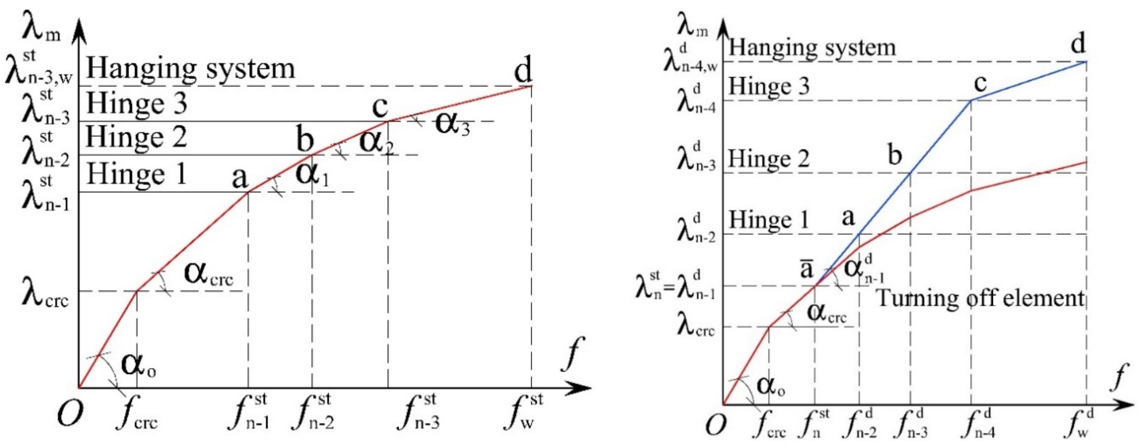

a b

Figure 2. “Relative parametric load – deflection $(\lambda_m - f)$” curves of a cross-section of a reinforced concrete element of a physical and constructive nonlinear system: a – under static loading; b – under static loading and dynamic additional loading.

We define the characteristic points of these graphs. Let a statically indeterminate frame-rod constructive system be given, loaded with forces λP_i applied at arbitrarily given points at distances $al_1,\ al_2$ from the supports along the length of the span of each beam (Figure 3). Moreover, the load on the beam is accepted as parametric, and their change occurs in proportion to a certain parameter λ. Cross-sections $C_1, C_2, ..., C_k$ where it is possible to turn off connection (the formation of plastic hinges or brittle failure of a cross-section on compressed concrete) as the parameter λ increase are known: these are nodes of the frame-rod system, points of application of concentrated forces, points of change in the stiffness of the rod system.

As the frame-rod system is loaded to the level $\lambda_{crc}P_i$ (see Figure 2a), cracking begins in the most stressed cross-section of one of the elements of the constructive system. Accordingly, the stiffness of the considered cross-section changes from the initial stiffness $B_0 = tg\alpha_0$ to the stiffness of the element with cracks $B_{crc} = tg\alpha_{crc}$. The calculation of this stiffness is performed according to the dependences known in the theory of reinforced concrete, for example, the formulas of [29].

With further loading of the constructive system with a static load in the frame structure, the process of cracking in the considered and other frame elements continues. At a certain level of load $\lambda_1 P_i$, in one of the cross-sections of the most stressed element, the first plastic hinge is formed, and its rigidity will accordingly decrease to a value $B_1 = tg\alpha_1$. A further increase in the load to levels $\lambda_2 P_i$ and $\lambda_3 P_i$ will lead to the formation of a second and then a third plastic hinge in the beam and the element under consideration turns from rigid to flexible. The reinforcement begins to work in tension as a cable.

After an accidental action is imposed on the loaded constructive system in the form of a sudden column removal from the frame system, its static indeterminacy decreases, and the force flows are redistributed from the structural rearrangement of the constructive system. Accordingly, the forces M_j in the cross-sections of the beams of the frame change, and the loading regime of the beam changes from static to dynamic. The determination of forces M_j in a constructive system after such an action can be performed using an extraordinary version of the mixed method [30]. The essence of the method is that the mixed calculation method's main system is selected in the form of a hinged-rod polygon with the connections removed at the places of possible switching off and replacing them with unknown ones M_j $(j = 1, 2, ..., k)$ (Figure 3a, b). If a geometrically variable main system is formed when the connections are removed, then additional connections are superimposed Z_i $(i = k+1, k+2, ..., n)$.

In this case, the stage of static loading with initial stiffness to the level $\lambda_{crc}P_i$ remains unchanged. Then, upon further loading of the *n*-times static indeterminate constructive system to the level of the given static load λ_n^{st} (see Figure 2b), the cross-section of the beam is deformed as in the case of static loading of the initial *n*-times statically indeterminate frame.

Using the main system selected as described, the relative parametric load $\lambda_m P_i$ can be determined at which one of the criteria for an accidental limiting state is achieved in the most stressed cross-section of the beam under static-dynamic loading of the frame. As with static loading, the index *m* determines the level of relative load $\lambda_m P_i$ at which, after the imposition of accidental action in the form of removing one of the columns of the frame in one of the cross-sections of the most loaded beam adjacent to the removed column, the ultimate moment is reached, i.e., the first plastic hinge is formed. Then, as the dynamic load increases, the second and third hinges are formed (on the curve, the hinges' formation is indicated by points $\lambda_{n-2}^d, \lambda_{n-3}^d, \lambda_{n-4}^d$, respectively). If, after the formation of the third plastic hinge, the deformation of the reinforcement does not reach the limiting values and its anchoring in the support cross-sections of the beam is not violated, then the construction of the continuous beam from a rigid beam turns into a variable cable system, which only resists tension. On the graphs "$\lambda_m - f$" this relative load is indicated by $\lambda_{n-4,w}^d$. In this case, the third criterion for the accidental limiting state is checked - the criterion for the maximum allowable deflection of the structure f_w^d.

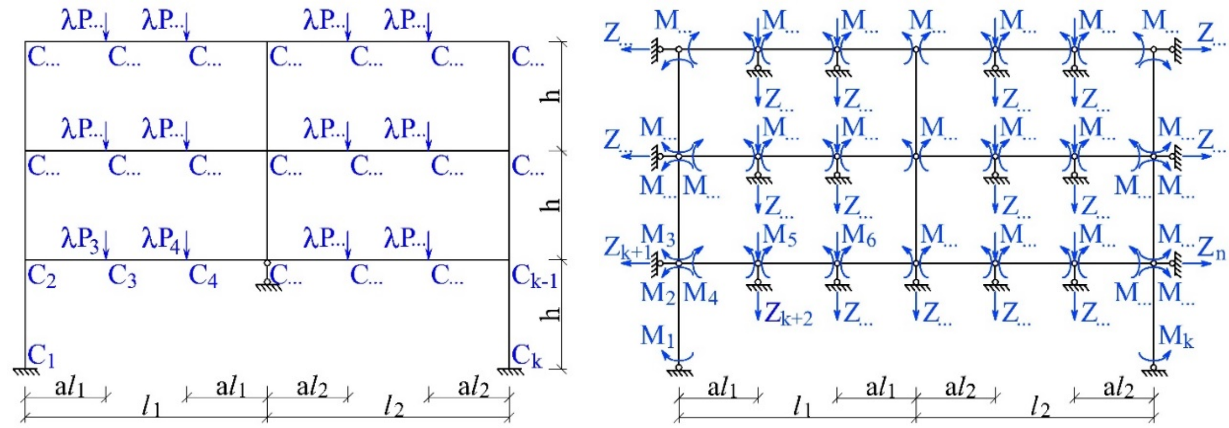

a b

Figure 3. The specified (a) and main (b) system of the mixed method for determining the parametric load.

Analyzing the capacity curve of the cross-section of the reinforced concrete element can be noted that the segment of the successive formation of plastic hinges «$\overline{a}-a-b-c$» in the static-dynamic capacity curve differs from the analogous segment in the static capacity curve of the cross-section in that it does not have turning point caused by the reduced and manifest in the time of bending stiffness of the beam cross-sections. The absence of these turning points in the segment of the dynamic capacity curve «$\overline{a}-a-b-c$» of the beam cross-section is explained by the adopted two-element model of high-speed dynamic deformation of reinforced concrete [16, 31] according to which the work of a purely viscous element (Kelvin-Voigt) ends at a very small value of time t, reported from the moment of the beginning of dynamic loading, having, according to experimental data [3, 29, 32, 33] the order of tenths and even hundredths of a second. However, over this interval of time, the viscous element in the two-element model contributes to the inhibition of the development of strains initiated in the elastic element and, consequently, to an instantaneous increase in the cross-section stiffness on the segments of dynamic deformation "$\overline{a}-a-b-c$" equal to $B_{n-1}^{d}=tg\alpha_{n-1}^{d}$ (see Fig. 2b).

The parameters of the presented static-dynamic capacity curve “relative parametric load-deflection” for an arbitrary cross-section of the frame-rod system can be calculated using a specially constructed system of canonical equations of an extraordinary version of the mixed method (see Fig. 3), in which the load coefficients are presented in the form two terms [30].

$$\left.\begin{aligned} A\cdot\vec{M}+B\cdot\vec{Z}+\vec{\Delta}_q+\vec{\delta}_p\cdot\lambda=0 \\ C\cdot\vec{M}+D\cdot\vec{Z}+\vec{R}_q+\vec{r}_p\cdot\lambda=0 \end{aligned}\right\}, \tag{1}$$

where $A, B, \vec{\Delta}_q, C, D, \vec{R}_q$ are the matrix coefficients of unknowns mixed method; $\vec{\delta}_p$ is the matrix of displacements in the direction of remote connections from an external parametric load P_i at $\lambda=1$; $\vec{r}_p$ is the reaction matrix in superimposed connections of the main system from an external parametric load at $\lambda=1$.

Given the properties of the canonical equations of the mixed method $C=-B^T$, where the index "T" means the transpose operation, we rewrite the system of equations in the form:

$$\begin{Vmatrix} A & B \\ -B^T & 0 \end{Vmatrix}\cdot\begin{Vmatrix} \vec{M} \\ \vec{Z} \end{Vmatrix}+\begin{Vmatrix} \vec{\Delta}_q \\ \vec{R}_q \end{Vmatrix}+\begin{Vmatrix} 0 \\ \vec{r}_p \end{Vmatrix}\cdot\lambda=0. \tag{2}$$

The solution to this system is:

$$\begin{Vmatrix} \vec{M} \\ \vec{Z} \end{Vmatrix}=\begin{Vmatrix} \vec{M}_q \\ \vec{Z}_q \end{Vmatrix}+\begin{Vmatrix} \vec{m}_p \\ \vec{z}_p \end{Vmatrix}\cdot\lambda \tag{3}$$

where

$$\left\|\begin{matrix}\vec{M}_q \\ \vec{Z}_q\end{matrix}\right\| = -\left\|\begin{matrix}A & B \\ -B^T & 0\end{matrix}\right\|^{-1} \cdot \left\|\begin{matrix}\vec{\Delta}_q \\ \vec{R}_q\end{matrix}\right\|; \quad \left\|\begin{matrix}\vec{m}_p \\ \vec{z}_p\end{matrix}\right\| = -\left\|\begin{matrix}A & B \\ -B^T & 0\end{matrix}\right\|^{-1} \cdot \left\|\begin{matrix}0 \\ \vec{r}_p\end{matrix}\right\|. \tag{4}$$

The value of the forces in the turned off connections of the constructive system from the total action of the given and parametric loads are calculated by the formulas:

$$M_j = M_{jq} + m_{jp} \cdot \lambda, \left(j = 1, 2, ..., k\right), \tag{5}$$

where M_{jq} and m_{jq} are the column matrix elements $\vec{M}_p$ and $\vec{m}_p$.

Criteria verification of survivability[1] of a physical and constructive nonlinear system under accidental action is performed based on the calculation of the parameters of capacity curve “ $\lambda_m - f$ ”. Turning off the moment connection (the formation of a plastic hinge with a limited deformation branch) in one of the elements of the frame system after removing one of the columns will occur in the case when, at the ultimate moment $M^d_{j,ult}$ in compressed concrete or tensile reinforcement, ultimate deformations are reached. Then, for all forces in turning off moment connections, the system of inequalities must be satisfied:

$$\left|M_j\right| = \left|M_{jq} + m_{jp} \cdot \lambda\right| \le M^d_{j,ult}, \left(j = 1, 2, ..., k\right), \tag{6}$$

where $M^d_{j,ult}$ is the ultimate value of the dynamic forces in the turned off connection.

On the left side of the system of inequalities (6), M_j is taken in absolute value, since the presence of a negative sign of M_j indicates that the direction of this force is opposite to the ultimate value of the force accepted in the main system.

The minimum value of the parametric load λ_m $(m = 1, 2, 3)$ at which the maximum value of the moment is reached in the most loaded cross-section of the beam C_j under the considered accidental action can be determined by the formula:

$$\lambda_m = \min\left(\frac{M^d_{j,ult} \pm \left|M_{jq}\right|}{m_{jp}}\right), \left(j = 1, 2, ..., k\right). \tag{7}$$

The “minus” sign in the numerator is accepted if M_{jq} and m_{jp} match and vice versa.

The end of the beam's deformation stage as an invariable structure $\lambda = \lambda^d_m$ $(m = n-2, n-3, n-4)$ occurs when the ultimate values of the moments are reached in the three cross-sections of the beam, and the cross-sections undergo local failure in compressed concrete at $\varepsilon_b = \varepsilon_{bu}$ (Figure 4a).

Up to this moment, the displacements (deflections) of cross-sections where the ultimate deformations of concrete $\varepsilon_b = \varepsilon_{bu}$ are achieved occur as in a rigid-plastic body from bending and turning cross-sections. If the reinforcement deformations do not reach the limiting values $\varepsilon_s < \varepsilon_{su}$, then the work of the beam construction passes from the stage of elastic-rigid-plastic deformation to the stage of work as a hanging system, when the reinforcement A_s and $A_s^{'}$ acts as tensile cables(Figure 4b). Rigid concrete blocks "hang" on reinforcing bars (cables). The limit value of the deflection of the beam at this stage is determined as for a cable system by the known dependencies of structural mechanics. In this case, the criterion of an accidental limiting state becomes the maximum deflection $f = f^d_w$ determined by calculation as for a hanging system. The experimental data on the relative value of this deflection before the rupture of the

[1] Here, the term "verification of survivability" refers to modeling the progressive collapse resistance of the constructive system of a building, which boils down to finding an initial local failure in one of the most stressed cross-sections of the system and sequentially propagating this failure (the sequence for turning off new connections), taking into account a decrease in the degree of static indeterminateness of the system, and also the dynamic effect caused by the sudden turning off the first and subsequent connections.

reinforcement in the tests of different authors vary significantly and range from 1/30 span in the studies [23, 25, 34] to 1/20 and even 1/10 in the study [35–37]. As a standardized value in Russian Standards SP 385.1325800.2018, carefully, for all types of reinforcement, the value 1/50 of the span is taken.

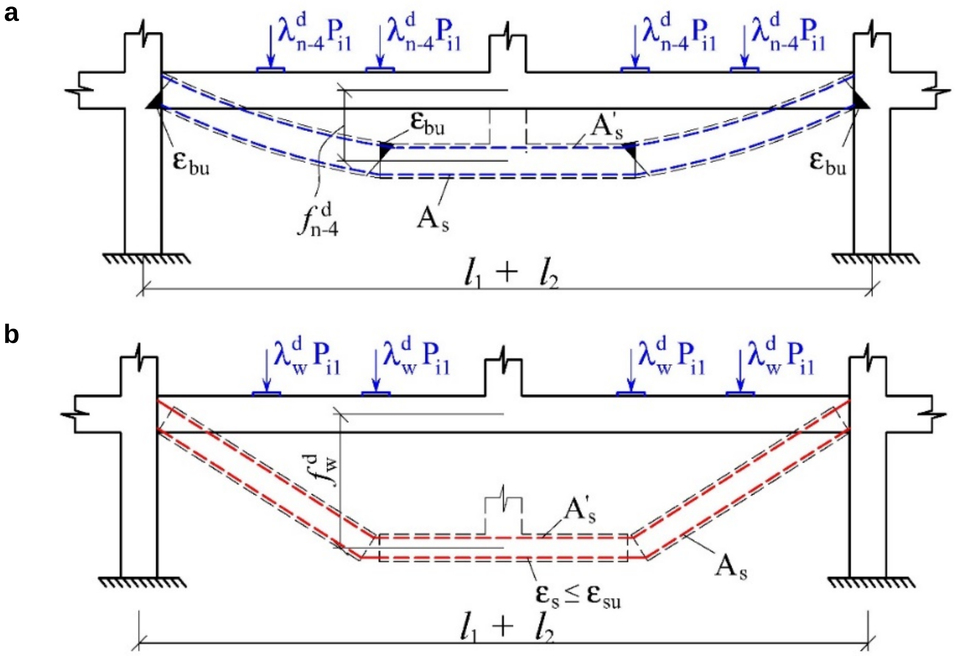

Figure 4. The scheme of displacement in the considered double-span beam substructure as an elastic-rigid-plastic body (a) and as a cable (b).

3. Results and Discussion

The reliability of the proposed model was evaluated by comparing the experimental results conducted by the author and other scientists.

3.1. Static-dynamic tests

For analysis, experimental studies of the static-dynamic frame test carried out in [29] are considered. In the experimental structure of a two-span three-story frame of the third series, the beams' reinforcement is symmetrical in the upper and lower zones by two rods with a diameter of 8 mm of class A500. The reinforcement scheme of the experimental structure is shown in Fig. 1. The beams' transverse reinforcement is adopted from a wire with a diameter of 2 mm in increments of 50 mm and 100 mm. The construction is made of fine-grained concrete of class B40.

When calculating the experimental frame structure, a two-stage regime of its loading is considered. At the first stage, the structure was loaded with concentrated forces λP_i according to the scheme of Figure 3a, symmetrically applied by two forces to each beam to the level of relative value $\lambda = 1$. The value of the relative load corresponding to the formation of cracks λ^{st}_{crc} was 0.44. The actual value of the load at the first stage of loading was $\lambda P = 2.64$ kN. At the second stage of loading, an accidental action was applied to the loaded structure with the load of the first stage in the form of the sudden removal of the central column.

The parameters of the "relative load-deflection" curve for the most strained cross-section of the beam 1-1 above the first floor of the frame (see figure 1) were calculated using the considered algorithm and the Matlab program for solving the system of equations (3). The cross-sectional stiffness of the beam B_{crc}, B^d_{n-1} respectively determined by crack formation during loading of the constructive system and its structural rearrangement after removal of the central column, were calculated using the formulas of [29]. At the same time, an increase in the dynamic stiffness of the considered cross-section caused by high-speed loading of constructive system elements under accidental action was taken into account in the segment $\overline{a} - c$ of the static-dynamic capacity curve (Figure 5).

The obtained parametric "relative load-deflection" ("$\lambda_m - f$") curve allows us to analyze the nature of nonlinear deformation of the frame-rod constructive system taking into account crack formation in the cross-sections of the beams (λ_{crc}^{st}) at the first loading stage $0-\bar{a}$, to determine the beginning of the structural rearrangement of the system ($\lambda_n^{st} = \lambda_{n-1}^{d} = 1$) the formation sequence of the first and second plastic hinges in the beam ($\lambda_{n-2}^{d} = \lambda_{n-3}^{d} = 1.22$ and $\lambda_{n-4}^{d} = 1.84$), as well as the beginning of the failure of the considered structure of the beam ($\lambda_{n-4,w}^{d}$) due to the formation of a third plastic hinge and the transformation of the beam into the hanging system.

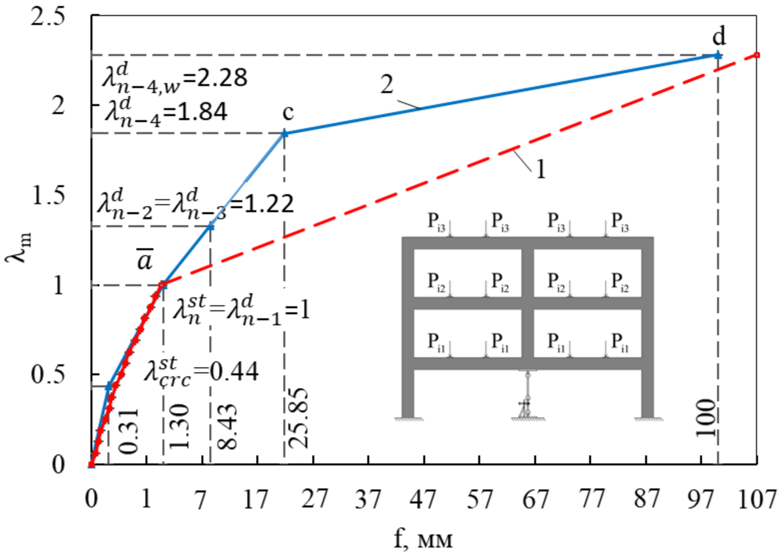

Figure 5. Capacity curves of static-dynamic loading "$\lambda_m - f$" of cross-section 1-1 of the beam of a physical and constructive nonlinear frame of the third series [29]: experiment (1); calculation (2).

A comparison of the experimental and calculated curves of static and static-dynamic deformation of the studied reinforced concrete frame-rod system (curves 1 and 2) indicates the acceptability of using the presented analytical dependences to calculate the main parametric points of the "parametric load-deflection" capacity curve graph describing the deformation of physical and constructive nonlinear frame rod systems under accidental actions caused by sudden structural rearrangement in such systems.

3.2. Quasi-static tests

The test results of the double-span beam substructures given by Jun Yu and Kang Hai Tan in [23] are also considered for analysis. The loading regime of the substructures in the first and second stages was static. Fig. 6 shows the "relative parametric load-deflection" curve for the structures of two experimental series. Substructures differed among themselves in the percentage of reinforcement of cross-sections.

The following conclusions can be drawn from the analysis of Figure 6. The calculated capacity curves satisfactorily describe the key points of the experimental curves: $\lambda_{n-1}^{st}, \lambda_{n-2}^{st}, \lambda_{n-3}^{st}, \lambda_{n-3,w}^{st}$. The theoretical ratio $\lambda_{n-3}^{st} / \lambda_{n-1}^{st} = 1.4$ agrees well with the experimental data and confirms the significant influence of constructive nonlinearity established in experiments on the survivability of the structure. An increase in the reinforcement ratio of a structure significantly increases its bearing capacity at the stage of work as a hanging system ($\lambda_{n-3,w}^{st} = 2.88$ at $\mu = 1.87\%$ and $\lambda_{n-3,w}^{st} = 2.1$ at $\mu = 1.24\%$). The ultimate deflection of the structure at the stage of work as a hanging system was 1/30-1/10 of the span, which is in good agreement with the data obtained in similar studies under static loading regimes of constructive nonlinear systems [28, 32, 35, 36].

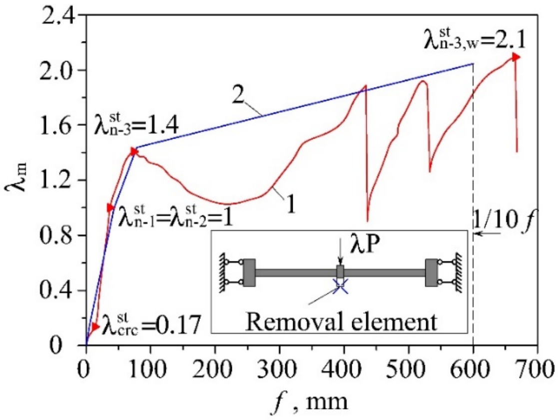

a)

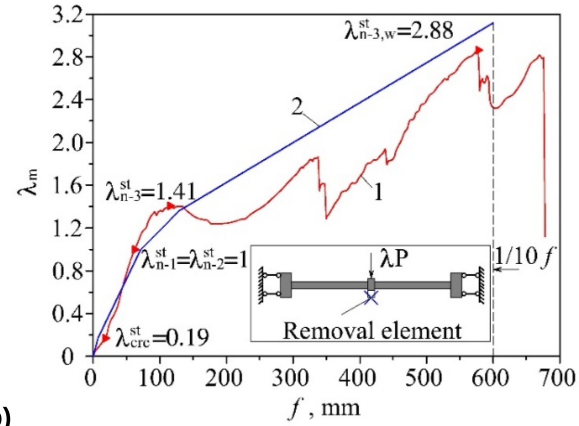

b)

Figure 6. Capacity curves under quasi-static loading "$\lambda_m - f$" for the structure of beams with different percentages of reinforcement (μ): a- at $\mu = 1.24\%$, b- at $\mu = 1.87\%$; experiment (1), calculation (2).

4. Conclusions

1. The presented methodology and algorithm make it possible to calculate the parameters of the "relative load-deflection" curve of the cross-sections of reinforced concrete elements of constructive systems under static loading and their subsequent dynamic additional loading, taking into account physical and constructive nonlinearity.

2. To determine the calculated parameters of the capacity curve of reinforced concrete elements the constructed system of canonical equations of an extraordinary version of the mixed method is proposed in a special way, which allows one to calculate the parametric load at which ultimate forces are reached in the cross-sections of the constructive system elements, accordingly, the degree of static indeterminacy of the constructive system changes and its survivability is exhausted.

3. The proposed algorithm for calculating the parameters of the “parametric load-deflection” curves for physical and constructive non-linear reinforced concrete frame-rod constructive systems can be used in designing the protection of building and structures frames from progressive collapse under accidental actions.

References

1. Russell, J.M., Sagaseta, J., Cormie, D., Jones, A.E.K. Historical review of prescriptive design rules for robustness after the collapse of Ronan Point. Structures. 2019. Vol. 20. Pp. 365–373. DOI: 10.1016/j.istruc.2019.04.011
2. Bondarenko, V.M., Kolchunov, V.I. Kontseptsiya i napravleniya razvitiya teorii konstruktivnoy bezopasnosti zdaniy i sooruzheniy pri silovykh i sredovykh vozdeystviyakh [The Concept and Directions of Development of the Theory of Structural Safety of Buildings and Structures under the Influence of Force and Environmental Factors]. Promyshlennoe i grazhdanskoe stroitel 'stvo [Industrial and Civil Engineering]. 2013. No. 2. Pp. 28–31. (rus)
3. Geniev, G.A., Kolchunov, V.I., Klyueva, N.V., Nikulin, A.I., Pyatikrestovskiy, K.P. Prochnost' i deformativnost' zhelezobetonnykh konstruktsiy pri zaproektnykh vozdeystviyakh [Strength and deformability of reinforced concrete structures with beyond design actions]. ASV. Moscow, 2004. 216 p. (rus)
4. Starossek, U., Haberland, M. Disproportionate Collapse: Terminology and Procedures. Journal of Performance of Constructed Facilities. 2010. 24 (6). Pp. 519–528. DOI: 10.1061/(ASCE)CF.1943-5509.0000138
5. Adam, J.M., Parisi, F., Sagaseta, J., Lu, X. Research and practice on progressive collapse and robustness of building structures in the 21st century. Engineering Structures. 2018. Vol. 173. Pp. 122–149. DOI: 10.1016/j.engstruct.2018.06.082
6. Zenin, S.A., Sharipov, R.Sh., Kudinov, O.V., Shapiro, G.I., Gasanov, A.A. Raschety krupnopanel'nykh zdaniy na ustoychivost' protiv progressiruyushchego obrusheniya metodami predel'nogo ravnovesiya i konechnogo elementa [Methods of calculating of large-panel buildings: how to prevent progressing collapse]. Academia. Arkhitektura i stroitel'stvo [Academia. Architecture and construction]. 2016. No. 4. Pp. 109–113. (rus)
7. Kabantsev, O., Mitrovic, B. Deformation and power characteristics monolithic reinforced concrete bearing systems in the mode of progressive collapse. MATEC Web of Conferences. 2018. Vol. 251. DOI: 10.1051/MATECCONF/201825102047
8. Li, Y., Lu, X., Guan, H., Ye, L. An improved tie force method for progressive collapse resistance design of reinforced concrete frame structures. Engineering Structures. 2011. 33 (10). Pp. 2931–2942. DOI: 10.1016/j.engstruct.2011.06.017
9. Brunesi, E., Nascimbene, R., Parisi, F., Augenti, N. Progressive collapse fragility of reinforced concrete framed structures through incremental dynamic analysis. Engineering Structures. 2015. Vol. 104. Pp. 65–79. DOI: 10.1016/j.engstruct.20-15.09.024
10. Kodysh, E.N. Proektirovanie zashchity zdaniy i sooruzheniy ot progressiruyushchego obrusheniya s uchetom vozniknoveniya osobogo predel'nogo sostoyaniya [Designing the Protection of Buildings and Structures Against Progressive Collapse in View of the Emergence of a Special Limiting State]. Promyshlennoe i grazhdanskoe stroitel 'stvo [Industrial and Civil Engineering]. 2018. No. 10. Pp. 95–101. (rus)

11. Travush, V.I., Shapiro, G.I., Kolchunov, V.I., Leont'ev, E.V., Fedorova, N.V. Proektirovanie zashchity krupnopanel'nykh zdaniy ot progressiruyushchego obrusheniya [Design of Protection of Large-Panel Buildings against Progressive Collapse]. Zhilishchnoe stroitel'stvo [Housing Construction]. 2019. No. 3. Pp. 40–46. (rus)
12. Belostotsky, A.M., Akimov, P.A., Aul, A.A., Dmitriev, D.S., Dyadchenko, Yu.N., Nagibovich, A.I., Ostrovskiy, K.I., Pavlov, A.S. Raschetnoe obosnovanie mekhanicheskoy bezopasnosti stadionov k Chempionatu mira po futbolu 2018 goda [Analysis of Mechanical Safety of Stadiums for the World Cup 2018]. Academia. Arkhitektura i stroitel'stvo [Academia. Architecture and construction]. 2018. No. 3. Pp. 118–129. (rus)
13. Semenov, A.A., Porivaev, I.A., Kuznetcov, D.V., Nguen, T.H., Saitgalina, A.S., Tregubova, E.S. Stress-strain state of high-rise building under wind load and progressive collapse. Construction of Unique Buildings and Structures. 2017. 59 (8). Pp. 7–26. DOI: 10.18720/CUBS.59.1. (rus)
14. Yu, J., Luo, L., Li, Y. Numerical study of progressive collapse resistance of RC beam-slab substructures under perimeter column removal scenarios. Engineering Structures. 2018. Vol. 159. Pp. 14–27. DOI: 10.1016/j.engstruct.2017.12.038
15. Kolchunov, V.I., Fedorova, N.V., Savin, S.Y., Kovalev, V.V., Iliushchenko, T.A. Failure simulation of a RC multi-storey building frame with prestressed girders. Magazine of Civil Engineering. 2019. 92 (8). Pp. 155–162. DOI: 10.18720/MCE.92.13
16. Kolchunov, V.I., Androsova, N.B. Nonequilibrium processes of power and enviromental resistance of reinforced concrete structures to progressive collapse. Journal of Physics: Conference Series. 2019. Vol. 1425. DOI: 10.1088/1742-6596/1425/1/012053
17. Geniev, G.A. Ob otsenke dinamicheskikh effektov v sterzhnevykh sistemakh iz khrupkikh materialov [Evaluation of dynamic effects in rod systems made of brittle materials]. Beton i zhelezobeton [Concrete and reinforced concrete]. 1992. (9). Pp. 25–27. (rus)
18. Stylianidis, P.M., Nethercot, D.A., Izzuddin, B.A., Elghazouli, A.Y. Modelling of beam response for progressive collapse analysis. Structures. 2015. Vol. 3. Pp. 137–152. DOI: 10.1016/j.istruc.2015.04.001
19. Stylianidis, P.M., Nethercot, D.A., Izzuddin, B.A., Elghazouli, A.Y. Study of the mechanics of progressive collapse with simplified beam models. Engineering Structures. 2016. Vol. 117. Pp. 287–304. DOI: 10.1016/j.engstruct.2016.02.056
20. Mohajeri Nav, F., Usefi, N., Abbasnia, R. Analytical investigation of reinforced concrete frames under middle column removal scenario. Advances in Structural Engineering. 2018. 21 (9). Pp. 1388–1401. DOI: 10.1177/1369433217746343
21. Tusnin, A. Dynamic factors in case of damaging continuous beam supports. Magazine of Civil Engineering. 2018. 78 (2). Pp. 47–64. DOI: 10.18720/MCE.78.4
22. Alogla, K., Weekes, L., Augusthus-Nelson, L. Theoretical assessment of progressive collapse capacity of reinforced concrete structures. Magazine of Concrete Research. 2017. 69 (3). Pp. 145–162. DOI: 10.1680/jmacr.16.00319
23. Yu, J., Tan, K.H. Structural behavior of RC beam-column subassemblages under a middle column removal scenario. Journal of Structural Engineering. 2013. 139 (2). Pp. 233–250. DOI: 10.1061/(ASCE)ST.1943-541X.0000658
24. Al-Salloum, Y.A., Alrubaidi, M.A., Elsanadedy, H.M., Almusallam, T.H., Iqbal, R.A. Strengthening of precast RC beam-column connections for progressive collapse mitigation using bolted steel plates. Engineering Structures. 2018. Vol. 161. Pp. 146–160. DOI: 10.1016/j.engstruct.2018.02.009
25. Alshaikh, I.M.H., Abu Bakar, B.H., Alwesabi, E.A.H., Akil, H.M. Progressive collapse of reinforced rubberised concrete: Experimental study. Construction and Building Materials. 2019. Vol. 226. Pp. 307–316. DOI: 10.1016/j.conbuildmat.20-19.07.270
26. Almazov, V.O. Problemy progressiruyushchego razrusheniya [The problems of progressive collapse]. Stroitel'stvo i rekonstruktsiya. 2014. 6 (56). Pp. 3–10. (rus)
27. Choi, H., Kim, J. Progressive collapse-resisting capacity of RC beam–column sub-assemblage. Magazine of Concrete Research. 2011. 63 (4). Pp. 297–310. DOI: 10.1680/macr.9.00170
28. Weng, J., Lee, C.K., Tan, K.H., Lim, N.S. Damage assessment for reinforced concrete frames subject to progressive collapse. Engineering Structures. 2017. Vol. 149. Pp. 147–160. DOI: 10.1016/j.engstruct.2016.07.038
29. Kolcunov, V.I., Tuyen, V.N., Korenkov, P.A. Deformation and failure of a monolithic reinforced concrete frame under accidental actions. IOP Conference Series: Materials Science and Engineering. 2020. Vol. 753. DOI: 10.1088/1757-899X/753/3/032037
30. Travush, V.I., Fedorova, N.V. Survivability of structural systems of buildings with special effects. Magazine of Civil Engineering. 2018. 81 (5). Pp. 73–80. DOI: 10.18720/MCE.81.8
31. Savin, S.Y., Fedorov, S.S. Stability analysis of reinforced concrete building frames damaged by corrosion under static-dynamic loading. Journal of Physics: Conference Series. 2019. Vol. 1425. DOI: 10.1088/1742-6596/1425/1/012043
32. Tian, Y., Su, Y. Dynamic response of reinforced concrete beams following instantaneous removal of a bearing column. International Journal of Concrete Structures and Materials. 2011. 5 (1). Pp. 19–28. DOI: 10.4334/IJCSM.2011.5.1.019
33. Pham, A.T., Tan, K.H. Experimental study on dynamic responses of reinforced concrete frames under sudden column removal applying concentrated loading. Engineering Structures. 2017. Vol. 139. Pp. 31–45. DOI: 10.1016/j.engstruct.2017.02.002
34. Qian, K., Li, B. Slab Effects on Response of Reinforced Concrete Substructures after Loss of Corner Column. ACI Structural Journal. 2012. 109 (6). Pp. 845–856. DOI: 10.14359/51684128
35. Alogla, K., Weekes, L., Augusthus-Nelson, L. A new mitigation scheme to resist progressive collapse of RC structures. Construction and Building Materials. 2016. Vol. 125. Pp. 533–545. DOI: 10.1016/j.conbuildmat.2016.08.084
36. Ren, P., Li, Y., Lu, X., Guan, H., Zhou, Y. Experimental investigation of progressive collapse resistance of one-way reinforced concrete beam–slab substructures under a middle-column-removal scenario. Engineering Structures. 2016. Vol. 118. Pp. 28–40. DOI: 10.1016/j.engstruct.2016.03.051
37. Peng, Z., Orton, S.L., Liu, J., Tian, Y. Experimental Study of Dynamic Progressive Collapse in Flat-Plate Buildings Subjected to an Interior Column Removal. Journal of Structural Engineering. 2018. 144 (8). DOI: 10.1061/(ASCE)ST.1943-541X.0002106

Contacts:

Nataliya Fedorova, fenavit@mail.ru

Ngoc Tuyen Vu, ngoctuyennd91@gmail.com

Magazine of Civil Engineering. 2022. 109(1). Article No. 10903

Magazine of Civil Engineering

ISSN 2712-8172

journal homepage: http://engstroy.spbstu.ru/

DOI: 10.34910/MCE.109.3

Mathematical modelling of hydraulics and water quality characteristics for small dam maintenance

R.M.S. Prastica*[a,b], H. Soeryantono[c], D.R. Marthanty[c]

[a] *Universitas Gadjah Mada, Yogyakarta, Indonesia*

[b] *Public Works Polytechnic, Semarang, Indonesia*

[c] *Universitas Indonesia, Kota Depok, Indonesia*

**E-mail: rianmantasasp@gmail.com; rian.mantasa.s.p@ugm.ac.id*

Keywords: small dam maintenance, hydrodynamics analysis, model validation, numerical modelling

Abstract. Along the inclining events of flooding events, maintenance towards water infrastructure such as urban small dam is needed. The maintenance needs interdisciplinary approach involving hydrology, hydraulics, water quality, and sediment factors. Due to lack of studies in those fields, the study aims to construct a model by using RESOURCE MODELLING ASSOCIATES program to study behaviours of hydraulics and water quality as small dam management. Numerical modelling, hydrology analysis, hydraulics assessment, water quality tests, and field works are employed in this study, with Agathis small dam as a case. The model could run successfully which the result concludes that the model produces reasonable result with acceptable errors and value of R2. A scenario of constructed wetland is proposed and has good accuracy for future maintenance for hydrology, hydraulics, and environmental management. In addition, the models also could be applied to other problem such as an agricultural field also. In the near future, studies about hydrodynamics and water quality modelling especially sediment on small dams need to be more explored because few studies still have limited information meanwhile they have essential impact towards urban water management.

1. Introduction

1-D, 2-D, or 3-D hydrodynamic and water quality modeling are rapidly developing and reaching their contributive applications such as modeling of microbial contamination in coastal and river [1–3], river water quality [4–7], water quality in reservoir and lagoon [8–10], and water quality within basin or watershed [11–13]. Despite the successful modeling in several topics, few studies of water quality, hydraulics, and sediment modeling on urban small dam or lakes have been published. Meanwhile, the modeling on those sites [14–16] is compulsory realized as a strategic process to tackle urban disaster events [17–19].

The most recent example to support the need for this research is the biggest flooding event in Jakarta, Indonesia. Jakarta Flood of January 1, 2020, triggered an enormous stop of construction projects in several places due to high level of inundation area. Table 1 provides the rainfall data in that day. The table indicates that the amount of rainfall makes this flood of the most impactful in the recorded history of Jakarta. The dynamics of hydrology condition and climate change patterns affect environmental damage such as the huge amount of nutrient loading to water resources – lakes and small dams. Because of the declared situation, there is a dire need to protect the water resources from hydrology aspects, improve hydraulics characteristics, and water quality conditions.

Prastica, R.M.S., Soeryantono, H., Marthanty, D.R. Mathematical modelling of hydraulics and water quality characteristics for small dam maintenance. Magazine of Civil Engineering. 2022. 109(1). Article No. 10903. DOI: 10.34910/MCE.109.3

Table 1. 24-hour precipitation on 1 January 2020 (in mm).

Station	Elevation	Value
Halim Perdana Kusuma	–1	377.0
AWS TMII	0	335.2
Pintu Air Pulo Gadung	20	260.0
Citayam	–1	243.0
Sunter Hulu	54	236.0
ARG Tomang	0	225.6
Kedoya	30	211.6
Tangerang Selatan Climatology Station	27	200.0
Waduk Melati	25	191.0
Manggarai	33	189.0
Balai II Ciputat	–1	184.9
Lebak Bulus	–1	176.0
Rorotan	23	172.0
Pasar Minggu	58	155.0
Ragunan	65	155.0
Lemah Abang	14	151.0
Pesanggrahan Depok	86	148.0
Soekarno Hatta Meteorology Station	11	147.9
Istana	30	147.0
Maritim Tanjung Priok Meteorology Station	3	146.1
Kemayoran Meteorology Station	4	145.3
Sunter III Rawabadak	19	144.0
Pakubuwono	54	142.0
Beji Depok	0	142.0
Pompa Cideng	21	135.0
AWS Jagorawi Bogor	0	131.5
Sunter Timur I Kodamar	25	121.0
Angke Hulu	17	120.0
Karet	38	118.0
Teluk Gong	23	113.0
ARG Ciganjur	0	110.4
Setiabudi Timur	29	105.0
Krukut Hulu	80	104.0
Depok 1	93	92.0
AWS IPB Bogor	0	75.8
Citeko Meteorology Station	920	60.0
Katulampa	361	57.4
Stamet Curug	–1	54.0

Furthermore, even without flash flooding, Jakarta as the urban area has an initial issue of high demand for infrastructure construction every year. Rapid urban development makes it difficult for rainwater to infiltrate the ground due to dense impervious cover. In recent years the population growth snowballs [20] along with the development of settlement for them to live. In addition, urbanization attracts population growth to particular areas. Urbanization becomes a threat worldwide, especially in developing countries. According to Thorn et al. [21], the main threat comes from the impervious surface. Wong et al. [22] stated that the impervious surface could be defined as buildings, roads, and other infrastructures. This water-resistant surface is highlighted as the main root of flooding in urban areas. Also, the changes in land cover drive ecosystem changes [21].

Urban small dam or lake management plays a proper role in flood risk management and ensures a construction project runs well. Henny et al. [23] mention that urban lake management gives a contribution to watershed management to reduce the impact of flash flooding. Urban lakes situated in the large watershed are small, shallow, and surrounded mostly by impervious land [23]. Natural lakes that are usually found in rural regions differ from man-made lakes or urban lakes. Most natural lakes are sources of pollution of different kind. Lakes suffer eutrophication along with the increasing of agricultural activities, for example, fish aquaculture, crops, and livestock farming [24–26]. Industrial and urban activities, as well as regional construction bring urban lakes' contaminants, such as sediment that contains heavy metals harmful to the aquatic environment [27, 28]. As small dam conservation is in high demand due to the declining of lake quality and lack of hydraulics management, hence, it is important to construct hydrodynamic and water quality model for small dams which could describe cost-effective urban dam management and maintenance.

From the above review, we can conclude that the development of mathematical modeling to simulate hydrodynamics, water quality, and sediment for urban small dam maintenance is necessary due to limited published works on water management and strategy of future condition.

According to the declared problems, the research aims to create mathematical model, provided by Resource Modelling Associates (RMA) program, to describe and obtain detailed characteristics of hydraulics and water quality, especially for sediment, in small dams. The model is studied in one of small dams in urban area of West Java, Agathis. After the model is well-constructed and represented the field condition, proposed scenario is tested as water management and strategy.

2. Methods

Hydraulics, hydrology, and water quality problems are usually investigated by means of individual methods, while the optimum maintenance for civil infrastructures needs all of those aspects. Table 2 shows the current methods to develop a solution to the declared problems. Research gap in Table 2 provides opportunities for further research. The gap defines the involvement of hydrology, hydraulics, and water quality quantifications. In this research, all aspects are employed to obtain the research goals.

Table 2. Methods of evaluation and maintenance for water infrastructures.

Cases	Research Method	Research gap	Location	Reference(s)
Damage of building due to flooding	Hydrology assessment	Quantitative and deterministic models	United Kingdom	[29]
Flood disaster	Hydrology forecasting, hydrodynamics model	No hydraulics and environmental analysis	Malaysia	[30]
Floods and landslide hazard	Spatial technology	No hydraulics and environmental analysis	Malaysia	[31]
Flooding	Hydrology and hydraulics assessment	Water quality	Philippines	[32]
Impact of climate change to flood regimes	Hydrology and spatial analysis	Water quality	France	[33]
Flash floods	Hydrology assessment, spatial simulation	Water quality	Australia	[34]
Chronic flood-affected areas	Qualitative research	Hydrology, hydraulics, and water quality assessment	India	[35]
Flood hazard	Hydro-geomorphological study	Hydraulics and water quality	Morocco	[36]
Frequent flooding	Interviews	Hydrology, hydraulics, and water quality assessment	Africa	[37]
Damage of building structures to flood	Field survey, laboratory experiments, interviews	Hydrology, hydraulics, and water quality assessment	Tanzania	[38]
Structural flood damage	Computational fluid dynamics	Hydrology, water quality	United Kingdom	[39]
Flood and high rainfall	Spatial analysis	Hydraulics, water quality	Japan	[40], [41]
Flooding	Spatial analysis	Hydraulics, water quality	Australia	[42]

Cases	Research Method	Research gap	Location	Reference(s)
Flooding	Spatial model	Hydrology, hydraulics, and water quality assessment	Indonesia	[43]
Flooding	Low impact development	Water quality assessment	Greece	[44]
Flooding	Hydrology, hydraulics, and water quality assessment	–	Indonesia	This research

To achieve the research goals, the research recalls the hydrodynamics equations as basic hydrology, hydraulics and water quality characteristics of the water body. They are described in the following equations:

$$\frac{\partial u}{\partial x}+\frac{\partial v}{\partial y}=0, \tag{1}$$

$$\rho\left[\frac{\partial u}{\partial t}+u\frac{\partial u}{\partial x}+v\frac{\partial u}{\partial y}\right]=\frac{\partial\left(\sigma_x-p\right)}{\partial x}+\frac{\partial \tau_{xy}}{\partial y} \tag{2}$$

$$\rho\left[\frac{\partial v}{\partial t}+u\frac{\partial v}{\partial x}+v\frac{\partial v}{\partial y}\right]=\frac{\partial \tau_{xy}}{\partial x}+\frac{\partial\left(\sigma_y-p\right)}{\partial y} \tag{3}$$

$$\sigma_x=2\mu\frac{\partial u}{\partial x} \tag{4}$$

$$\sigma_y=2\mu\frac{\partial v}{\partial y} \tag{5}$$

$$\tau_{xy}=\mu\left[\frac{\partial u}{\partial y}+\frac{\partial v}{\partial x}\right] \tag{6}$$

where u and v represent the components for velocity, p is interpreted as pressure, ρ describes density, and μ describes the viscosity. According to the substitution of Equations (1) – (6), the system of relations for velocity distribution formulae is described as Equation (7) for x direction and Equation (8) for y direction:

$$\begin{gathered}-\rho\left[\frac{\partial u}{\partial t}+u\frac{\partial u}{\partial x}+v\frac{\partial u}{\partial y}\right]+\frac{\partial}{\partial x}\left[2\mu\frac{\partial u}{\partial x}-p\right]+\mu\frac{\partial}{\partial y}\left[\frac{\partial u}{\partial y}+\frac{\partial v}{\partial x}\right]+\\+u\frac{\Delta t}{2}\frac{\partial}{\partial x}\left[u\frac{\partial u}{\partial x}+v\frac{\partial u}{\partial y}\right]+v\frac{\Delta t}{2}\frac{\partial}{\partial x}\left[u\frac{\partial u}{\partial x}+v\frac{\partial u}{\partial y}\right]=0,\end{gathered} \tag{7}$$

$$\begin{gathered}-\rho\left[\frac{\partial v}{\partial t}+u\frac{\partial v}{\partial x}+v\frac{\partial v}{\partial y}\right]+\frac{\partial}{\partial y}\left[2\mu\frac{\partial v}{\partial y}-p\right]+\mu\frac{\partial}{\partial x}\left[\frac{\partial u}{\partial y}+\frac{\partial v}{\partial x}\right]+\\+u\frac{\Delta t}{2}\frac{\partial}{\partial x}\left[u\frac{\partial v}{\partial x}+v\frac{\partial v}{\partial y}\right]+v\frac{\Delta t}{2}\frac{\partial}{\partial x}\left[u\frac{\partial v}{\partial x}+v\frac{\partial v}{\partial y}\right]=0.\end{gathered} \tag{8}$$

Furthermore, the governing equation of water quality is affected by the advection and dispersion aspects and depicted as the following Equation (9) [45]. In this research, total suspended solids, as one of the most problematic issues in urban areas, is used as a study model in the water quality section.

$$\begin{gathered}\partial_t(HS)+\partial_x(HuS)+\partial_y(HvS)+\partial_z(w_sS)\\=\partial_x(HA_H\partial_xS)+\partial_y(HA_H\partial_yS)+\partial_z\left(\frac{A_v}{H}\partial_zS\right)+Q_s\end{gathered} \tag{9}$$

where H is water depth;

u and v are horizontal velocity component in horizontal Cartesian x and y;

w is vertical velocity in coordinate vertical stigma of z;

w_s is sediment settling velocity;

S is sediment concentration;

A_v and A_H are vertical and horizontal turbulent diffusion coefficient;

Q_S is external source and sink.

Based on the declared governing equations and research background, the analysis is employed by using “Resource Modelling Associates (RMA)” program. The program could visualize the analysis with an in-depth and comprehensive result. The problem associated with the research takes place in the urban small dam. Therefore, a model of the urban lake is proposed to the research to develop the model. The research uses Agathis Lake site which is located in Depok, West Java, Indonesia.

From the continuity governing equation (1) – (8), partial differential equation is analyzed through discretization, approximation, and finally the last form of momentum equation for both x and y directions, as described in Equations (10) and (11).

Momentum equation for x direction is:

$$\begin{aligned}&\int_V\left[\left(\rho\psi\psi^T\frac{\partial u}{\partial t}\right)+\rho\left[\psi\left(\psi^T u\right)\frac{\partial\psi^T}{\partial x}+\psi\left(\psi^T v\right)\frac{\partial\psi^T}{\partial y}\right]\right]udV\\&+\int_V\left[2\mu\frac{\partial\psi}{\partial x}\frac{\partial\psi^T}{\partial x}+\mu\frac{\partial\psi}{\partial y}\frac{\partial\psi^T}{\partial y}\right]udV\\&+\frac{\Delta t}{2}\int_V\left[uu\frac{\partial\psi}{\partial x}\frac{\partial\psi^T}{\partial x}+uv\frac{\partial\psi}{\partial x}\frac{\partial\psi^T}{\partial y}+vu\frac{\partial\psi}{\partial y}\frac{\partial\psi^T}{\partial x}+vv\frac{\partial\psi}{\partial y}\frac{\partial\psi^T}{\partial y}\right]udV\\&+\int_V\left[\left(\mu\frac{\partial\psi}{\partial y}\frac{\partial\psi^T}{\partial x}\right)v-\left(\frac{\partial\psi}{\partial x}\phi^T\right)p\right]dV=\int_V\rho\psi f_i dV\end{aligned}\tag{10}$$

while momentum equation for y direction is:

$$\begin{aligned}&\int_V\left[\left(\rho\psi\psi^T\frac{\partial v}{\partial t}\right)+\rho\left[\psi\left(\psi^T u\right)\frac{\partial\psi^T}{\partial x}+\psi\left(\psi^T v\right)\frac{\partial\psi^T}{\partial y}\right]\right]vdV\\&+\int_V\left[2\mu\frac{\partial\psi}{\partial x}\frac{\partial\psi^T}{\partial x}+\mu\frac{\partial\psi}{\partial y}\frac{\partial\psi^T}{\partial y}\right]vdV\\&+\frac{\Delta t}{2}\int_V\left[uu\frac{\partial\psi}{\partial x}\frac{\partial\psi^T}{\partial x}+uv\frac{\partial\psi}{\partial x}\frac{\partial\psi^T}{\partial y}+vu\frac{\partial\psi}{\partial y}\frac{\partial\psi^T}{\partial x}+vv\frac{\partial\psi}{\partial y}\frac{\partial\psi^T}{\partial y}\right]vdV\\&+\int_V\left[\left(\mu\frac{\partial\psi}{\partial y}\frac{\partial\psi^T}{\partial x}\right)u-\left(\frac{\partial\psi}{\partial y}\phi^T\right)p\right]dV=\int_V\rho\psi f_i dV\end{aligned}\tag{11}$$

where Q is weight function for Galerkin method, pressure weight;

W is velocities weight;

Ψ is interpolation function;

Φ is interpolation function;

u is velocity vector;

v is velocity vector;

p is pressure vector.

With the same ways as the continuity equation, the governing Equation (9) of sediment transport for advection and dispersion components are elaborated into Equation (12), as follows:

$$\int_V \left[\frac{\partial(H)}{\partial t} \sum_{k=1}^{m} S_k \frac{\partial \varphi_j}{\partial t} + \frac{\partial(Hu)}{\partial x} \sum_{k=1}^{m} S_k \frac{\partial \varphi_j}{\partial t} \right] dV +$$
$$+ \int_V \left[\frac{\partial(Hv)}{\partial y} - \frac{\partial(HA_H)}{\partial x} \sum_{k=1}^{m} S_k \frac{\partial \varphi_k}{\partial x} \frac{\partial \varphi_j}{\partial x} \right] dV - \tag{12}$$
$$- \int_V \left[\frac{\partial(HA_H \partial_y)}{\partial y} \sum_{k=1}^{m} S_k \frac{\partial \varphi_j}{\partial y} \right] dV - \int_V Q_s dV = 0$$

3. Results and Discussion

3.1. Study Area

The study area, depicted in Fig. 1, is in Agathis small dam, West Java, Indonesia. The small dam is also close to The Greater Jakarta. The green and red mark a constructed wetland area which does not exist yet, but will be modelled after the calibration stage of the model. Location I is inlet of sediment trap, Location II indicates its outlet, Location III is floodway, Location IV indicates the inlet of the small dam, Location V is the water body, while Location VI is the small dam's outlet.

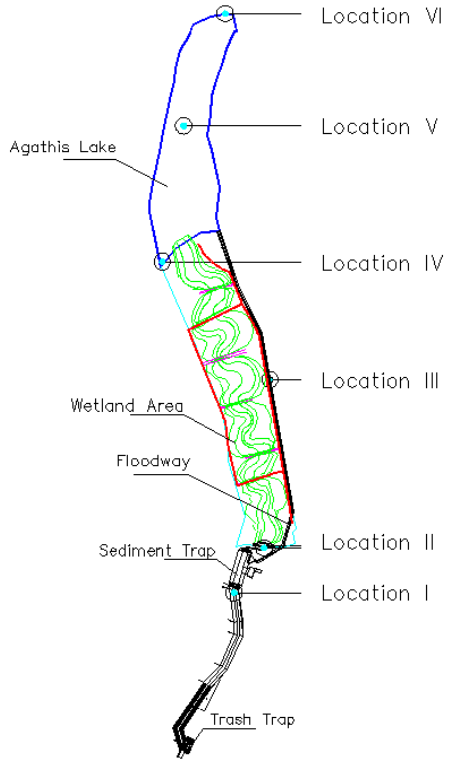

Figure 1. Agathis small dam physical features.

3.2. Model Calibration and Accuracy

According to the relations (7), (8), and (9), RMA is developed to simulate both computational and field experiments. RMA is divided into two main running programs: RMA-10 for hydraulics analysis and RMA-11 for water quality analysis. Firstly, the research constructs urban small dam on the basis of the finite element method theory. The results of RMA-10 and RMA-11 are depicted in Fig. 2 and Fig. 3, respectively. The programs are running well to model velocity distribution for hydraulics management and total suspended solid distribution for water quality analysis, but they should be verified by the actual condition in the field. Thus, field and laboratory experiments are conducted. The main purpose of model calibration and validation is to create scenarios for small dam evaluation and management.

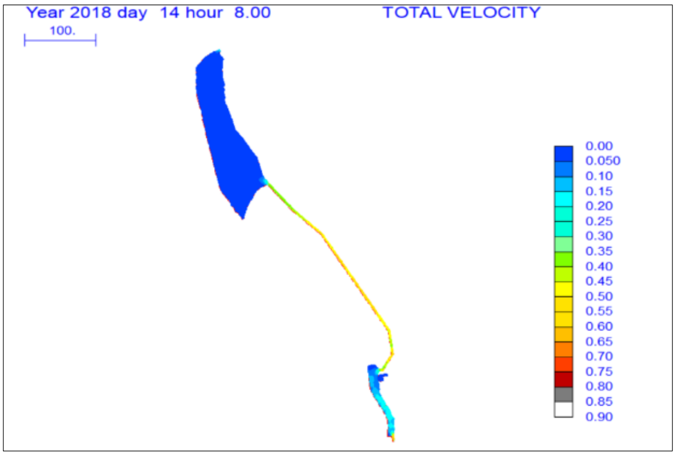

Figure 2. Agathis small dam in RMA-10 program visualization.

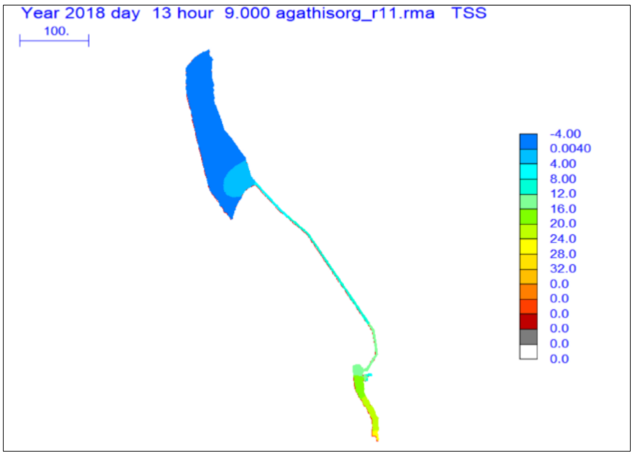

Figure 3. Agathis small dam in RMA-11 program visualization.

Data validation and calibration need velocity and total suspended solid data for RMA-10 and RMA-11 programs. The field experiments are carried out in 24-hour sampling time. After laboratory works, Table 3 illustrates the data result and the predicted data for model calibration. The experiments failed in inlet location at 1.00 – 2.00 pm due to inability to take appropriate samples caused by harmful and poisoned contaminants at the location access, so the errors are not calculated.

Table 3. Data for model calibration in small dam.

Time	Location	TSS field data (mg/l)	Model prediction of TSS data (mg/l)	SSE (%)	Velocity field data (m/s)	Model prediction of velocity data (m/s)	SSE (%)
8:00:00 AM	Inlet Sediment Trap	30	29.37	2.10	0.47	0.51	8.51
9:00:00 AM	Inlet Sediment Trap	27.7	25.52	7.87	0.45	0.45	0.00
10:00:00 AM	Outlet Sediment Trap	13.3	11.42	14.14	0.32	0.32	0.00
11:00:00 AM	Inlet floodway	13.5	8.678	35.72	0.3	0.32	6.67
12:00:00 PM	Floodway	4.0	5.66	41.50	0.4	0.42	5.00
1:00:00 PM	Inlet	2.7	8.79	NA	0.15	0.21	NA
2:00:00 PM	Inlet	2.6	8.38	NA	0.18	0.21	NA
3:00:00 PM	Water body	0.9	0.93	3.33	0.01	0.01	0.00
4:00:00 PM	Water body	1.1	0.91	17.27	0.01	0.01	0.00
5:00:00 PM	Water body	2.0	1.98	1.00	0.01	0.01	0.00
6:00:00 PM	Water body	3.0	2.59	13.67	0.01	0.01	0.00
7:00:00 PM	Water body	3.0	2.60	13.33	0.01	0.01	0.00
8:00:00 PM	Outlet	1.3	1.02	21.54	0.05	0.04	20.00
9:00:00 PM	Outlet	1.3	1.02	21.54	0.04	0.04	0.00
7:00:00 AM	Outlet	2.5	2.19	12.40	0.04	0.04	0.00
8:00:00 AM	Outlet	2.5	2.19	12.40	0.04	0.04	0.00

To make the validation of hydraulics characteristic clearer, we sampled data at certain times in several places. Fig. 4 depicts the result of the hydraulics experiment with velocity measured at certain distances and in specific time intervals. Not only hydraulics but also water quality analyses are conducted in the same manner. The calibration result of water quality is described in Fig. 5, where the concentrations are observed in several time steps. The correlation coefficient of both hydraulics and water quality calibration are 0.8686 and 0.9340, respectively.

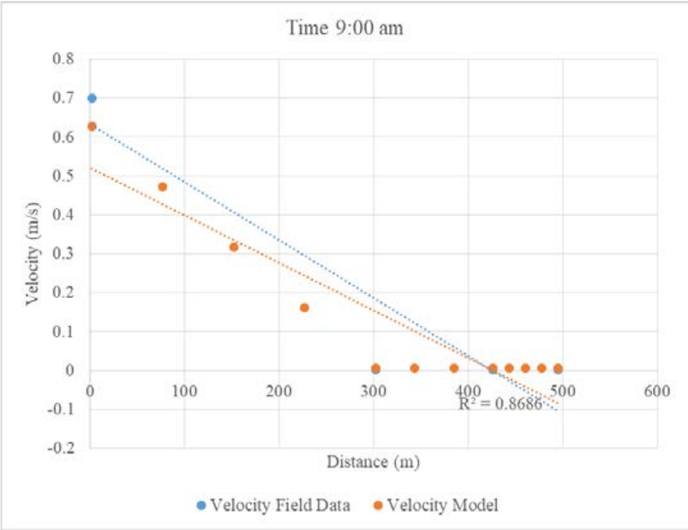

Figure 4. Calibration data of hydraulics characteristic.

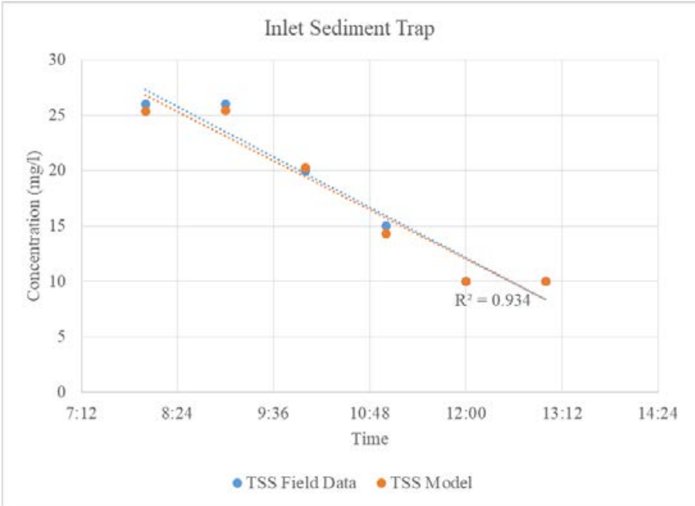

Figure 5. Calibration data of water quality characteristic.

Study in Lake Tenkiller [45] had the same procedures and experiments but different model and type of water quality parameter to simulate. The study observed dissolved oxygen (DO) with relative errors varying from 10.86 % to 28.26 %. Ji [45] concluded that the model was applicable to process comprehensive and detailed demonstration of several case scenarios. As a result, compared to this study with the error varying from 1 % to 41.50 %, the model can be seen as a well-designed simulation. However, further studies need to be developed due to limited and different parameters observed.

In addition, a study in Lake Manzala [46] on salinity parameter employed MIKE21 software and the same procedures of calibration as in this study. The error of total period for salinity varied from 0.088 to 0.282 and value of R^2 varied from 0.985 to 0.991. Since this study has a sample of R^2 value with 0.8686 and 0.934, again, the results can be used as a good model for the same characteristics but still cannot be applied to lakes of various conditions due to different parameters and limited studies on them.

Researches conducted in Tanglin Bay, Guozheng Bay, Shuiguo Bay, and Yingwo Bay [47] concluded that the model result could provide reasonable patterns and magnitudes of reproduction to model water quality parameters without providing extended explanation about the occurred errors in the model. Researchers only displayed the model result, as depicted in Fig. 6 as TP modelling result. The model simulated both total nitrogen (TN) and total phosphorus (TP). Again, the results could not be well compared due to different parameters and water bodies.

Different water quality constituents, COD, TN, and TP were modelled in Xi'an Yanming Lake, China [48] as well. The research provided the errors and R^2 value in one sample point for COD, TN, and TP with 0.15, 0.16, and 0.0086 error value, respectively, and 0.99, 0.9972, and 0.987 for R^2 value in the other, respectively.

Furthermore, Hg and VOP studies on North China Plain were conducted by employing both WHYSWESS-WQ and MIKE 11 [49]. The simulation accuracy of MIKE 11 hydrodynamic module in the research was 0.56 % of maximum error, and deemed to be an acceptable result, because of MIKE 11 validation parameter varying from -0.24 % to 0.56 % [49].

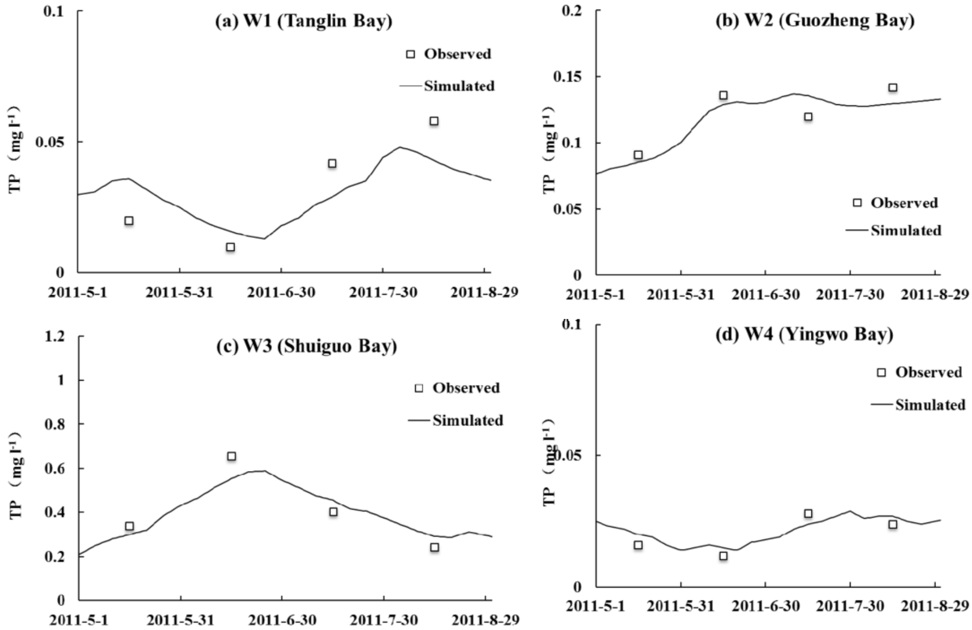

Figure 6. Comparison of predicted and observed value of TP at Bays of:
(a) Tanglin; (b) Guozheng; (c) Shuiguo; and (d) Yingwo [47].

Due to lack of sufficient studies about this research field, the occurred errors which vary from 1 % to 41.50 % and R^2 value sample with 0.8686 and 0.934 could be accepted as reasonable model results according to mentioned literature studies. Furthermore, all mentioned models do not provide 24-hour analysis of predicted and observed data as this study does. Hence, the reviews indicate the importance to develop further hydrodynamic modelling on lakes or small dams to simulate hydraulics, water quality, and sediment altogether.

3.3. Model Scenario

After the model is well constructed and calibrated, it could be used as an estimation in various civil engineering problems. The results are used to predict the hydrological condition of water infrastructure in small dams, to prevent flooding as the construction project barrier, and to estimate better dimension for irrigation [50–54] and drainage system [55–61] which have issues like sediment and nutrient loading. According to these phenomena, the incoming trend to model hydraulics, hydrology, and water quality would facilitate construction and engineering activities.

To study the model, the research evaluates one scenario of the existing wetland in the surrounding water infrastructure. The study examines the effect of constructed wetland in terms of decreasing contamination of Agathis small dam. The simulation is conducted by employing RMA. Fig. 7 depicts the result of wetland discretization. The study concludes that the wetland could reduce the amount of contaminants in the small dam 35 %, involving the direct influence of the velocity and hydraulics dimension of the small dam. Fig. 5 depicts the visualization of the new model. According to the research study, there are more issues for investigation in the field of water resource and environmental engineering. In this research, the reduction of nutrient loading is calculated numerically. Since we could also investigate it with respect to physical parameters, the future research could present a comparison of both the methods.

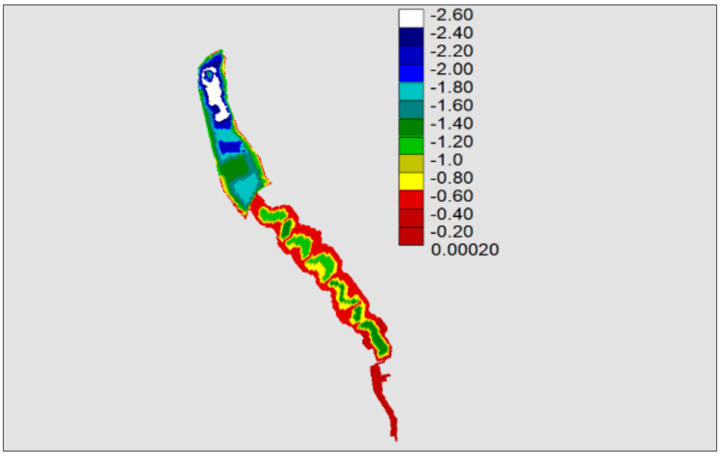

Figure 7. Agathis small dam with the constructed prospective wetland.

4. Conclusion

The hydrodynamics equations, both hydraulics and water quality, became the basis for developing a model in the RMA programs. The models are then verified by field investigation and laboratory tests to ensure comprehensive analysis. A 24-hour sampling produces various packages of data which allow us to draw a general conclusion that the model ran successfully. Conclusions obtained in the course of this study are summarized in the following component statements.

1. Continuity and hydrodynamics equations in both *x* and *y* directions support the finite element method analysis to describe the hydraulics and water quality characteristics of small dams.

2. The model error ranges between 1 % and 41.5 % and values of R^2 vary from 0.8686 and 0.934 after 24-hour sampling to analyze prediction and observation data. The model could describe the condition more comprehensively due to the hours instead of days' simulation.

3. The water quality and hydraulic characteristics on small dams are successfully simulated by Resource Modelling Associates program.

4. The conducted numerical studies of scenario using constructed wetland infrastructure indicate the reduction of sediment or erosion pollutants from urban areas. Any intervention to the existing small dam such as the construction of wetland could reduce the flooding rate and level of contamination by 35 %. Further scenarios could be developed too.

5. Due to lack of studies in the field of hydraulic, water quality, and sediment on small dams, there is still a need for further observations.

5. Acknowledgement

The research was fully supported by Hydrology and River Laboratory, Universitas Indonesia, and Hydraulics and Water Infrastructure Laboratory, Universitas Gadjah Mada. The first and third authors dedicate this research to our beloved late lecturer and researcher, Herr Soeryantono, Ph.D. for his dedication to spread out knowledge in water resources and hydraulics engineering to the current engineers in Indonesia. Rest in peace.

References

1. Eregno, F.E., Tryland, I., Tjomsland, T., Kempa, M., Heistad, A. Hydrodynamic modelling of recreational water quality using Escherichia coli as an indicator of microbial contamination. J. Hydrol. 2018. Vol. 561. Pp. 179–186.
2. Taghipour, M., Shakibaeinia, A., Sylvestre, É., Tolouei, S., Dorner, S. Microbial risk associated with CSOs upstream of drinking water sources in a transboundary river using hydrodynamic and water quality modeling. Sci. Total Environ. 2019. Vol. 683. Pp. 547–558.
3. Zhang, L., et al. Three-dimensional water quality model based on FVCOM for total load control management in Guan River Estuary, Northern Jiangsu Province. J. Ocean Univ. China. 2016. Vol. 15. No. 2. Pp. 261–270.
4. Cui, F., Park, C., Kim, M. Application of curve-fitting techniques to develop numerical calibration procedures for a river water quality model. J. Environ. Manage. 2019. Vol. 249. No. March. Pp. 109375.
5. Björklund, K., Bondelind, M., Karlsson, A., Karlsson, D., Sokolova, E. Hydrodynamic modelling of the influence of stormwater and combined sewer overflows on receiving water quality: Benzo(a)pyrene and copper risks to recreational water. J. Environ. Manage. 2018. Vol. 207. Pp. 32–42.
6. Sharma, D., Singh, R.K. DO-BOD modeling of River Yamuna for national capital territory, India using STREAM II, a 2D water quality model. Environ. Monit. Assess. 2009. Vol. 159. No. 1–4. Pp. 231–240.

7. Yao, H., Ni, T., Zhang, T. Estimation of phosphorus flux into the sea through one reversing river using continuous turbidities and water quality modeling. Environ. Dev. Sustain. 2019. No. 0123456789.
8. Xu, C., Zhang, J., Bi, X., Xu, Z., He, Y., Gin, K.Y.H. Developing an integrated 3D-hydrodynamic and emerging contaminant model for assessing water quality in a Yangtze Estuary Reservoir. Chemosphere. 2017. Vol. 188. Pp. 218–230.
9. Panda, U.S., Mahanty, M.M., Ranga Rao, V., Patra, S., Mishra, P. Hydrodynamics and water quality in Chilika Lagoon-A modelling approach. Procedia Eng. 2015. Vol. 116. No. 1. Pp. 639–646.
10. Lindenschmidt, K.E., Carr, M.K., Sadeghian, A., Morales-Marin, L. CE-QUAL-W2 model of dam outflow elevation impact on temperature, dissolved oxygen and nutrients in a reservoir. Sci. data. 2019. Vol. 6. No. 1. Pp. 312.
11. Bui, H.H. et al. Integration of SWAT and QUAL2K for water quality modeling in a data scarce basin of Cau River basin in Vietnam. Ecohydrol. Hydrobiol. 2019. Vol. 19. No. 2. Pp. 210–223.
12. Hwang, J.Y., Do Kim, Y., Kwon, J.H., Park, J.H., Noh, J.W., Yi, Y.K. Hydrodynamic and water quality modeling for gate operation: A case study for the Seonakdong River basin in Korea. KSCE J. Civ. Eng. 2014. Vol. 18. No. 1. Pp. 73–80.
13. hsu Lin, C., hsiu Huang, T., Shaw, D. Applying water quality modeling to regulating land development in a watershed. Water Resour. Manag. 2010. Vol. 24. No. 4. Pp. 629–640.
14. Li, Y., Zhang, Q., Ye, R., Yao, J., Tan, Z. 3D hydrodynamic investigation of thermal regime in a large river-lake-floodplain system (Poyang Lake, China). J. Hydrol. 2018. Vol. 567. No. September. Pp. 86–101.
15. Persaud, E.M., et al., Integrated Modelling to Assess Climate Change Impacts on Groundwater and Surface Water in the Great Lakes Basin using Diverse Climate Forcing. J. Hydrol. 2020. Pp. 124682.
16. Ye, X., Chu, P.Y., Anderson, E.J., Huang, C., Lang, G.A., Xue, P. Improved thermal structure simulation and optimized sampling strategy for Lake Erie using a data assimilative model. J. Great Lakes Res. 2020. Vol. 46. No. 1. Pp. 144–158.
17. Prastica, R.M.S., Apriatresnayanto, R., Marthanty, D.R. Structural and green infrastructure mitigation alternatives prevent Ciliwung River from water-related landslide. Int. J. Adv. Sci. Eng. Inf. Technol. 2019. Vol. 9. No. 6. Pp. 1825–1832.
18. Malalgoda, C., Amaratunga, D., Haigh, R. Creating a disaster resilient built environment in urban cities: The role of local governments in Sri Lanka. Int. J. Disaster Resil. Built Environ. 2013. Vol. 4. No. 1. Pp. 72–94.
19. Irajifar, L., Sipe, N., Alizadeh, T. The impact of urban form on disaster resiliency: A case study of Brisbane and Ipswich, Australia. Int. J. Disaster Resil. Built Environ. 2016. Vol. 7. No. 3. Pp. 259–275.
20. Hameed, H.M. Estimating the effect of urban growth on annual runoff volume using GIS in the Erbil Sub-Basin of the Kurdistan Region of Iraq. Hydrology. 2017. Vol. 4. No. 1.
21. Thorn, A.M., Wake, C.P., Grimm, C.D., Mitchell, C.R., Mineau, M.M., Ollinger, S.V. Development of scenarios for land cover, population density, impervious cover, and conservation in New Hampshire, 2010–2100. Ecol. Soc. 2017. Vol. 22. No. 4.
22. Wong, K., Zhang, Y., Tsou, J.Y., Li, Y. Assessing impervious surface changes in sustainable coastal land use: A case study in Hong Kong. Sustain. 2017. Vol. 9. No. 6. Pp. 6–9.
23. Henny, C., Meutia, A.A. Urban Lakes in Megacity Jakarta: Risk and Management Plan for Future Sustainability. Procedia Environ. Sci. 2014. Vol. 20. Pp. 737–746.
24. Brooks, B.W., et al. Are harmful algal blooms becoming the greatest inland water quality threat to public health and aquatic ecosystems?" Environ. Toxicol. Chem. 2016. Vol. 35. No. 1. Pp. 6–13.
25. Geist, J., Hawkins, S.J. Habitat recovery and restoration in aquatic ecosystems: current progress and future challenges. Aquat. Conserv. Mar. Freshw. Ecosyst. 2016. Vol. 26. No. 5. Pp. 942–962.
26. Hickey, J.T., Huff, R., Dunn, C.N. Using habitat to quantify ecological effects of restoration and water management alternatives. Environ. Model. Softw. 2015. Vol. 70. Pp. 16–31.
27. Hasegawa, H., Rahman, M.A., Kitahara, K., Itaya, Y., Maki, T., Ueda, K. Seasonal changes of arsenic speciation in lake waters in relation to eutrophication. Sci. Total Environ. 2010. Vol. 408. No. 7. Pp. 1684–1690.
28. Xu, J., Chen, Y., Zheng, L., Liu, B., Liu, J., Wang, X. Assessment of heavy metal pollution in the sediment of the main tributaries of Dongting Lake, China. Water (Switzerland). 2018. Vol. 10. No. 8. Pp. 1–16.
29. Nicholas, J., Holt, G.D., Proverbs, D.G. Towards standardising the assessment of flood damaged properties in the UK. Struct. Surv. 2001. Vol. 19. No. 4. Pp. 163–172.
30. Billa, L., Mansor, S., Mahmud, A.R. Spatial information technology in flood early warning systems: An overview of theory, application and latest developments in Malaysia. Disaster Prev. Manag. An Int. J. 2004. Vol. 13. No. 5. Pp. 356–363.
31. Mansor, S., Shariah, M.A., Billa, L., Setiawan, I., Jabar, F. Spatial technology for natural risk management. Disaster Prev. Manag. An Int. J. 2004. Vol. 13. No. 5. Pp. 364–373.
32. Abon, C.C., David, C.P.C., Tabios, G.Q. Community-based monitoring for flood early warning system: An example in central Bicol River basin, Philippines. Disaster Prev. Manag. 2012. Vol. 21. No. 1. Pp. 85–96.
33. Radojevic, B.D., Breil, P., Chocat, B. Assessing impact of global change on flood regimes. Int. J. Clim. Chang. Strateg. Manag. 2010. Vol. 2. No. 2. Pp. 167–179.
34. Liu, C., Li, Y. Measuring eco-roof mitigation on flash floods via GIS simulation. Built Environ. Proj. Asset Manag. 2016. Vol. 6. No. 4. Pp. 415–427.
35. Bera, M.K. Collective efforts of people to reduce disasters in the Indian Sundarban islands. Disaster Prev. Manag. An Int. J. 2019. Vol. 28. No. 5. Pp. 691–705.
36. Bennani, O., Druon, E., Leone, F., Tramblay, Y., Saidi, M.E.M. A spatial and integrated flood risk diagnosis: Relevance for disaster prevention at Ourika valley (High Atlas-Morocco). Disaster Prev. Manag. An Int. J. 2019. Vol. 28. No. 5. Pp. 548–564.
37. Bang, H., Miles, L., Gordon, R. Evaluating local vulnerability and organisational resilience to frequent flooding in Africa: the case of Northern Cameroon. Foresight. 2019. Vol. 21. No. 2. Pp. 266–284.
38. Kikwasi, G., Mbuya, E. Vulnerability analysis of building structures to floods: The case of flooding informal settlements in Dar es salaam, Tanzania. Int. J. Build. Pathol. Adapt. 2019. Vol. 37. No. 5. Pp. 629–656.
39. Chung, H.C.P., Adeyeye, K. Structural flood damage and the efficacy of property-level flood protection. Int. J. Build. Pathol. Adapt. 2018. Vol. 36. No. 5. Pp. 471–499.
40. Lummen, N., Nakajo, S., Yamada, F. Flooding due to torrential rainfall in Kumamoto, 2012. Int. J. Disaster Resil. Built Environ. 2014. Vol. 5. No. 3. Pp. 260–276.

41. Lummen, N.S., Shirozu, H., Okada, N., Yamada, F. Flood risk management an illustrative approach. Int. J. Disaster Resil. Built Environ. 2016. Vol. 7. No. 4. Pp. 388–405.
42. Espada, R.J., Apan, A., McDougall, K. Vulnerability assessment and interdependency analysis of critical infrastructures for climate adaptation and flood mitigation. Int. J. Disaster Resil. Built Environ. 2015. Vol. 6. No. 3. Pp. 313–346.
43. Rahayu, H.P., Haigh, R., Amaratunga, D., Kombaitan, B., Khoirunnisa, D., Pradana, V. A micro scale study of climate change adaptation and disaster risk reduction in coastal urban strategic planning for the Jakarta. Int. J. Disaster Resil. Built Environ. 2019. Vol. 11. No. 1. Pp. 119–133.
44. Kourtis, I.M., Tsihrintzis, V.A., Baltas, E. Simulation of Low Impact Development (LID) Practices and Comparison with Conventional Drainage Solutions. Proceedings. 2018. Vol. 2. No. 11 Pp. 640.
45. Ji, Z.-G. Hydrodynamics and Water Quality. New Jersey: John Wiley & Sons, Inc., 2008.
46. Khadr, M.E.M., Ahmed, Y.A.A. Hydrodynamic and water quality modeling of Lake Manzala (Egypt) under data scarcity. Environ. Earth Sci. 2016. Vol. 75. No. 19. Pp. 1–13.
47. Huang, M., Tian, Y. An Integrated Graphic Modeling System for Three-Dimensional Hydrodynamic and Water Quality Simulation in Lakes. 2019.
48. Sun, J.L., Wang, Y., Chen, J., Zhang, Q.L., Zhang, Y., Guo, Y.J. Simulation of hydrodynamics and water quality in Xi ' an Yanming Lake Simulation of hydrodynamics and water quality in Xi ' an. in IOP Conference Series: Earth and Environmental Science. 2018. Vol. 191.
49. Yi, Y., Tang, C., Yang, Z., Zhang, S., Zhang, C. A One-Dimensional Hydrodynamic and Water Quality Model for a Water Transfer Project with Multihydraulic Structures. 2017. Vol. 2017.
50. Kato, T., Kuroda, H., Nakasone, H., Kiri, H. Evaluation of pollutant removal in a constructed irrigation pond. Paddy Water Environ. 2007. Vol. 5. No. 3. Pp. 189–199.
51. Lee, H., Masuda, T., Yasuda, H., Hosoi, Y. The pollutant loads from a paddy field watershed due to agricultural activity. Paddy Water Environ. 2014. Vol. 12. No. 4. Pp. 439–448.
52. Mosley, L.M., Fleming, N. Pollutant loads returned to the lower murray river from flood-irrigated agriculture. Water. Air. Soil Pollut. 2010. Vol. 211. No. 1–4. Pp. 475–487.
53. Smith, D.C., Senior, E., Dicks, H.M. Irrigation of soil with synthetic landfill leachate - Breakthrough behaviour of selected pollutants. Water. Air. Soil Pollut. 1999. Vol. 109. No. 1–4. Pp. 327–342.
54. Wang, H., He, P., Shen, C., Wu, Z. Effect of irrigation amount and fertilization on agriculture non-point source pollution in the paddy field. Environ. Sci. Pollut. Res. 2019. Vol. 26. No. 10. Pp. 10363–10373.
55. Hatt, B.E., Fletcher, T.D., Walsh, C.J., Taylor, S.L. The influence of urban density and drainage infrastructure on the concentrations and loads of pollutants in small streams. Environ. Manage. 2004. Vol. 34. No. 1. Pp. 112–124.
56. Nieto, J.M., Sarmiento, A.M., Canovas, C.R., Olias, M., Ayora, C. Acid mine drainage in the Iberian Pyrite Belt: 1. Hydrochemical characteristics and pollutant load of the Tinto and Odiel rivers. Environ. Sci. Pollut. Res. 2013. Vol. 20. No. 11. Pp. 7509–7519.
57. Yu, J.Y. A mass balance approach to estimate the dilution and removal of the pollutants in stream water polluted by acid mine drainage. Environ. Geol. 1998. Vol. 36. No. 3–4. Pp. 271–276.
58. Zhang, S., Meng, Y., Pan, J., Chen, J. Pollutant reduction effectiveness of low-impact development drainage system in a campus. Front. Environ. Sci. Eng. 2017. Vol. 11. No. 4. Pp. 1–8.
59. Prastica, R.M.S., Wicaksono, D. Integrated multimodal disaster mitigation management for urban areas: A preliminary study for 2-d flood modeling. IOP Conference Series: Materials Science and Engineering. 2019. Vol. 650. No. 1.
60. Nav, J., Jose, A., Suár, J., Pu, J. Hydraulic, wash-off and sediment transport experiments in a full- scale urban drainage physical model. 2020. Pp. 1–13.
61. Zeng, J., Huang, G., Luo, H., Mai, Y., Wu, H. First flush of non-point source pollution and hydrological effects of LID in a Guangzhou community. Sci. Rep. 2019. Vol. 9. No. 1. Pp. 1–10.

Contacts:

Rian Mantasa Salve Prastica, rianmantasasp@gmail.com; rian.mantasa.s.p@ugm.ac.id

Herr Soeryantono, herr.soeryantono@ui.ac.id

Dwinanti Rika Marthanty, dwinanti@gmail.com

Magazine of Civil Engineering. 2022. 109(1). Article No. 10904

Magazine of Civil Engineering

ISSN 2712-8172

journal homepage: http://engstroy.spbstu.ru/

DOI: 10.34910/MCE.109.4

Long–term behavior of composite steel plate-concrete slabs incorporating waste plastic fibers

H. Kuhair, S. Hama*, K. Aziz

University Of Anbar, Ramadi, Anbar, Iraq

**E-mail: drsheelan@uoanbar.edu.iq*

Keywords: composite structure, load-deflection behavior, load-slip relation, long-term, plastic waste

Abstract. This research has been conducted to investigate the effect of adding waste plastic fibers (WPF) in concrete on behavior of composites steel plate-concrete slabs. The WPF were produced by cutting plastic bottles used to preserve carbonated beverages. Both mid-span deflection and slip between concrete layer and steel plate are measured using an electronic gauge at 7, 28, 56, 90, 120, 180 and 270 day age. Percentages calculations of plastic fiber by volumetric rates ranging between (0 %) to (1 %) were carried out. Reference concrete slab without plastic fibers was cast for comparison. Short-term test was conducted on the slabs to determine the ultimate load. The tests results showed that 1 % WPF has led to lower value of deflection and highest slip between steel plate and slab concrete. There is a slight difference between the results of 0.75 % and 1 %WPF.

1. *Introduction*

Utilizing waste plastic fiber in concrete not only enhances properties of the concrete but also benefits environment by reducing this type of waste. The main objective of this study is to examine the time-dependent behavior of composite steel-concrete slabs, in which concrete incorporates waste plastic fibers. In addition, we examined other factors such as the degree of interaction and type of connection between stud shear connector and steel plate (weld and epoxy).

Hama investigated the effects of the presence of waste plastic chips on the fresh properties of concrete, as well as strength and impact resistance characteristics of a concrete slab. The tests result indicated a decrease in strength properties and impact, but the compact resistance and energy capacity absorption of concrete improvemed due to the addition of plastic chips as aggregate [1, 2]. In general, adding waste plastic led to reduced workability of concrete [1, 2]. Nibudey et al. studied the performance of concrete in presence of waste plastic fiber (0 to 3 %). Compressive and tensile strength were investigated. Results of tests showed that 1 % waste plastic fiber improved mechanical characteristics of tested specimens compared to reference specimens without fibers [3]. Ganesh et al. investigated the effect of replacing natural fine aggregate with fine waste plastic. Twenty-seven specimens were tested. The sand was replaced by (0.5, 1.0, and 1.5 %) fine waste plastic by volume. Test results showed that 1.0 % fine waste plastic gave the best results in terms of both compressive and tensile strength [4]. Al-Rawi study the flexural behavior of reinforced concrete beams incorporating waste plastic fiber by (0.0, 0.5, 1.0, 1.5, and 2.0 %) as volume fraction. Test results showed a reduction in deflection with an increase in fibers content up to (1%) [5]. Al-Ani studied the possible way to use waste plastic material as fine aggregate in structural elements by evaluating the mechanical properties of concrete. Various ratios of waste plastic were considered (2.5 %, 5.0 %, and 7.5 %) by volume. Test results indicated that the presence of waste plastic reduces concrete workability and decreased the compressive strength and modulus of elasticity compared with control concrete [6]. Faisal et al. studied the influence of ring-shaped waste plastic on flexural toughness of concrete. Results showed an increase in the toughness of about 23 % for (5 mm) plastic width

Kuhair, H., Hama, S., Aziz, K. Long– term behavior of composite steel plate- concrete slabs incorporating waste plastic fibers. Magazine of Civil Engineering. 2022. 109(1). Article No. 10904. DOI: 10.34910/MCE.109.4

and 40 % for 10 mm width [7]. Hama showed that adding plastic fibers to lightweight concrete led to improving its mechanical properties, especially flexural strength [8]. Another study showed that plastic fibers increased the slip between concrete and steel sections in the push-out test [9]. Another study showed that adding plastic aggregate with waste glass powder improved mechanical properties and bond strength compared to specimens with waste plastic without glass powder [10]. Marthong and Sarma [11] investigated the influence of plastic fibers geometry (straight, flattened end deformed, and crimped end fiber). The straight one gave the poorest and weakest bond with concrete matrix among other types while other types clearly improved the anchorage effect. Ollgaard et al. [12] investigated the behavior of shear connectors (stud type) in normal and lightweight concrete. Results showed that the shear strength of the stud shear connector embedded in normal or lightweight concrete was affected by both compressive strength and modulus of elasticity of concrete. The behavior of headed shear connectors on trapezoidal profiled steel sheets push-out tests have been investigated by Lloyd and Wright [13]. Results showed that the shear strength of connectors was affected by the stiffness of transverse reinforcement. Shim et al. [14] studied stress-slip relation of large diameter stud connector using a static push-out test.

There is no existing research about the effect of plastic fibers on the long-term behavior of steel-concrete slabs under sustained load. Therefore, this research provides useful data in this field.

2. Methods

2.1. Material

Ordinary Portland cement (OPC – Type I) was used to cast all specimens. Test results indicate that the adopted cement conforms to the Iraqi specifications (I.Q.S.) No.5/ 1984 [15] as shown in Tables 1 and 2, respectively.

Table 1. Physical properties of cement.

Physical properties	Test result	Limits of I.Q.S No.5/1984
Specific surface area (Blaine Method) (m^2/kg).	300	> 230
Setting time :		
-Initial setting (min.)	90 min.	≥ 45 minute
-Final setting (min.)	225	≤ 600 minute
Compressive strength of mortar (MPa):		
3-days	21	≥ 15
7-days	27	≥ 23
Soundness % (Autoclave)	0.2	≤ 0.8

Table 2. Chemical properties of cement.

Oxide composition	by weight%	Limits of I.Q.S No.5/1984
CaO	61	–
SiO_2	19.84	–
Al_2O_3	5.28	–
Fe_2O_3	4.2	–
SO_3	2.49	≤ 5 %
MgO	2.48	≤ 2.8 %
Loss on Ignition (L.O.I.)	3.8	≤ 4 %
Lime saturation Factor (L.S.F.)	0.92	0.66-1.02
Insoluble residue (I.R.)	1.13	≤ 1.5 %

Natural fine aggregate from the local Al-Akhadir area was used. Table 3 presents the sieve analysis. Table 4 shows physical properties of the used sand.

Table 3. Sieve analysis of fine aggregate.

Sieve size(mm)	% passing	Limits of I.Q.S No. 45/1984 % passing Zone (2) [16]
10	100	100
4.75	91	90–100
2.36	79	75–100
1.18	67	55–90
0.6	48	35–59
0.3	15	8–30
0.15	2	0–10

Table 4. Physical and chemical properties of the used fine aggregate.

Physical properties	Test result	Iraqi Specification [16]
Specific gravity	2.60	
Sulfate content (SO_3%)	0.42%	0.5 % (max)
Absorption%	0.75%	–
Fineness modulus	2.97	–

Crushed gravel from the AL-Nibaey area with a maximum size of 10 mm was used as coarse aggregate. Tables 5 and 6 present sieve analysis of the coarse aggregate and the physical and chemical properties of coarse aggregate respectively with the limit specified by Iraqi Specification No.45/1984.

Table 5. Sieve analysis of coarse aggregate.

Sieve Size (mm)	% Passing	Iraqi specifications No. 45/1984
12.5	100	100
9.5	86	85–100
4.75	5.5	0–25
2.36	1	0–5

Table 6. Physical and chemical properties of coarse aggregate.

Properties	Test results	Iraqi specifications No.45/1984
Specific gravity	2.65	–
Sulfate content	0.09	≤ 0.1
Absorption %	0.52 %	–

The geometrical characteristics of plastic fibers throughout the experimental work are illustrated in Table 7. A shredder machine was used to cut plastic, see Fig. 1. Fibers were added to the mixes with these ratios by volume of mixture: 0.00, 0.50, 0.75, and 1.00 respectively. Two types of epoxy were used for connection between stud and steel plate, and between steel plate and concrete slabs. Each type consists of two parts (A and B) which were mixed with specific percentages to get the final resin.

Table 7. Characteristics of plastic fibers.

Properties	Length(mm)	Width(mm)	Thickness(mm)	Specific gravity (gm/cm^3)
Plastic fibers	35	4	0.30	1.1

Headed shear stud connector is commonly used in composite structures, and therefore was selected for the RC composite slabs. The diameter of the stud is (6 mm) with height of (35 mm), and the head diameter is (10 mm). The mechanical properties comply with ASTM A615-14 [17], see Table 8.

Table 8. Tensile properties of the used stud shear connectors and steel plate.

Details of steel	Yield Tensile Strength (MPa)	Average of Ultimate Tensile Strength (MPa)	Modulus of Elasticity (MPa)	% Elongation at Ultimate Stress
Steel plate (Actual thickness 3 mm) 93 mm	320	420	203000	18
Stud (Actual dia. 6 mm)	610	760	201000	20

Figure 1. Preparation of plastic fibers: shredding machine(left), and plastic fibers(right).

Steel plate with dimensions (1000*1000) mm, properties listed in Table 8, was used in the present study. According to ASTM A36/A [18], the yield and tensile strength were evaluated. The steel plate and the welded stud shear connectors before casting concrete are shown in Fig. 2.

Figure 2. Steel plate with welded stud shear connectors.

WWF (Welded Wire – Fabric) is the type of reinforcement that was used to reinforce the RC composite slabs. The mechanical properties and geometry are listed in Table 9. The WWF was placed (20 mm) from the top. According to ASTM A185-07, the yield and tensile strength were evaluated.

Table 9. WWF geometry and mechanical properties.

Square opening (mm)	Yield Tensile Strength (MPa)	Ultimate Tensile Strength (MPa)	Modulus of Elasticity (MPa)	Elongation at Ultimate Stress (%)
90*90	520	630	210000	11

2.2. Mixing Proportion And Specimens Tests

The mix proportions were listed in Table 10. Waste plastic fibers were added to the chosen mix as a percentage of the volume of concrete (0, 0.5, 0.75, and 1 %). Compressive strength and flexural strength were measured according to ASTM C39-03 [19] and ASTM C78-03 [20] respectively. An average of three specimens was considered for each test.

Table 10. Mix proportions.

Symbol	Cement (kg/m^3)	Fine aggregate (kg/m^3)	Coarse aggregate (kg/m^3)	% (w/c)	Plastic fiber (%)	Compressive strength (MPa)	Flexural strength (Mpa)
1	420	720	950	0.5	0.00	26.91	2.8
2	420	720	950	0.5	0.50	26.99	3.5
3	420	720	950	0.5	0.75	29.49	4.34
4	420	720	950	0.5	1.00	24.78	4.9

2.3. Composite Slab Details, Casting, Compaction, and Curing

Wood frames were fixed on the steel plate, and the BRC was fixed about 20mm from the top of the frame for concrete casting to form a composite slab. Compactions were made by using a mechanical vibrator to get more uniform mixing and prevent any voids inside concrete. Steel trowel was used to level the top surface of slabs and smooth it; Fig. 3 shows the slabs after casting. The composite slab details are clarified in Fig. 4. Before the tests, all specimens were cured in a fresh water tank to ensure the required time for the concrete to complete the hydration processes. The composite slab was warped in a nylon sheet to prevent evaporation during the hydration processes as well.

Figure 3. Slabs after casting.

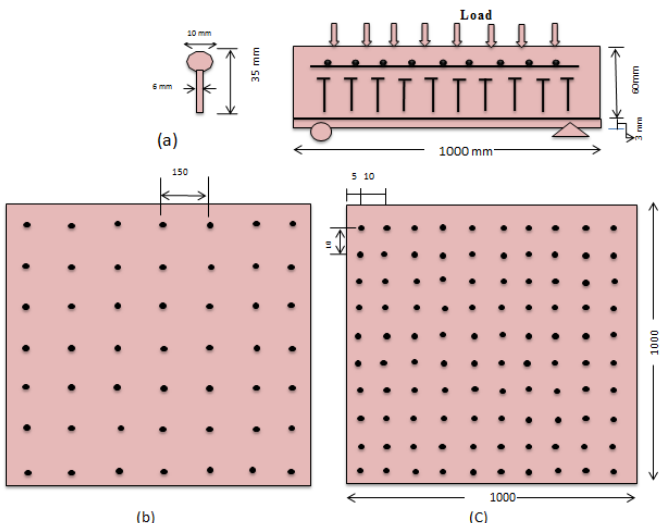

Figure 4. Details of the composite slab (all dimensions in mm)
a – Front view of the composite slab; b – Top view of partial composite slab (50 % D.O.I); c – Top view of the full composite slab (100 % D.O.I)

2.4. Composite Slabs Tests

2.4.1. Short-term test

The reinforced concrete composite slabs were tested under static short-term loading. A slab was resting at the testing machine with supports around the perimeter of the slab (simply-supported). A 5 mm thick steel plate was put on top of the slab with reinforcing steel bars were distributed at the top face of the steel plate in one layer. We added up to five steel plates one after another separated by steel bars (see Fig. 5). The load was applied at the center (top) of the R.C. slab utilizing a thick steel plate to distribute the loading. Initially, the load applied was up to (5 kN); then it was reset to zero to make the slab rest, and there was no effect of the friction that developed in supports. The load was applied gradually (load control) and the deflections and slip were recorded at each load step until the failure of the slab.

2.4.2. Long-term test

The long-term loading was tested by applying uniform service loading (around 40 % of ultimate load) at the top of the composite slab utilizing an equivalent weight of sand. The deflections and slips were measured at various times in a span of nine months using two fixed dial gauges: one at the end of the slab to measure the cumulative slips, and the second at the center bottom face of composite slabs to measure the deflections.

Deflection and slip were measured at mid-span and interface between the concrete slab and steel plate, respectively, by using a dial gauge, which has an accuracy of (0.001 mm) as shown in Fig. 6.

Figure 5. Short-term test **Figure 6. Dial gauge.**

2.4.3. Parametric Study

Ten slabs were tested: one under static load to fix the ultimate load, and nine under sustained load (40 % from ultimate load). The slabs were marked as shown in Table 11. Three parametric studies were taken in this work:

1. Degree of interaction D.O.I (0, 50,100 %);
2. Percentages of WPF (0, 0.5, 0.75, 1 %);
3. Type of connection between steel plate and stud shear connector (welding, epoxy).

Table 11. Specimen's details.

Mark	% WPF	% Degree of interaction	Type of connection
H1	0.75	50	Welding
H2*	0	100	Welding
H3	0.75	100	Welding
H4	0.75	No Stud	Glued plate by epoxy without stud
H5	0.75	0	N/A Concrete slab cast directly on the plate without a connection
H6	0.5	50	Welding
H7	1	50	Welding
H8	0.75	50	Glued stud by epoxy
H9	0	50	Welding
H10	0	0	Reference without plate with 74 mm RC slab only

All specimens were tested under sustained load but H2* was tested under short-term load.

3. Results and Discussion

3.1. Short Term Tests

A short-term test was done for composite slab (H2) with (100 % D.O.I) and (0 % WPF) to determine the ultimate load. The max deflection was 0.402 mm at 12.5 KN/m^2 maximum load. Load–deflection is shown in Fig. 7, and load–slip curve of composite slab behavior is shown in Fig. 8.

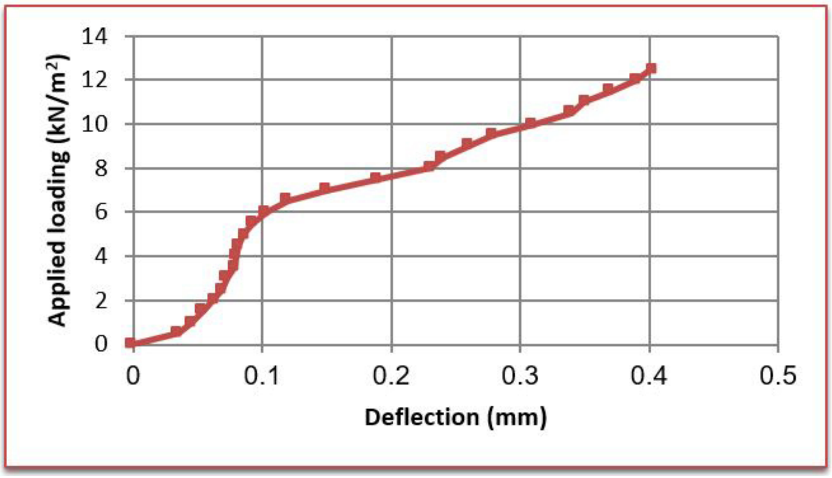

Figure 7. Load–deflection of the short-term test.

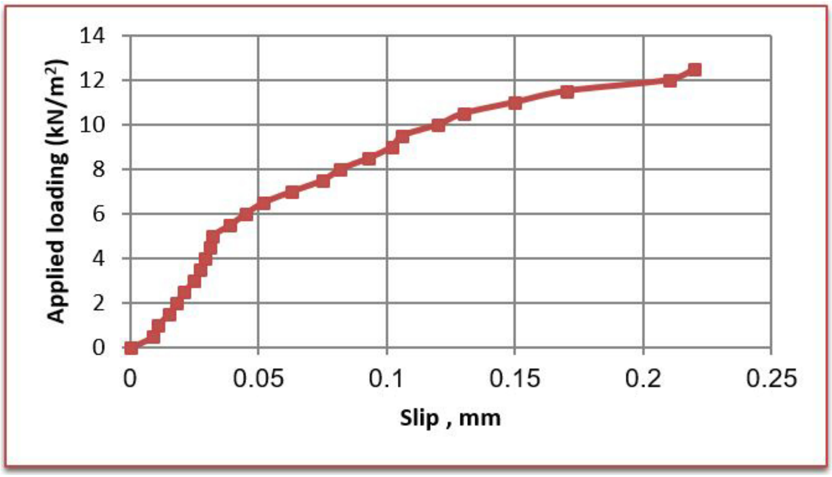

Figure 8. Load–slip curve of the composite slab (Short term tests).

3.2. Time – Depended Test

A total of nine specimens were tested under service loading of (40 %) from the ultimate loading which is equal to (5 KN/m^2). In experimental tests, dial gauges are fixed at the interface between reinforced concrete slab and steel plate to measure the relative horizontal displacement (slip). Another one was also fixed at the bottom of the specimen at the mid-span to measure the central deflection. The dead load was applied uniformly by brushing the sand over the slab. The tests yielded the following results according to considered parametric study.

3.2.1. Effects of Waste Plastic Fiber Percentages (WPF)

Fig. 9 shows deflection–time relationships for different (% WPF). The percentage of added fiber related decrease in deflection compared to reference slab (H9 without WPF) was 10.11 %, 37.19 %, and 40.14 % for 0.5 %,0.75 %, and 1 % WPF, respectively, at the age of (270 days). From the results, one can see that (1 % WPFC) gave the lowest deflection. The mechanical properties test showed that adding (1 % WPF) produced the best flexural tensile strength, which may be the reason why adding (1 % WPF) resulted in a deflection decrease.

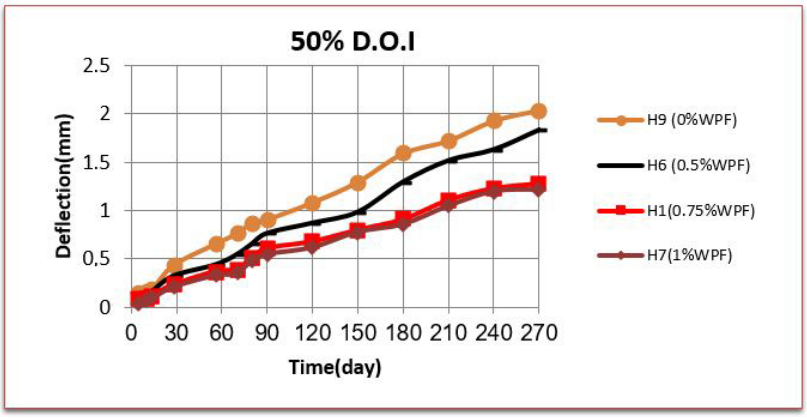

Figure 9. Effects of waste plastic fiber on deflection with time.

The slip values for various percentages of WPF are drawn in Fig. 10. The maximum slip values for H7 (1 % WPF) are more than other percentages and increase with time. It seems that plastic fiber distribution affected the adhesion between the concrete slab and steel plate and this reflects in slip values [9]. In comparison with reference concrete H9, the slip values are higher for the same age (270 days) with 8.3 % and 18 % for H6 (0.5 %) and H1 (0.75%) WPF respectively, but H7 (1 % WPF) has slip higher than the reference concrete by 23 %.

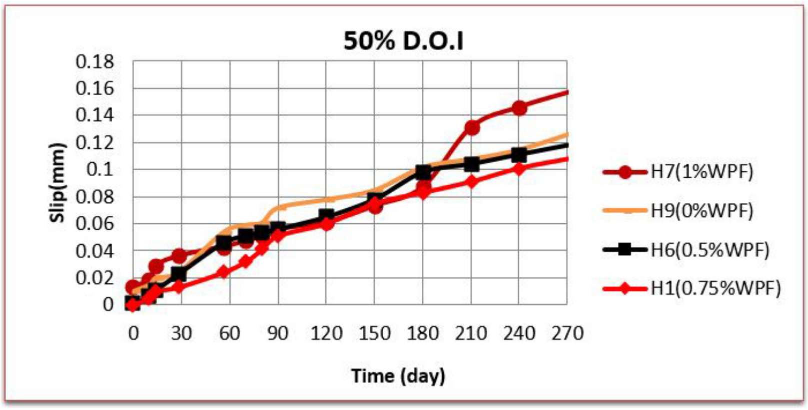

Figure 10. Effects of waste plastic fiber on the slip with time.

3.2.2. Type of Connection between Stud Shear Connector and Steel Plate (Welding and Epoxy)

Two methods were used to fix stud shear connectors to the steel plate: welding, and epoxy adhesive. Fig. 11 and Fig. 12 show that deflection and slip increased in the case of fixing the stud shear connectors with epoxy at the top of steel plate (H8) compared with welding studs shear connectors (H1), since epoxy is more flexible than welding. The deflections of H8 were higher than H1 by 2.3 % for the same age (270 days). The use of welding to fix the stud connectors increases the stuffiness of the composite slab which led to a decrease in deflection and the slip between concrete and steel plate. These results can also be explained according to the results of the push-out test carried by Azizi et al. [9], who found that the strength of the stud connector is higher in the case of welding connection with steel plate.

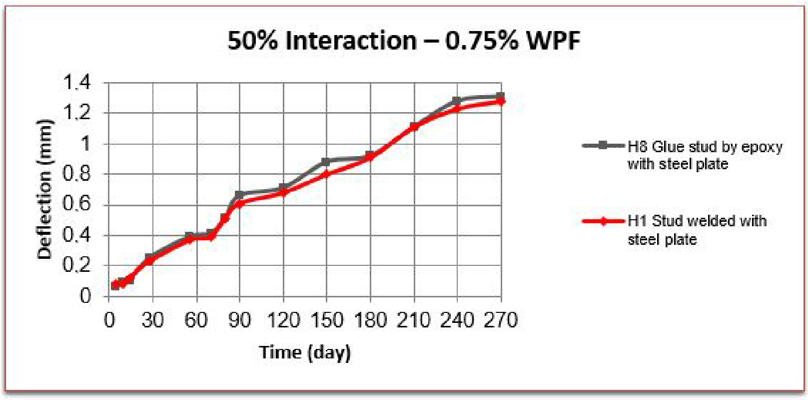

Figure 11. Effects of type of connections between shear stud and a steel plate on deflection with time.

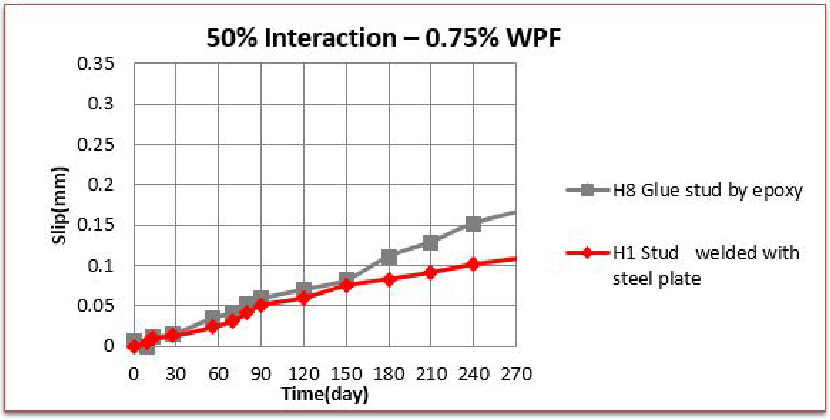

Figure 12. Effects of type of connections between shear stud and a steel plate on the slip with time.

3.2.3. Degree of Interaction (D.O.I)

Fig. 13 illustrates the relationship between deflection and time for (100 % D.O.I) H3, (50 % D.O.I) H1. H1 and H3 were compared with H5 (0 % D.O.I concrete that was cast directly over the plate without any shear connectors). Compared with H5 (using as control slab), at the age of 270 days, H3 has deflection lower by 57.5 %, while H1 has deflection lower by 42.1 %. Higher D.O.I gave lower deflection, H1 has higher deflection than H3 by 36.2 % at the age of (270 days) as show in the full interaction which gives the lower value of deflections because of full integrity between concrete slab and steel plate, so that the rigidity and stiffness become more rather than the 50 % and zero interaction. We compared two slabs with 0 % (D.O.I): H4 had concrete glued to the plate directly using epoxy, while H5 was cast directly above plate without any type of epoxy (0 % D.O.I), i.e. there was no interaction between concrete and steel plate. H5 has higher deflection than H4 by 36.4 % at the age of (270 days), because each material works separately, causing deflection to increase (see Fig. 14). Fig. 15 shows that the slip increases and becomes higher when the reinforced concrete slab was cast directly above the steel plate without any connections (0 % D.O.I), so that there are no connection nodes, no volume contact, and the two materials work separately. The specimens H3 and H1 (100 % and 50 % D.O.I) have slips less than specimen H5 by about 83 % and 76 % respectively at the same age (270 days), and H3 has slip higher than H1 by 31 %. When the interaction is full, the composite action works, so the stiffness and rigidity increase because of increasing in a moment of inertia and equivalent modulus of elasticity for a composite slab with full interaction and partial interaction compared to a composite slab without shear connection. Fig.16 shows the variations of slip in two types of interactions. First goes H5, the concrete slab cast above the steel plate without interactions, second is H4 specimen, and then the connections by epoxy without stud shear connectors. H4 has lesser slip than H5 by 28 %. This is due to the shear force that developed by the vertical force transfer from glue to the steel plate: the shear force distributes and is equal in opposite directions between the concrete slab and steel plate, therefore the slip was reduced and became lower than H5 specimen.

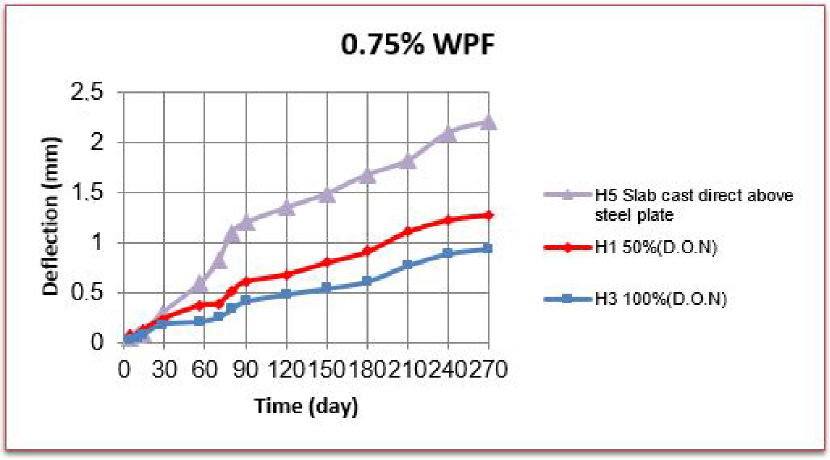

Figure 13. Effects of degree of connections on a deflection with time.

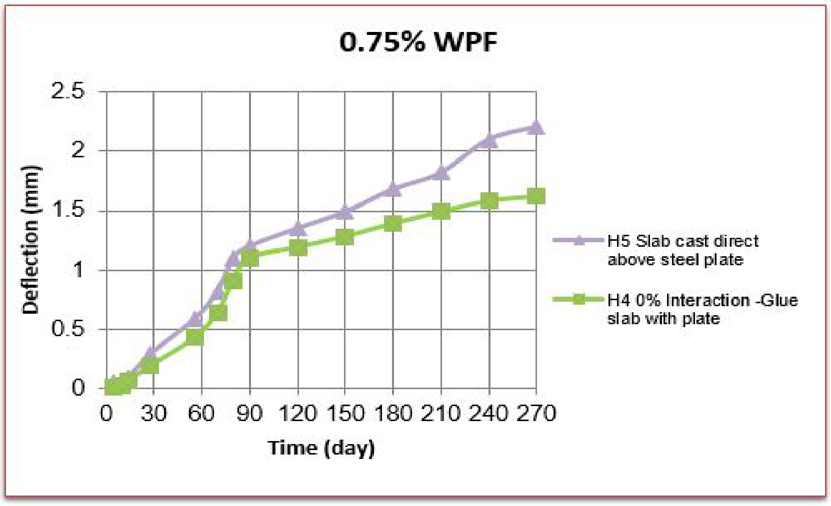

Figure 14. Comparison between deflection of slabs H5 and H4.

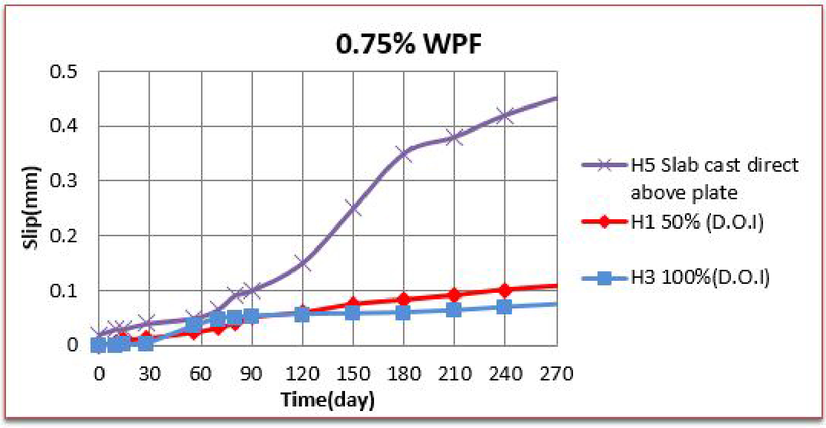

Figure 15. Comparison between the slip of slabs H1, H3, and H5.

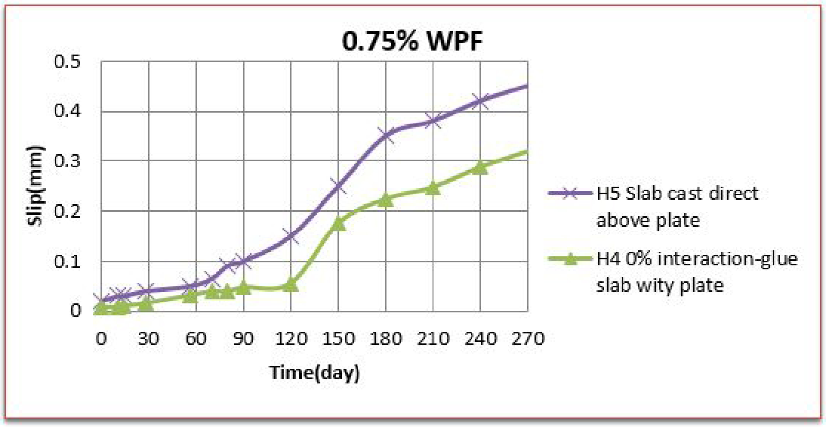

Figure 16. Comparison between the slip of slabs H4 and H5.

4. Conclusions

This experimental investigation shows that PET bottles can become a low-cost material, which can help to resolve solid waste problems and prevent environmental pollution, while at the same time enhancing the properties of concrete as concluded in this study. The results are as follows:

1. Decreased deflection due to adding the fiber in comparison with control slab (without WPF) by 4.3 %,7.2 %, and 11.6 % for 0.5 %, 0.75 %, and 1 % WPF, respectively at 270-days ages.
2. The deflection decreased when the degree of interaction increased, the percentages of decreasing were 57 and 42.1 % for the degree of interactions 100 and 50 %, respectively, compared with the reinforced concrete slab cast directly above steel plate without any connection types for the same age (270 days).

3. The deflection increases in the case of the non-composite slab as compared with the composite slab of 50 % D.O.I. at the same age (270 days) by 41 %.
4. The deflection increases in the case of gluing the stud connectors to steel plate by epoxy compared with welding stud connectors by (2.3 %) at the same age (270 days).
5. The slip increases as the percentage of WPF increases and the maximum value of slip at (1 % of WPF) equals 23 % compared with the control specimen at the same age (270 days).
6. The slip decreases as the degree of interaction goes higher. The percentages of the slip decrease were 83 % and 76 % for 100 % and 50 % D.O.I., respectively, as compared with no interaction case at the same age.
7. In the case of welded stud connectors, the slip is lower than in other types of connections compared with the control specimen at the same age.

References

1. Hama, S.M. Evalutions of strengths, impact and energy capacity of two-way concrete slabs incorprating waste plastic. Journal of King Saud University – Engineering Sciences. 2021. 33. Pp. 337–345. https://doi.org/10.1016/j.jksues.2020.09.007
2. Hama, S.M. Behavior of concrete incorporating waste plastic as fne aggregate subjected to compression, impact load and bond resistance. Eur J Environ Civ Eng. 2020. https://doi.org/10.1080/19648 189.2020.1798287
3. Nibudey, R.N., Nagarnaik, P.B., Parbat, D.K., Pande A.M. Strengths Prediction of Plastic fiber Reinforced concrete M3. International Journal of Engineering Research and Applications. 2013. 3(1). Pp. 1818–1825.
4. Prabhu, P. Ganesh, Kumar, C.A., Pandiyaraj, R., Rajesh, P., Kumar, I.S. Study on Utilization of Waste pet Bottle Fiber in Concrete. International Journal of Research in Engineering & Technology. 2014. 2 (5). Pp. 233–240.
5. Al-Rawi, M. Flexural Behavior of Reinforced Concrete Beams enhancement with Waste Plastic Fiber. M.Sc. Thesis, Department of Civil Engineering, University of Tikrit. 2015.
6. Al-Ani, M.F. Behavior of High-Performance Concrete by Using Waste Plastic as Aggregate. M.Sc. Thesis, Department of Civil Engineering. The University of Baghdad. 2015.
7. Faisal, S.K., Irwan, J.M., Othman, N., Wan Ibrahim, M.H. Flexural Toughness of Ring-Shaped Waste Bottle Fiber Concrete. MATEC Web of Conferences. 3rd International Conference on Civil and Environmental Engineering for Sustainability (IConCEES 2015). 2016. 47. 01002. http://dx.doi.org/10.1051/matecconf/20164701002
8. Hama, S.M. Improving mechanical properties of lightweight Porcelanite aggregate concrete using different waste material.International Journal of Sustainable Built Environment. 2017. 6(1). Pp. 81–90. http://dx.doi.org/10.1016/j.ijsbe.2017.03.002
9. Aziz K. I., Hama S. M. and Kuhair H. M. L. Effenciency of Waste Plastic Fiber on Behavior of Composite Steel Plate-Concrete Push Out Test," 2018 11th International Conference on Developments in eSystems Engineering (DeSE). 2018. Pp. 335–339, doi: 10.1109/DeSE.2018.00066.
10. Mohammed, T.K., Hama, S.M. Mechanical properties, impact resistance and bond strength of green concrete incorporating waste glass powder and waste fine plastic aggregate. Innov. Infrastruct. Solut. 2022. 7. 49. https://doi.org/10.1007/s41062-021-00652-4
11. Marthong, C., Sarma, D.K. Influence of PET fiber geometry on the mechanical properties of concrete: an experimental investigation. 2016. 7. Pp. 771–784. https://doi.org/10.1080/19648189.2015.1072112
12. Ollgaard, J.G., Slutter, R.G., Fisher, J.W. Shear strength of stud connectors in lightweight and normal weight concrete. Engineering Journal AISC. 1971. 8. Pp. 55–64.
13. Lloyd, R.M., Wright, H.D. Shear connection between composite slabs and steel beams. Journal of Structural Engineering. 1990. Pp. 255–285.
14. Shim, C.S., Lee, P.G., Yoon, T.Y. Static behaviour of large stud shear connectors", Engineering Structures. 2004. 26(12). Pp. 1853–1860.
15. Iraqi specification No. 5/1984. Portland Cement. Central Agency for standardization and Quality Control, Planning Council, Baghdad, Iraq.
16. Iraqi specification No. 45/1984. Aggregate from Natural Sources for concrete. Central Agency for Standardization and Quality Control, Planning Council, Baghdad, Iraq.
17. ASTM A615. Standard Specification for Deformed and Plain Carbon-Steel Bars for Concrete Reinforcement. ASTM International. 2009. 6 Pp.
18. ASTM A 36/A 36M.Standard Specification for Carbon Structural Steel", Annual book of ASTM standard, 01.05. 2005. Pp. 103–105.
19. ASTM C39/C39M. Standard Test Method for Compressive Strength of Cylindrical Concrete Specimens. 04.03. 2003.West Conshohocken, PA.
20. ASTM C78. Standard Test Method for Flexural Strength of Concrete Using Simple Beam with Third-Point Loading. Annual Book of ASTM Standard. 2003.

Contacts:

Huda Kuhair, Hudakuhair@yahoo.com
Sheelan Hama, drsheelan@uoanbar.edu.iq
Khalil Aziz, k_ibraheem@yahoo.com

Magazine of Civil Engineering

ISSN 2712-8172

journal homepage: http://engstroy.spbstu.ru/

DOI: 10.34910/MCE.109.5

The shear behavior of Anchored CFRP Strengthened RC beams

R. Al-Rousan

Jordan University of Science and Technology, Irbid, Jordan

E-mail: rzalrousan@just.edu.jo

Keywords: reinforced concrete, anchored, shear, flexural strength, fiber reinforced polymer, nonlinear, finite element analysis

Abstract. The primary objective of this paper is to study the effectiveness of anchorage on the performance of shear deficient beams externally strengthened with carbon fiber-reinforced polymers (CFRP) composites. The overall behavior of the tested beams loaded up to failure, the onset of the cracking, and crack development with increased load and ductility were described. The use of CFRP composites is an effective technique to enhance the shear capacity of reinforced concrete (RC) beams. The externally bonded CFRP can increase the shear capacity of the beam significantly making it 15–34 % more than that of the control beams, depending on the variables investigated. The use of CFRP composites is an effective technique to enhance the shear capacity of RC beams by using CFRP strips anchored into the tension side and from the top. Bonded anchorage of CFRP strips with width of 0.1h, 0.2h, and 0.3h to the beam resulted in a decrease in average interface bond stress and an increase in the effective strain of the FRP sheet at failure. This resulted in a higher shear capacity as compared with that of the U-wrapped beams without anchorage as well as helped delay or mitigate the sheet debonding from the concrete surface. Finally, an inclusive assessment of the NLFEA results is conducted using a large test database of well-known shear strength models.

1. Introduction

Premature debonding failure of reinforced concrete beams strengthened with externally bonded fiber reinforced polymers (FRP) is a frequent problem. Therefore, developing anchorage devices to enhance the composite action between the FRP sheets and the concrete beam is a big challenge to prevent the debonding of the FRP plates from a concrete beam. Mechanical anchorage is a useful method to prevent this mode of failure, therefore improving the performance of the conventional FRP-strengthening method. Knowledge of anchorage systems is limited and further experimental and numerical studies to understand their behavior are still necessary to optimize their performances.

Concrete structures (for example: buildings, bridge decks, girders, offshore structures, parking lots) are subject to damage because of: improper maintenance, steel corrosion, ageing, faulty design or construction, additional excessive loading such as heavy traffic, the seismic movements, and harsh environmental condition. Due to the old codes of design, or not complying with the new ones as in some countries, many structures are endangered, and need to be strengthened and/or rehabilitated [1]. It has been reported that 23 % of the concrete bridges in the USA are deficient or not in service [2]. Deficient structure can be repaired or demolished. However, the latter could cause damages, sometimes severe, to the adjacent structures, resulting in financial losses. Therefore, there is a need to find adequate techniques and materials to strengthen and/or repair such structures. The strengthening technique of bonding, externally, carbon-fiber reinforced polymer (CFRP) laminates has been widely adopted to repair, strengthen, and rehabilitate deficient or damaged structures [3–6]. The RC structures, commonly, fail or get defected in shear or flexure. Between these two, the deficiency in shear is much more serious because it occurs suddenly, without giving the element the chance to deal with the developed internal stresses. The

Al-Rousan, R. The shear behavior of Anchored CFRP Strengthened RC beams. Magazine of Civil Engineering. 2022. 109(1). Article No. 10905. DOI: 10.34910/MCE.109.5

shear failure could be due to improper designing, reduction in shear reinforcement (RFT) that is caused by steel corrosion or overloading. The use of externally-bonded FRP material's efficiency to enhance the shear capacity [7–11] is governed, mainly, by its: tensile strength, the ratio of shear reinforcement, the used configuration. In addition, the FRP's efficiency is also affected by the inclination angle of shear cracks, the concrete's compressive strength, and the yield strength of both the shear reinforcement and steel bars, adding to its ratio of tensile reinforcement. Reinforcing RC structural elements with externally-bonded FRP has been the focus of many researches [12–14]; several analytical investigations have been carried out to study the strengthened RC beams' shear performance in terms of strengthening methods [15, 16], section shape [17, 18], design equations [19, 20].

The use of CFRP composites in rehabilitating structures can greatly reduce maintenance requirements, increase life safety and service life of concrete structures. So far, the majority of research and applications carried out, using CFRP as strengthening material, has be devoted to use for flexural strengthening. A reinforced concrete beam must be designed to develop its full flexural strength to insure a ductile flexural failure mode under extreme loading. Hence, a beam must have a safety margin against other types of failure that are more dangerous and less predictable than flexural failure. The use of external FRP strengthening to beams may be classified as flexural and shear strengthening. The shear failure of an RC beam is distinctly different from the flexural one in that the flexural is ductile in nature, whereas the shear one is brittle and catastrophic. When the RC beam is deficient in shear, or when its shear capacity is less than the flexural capacity after flexural strengthening, shear strengthening of the beam must be considered. It is critically important to examine the shear capacity of RC beams which are intended to be strengthened in flexure. However, only a few studies on the shear strengthening of RC T-beams with externally bonded FRPs are reported in the literature. Deniaud and Cheng [21] studied the interaction of concrete, steel stirrups, and external fiber-reinforced polymer (FRP) sheets in carrying shear loads in RC T-beams. Bousselham and Chaallal [22] investigated the effect of the shear length to the beam depth ratio, the CFRP ratio and the internal transverse steel reinforcement ratio on the shear behavior of RC T-beams. Bousselham and Chaallal [23] evaluated the effect of the different parameters on the shear performance of strengthened RC T-beams. In addition, they [24] investigated the shear resistance mechanisms in RC T-beams strengthened in shear with externally bonded FRP.

The interface between FRP and concrete is the most important part in the process of repairing or strengthening concrete structures. To obtain high efficiency of repaired or strengthened concrete structures, we must provide sufficient bonding strength between the concrete surface and the FRP to ensure a good transmission between the concrete surface and the FRP since many failure modes occurs due to de-bonding between the concrete surface and the FRP materials. Many factors have been studied by researchers regarding the strength of the bond between the concrete surface and the FRP such as using anchoring system. The existing literature reports potential use of CFRP strips in strengthening the RC rectangular beams, but not on the beams with anchorage to the best knowledge of the authors. There are limited works on shear strengthening of RC beams using mechanically anchored FRP sheets (Lee et al. [25], Mofidi [26], and Mofidi et al. [27]).

Anchorage devices are useful tools to prevent, delay or shift this mode of failure to a less critical one; therefore, it improves the performance of the conventional FRP-strengthening method. The purpose of this study was to determine an effective technique for mechanical anchoring of reinforced concrete beams strengthened using FRP composites. A comprehensive review of existing literature was conducted to explore research findings related to debonding failure mechanisms and anchorage schemes for reinforced concrete structural elements with special attention to mechanical anchorage schemes. Based on the analysis of the data from the literature review, new anchoring technique was proposed. Based on the critical review of the existing literature. The main objectives of this study are to predict the shear strength of RC beams with different anchoring strengthened externally with CFRP composite using Nonlinear Finite Element Analysis (NLFEA) taking into account the effects of four major strengthening configurations in addition to control beam (without CFRP external strengthening) including: 1) RC beams with a depth of 225 mm strengthened externally with 90º U-wrap strip at a spacing of 100 mm without anchoring; 2) RC beams with a depth of 225 mm strengthened externally with 90º U-wrap strip at a spacing of 100 mm with 25 mm CFRP top strips anchoring; 3) RC beams with a depth of 225 mm strengthened externally with 90º U-wrap strip at a spacing of 100 mm with 50 mm CFRP top strips anchoring; and 4) RC beams with a depth of 225 mm strengthened externally with 90º U-wrap strip at a spacing of 100 mm with 75 mm CFRP top strips anchoring. As a result, five models have been constructed and subjected to four points loading. For this purpose, validation of the previous experimental study reported by Shbeeb et al. [28] is firstly simulated using ANSYS software. After that, a parametric study is extended for strengthened RC beams using different beam depth.

2. Methods

Nonlinear Finite Element analysis (NLFEA) is an important and effective tool in the analysis of complex structures. The main benefits that NLFEA provided include: 1) substantial savings in the cost, time, and effort compared with the fabrication and experimental testing of structure elements; 2) allows to change any parameter of interest to evaluate its influence on the structure, such as the compressive strength of concrete; 3) allows us to see the stress, strain, and displacement values at any location and at any load level; 4) the ability to change any parameter of interest, and the capability of demonstrating any interesting behavior at any load value and at any location in the system. Six full-scale models strengthened using CFRP are developed to carry out different investigated parameters.

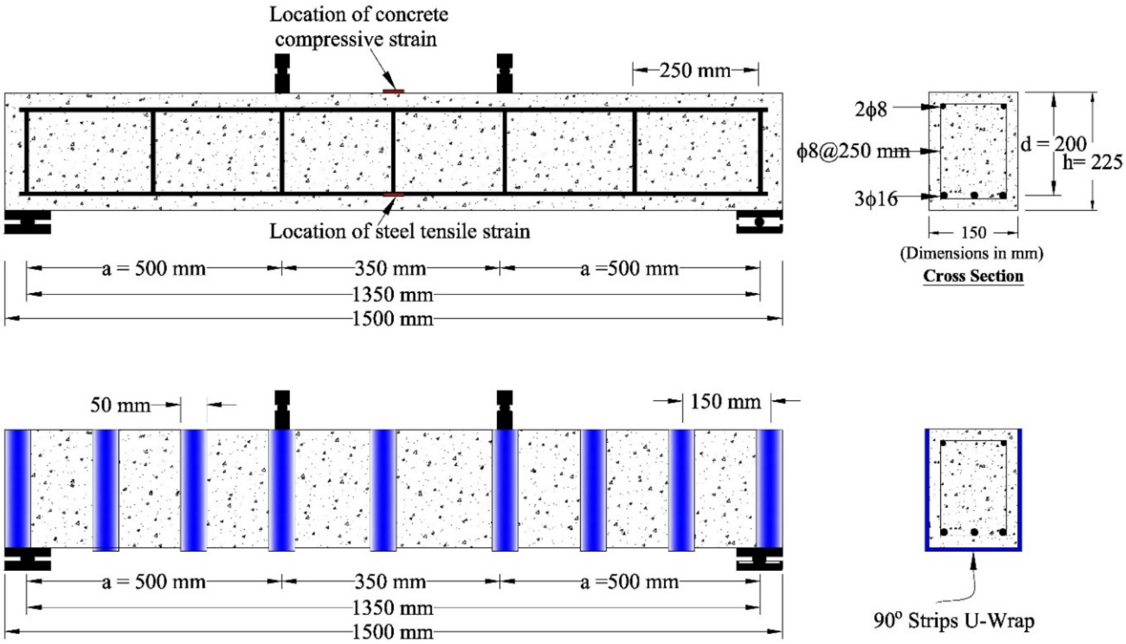

Figure 1. Setup and reinforcement details of the beams [28].

2.1. Experimental Work Review

The validation process of the finite element model is based on the experimental work performed by Shbeeb et al. [28]. High strength reinforced concrete (RC) beams (150 × 225 × 1500 mm) were designed with shear reinforcement of ϕ8 at 250 mm center to center along the entire beam length for all specimens as shown in Fig. 1. Twenty-two rectangular reinforced concrete beams, 150 × 225 mm with a total length of 1500 mm, were cast with the reinforcement of 2ϕ8 bars at the top and 3ϕ15 bars at the bottom. The design choices were made to ensure that shear failure would occur in the beams. Four beams were tested as control beams without strengthening and twenty-four beams were strengthened with different schemes with CFRP strips and sheets. Fig. 1 shows the reinforcement and the CFRP sheet and strips configurations for all the beams specimens. All specimens were tested as simply supported in a special designed built-up rigid steel frame. A hydraulic jack was used to apply a concentrated load through a hydraulic cylinder on a spread steel beam to produce two-point loading condition to generate a constant moment region at mid-span.

2.2. Description of Non-linear Finite Element Analysis (NLFEA)

Concrete is a quasi-brittle material and has different behavior in compression and tension. SOLID65 element is capable of predicting the nonlinear behavior of concrete materials using a smeared crack approach. The model is capable of predicting failure for concrete materials and accounts for both cracking and crushing failures. The two input strength parameters, ultimate uniaxial tensile and compressive strengths, are needed to define a failure surface for the concrete. Consequently, a criterion for failure of the concrete due to a multiaxial stress state can be calculated. Poisson's ratio of 0.2 was used for all beams. The shear transfer coefficient (β_t) represented conditions of the crack face. The value of β_t ranges from 0.0 to 1.0, with 0.0 representing a smooth crack (complete loss of shear transfer) and 1.0 representing a rough crack (no loss of shear transfer). The value of β_t was used in many studies of reinforced concrete structures; however, it varied between 0.05 and 0.25. Therefore, a value of 0.2 for β_t was used in this study. The concrete properties include concrete compressive strength of 55 MPa, initial Young's modulus (E_c) of 35063 MPa. In tension, the stress-strain curve for concrete is assumed to be linearly elastic up to the ultimate tensile strength. After this point, the concrete cracks and the strength decreases to zero. Fig. 2 shows the stress-strain relationships that are used in this study. The steel for the finite element models was assumed to be an elastic-perfectly plastic material identical in tension and compression.

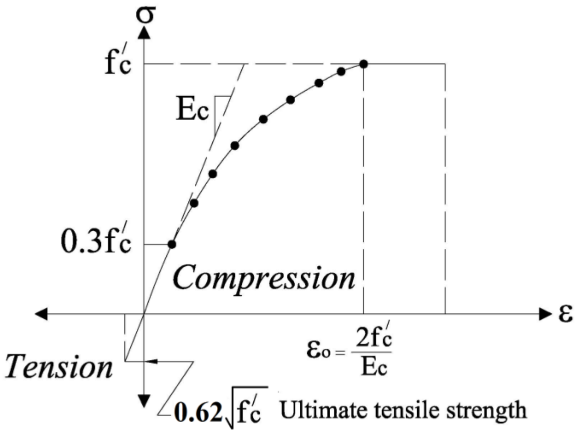

(a) Concrete

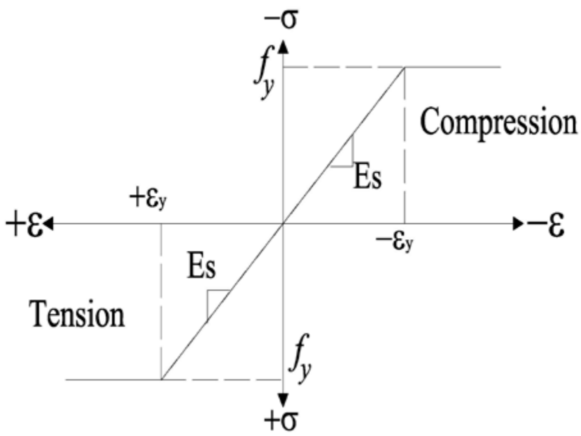

(b) Steel reinforcement

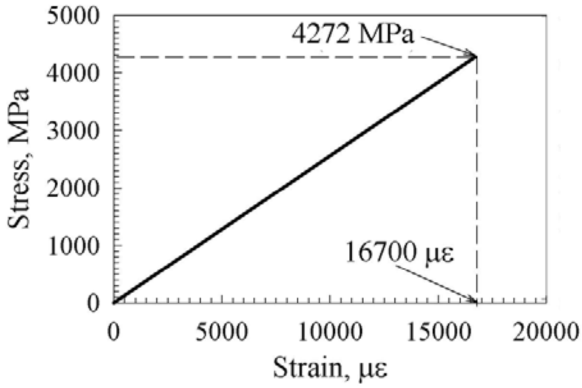

(c) CFRP composite

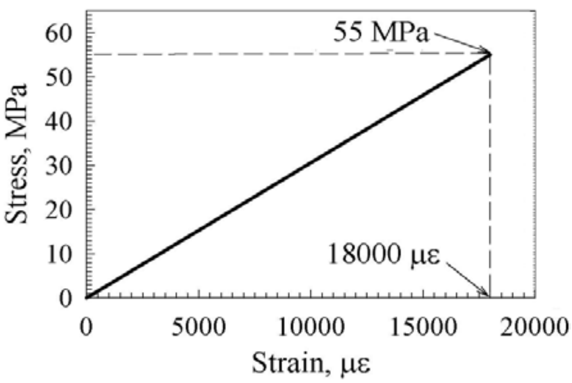

(d) Epoxy

Figure 2. Stress-strain curves [28].

Good results were attained upon utilizing the 3D LINK180 uniaxial tension-compression spar in the simulation of the steel reinforcement, separately, to make it possible to predict: the impact of plasticity, huge and rotational stains, and deflections. Poisson's ratio and yield stress of 0.3 and 413 MPa (Grade 60) respectively were used for the steel reinforcement. Fig. 2(b) shows the stress-strain relationship. Steel plates were added at both ends of the beams to provide a more even stress distribution over the support areas. The steel plates were assumed to be linear elastic materials with an elastic modulus equal to 200 GPa and Poisson's ratio of 0.3. The CFRP composite and epoxy are modeled by a layered solid element, SOLID46. The CFRP is assumed to be an orthotropic material of 0.165 mm thick, tensile strength of 3790 MPa, elastic modulus of 228 GPa, and ultimate tensile strain of 0.017 mm/mm. The epoxy used is 0.343 mm thick, ultimate tensile strength was 55 MPa, elastic modulus was 30 GPa, and ultimate tensile strain was 1800 $\mu\varepsilon$. In the other directions perpendicular to the fiber direction, the elastic modulus of CFRP was assumed to be 10^{-6} times that of the main direction. Linear elastic properties were assumed for both CFRP composites and epoxy.

The total load applied was divided into a series of load increments or load steps. Newton–Raphson equilibrium iterations provide convergence at the end of each load increment within tolerance limits equal to 0.001. Load step sizes were automated by ANSYS program for the maximum and minimum load step sizes. In a concrete element, cracking occurs when the principal tensile stress in any direction lies outside the failure surface. After cracking, the elastic modulus of the concrete element is set to zero in the direction parallel to the principal tensile stress direction. Crushing occurs when all principal stresses are compressive and lies outside the failure surface; subsequently, the elastic modulus is set to zero in all directions, and the element effectively disappears. The finite element model fails impulsively when the crushing capability of the concrete is turned on. Crushing of the concrete started to develop in elements located directly under the loads. Afterwards, adjacent concrete elements crushed within several load steps as well, significantly reducing the local stiffness. Finally, the model showed a large displacement, and the solution diverged. Therefore, the crushing capability was turned off and cracking of the concrete controlled the failure of the finite element models. During concrete cracking and ultimate load stages in which a large number of cracks appeared, the loads were applied gradually with smaller load increments. Failure for each model was identified when the solution for 0.0045 kN load increment was not converging.

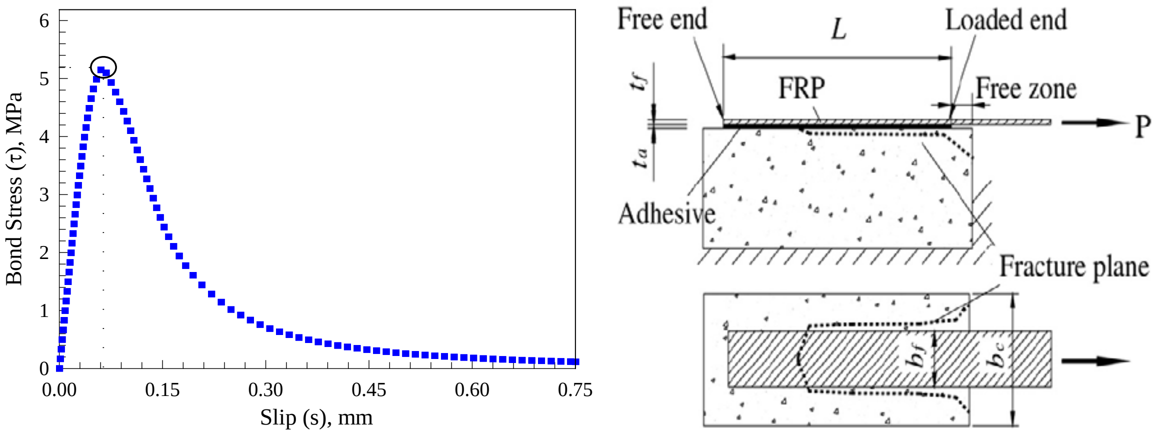

Figure 3. CFRP to concrete bond slip model [29].

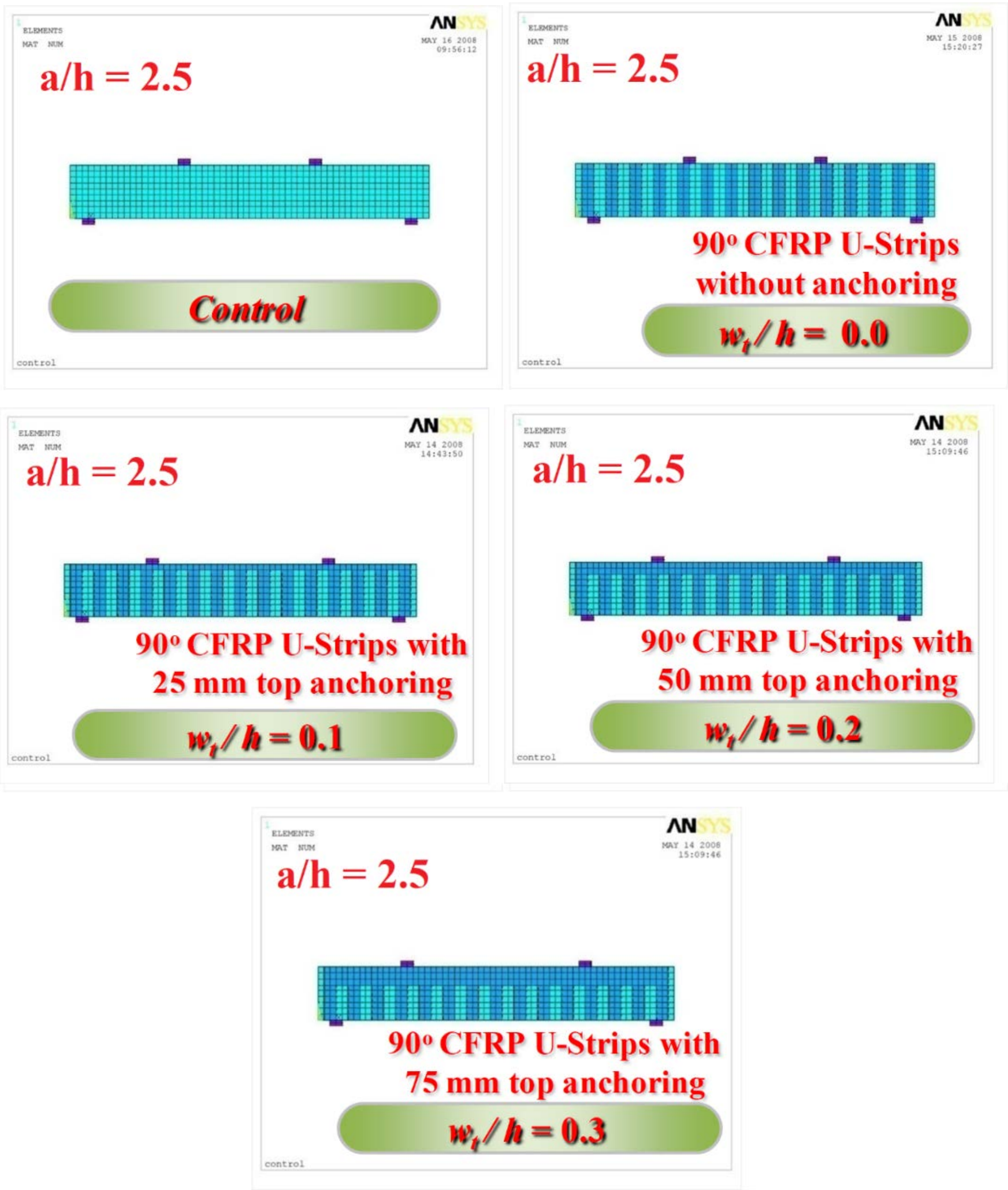

Figure 4. Typical finite element meshing of the beams.

CONTA174 element was used to model the layer between the concrete and epoxy layer. This element is an 8-node element that is intended for general rigid-flexible and flexible-flexible contact analysis. In a general contact analysis, the area of contact between two (or more) bodies is generally not known in advance. Also, CONTA174 element is applicable to 3-D geometries. It may be applied for contact between solid bodies or shells. One of the most accurate bond stress slip models that can be incorporated into a finite element analysis is that proposed by Lu et al. [29]. The mechanical behavior of the FRP/concrete interface is represented by a relationship between the local shear stress (τ) and the relative displacement (s), between the FRP composites and the concrete. Three different bond slip relations have been suggested by these authors; these are classified according to their level of sophistication and are referred to as the precise, the simplified, and the bilinear models. In the current study, the simplified model, as shown in Fig. 3, is adopted for its simplicity.

Square and rectangular elements were created for the rectangular volumes (concrete, CFRP, epoxy, and steel plates) using the volume-mapped command. This properly sets the width and length of the steel reinforcement elements to be consistent with the elements and nodes of the concrete. A convergence study was carried out to determine the appropriate mesh density as shown in Fig. 4 in which (a/d) represents the shear span to beam effective depth ratio and (w_f/h) represents the width of the anchored CFRP to the total depth of the beam. The meshing of the reinforcement was a special case and the individual elements were created in the modeling process. However, the necessary mesh attributes for the concrete were set before each section of the reinforcement was created. SOLID46 elements for epoxy and CFRP layers had the same meshing as SOLID65 elements for concrete to allocate the node over the node of each element. The command merge item was used to merge separate entities that have the same location into single entities. To ensure proper modeling, displacement boundary conditions were applied at the planes of symmetry. The symmetry boundary conditions were set first. Nodes defining a plane through the beam cross section at the center of the beam define one plane of symmetry. The support was modeled as a roller and hinge that allows the beam to rotate at the support. The force was applied across the entire centerline of the steel plate. The beams were analyzed simulating 4-point loading case, the distance between the 2-point of loading is 550 mm. The total applied load was divided into a series of small load increments, each 0.45 kN, and the Modified Newton–Raphson equilibrium iterations were used to check the convergence at the end of each load increment within a tolerance value of 0.001. The static analysis type was utilized to obtain the behavior of the beams. The model failure was identified when the solution of 0.0045 kN load increment was not converging.

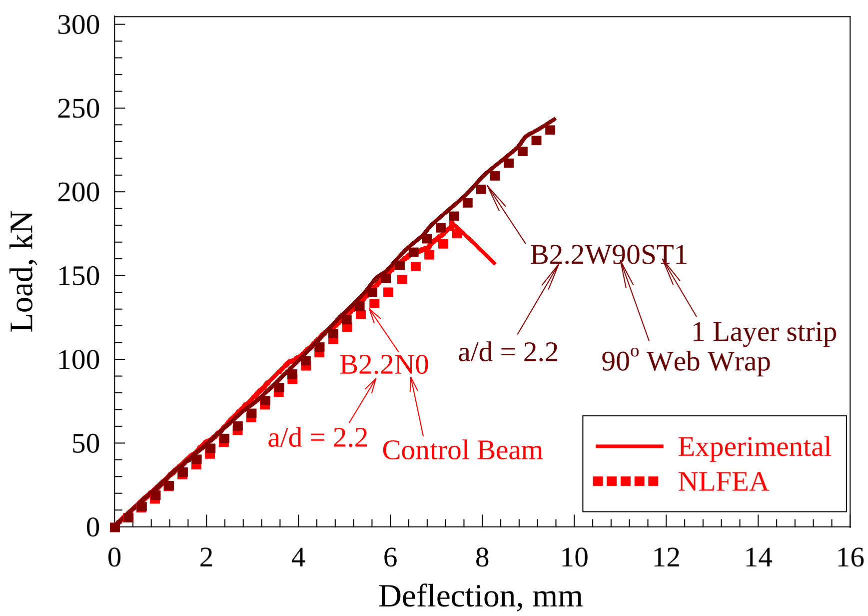

Figure 5. Experimental [28] and NLFEA load-deflection curves.

2.3. Validation Process

Fig. 5 shows the load deflection behavior of experimental and NLFEA results. Inspection of Fig. 5 in terms of pre-cracking stage, after-cracking stage, post-cracking stage, and at failure reveals that the load deflection curves for strengthened beams consist of pre-cracking straight segment followed by a change in slope of the curves after beams cracked at almost 100 kN, which is called “after-cracking”. With further load increase, the beams strengthened with web CFRP strips or sheet failed in shear due to debonding of CFRP strips or sheet before reaching ultimate flexural capacity. The values of the ultimate strengths and the corresponding percentage increase in the ultimate shear strength of the strengthened beams over the control beam indicated that the performance of the shear deficient beams is enhanced due to the use of CFRP composites. Fig. 5 shows that the NLFEA results correlates well with the experimental data at ultimate load capacity. Fig. 6 shows typical stress contours of the control and strengthened beams.

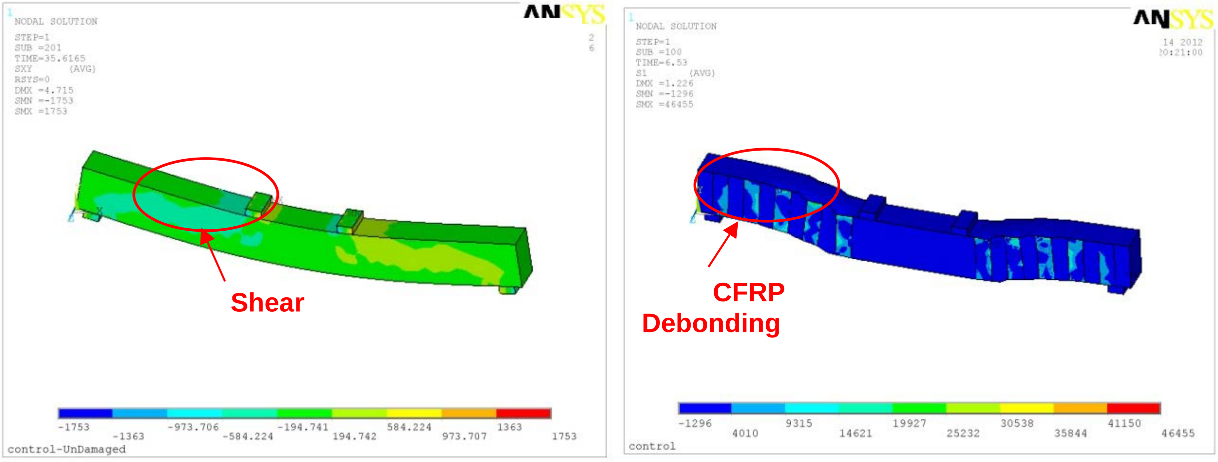

Figure 6. Typical NLFEA stress contours of NLFEA beams.

3. Results and Discussion

3.1. Failure Mode

Fig. 7 shows the representative cracking pattern of B2.7N0. The initial flexural crack of control beam without reinforcement started at the center of the beam within the constant moment region at 23.1 kN. Beyond this load, cracks extended toward the top fiber, and additional flexural cracks developed throughout the beam length. At 77 kN, a 33-degree angle shear crack developed independently of the existing flexural cracks in the center of the shear span. With further load increase, the cracks extended both towards the support and the load point, leading to a sudden, brittle shear failure at 127.3 kN as shown in Fig. 7 and Table 1.

Fig. 7 shows the representative cracking pattern of B2.7U90STA0. The initial flexural crack started at the center of the beam within the constant moment region at 34.2 kN. Beyond this load, cracks extended toward the top fiber, and additional flexural cracks developed throughout the beam length. At 112.5 kN, a 37-degree angle shear crack developed independently of the existing flexural cracks in the center of the shear span. With further load increase, the strip No. 4 debonded at 139.2 kN followed by the debonding of strip No.3 at 142.8 kN. The beam failed successively at 146.0 kN after the debonding of strip No. 5 as shown in Fig. 7 and Table 1. Debonding of the CFRP strip is a delamination between the strip-adhesive-concrete at the strip-end region of the strengthened beam. This failure was a result of the maximum stresses in the adhesive being not greater than the bonding strength between strip-adhesive-concrete at the strip-end region.

Fig. 7 shows the representative cracking pattern of B2.7U90STA1. The initial flexural cracks started at the center of the beam within the constant moment region at 34.2 kN. Beyond this load, cracks extended toward the top fiber, and additional flexural cracks developed throughout the beam length. At 112.1 kN, a 37-degree angle shear crack developed independently of the existing flexural cracks in the center of the shear span. With further load increase, Strip No. 4 debonded at 34 kip followed by the debonding of Strip No. 3 at 161.5 kN. The beam failed successively in shear at 154.4 kN after the debonding of top anchoring strip over Strip No. 3, 4, and 5, respectively, as shown in Fig. 7 and Table 1.

Fig. 7 shows the representative cracking pattern of B2.7U90STA2. The initial flexural crack started at the center of the beam within the constant moment region at 33.8 kN. Beyond this load, cracks extended toward the top fiber, and additional flexural cracks developed throughout the beam length. At 115.6 kN, a 37-degree angle shear crack developed independently of the existing flexural cracks in the center of the shear span. With further load increase, Strip No. 4 debonded at 124.5 kN followed by the debonding of Strip No. 3 at 140.1 kN. The beam failed successively in shear at 163.3 kN after the debonding of top anchoring strip over Strip No. 3 and 4, respectively, as shown in Fig. 7 and Table 1.

Fig. 7 shows the representative cracking pattern of B2.7U90STA3. The initial flexural crack started at the center of the beam within the constant moment region at 34.2 kN. Beyond this load, cracks extended toward the top fiber, and additional flexural cracks developed throughout the beam length. At 112.5 kN, a

37-degree angle shear crack developed independently of the existing flexural cracks in the center of the shear span. With further load increase, Strip No. 4 debonded at 169.0 kN followed by the debonding of Strip No. 3 at 169.9 kN. The beam failed successively in flexure at 170.9 kN after the debonding of top anchoring strip over Strip No. 3 and 4, respectively, as shown in Fig. 7 and Table 1.

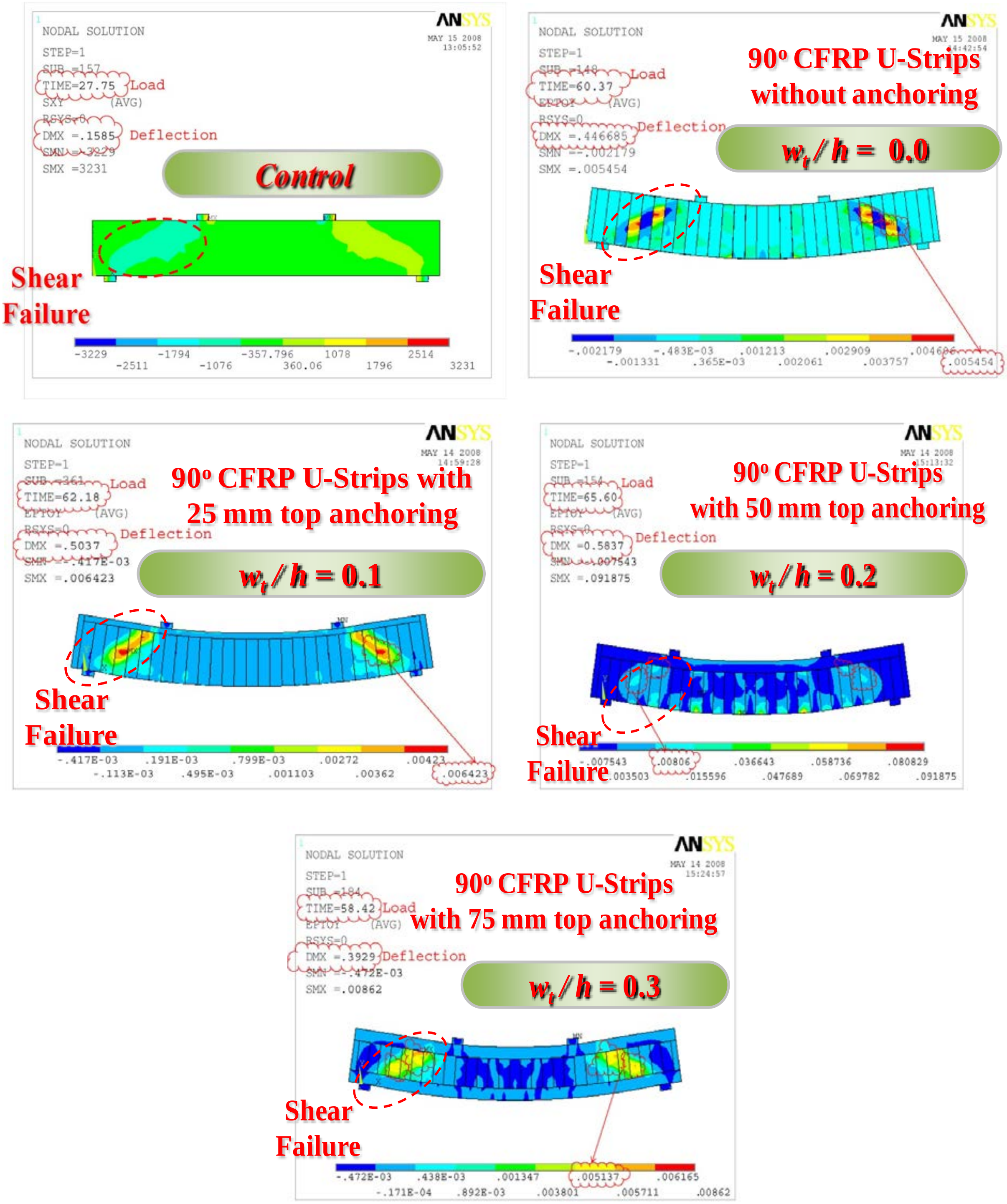

Figure 7. Typical NLFEA stress contours of control NLFEA beams.

Table 1. The details, ultimate load and mode of failure of NLFEA shear beams.

Beam Designation	Type of Strengthening	Ultimate load, kN	Percentage of increase w.r.t control beam, %	Failure mode
B2.7N0	None	127.3	0	Shear failure followed by 33º diagonal crack
B2.7U90STA0	Strip@ 90º U-wrap without anchoring	146.0	15	Shear failure followed by 37º diagonal crack, debonding of CFRP strips
B2.7U90STA1	Strip@ 90º U-wrap with 25 mm CFRP top strips anchoring	154.4	21	Shear failure followed by 37º diagonal crack, debonding of CFRP strips
B2.7U90STA2	Strip@ 90º U-wrap with 50 mm CFRP top strips anchoring	163.5	28	Shear failure followed by 37º diagonal crack, debonding of CFRP strips
B2.7U90STA3	Strip@ 90º U-wrap with 75 mm CFRP top strips anchoring	170.9	34	Flexural failure followed by crushing of concrete in compression zone

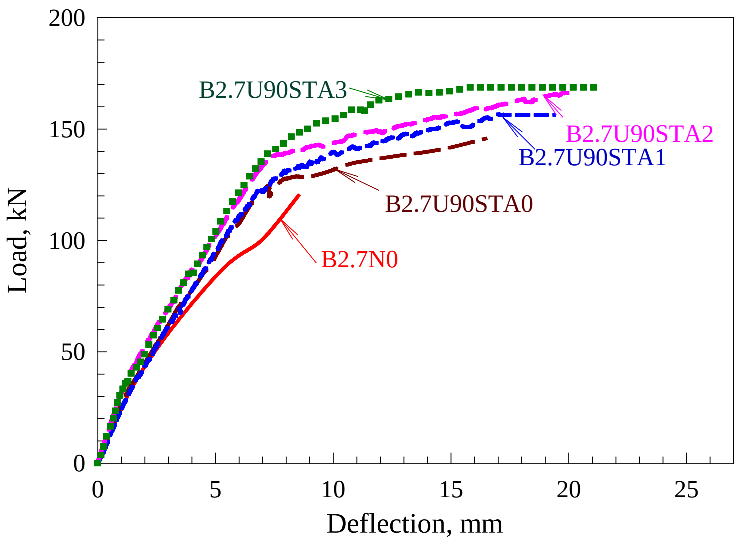

Figure 8. NLFEA load-deflection curves.

3.2. Load-deflection behavior

Fig. 8 shows the load deflection curves for B2.7N0, B2.7U90STA0, B2.7U90STA1, B2.7U90STA2, and B2.7U90STA3. All strengthened beams exhibited almost liner load deflection relationships up to the load of 133.0 kN that equals the failure load of control beam. This indicates that the CFRP started to carry the load after the formation of the diagonal shear. Inspection of Figure 8 shows that the ultimate load capacity of the beams increased with the increase of anchoring system width, while an increase in stiffness can be observed from the rotation angle of the elastic stage curve of the NLFEA beams. In addition, Fig. 8 shows that the ductility of the beam increased with the increase of anchoring system width exactly mirroring the mode of failure.

3.3. Concrete compressive strain

Fig. 9 exhibits the concrete's compressive strain's (Fig. 1) relationship with the applied load for: B2.7N0, B2.7U90STA0, B2.7U90STA1, B2.7U90STA2, and B2.7U90STA3. When the load was raised, the concrete’s compression strain enhanced. In the beams: B2.7N0, B2.7U90STA0, B2.7U90STA1, B2.7U90STA2, and B2.7U90STA3, the load values corresponding to a compressive strain of 1150 $\mu\varepsilon$, were 118.3, 128.5, 130.3, 140.6, and 141.5 kN, respectively. This indicates that the more the width of the anchorage, the less the concrete's compressive strain. The largest level of strain was observed in the B2.2W45ST1 beam, which was strengthened with sheets of CFRP. Furthermore, the load-compressive strain curves of the beams in the second group, the concrete in the beam B2.7U90STA3 had a strain higher than 3000 με.

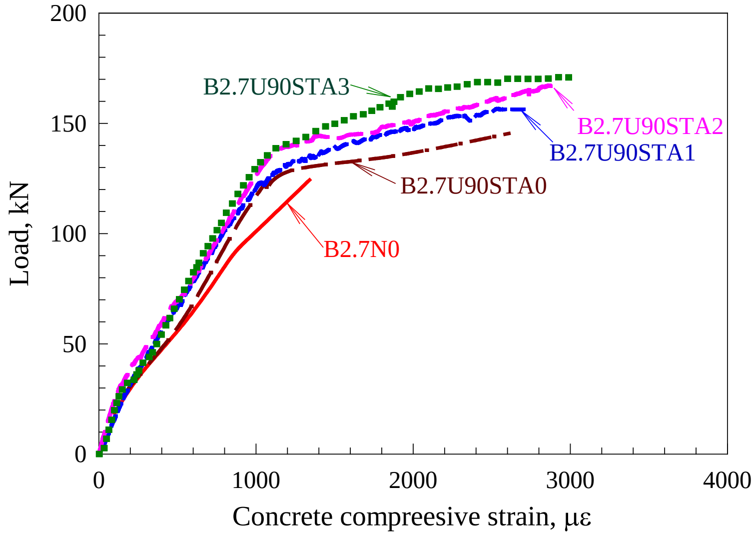

Figure 9. NLFEA load-concrete compressive strain curves.

3.4. CFRP tensile strain

Fig. 10 shows the relationship between the load and CFRP sheet tensile strain for B2.7U90STA0, B2.7U90STA1, B2.7U90STA2, and B2.7U90STA3 RC beams. According to Fig. 6, the tension strain was initiated in the CFRP sheet after the diagonal shear crack started to form at loads of 77.0, 85.8, 85.2, 87.6, and 90.3 kN for B2.7N0, B2.7U90STA0, B2.7U90STA1, B2.7U90STA2, and B2.7U90STA3 beams, respectively. Fig. 10 also shows that the development of strains becomes sluggish around a load of 93.4 kN in all beams. Inspection of Fig. 10 reveals that the CFRP tensile sheet strain increased with the increase in the width of the anchorage system. From this, it is known that the development of strain gets slower as the anchoring system width decreases. At ultimate load, the tensile strains were 3165 με, 5960 με, 8230 με, and 11800 με for B2.7U90STA0, B2.7U90STA1, B2.7U90STA2, and B2.7U90STA3 beams, respectively, which is equivalent to 0.19 ε_{fu}, 0.35 ε_{fu}, 0.48 ε_{fu}, and 0.69 ε_{fu}, respectively. These higher strains of CFRP strips reflected the efficiency of the anchorage system in the strengthening of shear deficient beams. Therefore, the B2.7U90STA3 strengthened beam showed higher tensile strain than other strengthened beams for the same load.

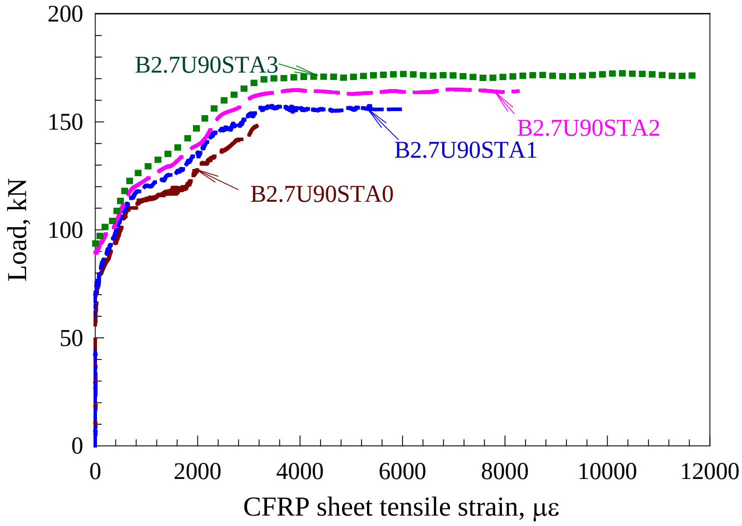

Figure 10. NLFEA load- CFRP tensile strain curves.

3.5. Steel tensile strain

Fig. 11 shows the relationship between the load and strain at the level of steel (Fig. 1) for B2.7N0, B2.7U90STA0, B2.7U90STA1, B2.7U90STA2, and B2.7U90STA3 RC beams. The load strain curve followed the same trend for all the beams before the cracking. After cracking, the slope of the curve was reduced as a result of reduction in stiffness. Inspection of Fig. 11 reveals that the steel tensile strain followed the same trend and behavior as the concrete compressive strain which increased with increasing the load, while the steel tensile strain in the concrete decreased with the increase in the width of the anchoring system. All the anchored beams reached the yielding point, while the steel reinforcement in B2.7U90STA3 strengthened beam experienced the highest tensile strain development among other beams at ultimate load.

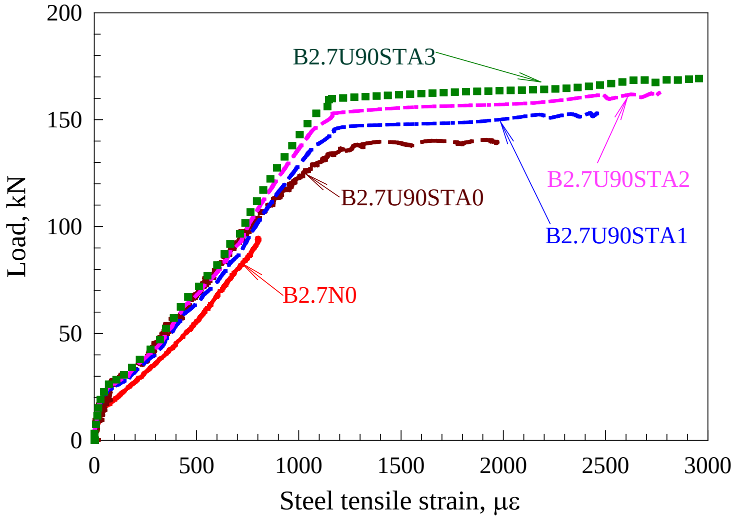

Figure 11. NLFEA load-steel tensile strain curves.

3.6. Crack opening behavior

Fig. 12 shows the relationship between the load and crack opening for B2.7N0, B2.7U90STA0, B2.7U90STA1, B2.7U90STA2, and B2.7U90STA3 RC beams. According to Fig. 8, crack began opening after the diagonal shear its initiation at load 77.0, 85.8, 85.2, 87.6, and 90.3 kN for B2.7N0, B2.7U90STA0, B2.7U90STA1, B2.7U90STA2, and B2.7U90STA3, respectively, after diagonal shear crack formed. Fig. 12 shows that the development of crack width becomes sluggish around 0.25 mm in all beams as well. It can be observed the crack developed at a slower rate as the anchoring system width increased. At ultimate load, the ultimate crack width is 1.78, 1.19, 1.12, 1.03, and 0.81 mm for B2.7N0, B2.7U90STA0, B2.7U90STA1, B2.7U90STA2, and B2.7U90STA3, respectively. Therefore, the B2.7U90STA3 strengthened beam showed less crack width for the same load than the other beams.

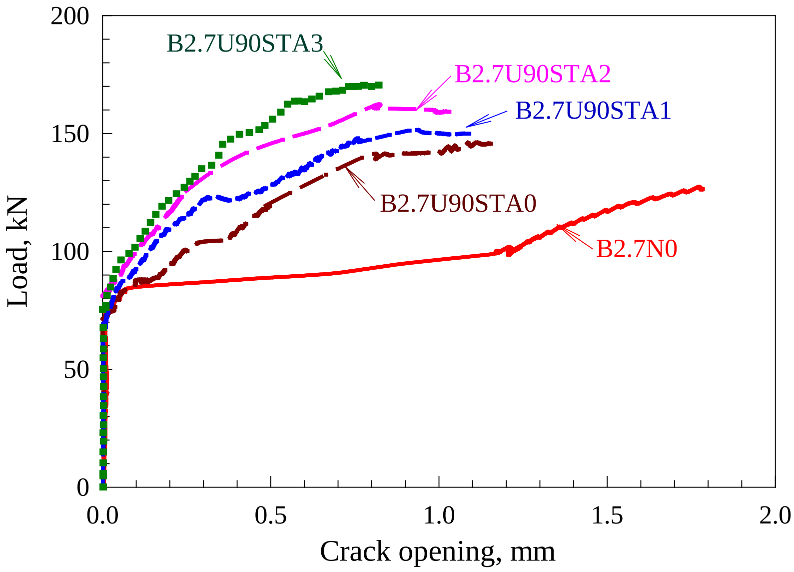

Figure 12. NLFEA load-crack opening curves.

3.7. Comparison of NLFEA with theoretical models

For purposes of comparison, the predictions of the NLFEA results are compared with those of the ACI model [30], Triantafillou model [31], and Colotti et al. model [32]. In the ACI, Triantafillou, and Colotti et al. models, the general design guidance is clearly derived from the experimental data and they are only applicable to external FRP reinforcement. Fig. 13 shows a comparison of the results predicted by the three models $V_{f,NLFEA}/V_{f,ACI}$ [30], $V_{f,NLFEA}/V_{f,Tri}$ [31], and $V_{f,NLFEA}/V_{f,Col}$ [32]. Note that the ACI and Triantafillou models were calibrated for CFRP and should be used with caution for other types of composites as shown in Fig. 13. The overall predictions by ACI model appear to be overestimated with a mean $V_{f,NLFEA}/V_{f,ACI}$ value of 1.32 and a coefficient of variation (COV) of 25 %, while the NLFEA results for Colotti et al. model are underestimated with a mean $V_{f,NLFEA}/V_{f,Col.}$ value of 0.70 and a COV of 20 %. However, Triantafillou et al. model shows a weak agreement with NLFEA results, with a mean $V_{f,NLFEA}/V_{f,Tri}$ value of 0.5 and (COV) of 18 %. It is also important to take into consideration that all the ACI and Triantafillou models are semi empirical in nature, with important governing parameters derived from test data for beams strengthened with FRP laminates, whereas the ACI model cannot be applied in certain cases. In addition, a careful inspection of Fig. 13 will show that the ACI model has a much wider range of NLFEA/theoretical failure load ratios of 0.95 to 1.74. The Triantafillou model also gives a non-acceptable range of NLFEA/theoretical mean values of 0.41 to 0.59. On the contrary, the Colotti et al. model gives a much larger range of NLFEA/theoretical mean values of 0.53 to 0.88 than Triantafillou model.

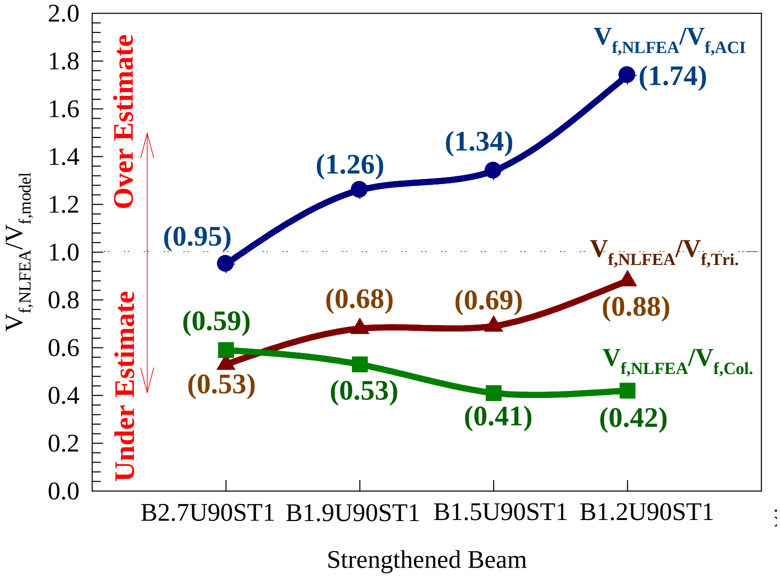

Figure 13. The normalized NLFEA FRP shear force with respect to analytical models.

4. Conclusions

1. The use of CFRP composites is an effective technique to enhance the shear capacity of RC beams. The externally bonded CFRP can increase the shear capacity of the beam significantly by 15–34 % compared to that of the control beams, depending on the variables investigated.

2. One of the observed failure modes was debonding of more than two CFRP strips. Test results seem to indicate that this mechanism can be prevented by providing CFRP strips anchorage in the beam from top side.

3. Bonded anchorage of CFRP strips with width of 0.1h, 0.2h, and 0.3h to the beam caused a decrease in average interface bond stress and an increase in the effective strain of the CFRP sheet at failure, which resulted in a higher shear capacity as compared with that of the U-wrapped beams without anchorage as well as helped delay or mitigate the sheet debonding from the concrete surface.

4. The inclination of the primary shear crack influenced the shear strength contribution of the external strengthening. As this study demonstrated, the shear crack angle determined the number of CFRP strips intersected by the crack and whether or not an intersected CFRP strip was fully effective.

5. The overall predictions by ACI model [30] appear to be overestimated with a mean value of 1.32 and a coefficient of variation (COV) of 25 % and underestimated in the NLFEA results for Colotti et al. model with a mean value of 0.70 and a COV of 20 %. However, Triantafillou et al. model shows a weak agreement with NLFEA results.

References

1. Ahmed, A., Kodur, V. The experimental behavior of FRP-strengthened RC beams subjected to design fire exposure. Engineering Structures. 2011. 33(1). Pp. 2201–2211. DOI: 10.1016/j.engstruct.2011.03.010

2. Mabsout, M., Tarhini, K., Jabakhanji, R., Awwad, E. Wheel load distribution in simply supported concrete slab bridges. J Bridge Eng. 2004. 9(2). Pp. 293–306. DOI: 10.1061/(ASCE)1084-0702(2004)9:2(147)
3. Al-Rousan, R., Abo-Msamh, I. Bending and Torsion Behaviour of CFRP Strengthened RC Beams. Magazine of Civil Engineering. 2019. 92(8). Pp. 62–71. DOI: 10.18720/MCE.92.8
4. Al-Rousan, R. Behavior of two-way slabs subjected to drop-weight. Magazine of Civil Engineering. 2019. 90(6). Pp. 62–71. DOI: 10.18720/MCE.90.6
5. Al-Rousan, R. The impact of cable spacing on the behavior of cable-stayed bridges. Magazine of Civil Engineering. 2019. 91(7). Pp. 49–59. DOI: 10.18720/MCE.91.5
6. Yu, B., Kodur, V.K.R. Fire behavior of concrete T-beams strengthened with nearsurface mounted FRP reinforcement. Engineering Structures. 2014. 80(1). Pp. 350–361. DOI: 10.1016/j.engstruct.2014.09.003
7. Triantafillou, T.C., Antonopoulos, C.P. Design of concrete flexural members strengthened in shear with FRP. J Compos Constr. 2000. 4(4). Pp.198–205. DOI: 10.1061/(ASCE)1090-0268(2000)4:4(198)
8. Bousselham, A., Chaallal, O. Shear strengthening reinforced concrete beams with fiber-reinforced polymer: assessment of influencing parameters and required research. ACI Struct J. 2004. 101(2). Pp. 219–227. DOI: 10.14359/13019
9. Belarbi, A., Bae, S., Brancaccio, A. Behavior of full-scale RC T-beams strengthened in shear with externally bonded FRP sheets. Constr Build Mater. 2012. 32 (1). Pp. 27–40. DOI: 10.1016/j.conbuildmat.2010.11.102
10. Khalifa, A., Nanni, A. Improving shear capacity of existing RC T-section beams using CFRP composites. Cem Concr Compos. 2000. 22 (1). Pp. 165–174. DOI: 10.1016/S0958-9465(99)00051-7
11. Mosallam, A., Banerjee, S. Shear enhancement of reinforced concrete beams strengthened with FRP composite laminates. Composites: Part B. 2007. 38 (1). Pp. 781–93. DOI: 10.1016/j.compositesb.2006.10.002
12. Ashrafuddin, M., Baluch, M.H., Sharif, A., Al-Sulaimani, G.J., Azad, A.K., Khan, A. Peeling and diagonal tension failures in steel plated R/C beams. Constr Build Mater. 1999. 13 (1). Pp. 459–467. DOI: 10.1016/S0950-0618(99)00044-6
13. Rangan, B.V. Shear design of reinforced concrete beams, slabs and walls. Cem Concr Compos. 1998. 20 (1). Pp. 455–464. DOI: 10.1016/S0958-9465(98)00027-4
14. Spadea, G., Bencardino, F., Swamy, R.N. Optimizing the performance characteristics of beams strengthened with bonded CFRP laminates. Mater Struct. 2000. 33 (1). Pp. 1119–1126. DOI: 10.1007/BF02484166
15. Malek, A.M., Saadatmanesh, H. Ultimate shear capacity of reinforced concrete beams strengthened with web-bonded fiber-reinforced plastic plates. ACI Struct J. 1998. 95 (4). Pp. 391–399. DOI: 10.14359/555
16. Triantafillou, T.C. Shear strengthening of reinforced concrete beams using epoxy-bonded FRP composites. ACI Struct J. 1998. 95 (2).Pp. 107–115. DOI: 10.14359/531
17. Khalifa, A., Nanni, A. Improving shear capacity of existing RC T-section beams using CFRP composites. J Cem Concr Compos. 2000. 22 (2). Pp.165–174. DOI: 10.1016/S0958-9465(99)00051-7
18. Hutchinson, R.L., Rizkalla, S.H. Shear strengthening of AASHTO bridge girders using carbon fiber reinforced polymer sheets. ACI Special Publications (SP-188). 1999. 188 (1). Pp. 945–958. DOI: 10.14359/5692
19. Zhang, Z., Hsu, C.T. Shear strengthening of reinforced concrete beams using carbon-fiber-reinforced polymer laminates. J Compos Constr. 2005. 9 (2). Pp. 158–169. DOI: 10.1061/(ASCE)1090-0268(2005)9:2(158)
20. Monti, G., Liotta, M.A. Tests and design equations for FRP-strengthening in shear. Constr Build Mater. 2007. 21 (24). Pp.799–809. DOI: 10.1016/j.conbuildmat.2006.06.023
21. Deniaud, C., Cheng, J.J.R. Shear behaviour of reinforced concrete T-beams with externally bonded fiber-reinforced polymer sheets. ACI Struct J. 2001. 98 (3). Pp. 386–394. DOI: 10.14359/10227
22. Bousselham, A., Chaallal, O. Behaviour of reinforced concrete T-beams strengthened in shear with carbon fiber-reinforced polymer–an experimental study. ACI Struct J. 2006. 103 (3). Pp. 339–347. DOI: 10.14359/15311
23. Bousselham, A., Chaallal, O. Effect of transverse steel and shear span on the performance of RC beams strengthened in shear with CFRP. Composites: Part B. 2006. 37 (1). Pp. 37–46. DOI: 10.1016/j.compositesb.2005.05.012
24. Bousselham, A., Chaallal, O. Mechanisms of Shear Resistance of Concrete Beams strengthened in shear with externally bonded FRP. J Compos Constr. 2008. 12 (5). Pp. 499–512. DOI: 10.1061/(ASCE)1090-0268(2008)12:5(499)
25. Lee, H.K., Cheong, S.H., Ha, S.K., Lee, C.G. Behaviour and performance of RC T-section deep beams externally strengthened in shear with CFRP sheets. J Compos Struct. 2011. 93 (1). Pp. 911–922. DOI: 10.1016/j.compstruct.2010.07.002
26. Gala, K., Mofidi, A. Shear strengthening of RC T-beams using mechanically- anchored unbonded dry carbon fibre sheets. ASCE, J Perform Constr Facil. 2010. 24(1). Pp. 31-39. DOI: 10.1061/(ASCE)CF.1943-5509.0000067
27. Mofidi, A., Chaallal, O., Benmokrane, B., Neale, K. Performance of end-anchorage systems for RC Beams strengthened in shear with epoxy bonded FRP. J Compos Constr. 2012. 16 (3). Pp. 322-331. DOI: 10.1061/(ASCE)CC.1943-5614.0000263
28. Shbeeb, N.I., Al-Rousan, R., Issa, M.A., Al-Salman, H. Impact of bonded carbon fibre composite on the shear strength of reinforced concrete beams. Proceedings of the Institution of Civil Engineers: Structures and Buildings. 2018. 171 (5). Pp. 364–379. DOI: 10.1680/jstbu.16.00145
29. Lu, X.Z., Teng, J.G., Ye, L.P., Jiang, J.J. Bond–slip models for FRP sheets/plates bonded to concrete. Engineering Structures Journal 2005. 27 (1). Pp. 920–937. DOI: 10.1016/j.engstruct.2005.01.014
30. ACI Committee 440. Design and Construction of Externally Bonded FRP Systems for strengthening Concrete Structures. *ACI440.2R-02. 2002. American Concrete Institute, Farmington Hills, Mich.: 45 pp. DOI: 10.1061/40753(171)159. ISBN: 9780870312854
31. Triantafillou, T.C. Shear strengthening of reinforced concrete beams using epoxy-bonded FRP composites. ACI Struct J. 1998. 95 (2).Pp. 107–115. DOI: 10.14359/531
32. Colotti, V., Spadea, G., Swamy, R.N. Structural Model to Predict the Failure Behavior of Plated Reinforced Concrete Beams. Journal of Composite Construction. 2004. 8 (2). Pp. 104–122. DOI: 10.1061/(ASCE)1090-0268(2004)8:2(104)

Contact:

Rajai Al-Rousan, rzalrousan@just.edu.jo

Magazine of Civil Engineering

ISSN 2712-8172

journal homepage: http://engstroy.spbstu.ru/

DOI: 10.34910/MCE.109.6

Factors and mechanisms of nanomodification cement systems in the technological life cycle

O.V. Artamonova[1], E.M. Chernyshov[1], G.S. Slavcheva[2] *

[1]Voronezh State University of Architecture and Civil Engineering, Voronesh, Russia,

[2]Voronezh State Technical University, Voronezh, Russia

**E-mail: gslavcheva@yandex.ru*

Keywords: cement system, nanomodification, hydration, hardening, structure, models, strength

Abstract. The paper presents an analysis of the kinetics of heterogeneous processes and patterns of solid formation to substantiate factors and technological methods for nanomodifying the structure and properties of cement-based composites. According to the general evolutionary model of solid formation and evolution of hydration hardening systems model, the main factors and criteria of cement systems nanomodification have been identified for all stages of the technological life cycle. In accordance with the factors of nanomodification of cement systems, the technological methods of nanomodification are identified. As a result of nanomodification, the effects in the structure formation of cement systems are predicted and confirmed by experimental data. Theoretical analysis and experimental results showed that the factors and methods of nanomodification meet the terms of controlling the fracture strength of the cement-based composites. Together, the effects of nanomodification of the structure and factors of increasing the fracture resistance will determine the effectiveness of solutions for engineering practice in terms of reducing the time and the energy costs for processes in the life cycle of cement-based composites, enhancing their quality.

1. Introduction

Dozens of solid-state kinetic models developed over the 20th century are used in kinetic studies. Detailed analysis and systematization of commonly employed models presented in [1] allow us to classify them as nucleation, geometrical contraction, diffusion, and reaction order.

Kinetic models used for cement systems are a special interpretation of the basic solid-state kinetic models. The earliest of the general approaches to the description and modeling of structure formation processes and the resulting structure of cement systems are presented in [2].

The proposed models mainly relate to the description of the kinetics and features of cement hydration processes, the formation of the hydration products' structure under the influence of various factors, hardening kinetics, and strength development.

For example, Poppe et al. [3] and Ye et al. [4] proposed a model of the hydration process and microstructure development of limestone concrete. Kishi and Saruul [5] and Maekawa et al. proposed a model for evaluating the heat release rate of hardening concrete. Lothenbach et al. [7] proposed thermodynamic modeling of concrete hardening. The nucleation effect and effect of the formation of monocarboaluminate phase were modeled in [8–9]. In [10–15], the authors proposed effective functions for taking into account the effects of limestone, silica fume, slag, and fly ash on cement hydration, heat production rate, microstructure and strength development of concrete. Concerning the problems of nanomodification, [16–18] also proposed several special models, which allow one to take into account the effects of nanosilica introduction for hydration processes. All of these models allow one to rather accurately

Artamonova, O.V., Chernyshov, E.M., Slavcheva, G.S. Factors and mechanisms of nanomodification cement systems in the technological life cycle. 2022. 109(1). Article No. 10906. DOI: 10.34910/MCE.109.6

quantitatively takes into account the influence of individual components in cement-based composites on the kinetics of hydration processes, structure, and properties.

However, these models relate to individual private processes in the total set of problems of modifying (including nanomodifying) the structure and properties of cement-based composites in their technological life cycle.

We consider nanomodification of the structure as an action for organizing the processes of hydration and hardening of cement systems. Therefore, when substantiating the means of nanomodification, it is necessary to influence their kinetics and energy. The result of nanomodification should be to increase the speed and reduce the time of hydration and hardening processes, reduce the energy costs of these processes, and increase the strength of cement-based composites. Therefore, to advance nanomodification principles of cement-based composite structures, it is necessary to identify factors and technological methods of nanomodification. This will allow us to determine the options for technological solutions for engineering practice.

Therefore, it seems necessary to isolate and systematize existing conceptual models for the main phenomena and processes of nanomodification of a structure that reveal the relationships in the system "nanomodification factor – nanomodification technology – the result of nanomodification of a structure".

In this article, concerning the cement system, we present a theoretical analysis:

1) of the kinetics of heterogeneous processes of solid formation;

2) of the patterns governing the destruction processes.

The purpose of the analysis of these processes and patterns is to substantiate factors and technological methods for nanomodifying the structure and properties of cement-based composites.

2. Methods

The presented study used theoretical analysis. The previous studies, which are discussed to confirm the result of the theoretical analysis, used the following methods.

The amount and size of the colloidal nanoparticles SiO_2 synthesized by the sol–gel process were determined using dynamic light scattering (Photocor Complex spectrometer), and transmission electron microscopy (TEM) (Transmission Electron Microscope H-9500, v_{acs} = 75 kV).

The phase composition of the hydration products was controlled by the XRD-method (ARL X'TRA diffractometer, CuKα radiation (λ = 1.541788 Å). X-ray decoding and phase identification were carried out using PDWin 4.0.

The morphology of the cement paste structure was examined on a JEOL JSM-7001F scanning electron microscope.

The hardening kinetics were evaluated by testing samples, cubes 5×5×5 cm in size, after 1, 3, 7, 14, 28 days of curing under normal temperature and humidity conditions (t = 20 ^{0}C, RH = 95 ± 5 %). The strength testing was carried out on a universal 4-column floor hydraulic test system INSTRON Sates 1500 HDS.

3. Results[1]

3.1. Analysis of the kinetics patterns of heterogeneous processes of solid phase formation in cement systems

The evolution of solids in a real heterogeneous system is a collection of parallel and sequential phenomena and processes of solid phase formation. Moreover, the evolutionary hardening route of cement systems is a variation of the general form of the evolutionary route [19]. It is characterized by the stages and processes:

– generation of hydration products' particles,

– growth and accumulation of hydration products' particles,

[1] Some of the result have been presented at Second International Conference on Mechanics of Advanced Materials and Structures (ICMAMS 2019) on 19-22 October, 2019

- agglomeration of individual primary particles of hydration products, by compacting them into aggregates,
- spontaneous structure formation (Ostwald ripening and recrystallization of hydration products' particles).

The nanomodification technology should be aimed at these stages and processes to obtain optimal crystal structures, their agglomerates and crystallites, hydration products in general.

Table 1 presents systemically the factors and technological control methods during nanomodification and the expected effect of nanomodification for each of the indicated stages and processes. The systematization is based on the thermodynamic Gibbs-Volmer theory of the formation of a new phase in the overseaable solutions (equations 1–4) that has been analyzed in [21]. Equations 5–8 are obtained in the J.D. Tretyakov's works, devoted to nonlinear dynamics and thermodynamics of irreversible processes in chemistry and technology and in the of E.A. Goodilin's works, devoted to the crystallization processes in chemical materials science. Let us consider them sequentially.

Table 1. To conceptual nanomodification models for the main stages of the evolutionary hardening route of cement systems.

ER stage	Scale	Transition phenomenon	Structure level	Structural parameters to be nanomodified	Conceptual kinetics models of heterogeneous processes of structure formation	Control factors for nano-modification	Control methods for nanomodification	Expected effect of nanomodification
The origin of the phase Particle growth	1 – 100 nm	Molecular selection	Single crystal	1) the ratio of cations and anions in the source system; 2) the critical radius of the crystal nucleus (rcr); 3) the shape factor of the crystal nucleus; 4) the number of point defects per unit of volume of the crystal nucleu.	Energy and size of a critical nucleus: $\Delta G_{cr} = \frac{16\pi\sigma^3 V_m^2}{3R^2T^2(\ln\gamma_{cr})^2};$ (1) $r_{cr} = \frac{2\sigma V_m C_1}{T(C - C_1)}.$ (2) The total number of crystallization centers $I_{cr} = a \cdot \exp\left[-\frac{1}{RT}\left(\frac{16\pi\sigma^3 V_m^2}{3(\Delta\mu)^2} + E_{act}\right)\right] + I_{\sec}$ (3) The total increment of the volume of a new phase $dV = \frac{4\pi J}{3}\left[V_0 - V(\tau)\right]\vartheta^3(t-\tau)^3 d\tau$ (4)	1) the degree of supersaturation of the initial solution; 2) the creation of additional crystallization centers	1) a change in the thermodynamic conditions of synthesis; 2) the introduction of nanoscale additives; 3) the introduction of surfactants.	1) acceleration of the formation of a molecular cluster; 2) lowering the activation energy of the process.

ER stage	Agglomeration
Scale	100 – 1000 nm
Transition phenomenon	Topological selection
Structure level	Crystalline intergrowth
Structural parameters to be nanomodified	1) the size and shape of the intergrowth estimated by the specific surface area (Sag); 2) the number of crystals in the intergrowth (Nc); 3) the number of crystal contacts in the intergrowth (Ncc); 4) the contact strength depending on its type (Rc); 5) the number of linear and planar defects in the intergrowth.
Conceptual kinetics models of heterogeneous processes of structure formation	Aggregate specific surface area $S_{ag} = \frac{1}{2} \cdot \pi \cdot d_0^2 \cdot N_0^{'} = 2\pi\eta_f (D_0 - d_0)^2$ (5) The number of particles in the aggregate $N_q = n_f \cdot \left(\frac{D_0}{d_0}\right)^3$ (6) Change in the area of the phase boundary: $\Delta S = n_f \cdot \left(\frac{D_0}{d_0}\right)^3 \cdot \pi \cdot d_0^2 - 2 \cdot \pi \cdot n_f (D_0 - d_0)^2 = = \pi \cdot n_f \cdot d_0^2 \left[\left(\frac{D_0}{d_0}\right)^3 - 2 \cdot \left(\frac{D_0}{d_0} - 1\right)\right]$ (7) System energy change $E_{aggl} = E_k + E_s - E_r.$ (8)
Control factors for nano-modification	1) the formation of a fractal network of the solvent; 2) a change in the type of physicochemical adsorption at the phase boundary.
Control methods for nanomodification	1) the introduction of nanoscale and ultrafine carbon particles; 2) the introduction of surfactants plasticizing
Expected effect of nanomodification	1) a change in the thermodynamics and kinetics of the hardening process; 2) a change in the structure and properties of the crystalline intergrowth

ER stage	Scale	Transition phenomenon	Structure level	Structural parameters to be nanomodified	Conceptual kinetics models of heterogeneous processes of structure formation	Control factors for nano-modification	Control methods for nanomodification	Expected effect of nanomodification
Spontaneous structure formation	1 – 100 μm	Morphological selection	Cementitious substance	1) the volume ratio of crystalline and amorphous phases; 2) the volumetric ratio of morphological differences: cryptocrystalline; fiber-needle; lamellar-prismatic; 3) the specific volume of crystalline and gel pores.	Jander's equation: $$\frac{dx}{dt}=\frac{k_2}{x}, \quad (9)$$ or $x=k_3\cdot\sqrt{t},\ x^2=k_4\cdot t.$ The magnitude of the change in the morphological parameter in the initial period of crystallization : $$\frac{\Delta l}{l}=\frac{1}{3}\cdot\frac{\Delta V}{V}\approx\frac{9\cdot\sigma\cdot l}{4\cdot\eta\cdot r}\cdot t,. \quad (10)$$ Arrhenius equation $$K=A\cdot e^{-\frac{E_a}{RT}} \quad (11)$$	1) a change in the intergranular surface of the system; 2) the formation of additional interfaces; 3) the formation of ordered hardening structures with close packing; 4) the optimization of the ratio of amorphous and crystalline phases and their morphology; 5) the regulation of the structure of porosity.	1) heat treatment; 2) pressing (compaction); 3) the introduction of additives of microparticles (microfillers); 4) dispersed structure reinforcement.	1) a change in the thermodynamics and kinetics of the hardening process; 2) a change in the structure and properties of the cementitious substance.

3.2. *The particle generation process of hydration products*

The use of nanotechnological control actions is motivated by the desire to accelerate the accumulation of hydration products, to reduce the energy costs of the process. At the same time, it is necessary to structurally divide the volume of accumulated hydration products in the system, bearing in mind the possibility of the formation of primary particles with controlled crystal-chemical and geometric characteristics.

To justify the factors controlling the development of the stage, let us turn to the analysis of conceptual models of the kinetics of the process (see Table). The process should be considered in the framework of the kinetic theory of the formation of a new phase. Therefore, in terms of control factors, it must be correlated with:

– the crystallization temperature (T);
– the specific surface free energy of crystals (σ);

- the molar volume of the new phase (V_m); the degree of supersaturation (γ), which is included in the ratio $\Delta\mu = RTln(\gamma + 1)$;
- the activation energy of the transition of ions, molecules from the medium to crystallization centers (E_{act});
- the intensity of secondary nucleation in the volume of the initial phase (I_{sec}), which is associated with external crystallization centers, for example, nanoscale particles.

In accordance with the Gibbs–Volmer theory [20], the formation of a critical-size nucleus (r_{cr}) is modeled by the equation for the total crystallization energy ΔG_{cr} (see Table). The appearance of nuclei becomes possible when a certain (critical) degree of supersaturation of the solution is reached with that substance whose molecules are involved in the formation of a new phase. The simplest ratio characterizing supersaturation has the form

$$\gamma = (C_m / L_{mj}) - 1, \tag{12}$$

where γ is the degree of supersaturation; C_m is the number of molecules or clusters from which the particles are built, per unit of volume of the medium; L_{mj} is the boundary value of C_m for the given particle.

The total number of the crystallization centers (I_{cr}) arising in a unit of volume of a solution, or the total intensity of their primary and secondary formation, depends on the kinetic coefficient of this process (α). The main means of control at this stage is the degree of supersaturation of the initial solution, which affects the rate of appearance and structure parameters of the crystal nucleus. With this in mind, in nanotechnology, one can turn to the methods of controlling the state of supersaturation, for example, introducing nanoparticles with a cognate crystal-chemical structure (to change C_m) and/or regulating solubility through thermal or other effects on the system (to change L_{mj}).

Regarding the first one, we can note that the chemical affinity (mineralogical and dimensional) of the introduced nanoparticles as possible centers of nucleation of particles of the solid phase is crucial for molecular selection in the system, that is, for the intensification of the first transition in the evolution path of a solid substance, "phase nucleation" – "growth particles". Against a decrease in the internal energy of the system, the phenomenon of molecular (ion) selection [21] acts, as a result of which clusters of molecules (ions) become nuclei, containing, first of all, molecules (ions) similar in structure and size.

Thus, the mechanism of the nanomodifying effect of additives at the level of formation of a single crystal is associated with the possibility of direct chemical participation of nanoparticles in heterogeneous processes of phase formation of hydration products, which accelerates the development of the molecular cluster of the particle nucleus. And this possibility is determined by the chemical and mineralogical composition of the introduced nanoparticles and the activity of their surface. Based on these features, one can characterize and select additives for nanomodification technology [23].

3.3. The growth and accumulation stage of the particles of hydration products

The development of crystals after their nucleation is realized as a heterogeneous process that occurs when the interface is formed between the initial phase and hydration products. At this stage, the morphology of the system is constantly changing, due to the logical development of the phenomenon of topological selection. During selection, the medium destroys and eliminates disordered forms and promotes the formation of ordered forms consisting of particles with close geometric parameters.

At this stage, as a result of nanomodification, structural parameters such as the shape coefficient of the crystal, the number of probable point defects per unit of volume of the crystal can be changed (see Table).

The consideration of the main conceptual models for this stage (in a quantitative formulation of the question) is based on the assumption that after the appearance of the crystallization center in the volume V_0 at the time t = 0, the growth of the new phase occurs isotropically with a constant linear rate υ [20]. Then, at time $t = \tau$, the volume that the new phase will occupy will be equal to

$$V(t) = \frac{4\pi}{3}\vartheta^3\tau^3. \tag{13}$$

The number of crystallization centers that appear in the system over a period of time from τ to $\tau + d\tau$ with a constant rate of nucleation of centers per unit of volume is $J[V_0 - V(\tau)]d\tau$. By the time $t > \tau$, the total increment of the volume of the new phase only due to the centers arising in the time interval from τ to $\tau + d\tau$ will amount to dV (see Table). Moreover, the conceptual model of the particle growth process has the form

$$\frac{V(t)}{V_0} = 1 - \exp\left[-\frac{\pi}{3} J \vartheta t^4\right]. \tag{14}$$

The substance is supplied to the growing supercritical nucleus due to diffusion (D) from the surrounding solution. The growth rate of the nucleus (υ) will be equal to the rate of increase of its radius due to the molecules deposited on the spherical surface of the nucleus.

The structure-forming role and the modifying effect of the addition of nanomodifiers at the stage of particle growth and accumulation are associated with the catalytic role of nanoparticles as crystallization centers with the corresponding effect of lowering the energy threshold of this process and its acceleration. It should be assumed that the main control factor at this stage is the creation of additional crystallization centers. This is ensured by the introduction of a reasonable dose of nanoadditives of optimal size and a suitable crystal-chemical structure.

In addition, it should be noted that to form the necessary dimensional habit of crystals it is advisable to introduce certain surface-active substances (surfactants), which can selectively block the growth of their faces. As a result, the geometry of the crystals changes, for example, the formation of long crystals, which determine the effect of self-reinforcing and hardening of the structure of hydration products.

In the evolutionary route, the second transition “particle growth” – “agglomeration” objectively occurs, as a result of which the cement system is structured at the level of crystalline intergrowth.

3.4. Agglomeration stages of the particle of hydration products

At this stage, a spatial grouping of hydration products’ particles takes place through adhesion. As a result, larger secondary particles are formed. Agglomeration occurs by binding of primary particles due to weak (leading to the formation of aggregates) or stronger (leading to the formation of agglomerates) interactions. Meanwhile, the primary particles in the agglomerate and aggregate to a large extent retain their primary shape and size.

Thus, in controlled agglomeration, the object of nanomodification is a polycrystalline intergrowth with the required characteristics and parameters.

Let us consider the basic conceptual models for this stage. The driving force of the agglomeration process is the desire of the system to reduce the area of the phase boundaries. The external surface area of the secondary particle is

$$S'_{ag} = \pi \cdot \eta_f \cdot (D_0 - d_0)^2. \tag{15}$$

On this surface of the aggregate, there are primary particles in the amount of

$$N'_0 = \frac{S'_{ag}}{\overline{s}_0} = 4 \cdot \eta_f \cdot \left(\frac{D_0}{d_0} - 1\right)^2, \tag{16}$$

where $\overline{s}_o = \pi \cdot d_0^2 / 4$ is the projection of one particle onto the surface.

From here, we can proceed to the ratio for the specific surface area of the aggregate (S_{ag}) in contact with the liquid phase (see table). The ratio takes into account the dependence of S_{ag} on the linear size of the aggregate (D_0), the diameter of the nanoparticle (d_0), and the packing density of particles in the aggregate (η_f). Based on this, it is possible to determine the number of particles entering the aggregate (N_q) and the change in the total area of the phase boundary (ΔS). With a decrease in the size of the initial particles of the nucleus during nanomodification, the number of released energy increases, which contributes to the intensification of agglomeration and the reduction in the duration of the process. The agglomeration process takes place in the liquid phase (in water), in which primary particles are present in a certain amount. In this case, the water fractal network can specify a certain structure during the formation of secondary particles, aggregates, agglomerates. This will be directly related to the energy effects of agglomeration. The energy released during agglomeration (E_{aggl}) can be composed of the energy E_k necessary to overcome the adhesion forces between the agglomerates, the energy costs to wet the formed surface of the agglomerate E_s and overcoming the resistance forces of the medium E_r when moving the agglomerate (see Table).

Thus, the special formation of the fractal structural network of the solvent (water) should be attributed to the main factor of nanomodification at this stage, since this causes a change in the mechanism of physicochemical adsorption at the phase boundary [24]. The formation of a fractal network of water can be achieved, for example, by introducing nanosized and ultrafine carbon-containing particles, which initially physically and chemically interact with a liquid medium (for example, mixing water), form its ordered “frame” structure due to hydrogen bonds and Van der Waals interactions. It is the resulting structural network that sets the necessary geometry of the crystalline structure (the number and packing density of aggregates and crystallites), that is, ensures its change, which ultimately affects the properties of the crystalline intergrowth.

The formation of a structured liquid phase can also be based on the method of introducing plasticizers and superplasticizers as a means of nanomodification. Their use allows us to control the process of agglomeration of crystals by changing the type of physicochemical adsorption at the phase boundary. The structure-forming participation of plasticizing additives is associated with mechanisms providing a change in the thermodynamics and kinetics of the process, making it possible to control the size and shape of the agglomerate, intergrowth, the number of crystals in them, and their contacts.

It is important to emphasize that the agglomeration process transfers the structure from the nanometer to micrometer size range. In this case, a structure is formed from individual crystals, which are represented by phases of typical mineralogy and morphology, filling the intergranular volume in the composite. The result is a continuous spatial framework of hydration products as a matrix of cement-based composites.

At the stage of growth and agglomeration, the arising formations are characterized by the disequilibrium of the thermodynamic state. Therefore, in the evolutionary route between the stages of “agglomeration” – “spontaneous structure formation”, the phenomenon of morphological selection develops, stimulated by the approximation of the size, shape, state of particles of their agglomerates, crystallites to equilibrium.

3.5. The stage of spontaneous structure formation of hydration products

In spontaneous structure formation, the size and shape of particle agglomerates change so that the minimum internal surface energy of the system is ensured. The morphological selection also determines the evolutionary transition of the structure to a new level – the level of hydration products.

The kinetics of processes at the stage of spontaneous structure formation is determined by:

- heat and mass transfer with a growth-supporting (internal and external) environment,
- molecular kinetic phenomena at the boundary “surface of the solid phase – medium”.

There are many conceptual models for describing this mechanism. Of these, Jander's equation [26] in our considerations can be applied under the assumption that the limiting stage of the process is the diffusion of reagents through the interaction product layer (dx/dt), and its diffusion layers on the grain surface of the initial components are flat. The rate of formation of a single three-dimensional crystalline structure is determined by:

- crystallization product layer thickness (x);
- constants depending on the properties of the reactants and the process conditions (coefficients k_2, k_3, k_4, characterizing the nature of the reacting substances) and process time (t) (see Table).

With this in mind, the regulation of the heat treatment modes may be the technological method of changing the thermodynamics and kinetics of the process at this stage.

The emerging morphology of the cementing substance is determined by a change in the morphological parameter ($\Delta l/l$) in the initial period of crystallization of an integrated three-dimensional crystalline structure. It depends on several factors:

- the initial length (l) and volume (V) of the solid phase,
- their changes (Δl) and (ΔV) over time t;
- the particle radius of the solid phase (r);

– the surface tension at the liquid – solid boundary (σ);

– the viscosity of the liquid phase (η).

As a result of the modifying effect, we can:

1. achieve a change in the state of the intergranular surface of the system;
2. promote the formation of additional types of interface;
3. form ordered hardening structures with close packing of crystals with a corresponding change in the structure of porosity of the crystalline intergrowth.

At the stage of spontaneous and self-organizing structure formation, the consequences of nanomodification undertaken in the previous stages will be manifested indirectly. For example, this may refer to the zoning phenomenon of the hydration products' structure.

3.6. The nanomodification of the structure of the cement system from the point of view of the fracture mechanics

According to the fundamentals of the manifestation of the structural properties of materials, let us indicate that the resistance of cement-based composites to destruction is based on three determining propositions [6]:

– the first propositions reflect the role and importance of physicochemical bonds that provide the level of possible resistance of the structure to mechanical stress;

– the second propositions take into account the conditions for the formation of the stress state of the material through the dependence of the measure of uniformity (heterogeneity) of the stress field arising in it on the uniformity of the composition and structure of the composite;

– the third propositions take into account the essence of the mechanism of destruction of the material in a direct relationship between the development of plastic deformation, the formation, and propagation of cracks in the material, and its composition and structure.

In problems of increasing the potential of the structure's resistance to fracture, it is advisable to single out the levels of its nanomodification:

– the level of a single crystal;

– the level of their agglomerates and crystalline intergrowth (crystallite);

– the level of hydration products.

When considering the factors of structural modification at the level of individual crystals, the well-known Hall-Petch equation can be used [27],

$$\sigma = m \cdot \sigma_0 + m \cdot k \cdot d^{-\frac{1}{2}}, \qquad (17)$$

where σ is the ultimate strength; m is the coefficient associated with the characteristics (crystal chemistry and morphology) of the structural unit; σ_0 is the stress required to cause the beginning of the fracture of the structural unit in the absence of resistance from the boundaries in the crystallite; d is the structural unit size; k is the stress concentration at the top of the initial crack, depending on the number and nature of defects in the structural unit.

This equation reflects the relationship of the ultimate strength σ of a structural unit with its size d, crystal-chemical and morphological characteristics and the degree of imperfection, that is, with those structural parameters that are subjected to change through nanomodification at the stage of nucleation of solid particles.

At the level of agglomerate and intergrowth of crystals (crystallite), the influence of individual crystals on strength is realized through the spatial-geometric design of their compacted structure. The strength of the contacts in the intergrowth is a probabilistic distribution function of values in the range from the maximum possible value for regular (for example, epitaxial) to the minimum for non-regular contacts of coalescence or contiguity. In general, the fracture resistance is determined by the features of the packing of crystals into enlarged crystalline agglomerates (aggregates) and intergrowth.

Shchurov A.F. proposed a relationship between the strength and the average size of agglomerates, crystallites in the form of a modified Griffiths-Orowan equation [27], which includes the value of the modulus of elasticity of the substance associated with the composition and crystal-chemical structure of the crystal included in the crystalline intergrowth:

$$\sigma_{pm} = \left(\frac{E_{pm} \cdot \gamma *}{r} \right)^{1/2} \cdot (1 - V_n)^n = C_v \cdot r^{-\frac{1}{2}} \cdot (1 - V_n)^n, \tag{18}$$

where σ_{pm} is the uniaxial compression stress; E_{pm} is the elastic modulus; $\gamma^* = \gamma + \Delta\gamma$ is the effective surface energy of fraction, here γ is the surface energy, and $\Delta\gamma$ is the additional work spent on producing local plastic deformation and the formation of stepped cleavage surfaces; r is the average crystallite size; C_v is the fracture toughness coefficient; V_n is the porosity; n is the empirical coefficient, which varies in the range from 2.6 to 4.3.

The strength of the agglomerate, the crystalline intergrowth R_{sc} in connection with the features of its formation into a continuous three-dimensional skeleton is determined by the following factors:

– the number of contacts per unit of geometric volume of the agglomerate, (crystalline intergrowth);

– the size distribution of crystals and submicron crystals

– the geometric packaging of elements in the agglomerate, intergrowth;

– the strength of individual contacts, determined by their type and type of bond in the contact (ionic, covalent, Van der Waals, etc.)

– the degree of defectiveness and the degree of the stress state of the contact.

In the transition to the technological tasks of nanomodification of the structure, these factors are the basis for considering controlling the stages of the evolutionary route of a solid-state formation. The control action through nanomodification for the structural levels of individual crystals and crystal intergrowth is carried out by regulation of

– the sizes, crystal-chemical and morphological characteristics, the measure of defectiveness of individual crystals;

– the geometry of the packing of crystals and submicron crystals in agglomerates (aggregates), crystalline intergrowth, the number and strength of contacts in them. It is precisely in connection with this that the problem of zoning the volume of the accumulating and changing submicrocrystalline and crystalline phases become obvious.

At the level of hydration products (as a matrix of cement-based composites), the resistance of the structure to fraction depends, first of all, on the spatial-geometric distribution and volumetric ratio of kinds of hydration products:

– cryptocrystalline, increasing the fracture toughness of the cementitious substance, providing an increase in energy expenditures for the production of plastic deformations of the solid phase until crack formation;

– fiber-needle, which increases the energy of fraction due to a large number of randomly placed contacts and interfaces;

– lamellar-prismatic, increasing elastic properties and additionally providing a self-reinforcing effect and an increase in the fracture toughness of a cementitious substance [28].

Very significant strength characteristics at this structural level are also determined by the specific volume of nano- and micropores, which are independent stress concentrators.

Summarized for the considered structural levels, we distinguished three groups of structural factors for controlling the resistance of cement-based composites to a fraction.

The first group of structural factors relates to controlling:

a) the type of physical and physicochemical internal bonds of crystals (submicron crystals) of the resulting solid phase of a substance by controlling their crystallochemical characteristics and chemical-mineralogical composition;

b) the number of bonds per unit volume of agglomerates and crystallites by controlling the dispersion and morphology of its constituent particles;

c) the volumetric content of neoplasms (crystals, agglomerates, crystallites) of the cementitious substance, filler grains in the matrix of cementitious substance;

d) the condition, quality of the bonds in the contact zone of the filler grains with the cementitious substance.

The second group of structural factors corresponds to controlling:

a) the volumetric ratio of structural elements in the geometric volume of the material as a whole and within the considered scale levels;

b) the size distribution function of the structural elements of the constituent material (cementitious particles, pores, grains of filling components, etc.);

c) a measure of the homogeneity of the spatial distribution of the structural components of the material in its volume.

The third group of factors takes into account the possibilities of controlling the force and energy conditions of plastic deformation, formation, inhibition of the development and propagation of cracks due to the structure's capabilities (including, for example, self-reinforcing). It is also possible to inhibit the development and propagation of cracks by introducing additional structural elements into the material that can change the conditions of plastic deformation.

We can note that the directional regulation of the selected structure parameters in science and technological practice of obtaining cement-based composites has been studied and used to a certain extent. The achieved effects of nanomodification of the structure at the level of individual crystals, their agglomerates, and crystalline intergrowth (crystallite) certainly manifest themselves at the level of structure of hydration products as a consequence of these effects. This is the result of nanomodification technology since it is the structure of hydration products that determines the properties of the resulting cement systems and cement-based composites.

4. Discussion

The efficiency of the provided theoretical approach has been affirmed by some of our experimental results. The resuls show efficiency of nanomodifying of cement systems with three kind of complex nanoaddictives:

1) CND based on SiO_2-nanoparticles,

2) CNT based on Nanocyl-7000 fulleroid,

3) ChN based on chrysotile nanotubes.

Methods of the synthesis of nanoadditives and the nanomodification of cement systems have been published earlier [22, 24, 25, 27].

The intensification of the first transition in the evolution path of a solid substance ("phase nucleation" – "particles growth") is achieved by the introduced nanoparticles as possible centers of particle nucleation. In [22], we showed that the introduced nanoparticles that have a mineralogical and dimensional affinity with hydration products can be effective crystallization centers. The significant change in the process of structure formation at the stage of "phase nucleation" can be obtained in case the critical particle size of nanoadditives has to be no more than 10 nm.

The second transition "particle growth" – "agglomeration" objectively occurs, as a result of which the cement system is structured at the level of crystalline intergrowth. In order to form the necessary dimensional habit of crystals, it is advisable to introduce certain surface-active substances (surfactants), which can selectively block the growth of their faces. As a result, the geometry of the crystals changes, for example, the formation of long crystals, which determine the effect of self-reinforcing and hardening of the structure of hydration products. The work [24] well affirms these statements. The use of all complex nanoadditives accelerates the speed of hydration processes by 20 – 25 times (Table 2.). The use of complex nanoadditives based on SiO_2-nanoparticles (CND) that have an affinity crystal-chemical structure with cement systems accelerates the speed of hydration processes during curation in low temperatures (Table 3.). According to X-ray analysis data volume of hydration products significantly was increased too. This is due to the catalytic effect of nanoparticles that decrease the activation energy of the hydration process by 2.5 – 2.8 times and participate in heterogeneous phase-formation processes (Table 4). As a result of the catalytic effect, the hydration process in cement systems with nanoadditives is substantially accelerated: by the daily duration of hardening at 20 ^{0}C (293 K), the degree of hydration reaches at least 70 – 75%.

At the stage of spontaneous and self-organizing structure formation, the size and shape of particle agglomerates change so that the minimum internal surface energy of the system is ensured. The morphological selection also determines the evolutionary transition of the structure to a new level – the level of hydration products. At this stage, the consequences of nanomodification undertaken in the previous stages will be manifested indirectly. For example, these indirect effects have been significantly shown when we used chrysotile nanotubes (ChN) as a modifier of cement systems [25]. It was obtained that using the chrysotile nanotubes with related crystal-chemical structure accelerated the speed of hydration processes by 30 times and increase the strength of hardened cement paste by 3 times (Table 5, Fig.1,2,3).

Table 2. The hydration degree of cement modified by different nanoadditives (0.01% mass cement).

Specimen ID	The cement hydration degree (mass%) – over line, volume of hydration products, m^3/m^3 – under line				
	1 day	3 day	7 day	14 day	28 day
C+W	21	35	58	65	75
	0.15	0.25	0.41	0.46	0.53
C+W+CND	76	90	92	93	94
	0.52	0.61	0.62	0.63	0.64
C+W+CNT	67	78	87	88	89
	0.41	0.50	0.55	0.57	0.59
C+W+ChN	83	90	92	93	94
	0.59	0.62	0.64	0.66	0.68

Table 3. The hydration degree of cement depending on temperature for cement paste modified by nanoadditives (0.01% mass cement).

Specimen ID	The cement hydration degree (mass%) for the process duration								
	hour					day			
	1	3	7	12	24	3	7	14	28
curing temperature 273 K									
C+W	11	12	15	18	20	40	45	48	51
C+W+CND	37	42	54	57	62	67	72	75	78
curing temperature 293 K									
C+W	39	41	49	53	55	61	65	68	75
C+W+CND	60	63	69	71	75	81	92	93	93
curing temperature 313 K									
C+W	42	48	51	59	68	75	81	83	89
C+W+CND	81	85	88	91	93	95	96	96	97
curing temperature 333 K									
C+W	71	75	79	85	91	92	93	95	95
C+W+CND	84	88	91	93	96	96	97	97	98

Table 4. Kinetic parameters of the hydration process of cement paste modified by nanoadditives (0.01% mass cement).

Specimen ID	Hydration rate constant $\bar{\mathbf{k}}$ in curing temperature				$\bar{n}$	EEA, kJ/mol
	273 K	293 K	313 K	333 K		
C+W	17.53	25.40	27.72	31.68	0.13	173.4
C+W+CND	46.53	54.19	56.71	57.19	0.08	61.7
C+W+CNT	42.84	53.55	56.00	57.29	0.08	76.2
C+W+ChN	49.63	55.89	58.62	59.91	0.07	57.7

Table 5. Criteria and efficiency ratios of cement paste nanomodification by the nanoadditives.

Criteria and efficiency ratios	Specimen ID			
	C+W	C+W+CND	C+W+CNT	C+W+ChN
EEA, kJ/mol	173.4	61.7	76.2	57.7
Required time to reach 75% cement hydration degree , day	28	1	3	3
Speed-up cement hydration degree ratio	-	28 – 30	9 10	25 – 28
Relative strength hardened cement paste $R(\tau) / D_h(\tau)$, MPa:				
in 1 day,	31	83	71	58
in 7 day,	58	74	62	78
in 28 day.	72	98	90	98
Strength hardened cement paste $R(\tau = 28\ day)$, MPa	55	90	80	140
Increase strength ratio $R(\tau = 28\ day)$,	-	1.64	1.45	2.54
Required time to reach 75% of strength hardened cement paste, day	7	1	7	3

This is due to a change in the phase composition and microstructure of cement hydration products modified by nanoaddictives, namely: an increase in the volume, density of hydration products; the predominance of high-strength phases of hydration products such as xCaO·SiO$_2$·zH$_2$O and 3CaO·Al$_2$O$_3$·xH$_2$O and absence low-strength phases Ca(OH)$_2$ (Fig. 4–7). At the agglomeration stages of the particle of hydration products, a spatial grouping of hydration products' particles takes place through adhesion. Thus, the special formation of the fractal structural network of the solvent (water) should be attributed to the main factor of nanomodification. The formation of a fractal network of water can be achieved by introducing nanosized and ultrafine carbon-containing particles, which initially physically and chemically interact with water. It is the resulting structural network that sets the necessary geometry of the crystalline structure (the number and packing density of aggregates and crystallites). In [25], it was shown that the introduced the carbon-nanoparticles in cement systems obtained zoning of the crystallization structure of cement hydration products. At the same time, the carbon-nanoparticles are nano-reinforcing elements in the structure of the cement hydration product. However, the kinetics of strength in this variant of nanomodification is noticeably different in that in the early stages of hardening, the curing is slower: achieving 70% of the strength of its values at the age of 28 days is provided in this variant for 7 days, and for 1-day cement paste gains only 20%. Based on this data, it can be observed that the introduction of a carbon nanotubes additive is less effective in comparison with the addition of nanoscale particles of SiO$_2$, and above all in terms of the kinetic parameters of hardening strength.

Therefore, we experimentally confirmed that the nanomodification effects associated with the catalytic role of nanoparticles in cement hydration processes, with a change in the morphology of hydration products, with zoning and clustering of the hardened cement paste microstructure. As a result, the introduction of various types of nanoadditives into cement systems contributes to the decrease of effective activation energy required for the process "start" by 2.3 – 2.8 times, the acceleration of cement hydration processes by 20 – 30 times, and the increase in strength by 1.5 – 3 times (See Table 5).

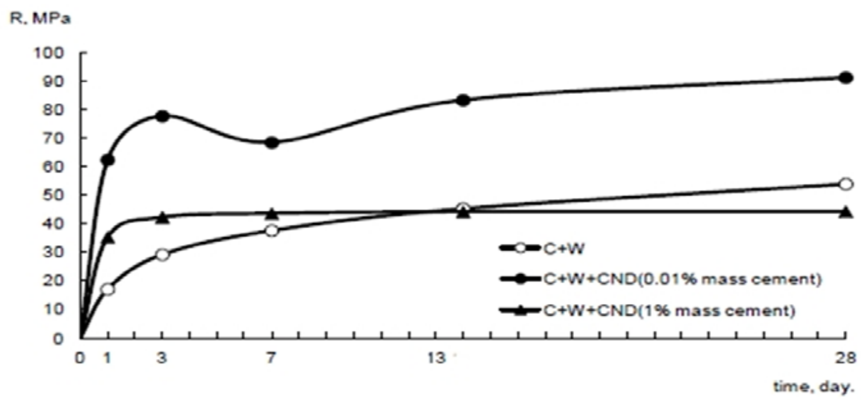

Figures 1. Strength kinetics curves of cement paste modifying by CND [24].

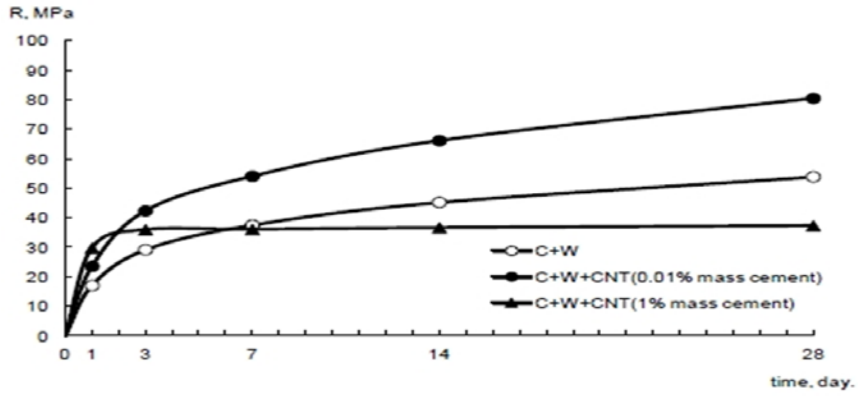

Figures 2. Strength kinetics curves of cement paste modifying by CNT [24].

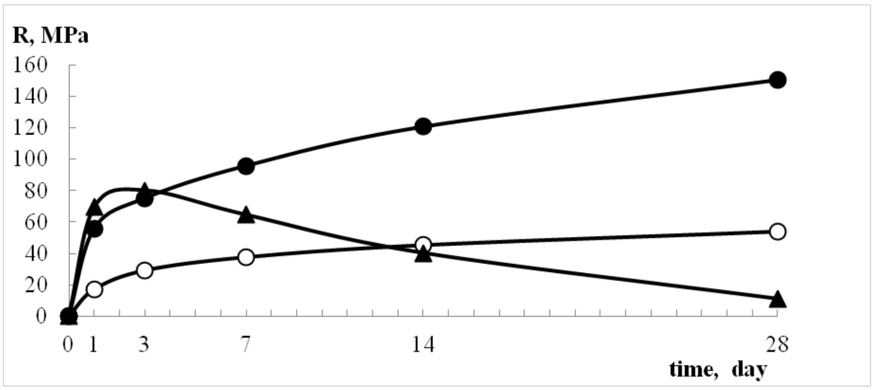

Figures 3. Strength kinetics curves of cement paste modifying by ChN [24].

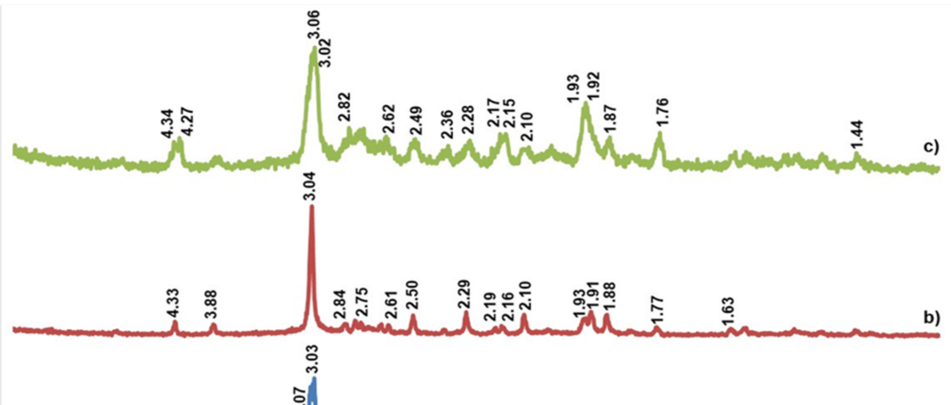

Figure 4. X-ray diffraction patterns for a nanomodified cement system modified by CND:
a) without addictives of 28-day curing; b) 1-day curing; c) 28-day curing.

$3CaO·SiO_2$ (d = 3.02; 2.75; 2.61; 2.18; 1.76; 1.48); $2CaO·SiO_2$ (d = 3.80; 3.01; 2.74; 1.80; 1.63); $Ca(OH)_2$ (d = 4.93; 3.11; 2.63; 1.93; 1.79; 1.69); $2CaO·SiO_2·H_2O$ (d = 4.77; 3.01; 2.92; 2.37; 2.25; 1.96); $xCaO·SiO_2·zH_2O$ (d = 3.06; 2.97; 2.80; 1.83; 1.67); $2CaO·SiO_2·0.5\ H_2O$ (d = 2.99; 2.77; 2.67; 2.58; 1.80)

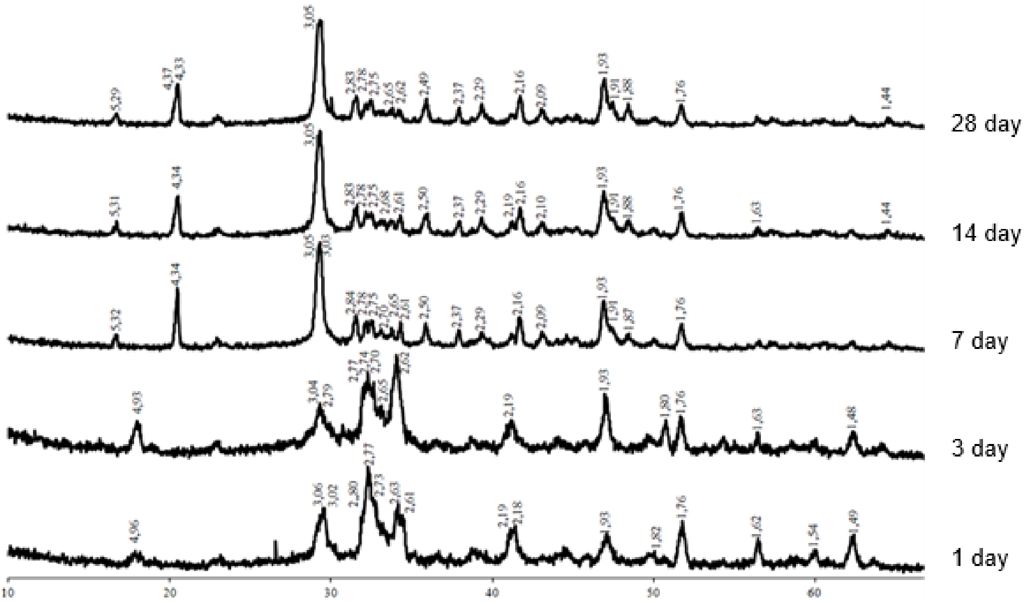

Figure 5. X-ray diffraction patterns for a nanomodified cement system modified by CNT.
$3CaO \cdot SiO_2$ (d = 3.02; 2.75; 2.61; 2.18; 1.76; 1.48); $CaO \cdot SiO_2 \cdot zH_2O$ (d = 5.6; 3.07; 2.97; 2.80; 2.28); $xCaO \cdot SiO_2 \cdot zH_2O$ (d = 3.07; 2.97; 2.80; 2.28; 2; 1.83); $2CaO \cdot SiO_2 \cdot H_2O$ (d = 3.04; 2.7; 1.9; 1.84; 1.49); $3CaO \cdot SiO_2 \cdot 2H_2O$ (d = 3.03; 2.47; 1.77; 1.63;1.51); $3(2CaO \cdot SiO_2) \cdot 2H_2O$ (d = 3.07; 2.82; 2.72; 2.28; 2.17).

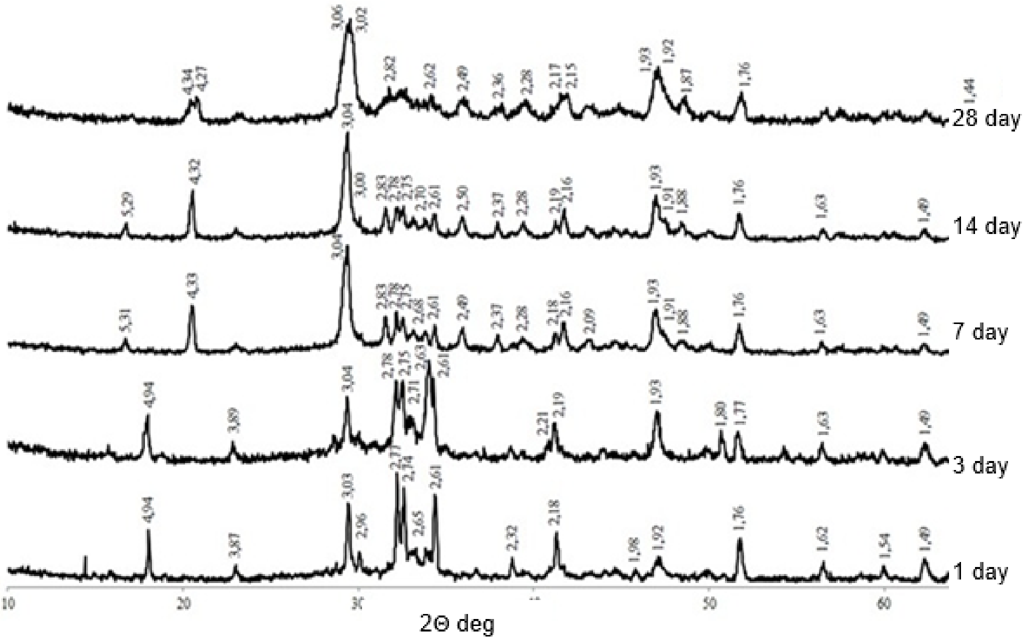

Figure 6. X-ray diffraction patterns for a nanomodified cement system modified by ChN. $3CaO \cdot SiO_2$ (d = 3.02; 2.75; 2.61; 2.18; 1.76; 1.48); $xCaO \cdot SiO_2 \cdot zH_2O$ (d = 3,07; 2,97; 2,80; 2,28; 2, 1,83); $CaO \cdot SiO_2 \cdot H_2O$ (d = 3,07; 2,8; 1,83; 1,67; 1,53); $3CaO \cdot SiO_2 \cdot 2H_2O$ (d = 3,03; 2,47; 1,77;1,63;1,51); $3CaO \cdot Al_2O_3 \cdot xH_2O$ (d = 2,86; 2,46; 2,31; 2,1; 1,93; 1,86).

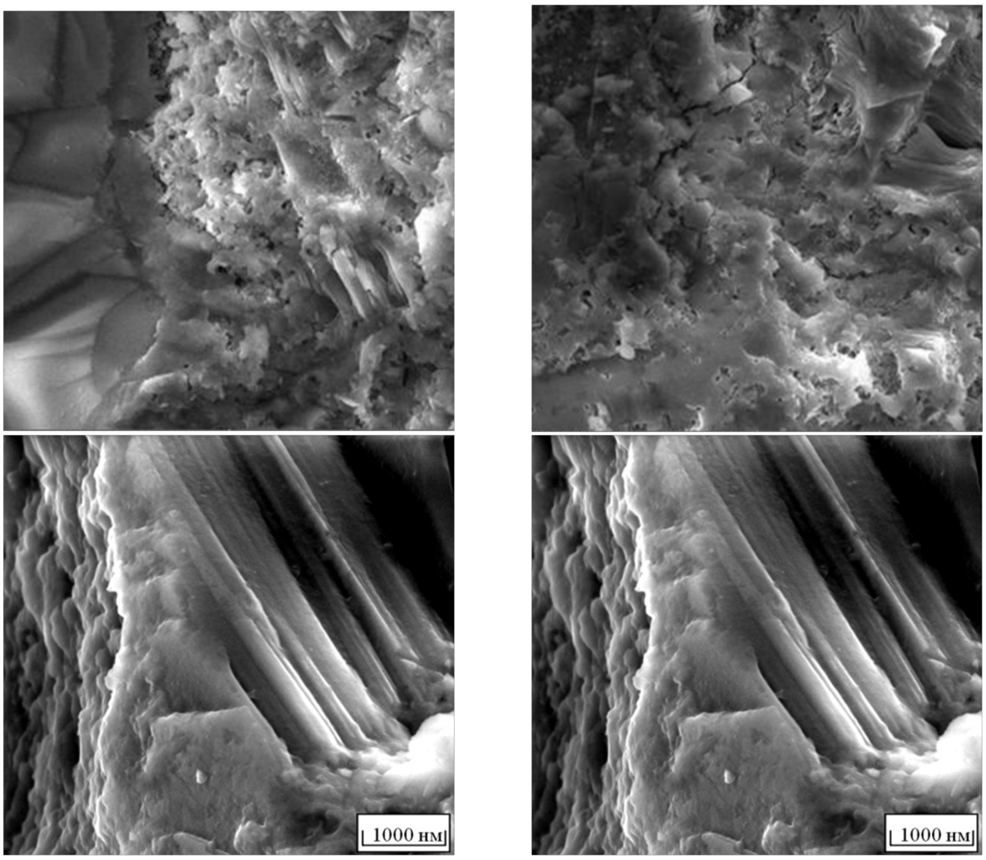

Figure 7. Hardened cement paste micrographs (hardening time 28 days, SEM)
a – without addictives; b – modified by CND; c – modified by CNT; d – modified by ChN.

5. Conclusions

1. The analysis of regularities of the kinetics of heterogeneous processes of the evolutionary route of hardening cement systems resulted in the systematization of the conceptual model of structure formation. Consequently, we proposed factors of nanomodification of cement systems. The factors of the nanomodification are represented by the degree of supersaturation of the initial solution, the creation of additional centers of crystallization, the change in the intercrystalline surface of the system, the formation of additional boundaries, the formation of ordered structures of hardening with a dense package, optimization of the ratio of amorphous and crystalline phases and their morphology, alteration of the intergranular system surface, the regulation of the porosity structure.

2. In accordance with the factors of nanomodification of cement systems, the technological methods of nanomodification are identified: heat treatment, pressing (compaction), dispersed structure reinforcing, the introduction of nanosized and ultrafine particles of different nature, the introduction of surface-active additives, changes in the thermodynamic conditions of the synthesis.

3. As a result of nanomodification the following effects in the structure formation of cement systems can be achieved: acceleration of the formation of a molecular cluster, lowering of the activation energy of the process, modifying the thermodynamics and kinetics of the hardening process, changes in the structure and properties of crystalline intergrowth, changes in the thermodynamics and kinetics of the hardening process, changes in the structure and properties of a cementitious substance. The factors and methods of nanomodification meet the terms of controlling the fracture strength of the cement-based composites.

4. Together, the effects of nanomodification of the structure and factors of increasing the fracture resistance will determine the effectiveness of solutions for engineering practice in terms of reducing the time and the energy costs for processes in the life cycle of cement-based composites, enhancing their quality. The research will further focus on effective nanotechnological solutions for engineering practice.

6. Acknowledgement

The experimental studies have been carried out using the facilities of the Collective Research Center named after Professor Yu.M. Borisov, Voronezh State Technical University, which is partly supported by the Ministry of Science and Education of the Russian Federation, Project No 075- 15-2021-662.

References

1. Khawam, A., Flanagan, D.R. Solid-state kinetic models: Basic and mathematical fundamentals. Journal of Physical Chemistry B. 2006. Vol. 110. Pp. 17315–1732.
2. Barnes, P. Structure and Performance of Cements. London (UK); New York (NY), USA: «Applied Science Publishers», 1983.
3. Poppe, A.M., de Schutter, G. Cement hydration in the presence of high filler contents. Cement and Concrete Research. 2005. Vol. 35. Pp. 2290–2299.
4. Ye, G., Liu, X., Poppe, A.M., de Schutter, G., van Breugel, K. Numerical simulation of the hydration process and the development of microstructure of self-compacting cement paste containing limestone as filler. Materials and Structures. 2007. Vol. 40. No. 9. Pp. 865–875. DOI: https://doi.org/10.1617/s11527-006-9189-6
5. Toshiharu, K., Saruul, D. Hydration heat modeling for cement with limestone powder. Iabse Colloquium Phuket. 1999. V. 81. Pp. 133 – 138.
6. 6. Maekawa, K., Ishida, T., Kishi, T. Multi-Scale Modeling of Structural Concrete. New York (NY) USA: «Taylor & Francis», 2009. 672 p.
7. Lothenbach, B., le Saout, G., Gallucci, E., Scrivener, K. Influence of limestone on the hydration of Portland cements. Cement and Concrete Research. 2008. V. 38(6). Pp. 848 – 860. DOI: https://doi.org/10.1016/j.cemconres.2008.01.002
8. Bentz, D.P. Influence of water-to-cement ratio on hydration kinetics: Simple models based on spatial considerations. Cement and Concrete Research. 2006. V. 36(2). Pp. 238 – 244. DOI:
9. Bentz, D.P. Modeling the influence of limestone filler on cement hydration using CEMHYD3D. Cement and Concrete Composites. 2006. V. 28. No. 2. Pp. 124 – 129. DOI: https://doi.org/10.1016/j.cemconcomp.2005.10.006
10. Cyr, M., Lawrence, P., Ringot, E. Mineral admixtures in mortars: Quantification of the physical effects of inert materials on short-term hydration. Cement and Concrete Research. 2005. V. 35. Pp. 719 – 730.
11. Zeng, Q., Li, K., Fen-Chong, T., Dangla, P. Determination of cement hydration and pozzolanic reaction extents for fly-ash cement pastes. Construction and Building Materials. 2012. V. 27. Pp. 560 – 569.
12. Yajun, J., Cahyadi, J.H. Simulation of silica fume blended cement hydration. Materials and Structures. 2004. V. 37. Pp. 397 – 404.
13. Wang, X.-Y. Modeling of hydration, compressive strength, and carbonation of portland-limestone cement (PLC) concrete. Materials. 2017. V. 10. No. 2 Pp. 115–120. DOI: https://doi.org/10.3390/ma10020115
14. De Schutter, G., Taerwe, L. General hydration model for portland cement and blast furnace slag cement. Cement and Concrete Research. 1995. V. 25(3). Pp. 593 – 604.
15. Jennings, H.M. A model for the microstructure of calcium silicate hydrate in cement paste. Cement and Concrete Research. 2000. V. 30. Pp. 101 – 116.
16. Moon, J., Reda Taha, M.M., Youm, K.S., Kim, J.J. Investigation of Pozzolanic Reaction in Nanosilica-Cement Blended Pastes Based on Solid-State Kinetic. Models and 29Si MAS NMR. Materials. 2016. V. 9. Pp. 99
17. Lee, H.S., Cho, H.K., Wang, X.Y. Experimental investigation and theoretical modeling of nanosilica activity in concrete. Journal of Nanomaterials. 2014. DOI: http://dx.doi.org/10.1155/2014/102392
18. Kim, J.J., Fan, T., Reda Taha, M.M. Homogenization model examining the effect of nanosilica on concrete strength and stiffness. Transportation Research Record. 2010. V. 2141. Pp. 28 – 35.
19. Artamonova, O.V, Chernishov, E.M. Concept and bases of technologies of nanomodification of building composites structures. Part 7. Final: Actual Generalization. Construction Materials. 2019. No. 11. Pp. 3 – 14. DOI: https://doi.org/10.31659/0585-430x-2019-776-11-3-14 (rus)
20. Goodilin, E.A., Eliseev, A.A. Protsessy kristallizatsii v khimicheskom materialovedenii [Crystallization processes in chemical materials science]. Moscow: «Moscow State University», 2006. 90 p. (rus)
21. Melikhov, I.V. Fiziko-khimicheskaya evolyutsiya tverdogo veshchestva [Physico-chemical evolution of solids]. Moscow: «BINOM. Knowledge lab», 2009. 309 p. (rus)
22. Artamonova O.V., Sergutkina O.R., Ostankova I.V., et al. Sintez nanodispersnogo modifikatora na osnove SiO2 dlya cementnyh kompozitov [Synthesis of SiO2-based nanodisperse modifier for cement composites]. Kondensirovannye sredy i mezhfaznye granicy. 2014. V. 16. No. 2. Pp. 152 – 162. (rus)
23. Korotkikh, D.N., Artamonova, O.V., Chernishov, E.M. O trebovaniyakh k nanomodifitsiruyushchim dobavkam dlya vysokoprochnykh tsementnykh betonov [On the requirements for nanomodifying additives for high-strength cement concretes. Nanotechnology in construction]. 2009. No. 2. Pp. 42 – 49. (rus)
24. Artamonova, O.V., Slavcheva, G.S., Chernishov, E.M. Effectiveness of combined nanoadditives for cement systems. Inorganic Materials. 2017. V. 53. No. 10. Pp. 1080 – 1085. DOI: 10.1134/s0020168517100028
25. Artamonova, O.V., Slavcheva, G.S., Shvedova, M.A. Effectiveness of nanotubular additives in the modification of cement systems. Inorganic Materials. 2020. V. 56. No. 1. Pp. 105 – 110. DOI: 10.1134/S0020168520010021
26. West A. Solid State Chemistry. Theory and applications in 2 hours. Part 1, 2. Moscow: «World», 1988. 336 p. (rus)
27. Chernishov, E.M., Dyachenko, E.I., Makeev, A.I. Neodnorodnost struktury i soprotivleniye razrusheniyu konglomeratnykh stroitelnykh kompozitov: voprosy materialovedcheskogo obobshcheniya i razvitiya teorii: monografiya. [Heterogeneity of structure and resistance to destruction of conglomerate building composites: issues of material science generalization and development of theory: monograph]. Voronezh: «Publishing House: Voronezh State University of Architecture and Civil Engineering», 2012. 98 p. (rus)
28. Timashev, V.V. Struktura samoarmirovannogo tsementnogo kamnya. Sintez i gidratatsiya vyazhushchikh materialov. [The structure of self-reinforced cement paste. Synthesis and hydration of binders]. Moscow: «Science», 1986. 400 p.

Contacts:

Olga Artamonova, ol_artam@rambler.ru

Evgeny Chernyshov, chem@vgasu.vrn.ru

Galina Slavcheva, gslavcheva@yandex.ru

Magazine of Civil Engineering

ISSN 2712-8172

journal homepage: http://engstroy.spbstu.ru/

DOI: 10.34910/MCE.109.7

Humidity regime in aerated concrete wall with finishing coating

V.I. Loganina , ***M.V. Frolov****

Penza State University of Architecture and Construction, Penza, Russia

**E-mail: mihail-frolovv@yandex.ru*

Keywords: Concretes, building materials, buildings, lime, energy efficiency, moisture

Abstract. The article estimates the influence of external finishing coating characteristics on the humidity regime in the walls of aerated concrete blocks with the density of 350–600 kg/m^3 (D350–D600 grades). The research is in demand due to the fact that condensation of excessive moisture in the enclosing structure is one of the most common reasons for the destruction of plaster coatings for walls of aerated concrete. To assess the humidity regime in the walls of aerated concrete, the temperature of the onset of moisture condensation t_{sk} was determined. The temperature of the onset of condensation t_{sk} is the temperature of the outside air: a temperature drops to this level causes formation of condensate in the enclosing structure. It was revealed that due to the use of the developed dry building mixture for D350–D600 concrete blocks finishing, moisture condensation begins at a significantly lower outdoor temperature. The moisture regime in the walls of D350–D600 aerated concrete blocks was studied for the conditions of various climatic zones on the example of three cities: Rostov-on-Don, Voronezh, Novosibirsk. A linear model is obtained that reflects the dependence of the temperature of the onset of condensation t_{sk} in the walls of D350–D600 aerated concrete blocks on the thermal properties of the wall material and the finishing layer.

1. Introduction

In accordance with the current regulatory documentation, the design of buildings should be carried out taking into account modern requirements for energy conservation [1–4]. Therefore, the development of new and improve old structures in order to increase their energy efficiency is a priority in the development of construction industry [5–8].

In recent years, aerated concrete has been increasingly used in the construction of external walls of buildings for various purposes [9, 10]. Such wide use of aerated concrete blocks is due to their good performance, low heat conductivity, high vapor permeability, relatively low cost, manufacturability of masonry and high labor productivity [11–13]. Using aerated concrete blocks of D300-D600 grades, it is possible to erect single-layer walls with sufficiently high heat-shielding properties.

A significant impact on the durability of operation of walls made from aerated concrete is exerted by the characteristics of the plaster compositions used for their decoration [14]. One of the most common reasons for the destruction of plaster coatings on aerated concrete is condensation of more moisture in the enclosing structure [15–18]. Moisture condensation in such enclosing structures occurs due to the significant difference in vapor permeability and thermal conductivity of the plaster coating and aerated concrete. To reduce the amount of condensing moisture in the enclosing structure, each subsequent layer in the direction from the internal surface to the external one should be characterized by greater vapor permeability and lower thermal conductivity compared to the previous layer. This requirement is rarely succeeded due to the fact that an increase in vapor permeability and a decrease in thermal conductivity of plaster coatings are associated with the appearance of an additional pore volume in their structure. That is why the operational properties of the resulting coatings, their frost resistance and moisture resistance may significantly deteriorate.

In the course of previous studies, we developed a compounding heat-insulating dry building mixture (DBM), designed specifically for finishing aerated concrete blocks. The recipe contains fluffy lime, aluminosilicate ash microspheres, a modifying additive based on a mixture of hydrosilicates and calcium aluminosilicates, white cement, ground waste from the production of aerated concrete, Melflux 2651 F, VINNAPAS 8031 H, sodium oleate [19–23]. We assume that using this DBM it is possible to significantly reduce the possibility of condensation and minimize its amount.

The purpose of the work is to investigate the influence of the characteristics of the external finishing layer on the humidity regime in aerated concrete enclosing structure. To achieve this goal it is necessary to solve the following tasks:

- to assess the influence of the characteristics of the external finishing layer on the temperature of the beginning of moisture condensation on the walls of aerated concrete blocks of grades D350-D600;

- to study the humidity conditions in the walls of aerated concrete blocks of grades D350-D600 for the conditions of various climatic zones on the example of three cities: Rostov-on-Don, Voronezh, Novosibirsk;

- to develop a model reflecting the dependence of the temperature of the start of condensation in the walls of aerated concrete blocks of grades D350-D600 on the characteristics of the materials used in the construction of the wall.

2. Methods

A large number of works are devoted to the study of the humidity regime of the operation of walls made of aerated concrete blocks. The probability of moisture condensation is usually determined using the Fokin-Vlasov graphoanalytical method [24]. In this method, the distribution of E_i and e_i the thickness of the enclosure at a certain temperature t_{out} is constructed. When using this method, the amount of condensing moisture in the wall is determined for the accepted design temperature of the outside air t_{out}. For the calculated outdoor temperature in various studies, they take: the average temperature the period of the year with negative average daily temperatures, the average monthly temperature for December, January or February, the average temperature of the coldest five-day period.

The studies conducted in this work are based on the technique proposed by V.N. Kupriyanov. In accordance with this technique, to assess the probability of moisture condensation in the external enclosure, the temperature of the onset of condensation t_{sk} was determined [25]. To determine it in the studied building envelope, the profiles of the partial pressure of water vapor e_i and the pressure of saturated water vapor E_i were constructed in Fig. 1.

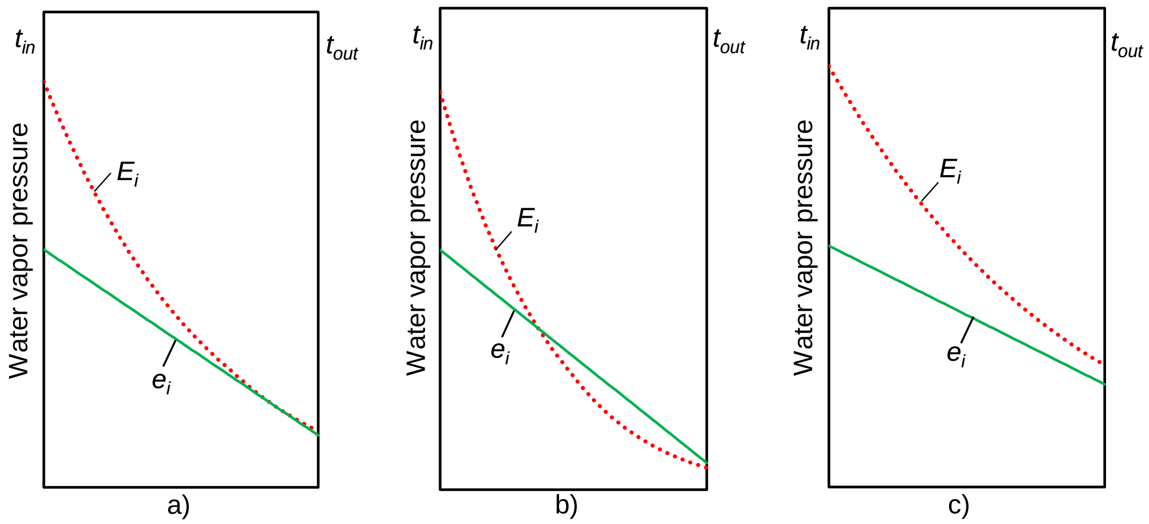

Figure 1. The determination method t_{sk}: a) $t_{out} = t_{sk}$; b) $t_{out} < t_{sk}$; c) $t_{out} > t_{sk}$.

The pressure of saturated water vapor E_i was determined by the temperature profile in accordance with the dependencies:

$$E_i = 610.5\exp\left(\frac{17.269 \cdot t_i}{237.3 + t_i}\right), t \geq 0\ °C; \quad (1)$$

$$E_i = 610.5\exp\left(\frac{21.875 \cdot t_i}{265.5 + t_i}\right), t \geq 0\ °C; \quad (2)$$

The temperature of the start of condensation t_{sk} was considered such an outdoor temperature at which the condition is satisfied:

$$e_i = E_i \quad (3)$$

For a mathematical explanation of the dependence of the temperature of the start of condensation t_{sk} on the characteristics of the outer finishing layer, we will use a generalized structural parameter k_{gdp} determined by the formula:

$$k_{gdp} = \frac{R_{Pi} / R_{Po}}{R_{Ti} / R_{To}} \quad (4)$$

where R_{Pi} is vapor resistance of layers located from the inner surface of the enclosure to the border of the plaster coating / aerated concrete, (m^2·h·Pa)/mg;

R_{Po} is vapor resistance of the whole enclosure, (m^2·h·Pa)/mg;

R_{To} is thermal conductivity of layers located from the inner surface of the enclosure to the border of the plaster coating / aerated concrete, (m^2· ºC)/W;

R_{Ti} is thermal conductivity of the entire enclosure, (m^2· ºC)/W.

In the work, the impact of the external finishing coating on t_{in} for the walls of buildings located in Rostov-on-Don, Voronezh, Novosibirsk is assessed.

The calculated parameters of the internal air are adopted according to Russian Set of Rules SP 50.13330.2012. Thermal protection of buildings. Updated edition of Russian Construction Norms and Rules SNiP 23-02-2003" for residential buildings: temperature t_{in}=20.0 °C relative humidity φ_{in}=55%.

The calculated parameters of the outdoor air are taken in accordance with the requirements of SP131.13330.2018 "SNiP 23-01-99* Construction climatology" (Table 1).

Table 1. Design parameters of outdoor air.

City	Heating period z_{hp}, day	Average temperature of the heating period, t_{hp} °C	Degree-day of the heating period °C·day	Humidity zone
Rostov-on-Don	166	-0.1	3336.6	Dry
Voronezh	190	-2.5	4275.0	Dry
Novosibirsk	222	-8.1	6238.2	Dry

The design of the wall under study is shown in Fig. 2.

For interior decoration of aerated concrete blocks, cement-slag plaster was used, layer thickness 0.01 m (Figure 1, layer 1). For exterior decoration of aerated concrete blocks, three types of DBM were used, layer thickness 0.01 m (Figure 1, layer 3): cement-sand plaster; Knauf GRUNBAND: developed by DBM. The thermal conductivity of the materials λ was determined on the samples 10×10×2.5 cm in size using an ITP-MG4 "100" device. Vapor permeability coefficient of materials μ was determined for each material according to Russian State Standard GOST 25898-2012. Building materials and products. Methods for determining vapor permeability and resistance to vapor permeability." Tests to determine the coefficients of vapor permeability and thermal conductivity were carried out for each material on 6 samples. The characteristics of the materials are presented in Table 2.

Characteristics of the materials are presented in Table 2.

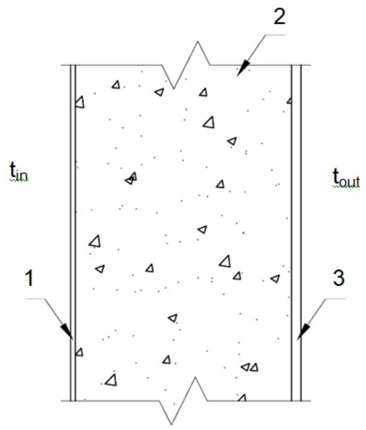

Figure 2. The design scheme of the wall envelope:
1 – layer 1, interior decoration; 2 – layer 2, aerated concrete; 3 – layer 3, exterior finish.

Table 2. Characteristics of the materials used in the wall.

Material	The average density of the material, kg/m^3	Coefficient of thermal conductivity λ_A, W/(m·K)	Vapor permeability coefficient μ, mg/(m·h·Pa)
cement slag plaster	1200	0.470	0.140
AAC D350	350	0.130	0.250
AAC D400	400	0.140	0.230
AAC D500	500	0.180	0.200
AAC D600	600	0.220	0.170
cement-sand plaster	1800	0.760	0.090
Knauf GRUNBAND	1100	0.350	0.100
being developed DBM	650	0.155	0.150

To simplify the work, the following conventions are used for the various designs of enclosing structures:

$$x / y / z \tag{5}$$

where x is first letter in city name (Rostov-on-Don – R; Voronezh – V; Novosibirsk – N);

y is aerated concrete density, kg/m^3;

z is the density of the outer finishing layer, kg/m^3.

3. Results and Discussion

Based on the climatic conditions of the cities of Rostov-on-Don, Voronezh and Novosibirsk, the minimum allowable wall thickness from aerated concrete grades D350, D400, D500, D600 was previously determined (Table 3).

Table 3. Aerated concrete layer thickness, m.

City	AAC brand			
	D350	D400	D500	D600
Rostov-on-Don	0.35	0.35	0.45	0.55
Voronezh	0.40	0.40	0.50	0.60
Novosibirsk	0.50	0.50	0.65	0.75

The choice of these cities is due to the fact that the parameters of the outdoor air in the cold season for these cities are characteristic of the widest list of climatic regions in which energy-efficient buildings using single-layer aerated concrete walls can be built.

The city of Rostov-on-Don is located in zone IIIB according to Russian Set of Rules SP 131.133300.2018. This climatic subarea is characterized by average monthly air temperature in January ranging from -5 °C to 2 °C. The results of studies to determine the temperature of the start of condensation in the walls for the city of Rostov-on-Don are presented in Figure 3.

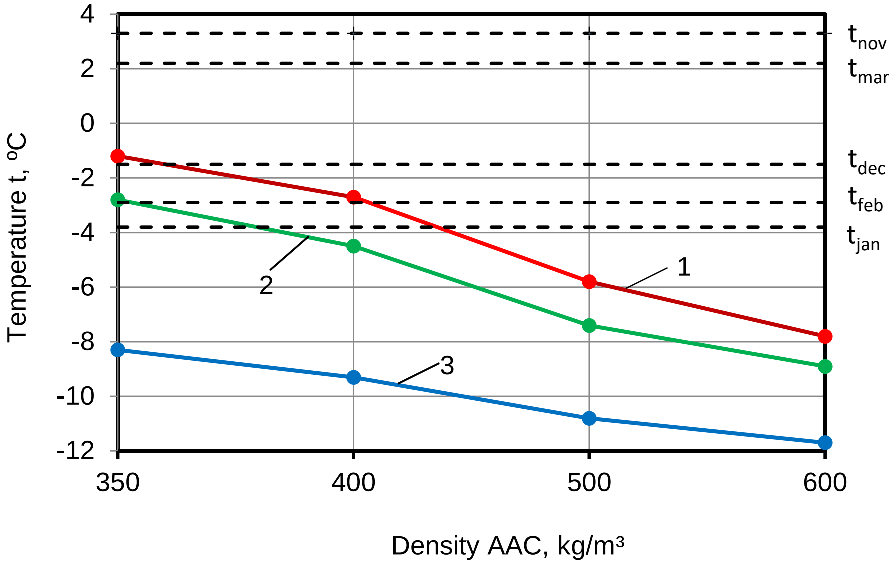

Figure 3. Dependence of the temperature of the start of condensation t_{sk} on the density of aerated concrete for the city of Rostov-on-Don: 1 – cement-sand plaster; 2 – Knauf GRUNBAND; 3 – developed by DBM.

It was found that moisture condensation in the R/350/1800 design begins at a temperature of –1.5 °C (Figure 3, curve 1). When using instead of cement-sand plaster DBM Knauf GRUNBAND, the temperature of the start of condensation t_{sk} decreases by only 1.4 °C (to –2.9 °C) (Figure 3, curve 2); when using the developed DBM, the temperature of the start of condensation t_{sk} decreases by 6.8 °C (to –8.3 °C) (Figure 3, curve 3).

With an increase in the density of aerated concrete, the start temperature of condensation t_{sk} decreases It should be noted that the temperature of the start of condensation t_{sk} in walls finished with cement-sand plaster or DBM Knauf GRUNBAND, to a much greater extent depends on the density of aerated concrete. Condensation start temperature t_{sk} in the enclosing structure R/350/1800 is 6.3 °C higher than the temperature of the beginning of condensation t_{sk} in the enclosing structure R/600/1800. Condensation start temperature t_{sk} in the enclosing structure R/350/650 is 3.3 °C higher than the temperature of the start of condensation t_{sk} in the enclosing structure R/600/650.

It was established that in the walls of aerated concrete blocks of grades D500 and D600, conditions for the formation of condensate will not be created. In the walls of aerated concrete blocks of grades D400, plastered with a cement-sand composition, condensate will precipitate at average monthly temperatures in January and February. In the walls of aerated concrete blocks of grades D350, plastered with a cement-sand composition, condensate will precipitate at average monthly temperatures in December, January and February. Condensation will form in the walls of aerated concrete blocks of D350 grades, plastered with DBM Knauf GRUNBAND, at average monthly temperatures in January and February. Thus, for the conditions of the city of Rostov-on-Don, the use of the developed DBM can significantly improve the humidity regime in the walls of aerated concrete blocks of grades D350 and D400.

The city of Voronezh is located in zone IIB according to Russian Set of Rules SP 131.133300.2018. This climatic subarea is characterized by average monthly air temperature in January, ranging from -14 °C to -4 °C. The results of studies to determine the temperature of the start of condensation in the walls for the city of Voronezh are presented in Figure 4.

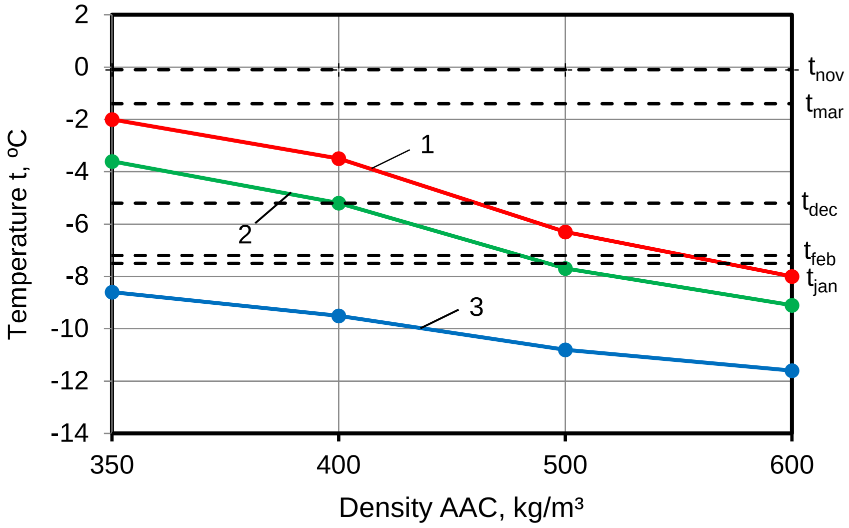

Figure 4. Dependence of the temperature of the start of condensation t_{sk} on the density of aerated concrete for the city of Voronezh: 1 – cement-sand plaster; 2 – Knauf GRUNBAND; 3 – developed by DBM.

It was established that in the walls of aerated concrete blocks of grades D350, D400, plastered with a cement-sand composition or DBM Knauf GRUNBAND, condensate will precipitate at average monthly temperatures in December, January and February (Figure 4, curve 1.2). In the walls of aerated concrete blocks of grades D500, plastered with a cement-sand composition, condensate will precipitate at average monthly temperatures in January and February. Thus, for the conditions of the city of Voronezh, the use of the developed DBM can significantly improve the humidity regime in the walls of aerated concrete blocks of grades D350, D400, D500.

The city of Novosibirsk is located in zone IB according to Russian Set of Rules SP 131.133300.2018. The air temperature in January ranges from -14 °C to -28 °C. The results of studies to determine the temperature of the start of condensation in the city of Novosibirsk are presented in Figure 5.

It was established that in the walls of aerated concrete blocks, regardless of the type of plaster coating used, condensation will occur at average monthly temperatures in December, January and February. At the same time, in the walls of aerated concrete blocks of grades D350, D400 and D500, plastered with a cement-sand composition or DBM Knauf GRUNBAND, conditions will also be created for the formation of condensate at average monthly temperatures in March and November (Figure 5, curve 1.2). When using the developed DBM, the conditions for the formation of condensate in November and March will not be created (Figure 5, curve 3).

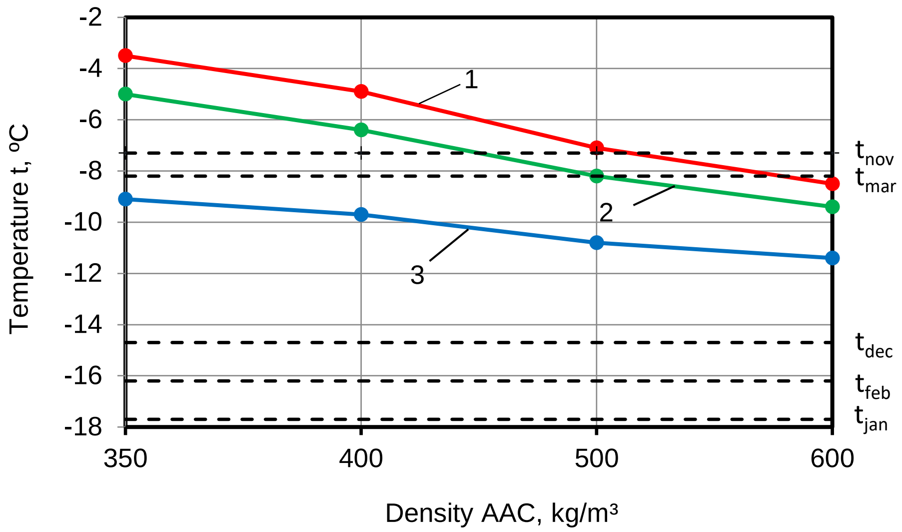

Figure 5. Dependence of the temperature of the start of condensation t_{sk} on the density of aerated concrete for the city of Novosibirsk: 1 – cement-sand plaster; 2 – Knauf GRUNBAND; 3 – developed by DBM.

The dependence of the condensation start temperature t_{sk} on the generalized design parameter k_{gdp} was studied for the studied enclosures made of aerated concrete blocks finished with a cement-sand composition (Figure 6).

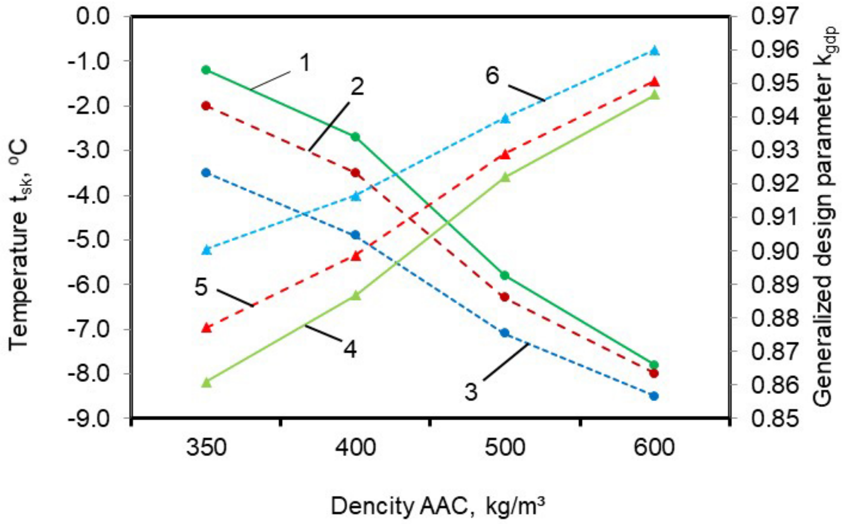

Figure 6. Dependence of the temperature of the start of condensation t_{sk} and generalized design parameter k_{gdp} on the density of AAC for walls, plastered developed by cement-sand plaster: 1 – Rostov-on-Don (t_{sk}); 2 – Voronezh (t_{sk}); 3 – Novosibirsk (t_{sk}); 4 – Rostov-on-Don (k_{gdp}); 5 – Voronezh (k_{gdp}); 6 – Novosibirsk (k_{gdp}).

The walling R/350/1800 is characterized by the lowest value of the generalized design parameter k_{gdp} = 0.861 (Figure 6, curve 4). Accordingly, this enclosure is characterized by the highest temperature at the start of condensation t_{sk} = -1.2 °C (Figure 6, curve 1). The condensation start temperature t_{sk} for enclosures V/350/1800 and N/350/1800, respectively, is -2.0 °C and - 3.5 °C (Figure 6, curve 2, 3). Smaller t_{sk} values for walls V/350/1800 and N/350/1800 are explained by large k_{gdp} values for these enclosures, equal to 0.877 and 0.901, respectively (Figure 6, curve 5,6). The same materials were used in the construction of the walls R/350/1800, V/350/1800, N/350/1800 and the different k_{gdp} values are explained by different wall thicknesses and, as a result, different fractions of the thickness of the external plaster coating from the total wall thickness. In the enclosure R/350/1800, the proportion of the thickness of the cement-sand plaster in the total wall thickness is 5.26 %, in the enclosure V/350/1800 – 4.65 %, in the enclosure N/350/1800 – 3.77 %.

The walling N/600/1800 is characterized by the highest value of the generalized design parameter k_{gdp} = 0.960 (Figure 6, curve 6). Correspondingly, this enclosure is characterized by the lowest condensation start temperature t_{sk} = -8.5 °C (Figure 6, curve 3). The condensation start temperature t_{sk} for the walling N/600/1800 is 7.3 °C lower than the condensation start temperature t_{sk} for the R/350/1800 fencing, the value of the generalized design parameter is higher by k_{gdp} 0.099. This is due to the fact that the difference in the values of thermal conductivity and vapor permeability coefficients between D600 aerated concrete blocks and cement-sand plaster is less significant compared to the difference in the thermal conductivity and vapor permeability coefficients between a D350 aerated concrete blocks and cement-sand plaster. The μ/λ ratio for aerated concrete blocks of the D350 grade is 1.92, for aerated concrete blocks of the D600 grade – 0.77, for cement-sand plaster – 0.12. This is also explained by the fact that in the wall N/600/1800 the proportion of the thickness of the cement-sand plaster in the total wall thickness is only 2.56 %. For the same reasons, the start temperature of condensation t_{sk} for enclosures made of aerated concrete blocks of grades D600 is less dependent on the city where the building is located compared to enclosures made of aerated concrete blocks of grades D350.

The dependence of the condensation start temperature t_{sk} on the generalized design parameter k_{gdp} for the studied enclosures from aerated concrete blocks trimmed with Knauf GRUNBAND DBM was investigated (Figure 7).

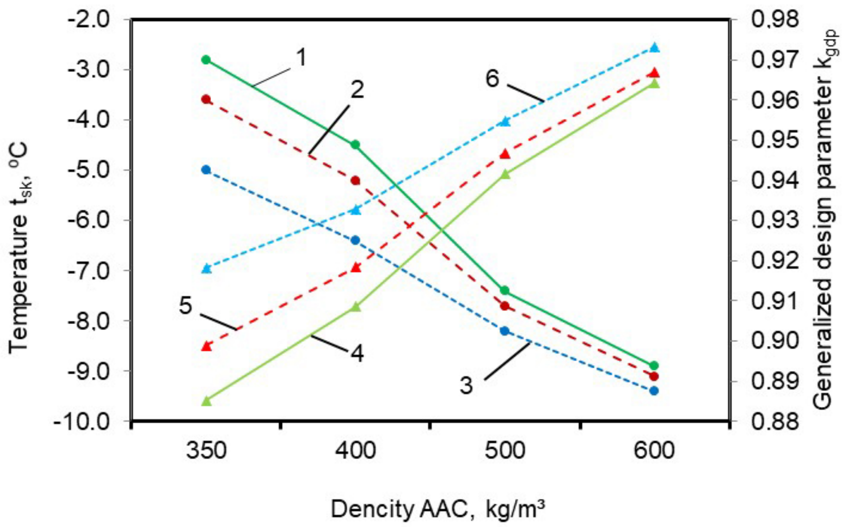

Figure 7. Dependence of the temperature of the start of condensation t_{sk} and generalized design parameter k_{gdp} on the density of AAC for walls, plastered developed by Knauf GRUNBAND: 1 – Rostov-on-Don (t_{sk}); 2 – Voronezh (t_{sk}); 3 – Novosibirsk (t_{sk}); 4 – Rostov-on-Don (k_{gdp}); 5 – Voronezh (k_{gdp}); 6 – Novosibirsk (k_{gdp}).

The main dependences typical for walls finished with cement-sand plaster were confirmed for walls decorated with DBM Knauf GRUNBAND. The maximum temperature at which condensation began was obtained for the R/350/1100 enclosure and amounted to -2.8 °C (Figure 7, curve 1), which is 1.6 lower than tsk for the R/350/1800 enclosure. The minimum temperature for the start of condensation was obtained for the N/600/1100 enclosure and amounted to -9.6 °C (Figure 7, curve 1), which is 1.1 °C lower than t_{sk} for the N/600/1800 enclosure. The values of the generalized design parameter for the enclosures trimmed by Knauf GRUNBAND DBM vary in the range k_{gdp}=0.885–0.973. The results are explained by higher vapor permeability and lower thermal conductivity of coatings based on Knauf GRUNBAND DBM in comparison with cement-sand plaster.

The dependence of the condensation onset temperature t_{sk} on the generalized design parameter k_{gdp} for the enclosures from aerated concrete blocks trimmed by the developed DBM was studied (Figure 8).

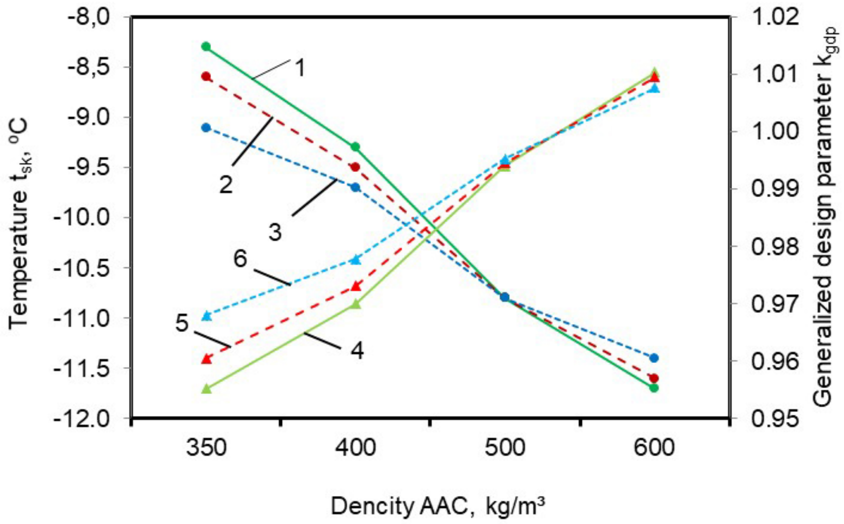

Figure 8. Dependence of the temperature of the start of condensation t_{sk} and generalized design parameter k_{gdp} on the density of AAC for walls, plastered developed by DBM: 1 – Rostov-on-Don (t_{sk}); 2 – Voronezh (t_{sk}); 3 – Novosibirsk (t_{sk}); 4 – Rostov-on-Don (k_{gdp}); 5 – Voronezh (k_{gdp}); 6 – Novosibirsk (k_{gdp}).

When using the developed DBM, the temperature of the start of condensation t_{sk} varies from -8.3 °C to -11.6 °C. A significant decrease in t_{sk} compared to enclosures finished with cement-sand plaster and DBM Knauf GRUNBAND is explained by an increase in the values of the generalized design parameter k_{gdp}, which varies in the range of 0.955–1.010. The t_{sk} values of the enclosures R/500/650, V/500/650 and N/500/650 are very close, which is explained by the close k_{gdp} values for these enclosures.

It has been established that the use of the developed DBM for enclosures R/500/650, V/500/650 and N/500/650 allows to lower the temperature of the start of condensation t_{sk} to values lower than would be without using the developed finishing coating. This conclusion can be made on the basis that the k_{gdp} values for these enclosures are higher than 1.

To develop a mathematical model that reflects the dependence of t_{sk} on the characteristics of the materials used in the construction of the wall, we construct the dependence of t_{sk} on k_{gdp} for 36 enclosures considered in the work (Figure 9).

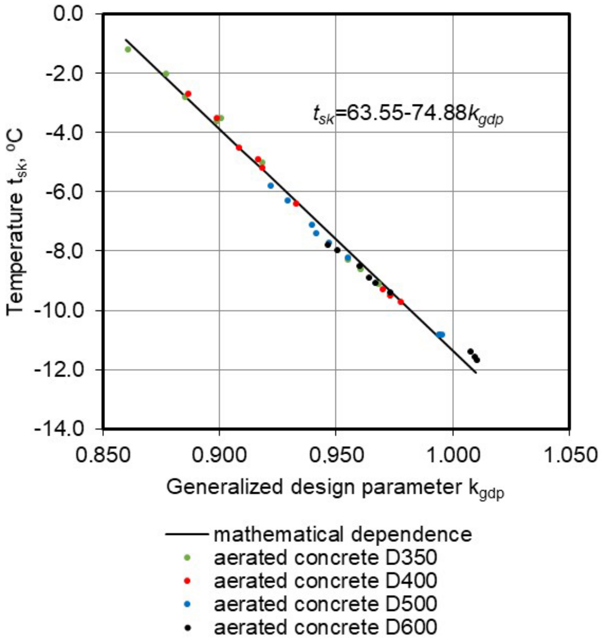

Figure 9. The dependence of the temperature of start of condensation t_{sk} from the generalized design parameter k_{gdp}.

As a result of the analysis of Figure 9, the following linear dependence of the start temperature of condensation t_{sk} on the generalized structural parameter of the fencing k_{gdp} was obtained:

$$t_{sk} = 63.55 - 74.88k_{gdp} \quad (6)$$

Analyzing equation 6, we can conclude that it allows to characterize the studied building envelopes with a fairly high accuracy. It should be noted that a quadratic dependence was obtained in paper of Kupriyanov V.N. [26]. The dependence obtained in this work makes it possible to more accurately determine t_{sk}. The deviations of the t_{sk} values calculated by the formula from the t_{sk} values determined during the research ranged from 0.00 to 0.49 °C. The deviation of the values calculated by the formula proposed by Kupriyanov V.N. from those obtained during the research is 0.3–5.The results obtained are in good agreement with other studies on this topic [27].

4. Conclusions

1. It was revealed that due to the use of the developed DBM for finishing concrete blocks of D350-D600 grades, moisture condensation begins at a significantly lower outdoor temperature. The condensation onset temperature t_{sk} for walls made of aerated concrete blocks finished with developed DBM varies from -8.3 °C to -11.7 °C, finished with Knauf GRUNBAND DBM from -2.8 °C to -9.4 °C, finished with cement-sand plaster from -1.2 °C to -8.5 °C.

2. Based on the studies, it was found that for cities located in climatic zones with an average monthly temperature of the coldest month above minus 14 °C, it is possible to use effective single-layer walls made of aerated concrete blocks of grades D350-600. When using DBM, allowing to obtain coatings characterized by values of thermal conductivity and vapor permeability close to aerated concrete blocks D350-600, in these walls conditions will not be created for the loss of a large amount of condensate. When erecting single-layer enclosing structures from aerated concrete blocks of D350-600 grades in the walls, conditions will be created for a large amount of condensate to fall out for the climatic conditions of cities located in areas with an average monthly temperature of the coldest month below minus 14 °C.

3. A linear dependence is obtained that reflects the relationship between the temperature of the start of condensation t_{sk} in the walls of aerated concrete blocks of grades D350-D600 on the generalized structural parameter of the fencing k_{gdp}. On the basis of the developed model, it is possible to rather easily and quickly evaluate the effect of the characteristics of the external finishing coating on the humidity conditions in the walls of aerated concrete blocks.

References

1. Choi, Y. hee, Song, D., Seo, D., Kim, J. Analysis of the variable heat exchange efficiency of heat recovery ventilators and the associated heating energy demand. Energy and Buildings. 2018. 172. Pp. 152–158. DOI: 10.1016/j.enbuild.2018.04.066.
2. Harmati, N., Jakšić, Ž., Vatin, N. Energy consumption modelling via heat balance method for energy performance of a building. Procedia Engineering. 2015. 1(117). Pp. 791–799.
3. Blengini, G.A., Di Carlo, T. Energy-saving policies and low-energy residential buildings: An LCA case study to support decision makers in piedmont (Italy). International Journal of Life Cycle Assessment. 2010. 15 (7). Pp. 652-665.
4. Taylor, T., Counsell, J., Gill, S. Energy efficiency is more than skin deep: Improving construction quality control in new-build housing using thermography. Energy and Buildings. 2013. No. 66. Pp. 222-231
5. Kovacic, I., Waltenbereger, L., Gourlis, G. Tool for life cycle analysis of facade-systems for industrial buildings. Journal of Cleaner Production. 2016. Vol. 130. Pp. 260–272. DOI: 10.1016/j.jclepro.2015.10.063.
6. Petritchenko, M.R., Nemova, D.V., Kotov, E.V., Tarasova, D.S, Sergeev, V.V. Ventilated facade integrated with the HVAC system for cold climate. Magazine of Civil Engineering. 2018. No. 1. Pp. 47–58. DOI: 10.18720/MCE.77.5.
7. Ananin, M., Perfilyeva, N., Vedishcheva, I., Vatin, N. Investigation of different materials usage expediency for a low-rise public building from the energy efficiency standpoint. IOP Conf. Series: Materials Science and Engineering. 2018. No. 365
8. D'Alessandro, F., Baldinelli, G., Bianchi, F., Sambuco, S., Rufini, A. Experimental assessment of the water content influence on thermo–acoustic performance of building insulation materials. Construction and Building Materials. 2018. No. 158. Pp. 264–274. DOI: 10.1016/j.conbuildmat.2017.10.028
9. Tasdemir, C., Sengul, O., Tasdemir, M.A. A comparative study on the thermal conductivities and mechanical properties of lightweight concretes. Energy and Buildings. 2017. Vol. 151. Pp. 469–475. DOI:10.1016/j.enbuild.2017.07.013
10. Qu, X., Zhao, X. Previous and present investigations on the components, microstructure and main properties of autoclaved aerated concrete – A review. Construction and Building Materials. 2017. Vol. 135 Pp. 505–516. DOI:10.1016/j.conbuildmat.2016.12.208
11. Vatin, N.I., Gorshkov, A.S., Korniyenko, S.V., Pestryakov, I.I. Potrebitelskiye svoystva stenovykh izdeliy iz avtoklavnogo gazobetona [The consumer properties of wall products from AAC]. Stroitelstvo unikalnykh zdaniy i sooruzheniy. 2016. No. 1. Pp. 78–101. (rus)
12. Narayanan, N., Ramamurthy, K. Structure and properties of aerated concrete: A review. Cement and Concrete Composites. 2000. 22 (5). Pp. 321–329.
13. Kočí, V., Maděra, J., Černỳ, R. Exterior thermal insulation systems for AAC building envelopes: Computational analysis aimed at increasing service life. Energy and Buildings. 2012. No. 47. Pp. 84–90.
14. Pastushkov, P.P., Grinfel'd, G.I., Pavlenko, N.V., Bespalov, A.E., Korkina, E.V. Raschetnoe opredelenie ekspluatacionnoj vlazhnosti avtoklavnogo gazobetona v razlichnyh klimaticheskih zonah stroitel'stva [Estimated determination of operational humidity of autoclaved aerated concrete in various climatic zones of construction]. 2015. No 2. Pp. 60–69. (rus)
15. Koudelka, T., Kruis, J., Maděra, J. Coupled shrinkage and damage analysis of autoclaved aerated concrete. Applied Mathematics and Computation. 2015. No. 267. Pp. 427–435. DOI: 10.1016/j.amc.2015.02.016
16. Nizovtsev, M.I., Stankus, S.V., Sterlyagov, A.N., Terekhov, V.I., Khairulin, R.A. Determination of moisture diffusivity in porous materials using gammamethod. International Journal of Heat and Mass Transfer. 2008. No. 51. Pp. 4161–4167
17. Yao, X.L., Yi, S.Y., Fan, L.W., Xu, X., Yu, Z.T., Ge, J. Effective thermal conductivity of moist aerated concrete with different porosities. Zhejiang Daxue Xuebao (Gongxue Ban). Journal of Zhejiang University (Engineering Science). 2015. 49(6). Pp. 1101–1107. DOI: 10.3785/j.issn.1008-973X.2015.06.014.
18. Rubene, S., Vilnitis, M., Noviks, J. Frequency Analysis and Measurements of Moisture Content of AAC Masonry Constructions by EIS. Procedia Engineering. 2015. No. 123. Pp. 471–478. DOI: 10.1016/j.proeng.2015.10.096
19. Loganina, V.I., Frolov, M.V. Research of Cracking Resistance of Thermal Insulation Coatings for Aerated Concrete. Materials Science Forum. 2019. No 974. Pp. 458-463. DOI:10.4028/www.scientific.net/MSF.974.458.
20. Loganina, V.I., Frolov, M.V. Heat-insulating Finishing Composition of the Optimal Structure with Microspheres. IOP Conf. Series: Materials Science and Engineering. 2019. 471(3). DOI:10.1088/1757-899X/471/3/032010
21. Loganina, V., Frolov, M., Fediuk, R. Developed Heat-insulating Dry Mortar Mixes for the Finishing of Aerated Concrete Walls. Magazine of Concrete Research. February 18. 2020. Pp. 1-45. DOI:10.1680/jmacr.19.00446
22. Loganina, V.I., Kislitsyna, S.N., Frolov, M.V. Addition on the Basis of Mix of the Synthesized Hydrosilicates of Calcium and Aluminosilikates for Dry Building Mixtures. 2016. Procedia Engineering. 150. Pp. 1627–1630. DOI: 10.1016/j.proeng.2016.07.141
23. Loganina, V.I., Frolov, M.V., Skachkov, Yu. P. Substantiation of selection of components at creation of thermal insulating dry building mixtures. International Journal of Engineering and Technology. 2018 Vol. 7. No. 4. Pp. 4341-4344. DOI: 10.14419/ijet.v7i4.10393

24. Korniyenko, S.V. O primenimosti metodiki SP 50.13330.2012 K raschetu vlazhnostnogo rezhima ograzhdayushchikh konstruktsiy s multizonalnoy kondensatsiyey vlagi [On the applicability of the methodology of SP 50.13330.2012 to the calculation of the humidity regime of building envelopes with multizone moisture condensation]. Stroitelstvo i rekonstruktsiya. 2014. 2(55). Pp. 29–37. (rus)
25. Petrov, A.S., Kupriyanov, V.N. Determination of Humidity Conditions of Enclosing Structures by the Color Indicator Method. IOP Conference Series: Materials Science and Engineering, December 2018. Vol. 463, Iss. 2. DOI: 10.1088/1757-899X/463/2/022064
26. Petrov, A.S., Kupriyanov, V.N. About operational factor influence on vapor permeability of heat-insulating materials. International Journal of Pharmacy and Technology. 2016. Vol 8, Iss. 1. Pp. 11248-11256.
27. Vatin, V.I., Gorshkov, A.S., Glumov, A.V. Vliyaniye fiziko-tekhnicheskikh i geometricheskikh kharakteristik shtukaturnykh pokrytiy na vlazhnostnyy rezhim odnorodnykh sten iz gazobetonnykh blokov [The influence of physical, technical and geometric characteristics of stucco coatings on the humidity conditions of homogeneous walls of aerated concrete blocks]. Magazine of Civil Engineering. 2011. 1(19). Pp. 28–33. (rus)

Contacts:

Valentina Loganina, loganin@mail.ru
Mikhail Frolov, mihail-frolovv@yandex.ru

Magazine of Civil Engineering

ISSN 2712-8172

journal homepage: http://engstroy.spbstu.ru/

DOI: 10.34910/MCE.109.8

Influence of cement type and chemical admixtures on the durability of recycled concrete aggregates

***Z. Tahar*[a], *E. Kadri*[a], *B. Benabed*[b]*, *T.T. Ngo*[a],**

[a] *CY Cergy Paris University, L2MGC Laboratory, Cergy, France*

[b] *Civil Engineering Research Laboratory (LRGC), Amar Telidji University, Laghouat, Algeria*

**E-mail: b.benchaa@lagh-univ.dz*

Keywords: recycled concrete aggregates (RCA), density, porosity, chloride ions diffusion, durability

Abstract. This study investigates the effect of replacement of natural aggregates with recycled concrete aggregates on the durability of concrete. Three different combinations of cement and chemical admixtures were considered, and the produced mixtures were assessed for their durability performance. The obtained results show a significant increase in the porosity of the mixtures with increasing in the percentage of recycled sand substitution, whereas the porosity increase was less pronounced for the natural gravel substitution. In addition, increasing the percentage substitution of recycled aggregates results in a decrease in density. However, this decrease is more pronounced in the case of substitution with recycled sand than for recycled gravel. Finally, the diffusion depth of the chloride ions increases with the increase of recycled gravel, regardless of the cement/admixture couple. This rise is less pronounced than in the case of concrete made with recycled sand.

1. Introduction

The demand for natural aggregates is quite high in developing countries due to the rapid progress of building infrastructure, and this leads to shortages of resources; this is why the construction field in developing countries is trying to find alternative materials to replace the demand for natural aggregates. Aggregates occupy 60 to 80 % of concrete's volume and play a significant role in the evolution of its properties. Most natural occurring rocks can be used as concrete aggregates as long as they comply the national and international specification standards. Raw materials for the production of natural aggregates (NA) and for those of recycled aggregates (RA) contribute to differences and variations in their overall properties [1, 2]. In fact, igneous, metamorphic or sedimentary rocks used in the production of NA are relatively homogeneous, unlike concrete wastes, which often have a heterogeneous composition. Typically, NA that come from igneous, metamorphic or sedimentary rocks are relatively homogenous and quite robust [1]. On the contrary, RA are in large characterized by a high degree of heterogeneity [2]. Concerning the use of RA from concrete waste in the manufacture of new mixtures, it appears that the replacement of coarse NA with coarse RA has an effect on the durability of the new concrete. However, the effect of the use of fine RA is still a matter of debate. The primary criticism by some for the use of fine RA in concrete manufacture is their high water absorption, which can lead to concretes with poor performance. Nevertheless, published data suggest that, the use of fine RA can be reliable at certain substitution percentages, with a saturation point beyond which further replacement with fine RA leads to reduction in both durability and mechanical performance of concretes [3–5]. This reduction in performance is due to the following factors: (i) the lower mechanical strength of RA; (ii) the high-water absorption of RA; (iii) the compromise of the interfacial transition zone (ITZ) in concrete. Poon et al [6] have studied the microstructure

Tahar, Z., Kadri, E., Benabed, B., Ngo, T.T. Influence of cement type and chemical admixtures on the durability of recycled concrete aggregates. Magazine of Civil Engineering. 2022. 109(1). Article No. 10908. DOI: 10.34910/MCE.109.8

of concretes made from recycled concrete and high performance concrete aggregates by the means of a scanning electron microscope (SEM). They found that the ITZ around RA was characterized by higher porosity. This can be problematic in terms of performance, as high porosity in the ITZ will lead in to two undesirable phenomena: the reduction in the ITZ strength (and hence of the composite in general) and in the increase of the permeability. The adhered cementitious matrix on the RA increases its overall apparent porosity, thereby increasing its specific surface area [7–9]. It is apparent that the properties of the cement paste that envelopes RA have a strong effect on the physic and mechanical properties of the RA [10, 11]. Nevertheless, early studies by Nagataki et al [12] showed that a critical aspect is the decontamination of RA from other construction waste and if this is done properly, the RA can be suitable alternative to coarse NA. Previous studies [13–16] have shown that the density of these RA is lower or that their absorption capacity is higher; this varies from 3 to 12 % whatever the size of the RA whereas the absorption of the natural aggregates is approximately 0.5 to 1 %. Moreover, their mechanical properties are known to be inferior to those of NA [10]. Barbudo et al [17] evaluated the influence of superplasticizers (SP) on the behavior of concrete utilizing fine RA. However, the authors found that SP had a greater influence on the behavior of NA-based concretes than on concretes based on fine RA. The loss of effectiveness of the admixtures was justified by the incorporation of the RA, which then caused an increase in the specific surface area of the aggregates. In addition, a parallel research on the influence of SP in concretes based on coarse RA was carried out by Pereira et al [18], which yielding similar observations.

In this context, the present work will study the effect of replacement of natural aggregates with recycled concrete aggregates on the durability of concrete. Three types of cement and chemical admixtures are used. The tests used to evaluate the durability are porosity and the diffusion of chloride ions in the concrete.

2. *Experimental program*

2.1. *Materials and testing methods*

2.1.1. Aggregates

RCA varies according to the origin of the concrete that is to say according to the basic formulation of the concrete called previous concrete in the literature [16]. Table 1 shows the water absorption coefficients of natural and recycled sand (NS, RS), natural and recycled gravel (NG, RG) measured according to NF EN-1097-6 [19]. The absorption coefficient of the RA are significantly higher than that of the NA. This is the most important parameter that differentiates RA from NA.

Table 1. Water absorption and density of aggregates used.

Type of aggregate	Water absorption (%)	Density (%)
NS (0/4 mm)	0.9	2.59
RS (0/4 mm)	10.0	2.71
NG (4/10 mm)	0.5	2.71
RG (4/10 mm)	5.1	2.17
NG (10/20 mm)	0.4	2.31
RG (10/20 mm)	5.7	2.29

a. Sand

The results of the morphological and chemical analysis of sand are shown in Fig. 1. Fig. 1a shows that NS has an angular shape. Fig. 1b shows the morphology of RS as an accumulation of grains of NS of angular shape, which are interconnected by cement paste and contains many pores.

The chemical analysis of NS reveals that the main peaks of its composition are calcium and silicon. It is then a silico-calcareous sand. The chemical analysis of RS reveals that the main peaks are calcium, silicon, iron, magnesium and aluminum; these latter compounds can be considered as originating from the cement paste attached to the sand grains.

b. Gravel

The results of morphological and chemical analysis of gravel are presented in Fig. 2. The NG has an angular shape (Fig. 2a). RG is the accumulation of NG grains of angular shape connected to each other by a small amount of cement paste with the presence of pores in this paste (Fig. 2b).

The elemental analysis spectrum obtained for NG shows that the main peaks represent its composition are calcium and silicon; it is a siliceous gravel. The spectrum obtained for RG reveals that the main peaks are of calcium, magnesium and aluminum. These latter compounds can be considered as being derived from the cement paste attached to the gravel grains.

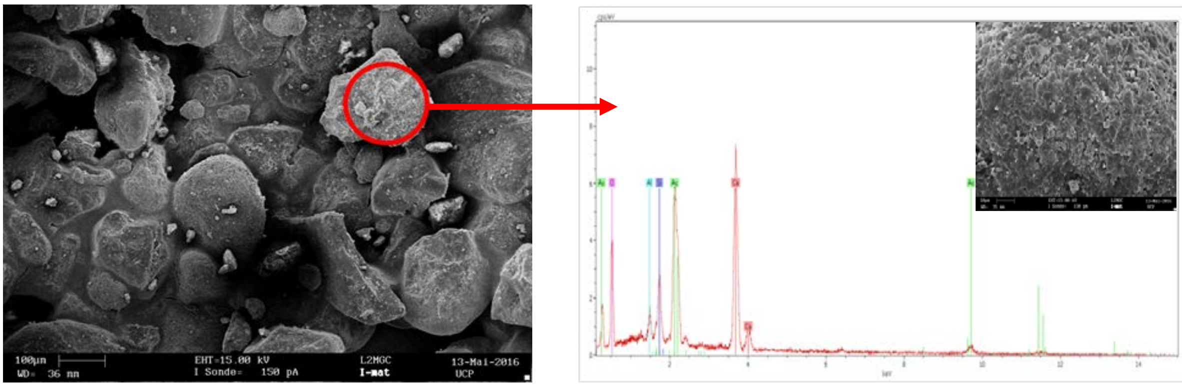

(a)

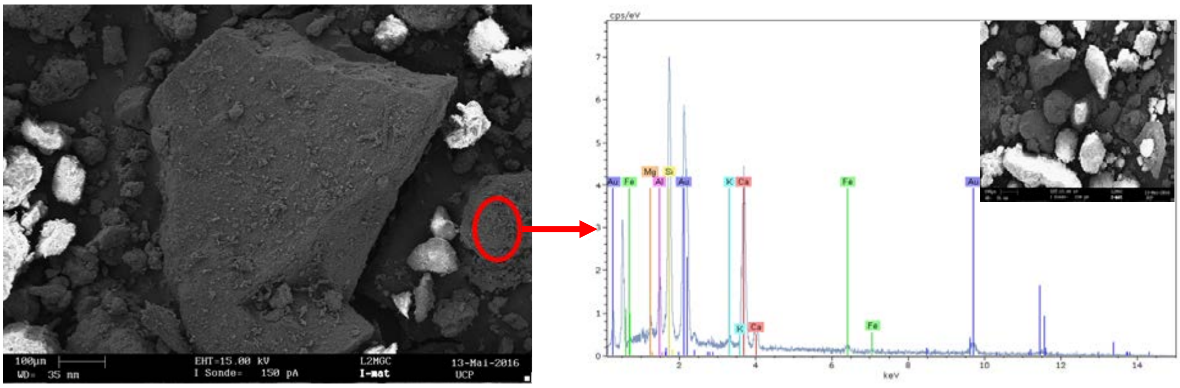

(b)

Figure 1. SEM of sand used: (a) NS, (b) RS.

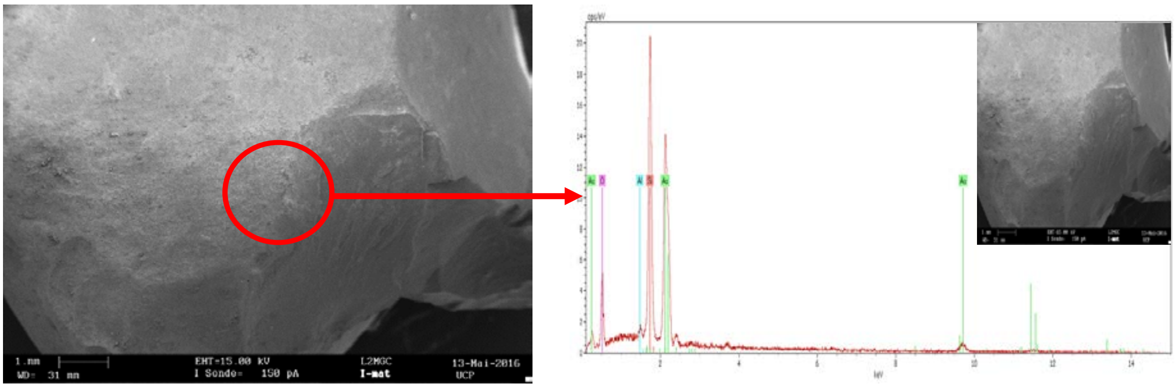

(a)

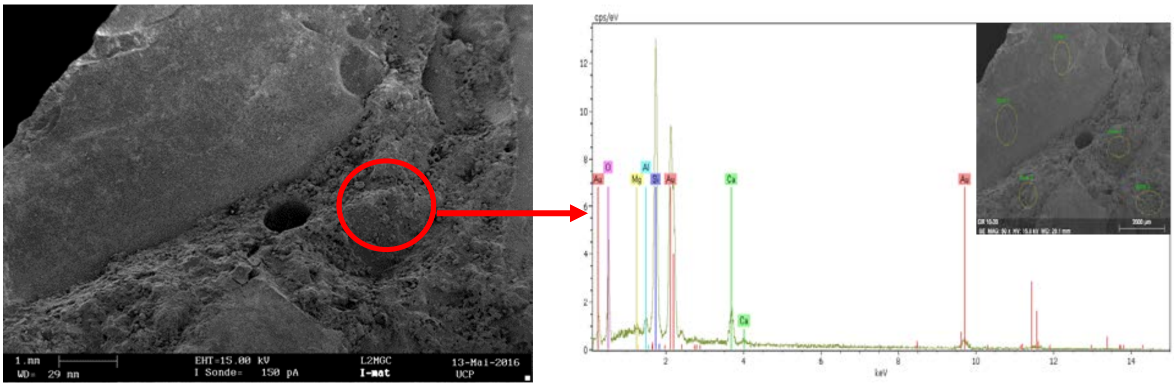

(b)

Figure 2. SEM of gravel used: (a) NG, (b) RG.

2.1.2. Cement

Three types of cement are used in this investigation. The chemical analysis and physical properties of cements used are presented in Table 2.

Table 2. Chemical analysis and physical properties of cements used.

Cement	C1	C2	C3
Physical properties			
Finesse Blaine (cm^2/g)	4520	3250	4110
Median diameter (µm)	9.7	16.5	12.3
Water demand (%)	27.2	26.0	26.5
Initial setting time (min)	120	165	140
Hydration heat at 41h (j/g)	328	300	320
Chemical analysis (%)			
S_iO_2	19.54	20.19	20.1
Al_2O_3	5.70	3.81	5.5
Fe_2O_3	3.06	2.99	4.8
CaO	60.10	61.50	59.70
SO_3	3.71	3.31	2.31
MgO	1.85	1.96	3.26
K_2O	0.86	0.81	1.81
Na_2O	0.19	0.17	0.22
Cl^-	0.07	0.02	0.06
Loss on ignition	0.33	0.68	0.78

2.1.3. Chemical admixtures

Three admixtures are used in this study; the properties of these admixtures are given in Table 3.

Table 1. Properties of chemical admixtures used.

Admixtures	A1	A2	A3
Chemical Type	Polycarboxylate	Ether polycarboxylique	Polycarboxylate
Type	High water reducing	Water reducing	Water reducing
Solids content (%)	22.5	22.5	20
Form	liquid	liquid	liquid
Color	light yellow	light brown	light yellow
pH	4 – 6	6 – 8	4.5 ± 1.0
Recommended Dosage (%)	0.1 – 3.0	0.2 – 1.9	0.1 – 3.0
Content Na2O (%)	≤ 1	≤ 1	≤ 0.5
Content ions Cl- (%)	≤ 0.1%	≤ 0.1	≤ 0.1

2.2. Testing methods

The mix proportions of different concrete mixtures made with NA and RA are given in Table 4.

The apparent density (ρ_d) and the porosity accessible to water (ε) were determined at the age of 28 days according the standard NF-EN 1097-6 [19].

The diffusion of chloride ions test was determined at the age of 28 days according to the standard (ASTM C 1202-97) [20].

Table 2. Mix proportion of different concretes made with NA and RA.

Group/C	Mixture	C	NS	RS	NG (4/10)	NG (10/20)	RG (4/10)	RG (10/20)	SP (%)	Water (kg/m^3)	W/C
		(kg/m^3)									
A/C1	0RS0RG	320	852	0	325	696	0	0	0.40	188	0.59
	15RS0RG		724	105					0.40	196	0.61
	30RS0RG		596	211					0.40	206	0.64
	50RS0RG		426	350					0.40	218	0.68
	70RS0RG		256	492					0.40	231	0.72
	100RS0RG		0	702					0.30	250	0.78
	0RS0RG		852	0	325	696	0	0	0.40	188	0.59
	0RS15RG				276	592	42	87	0.40	193	0.60
	0RS30RG				228	487	84	173	0.58	200	0.63
	0RS50RG				163	348	140	288	0.65	205	0.64
	0RS70RG				98	209	195	404	0.78	217	0.68
	0RS100RG				0	0	279	578	0.78	200	0.63
B/C2	0RS0RG	320	852	0	325	696	0	0	0.20	176	0.55
	15RS0RG		724	105					0.40	185	0.58
	30RS0RG		596	211					0.40	195	0.61
	50RS0RG		426	350					0.40	205	0.64
	70RS0RG		256	492					0.40	220	0.69
	100RS0RG		0	702					0.40	238	0.74
	0RS0RG		852	0	325	696	0	0	0.20	176	0.55
	0RS15RG				276	592	42	87	0.67	182	0.57
	0RS30RG				228	487	84	173	0.51	189	0.59
	0RS50RG				163	348	140	288	0.50	200	0.63
	0RS70RG				98	209	195	404	0.48	206	0.64
	0RS100RG				0	0	279	578	0.42	218	0.68
C/C3	0RS0RG	320	852	0	325	696	0	0	0.30	180	0.56
	15RS0RG		724	105					0.40	195	0.61
	30RS0RG		596	211					0.40	203	0.63
	50RS0RG		426	350					0.40	215	0.67
	70RS0RG		256	492					0.40	230	0.72
	100RS0RG		0	702					0.40	245	0.77
	0RS0RG		852	0	325	696	0	0	0.30	180	0.56
	0RS15RG				276	592	42	87	0.50	188	0.59
	0RS30RG				228	487	84	173	0.50	190	0.59
	0RS50RG				163	348	140	288	0.45	200	0.63
	0RS70RG				98	209	195	404	0.45	220	0.69
	0RS100RG				0	0	279	578	0.42	228	0.71

C: cement; NS: natural sand; RS: recycled sand; NG: natural gravel; RG: recycled gravel; SP: superplasticizer

3. Results and Discussion

3.1. Evolution of density and porosity accessible to water

The evolution of the porosity (ε) and the density (ρ_d) measured at 28 days are presented in Fig. 3 and 4 respectively. Fig. 3a shows that the 28-day porosity of concrete made with RS increases remarkably, when the substitution percentage of RS increases, regardless of the type of cement and chemical admixtures that are being tested. It reaches a 50 % increase for a 100 % substitution percentage of RS compared to NS. Fig. 3b shows a less marked increase when the substitution concerns NG by RG, regardless of the type of cement and admixtures tested. Indeed, the more the percentage of RG increases and the more the porosity of the concrete increases; this tendency to increase remains nevertheless reasonable (it is about + 20 % whatever the couple). Moreover, for the two series of concrete (RS and RG), the distinction of the results as a function of the type of cement and admixtures is not obvious.

Fig. 4 shows that increasing the percentage substitution of RA results in a decrease in density; however, this decrease is more pronounced in the case of substitution with RS (Fig. 4a) than for RG (Fig. 4b). This result also confirms the evolution of the porosity of the concretes, namely that the more the concrete is porous, the more the density decreases.

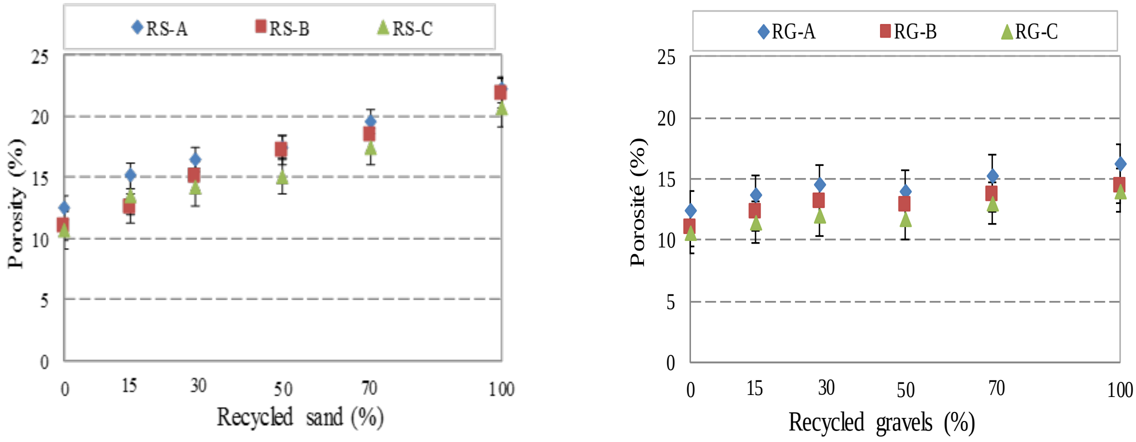

(a) (b)

Figure 3. Evolution of porosity of RCA: (a) RS; (b) RG.

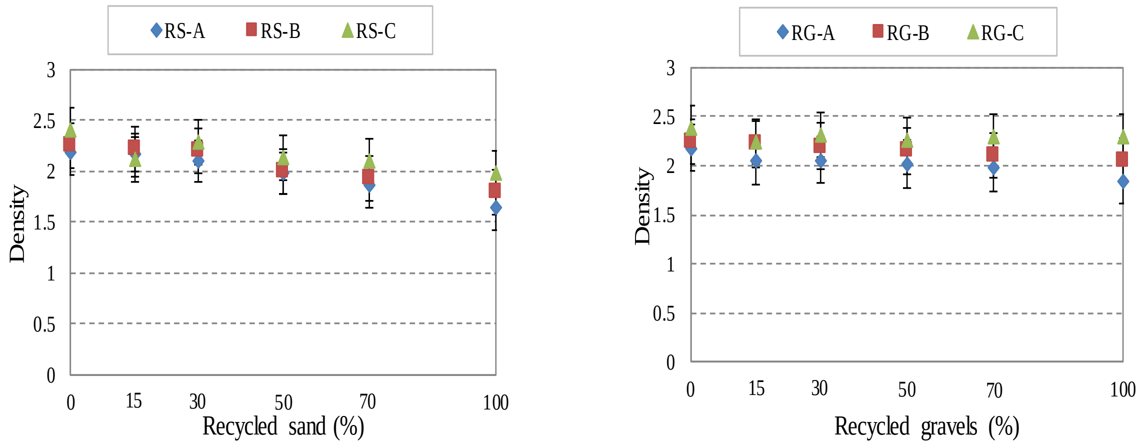

(a) (b)

Figure 4. Evolution of density of RCA: (a) RS; (b) RG.

3.2. Evolution of the diffusion of chloride ions

Fig. 5 shows the evolution of the diffusion depth of chloride ions as a function of the percentage of substitution of RS and RG for the three types of cement and admixtures at 28 days. Fig. 5a shows that in the case of RS concrete the depth of diffusion of the chloride ions increases dramatically and linearly with the increase in the percentage of substitution, irrespective of the couples cement / admixture. It can reach up to 40 mm deep in the case of the RS-A couple with 100 % substitution, an 85 % increase compared to concrete based on NS. It also increases linearly but less markedly in the case of concrete based on RG (Fig. 5b); the increase is 60 % for the RG-A couple. Indeed, the diffusion of chloride ions is influenced by the presence of pores in the concrete structure since these ions penetrate by capillary absorption. Therefore, more the concrete is porous the diffusion is greater, which is the case of concrete made with RS which thus present a deeper chloride ion penetration. It should also be noted that, the type of cement and admixtures affect the chloride ion diffusion depth results for both types of RA. The couple RS-A and RG-A have higher diffusion depths compared to the couple RS-B and RG-B and increased with the percentage of substitution. The couple RS-C as well as RG-C has average diffusion depths according to their percentages of substitution. This phenomenon can be explained by the fact that the amount of C_3A is greater in the couple of RS-A as well as RG-A compared to the couple RS-B and RS-C, as well as RG-B and RG-C. The couple RS-C as well as RG-C has average amount of C_3A.

The diffusion of chloride ions in concrete is closely related to the porous structure of the material [21]. Indeed, several researchers have demonstrated the tendency of chloride ions to react with the constituents of the cement to give a complex solid phase based on chloride known as *Friedel salt* ($C_3A.CaCl_2.10H_2O$)

[22]. The interactions between the chlorides and the cement constituents were firstly attributed to the C_3A phase in the cement. Subsequently, other studies have shown that the fixing capacity of the cement paste depends on the total aluminate content (composed of C_3A and C_4AF) [23–25]. In fact, the amount of fixed chloride ions increases with the C_3A content of the cement; nevertheless, starting from a certain content of C_3A, this quantity does not evolve any more, whatever the nature of the cement or the considered deadline. Experimental observations show that the factor limiting the diffusion of chloride ions is C_3A. The latter decreases during hydration [26]. It should also be noted that C_3A is less reactive than C_4AF and that hydration is very slow [27, 28].

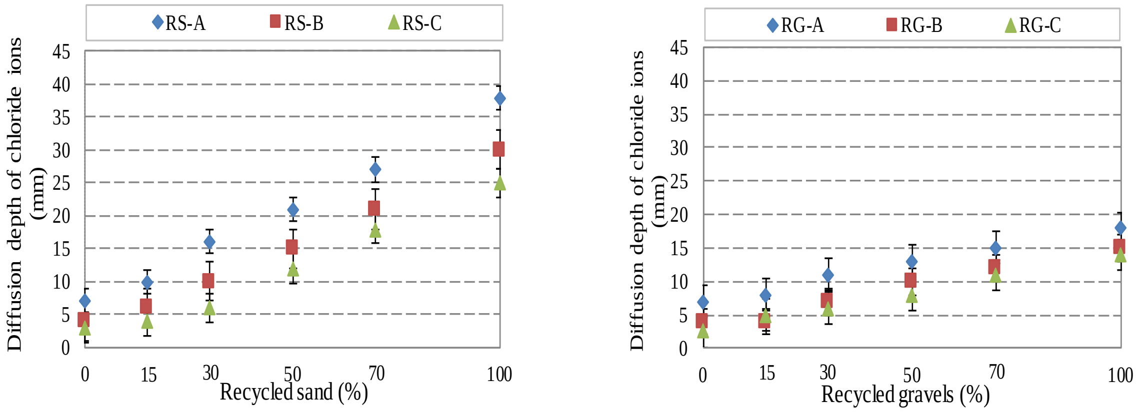

(a) **(b)**

Figure 5. Evolution of the diffusion depth of chloride ions of RCA: (a) RS; (b) RG.

3.3. Relationship between the durability parameters

3.3.1. Relationship between the density and porosity

Fig. 6 shows the existing relationship between density and porosity. According to the figure, the density decreases as porosity increases for RS and RG concrete. On the other hand, this decrease is more marked in the case of the RS concrete than for the RG concrete. This is explained by the small variation in the porosity of RG compared to RS.

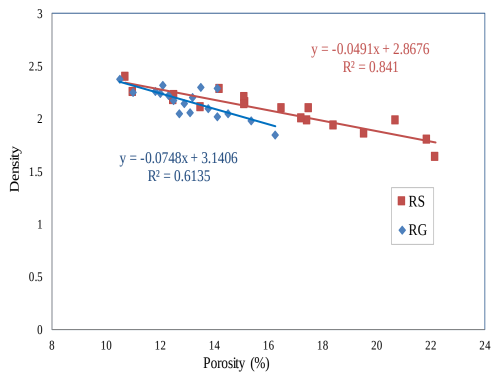

Figure 6. Relationship between the porosity and the hardened density of RCA.

3.3.2. Relationship between the diffusion depth of chloride ions and density

Fig. 7 shows that regardless of the type of RA and regardless of the couple cement/admixture, there is a linear relationship between chloride ions diffusion depth and density. Indeed, when the latter increases, the diffusion of chloride ions decreases. However, this relationship is more pronounced in the case of concretes made with RS since they experience a remarkable decrease as a function of the increase in density; this decrease is considerably diminished for the concrete made with RG. In addition, it should be noted that they experience a very low variation in density and depth of diffusion of chloride ions, regardless of their percentages of substitution. Concrete made with RS show a variation in density but above all the depth of diffusion of chloride ions higher; the slope showing the relationship for concrete made with RS is therefore much sharper than that of concretes made with RG. The relationship between the diffusion depth of the chloride ions and density for the concrete can be expressed as follows:

$$\text{For RS: } X_d = 19.44(\rho_d)^2 - 129.74\rho_d + 200 \text{ with } R^2 = 0.9, \tag{1}$$

$$\text{For RG: } X_d = 32.51(\rho_d)^2 - 162.15\rho_d + 207.4 \text{ with } R^2 = 0.5, \tag{2}$$

X_d is the depth of diffusion of chloride ions (mm);

ρ_d is the density in the cured state.

3.3.3. Relationship between the diffusion depth of chloride ions and porosity

Fig. 8 shows a reverse relationship to the one previously proposed. Indeed, an increase in the diffusion depth of chloride ions as a function of the increase in porosity is to be observed. This relationship is all the stronger as it concerns the concrete made with RS, although those of the concrete made with RG also experience an elevation of this depth according to the porosity. In addition, the variation of the values of the porosity and the diffusion depth of the chloride ions between the different percentages of RS is particularly high compared to that which exists for the same properties of the concrete made with RG. The equations reflecting the evolution of the porosity as a function of the diffusion depth of the chloride ions for the concrete made with RS and with RG are as follows:

$$\text{For RS: } X_d = 0.25\varepsilon^2 - 4.86\varepsilon + 27.01 \text{ with } R^2 = 0.9 \tag{3}$$

$$\text{For RG: } X_d = 0.23\varepsilon^2 - 3.05\varepsilon + 10.01 \text{ with } R^2 = 0.7 \tag{4}$$

X_d is the depth of diffusion of chloride ions (mm).

ε is the porosity accessible to water.

In addition, the variation of the values of the porosity and the diffusion depth of the chloride ions between the different percentages of RS is particularly high compared with that which exists for the same properties in the concrete made with RG. Two models of calculations of the chloride ions diffusion depth as a function of porosity were proposed from the values obtained by the experimental measurements as shown in Fig. 9.

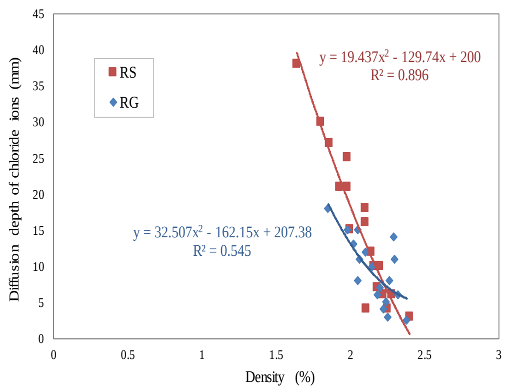

Figure 7. Relationship between the diffusion depth of chloride ions and the density of RCA.

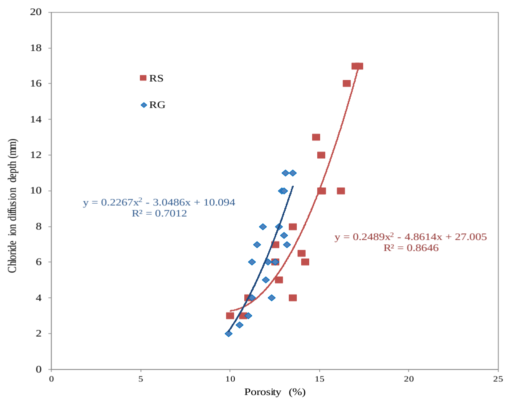

Figure 8. Relationship between the chloride ions diffusion depth and the porosity of RCA.

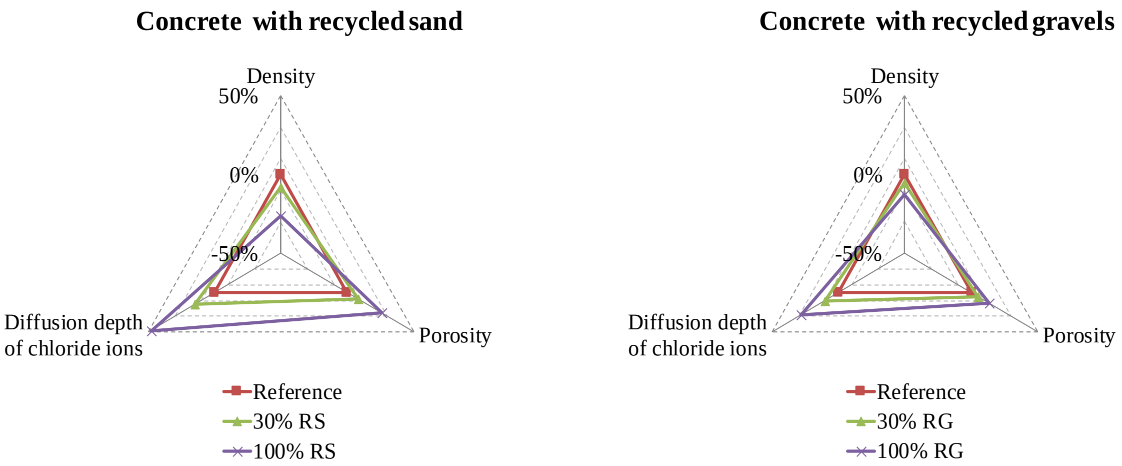

(a) **(b)**

Figure 9. Relationship between density, porosity and depth of chloride ions diffusion of RCA: (a) RS; (b) RG.

4. Conclusions

This study investigates the effect of replacement of NA with RCA on the durability performance of concrete. Based on the obtained results, the main conclusions may be drawn:

1. Regardless of the couple cement / admixture, there is a relationship between chloride ions diffusion depth and density. Indeed, when the latter increases, the chloride ions diffusion depth decreases considerably. However, this relationship remains qualitative.

2. A significant increase in the diffusion depth of the chloride ions as a function of the increase in porosity is observed. This increase is accompanied by a wide range of chloride ion diffusion depth values for the different percentages of RS. A model for calculating these two parameters has also been proposed based on the values obtained by the experimental measurements.

3. The diffusion depth of the chloride ions and the porosity increases significantly with the increase in the percentage of RG. Regardless of the couple of cement and admixtures. This rise is less pronounced than in the case of concrete made with RS.

4. The couple of cement and admixtures stand out because of their chloride ion diffusion depth results. This can be explained by the amount of C_3A that these couple contain. Indeed, the diffusion depth of the chloride ions is high when the C_3A content of the cement is important. The same observation concerning the concrete made with RS.

5. The relationship between chloride ions diffusion depth and density is linear regardless of the couple cement / admixture. Indeed, the variation of these two properties is very small. Furthermore, it has previously been found that the diffusion depth of the chloride ions of the concrete made with RS decreased significantly with increasing density. The slope showing the relationship for these concretes is therefore much sharper than that of concretes made with RG.

6. An increase in the diffusion depth of the chloride ions with the increase in porosity is observed. This relationship is all the stronger as it concerns the concrete made with RS, although those of the concrete made with RG also have an elevation of this depth according to the porosity.

References

1. Benabed, B. Effect of combined use of crushed sand and Algerian desert dune sand on fresh properties and strength of SCC. Epitoanyag- Journal of Silicate Based & Composite Materials. 2018. 70. Pp. 155–166. https://doi.org/10.14382/epitoanyag-jsbcm.2018.29
2. Abed, M., Nemes, R. Fresh properties of the self-compacting high performance concrete using recycled concrete aggregate. Epitoanyag-Journal of Silicate Based & Composite Materials. 2019. 71. Pp. 18–23. https://doi.org/10.14382/epitoanyag-jsbcm.2019.4
3. Evangelista, L., de Brito, J. Concrete with fine recycled aggregates: a review. Eur. J. Environ. Civ. Eng. 2014. 18. Pp. 129–172. https://doi.org/10.1080/19648189.2013.851038
4. Xuan, D., Zhan, B., Poon, C.S. Durability of recycled aggregate concrete prepared with carbonated recycled concrete aggregates. Cem. Concr. Compos. 2017. 84. Pp. 214–221. https://doi.org/10.1016/j.cemconcomp.2017.09.015
5. Evangelista, L., de Brito, J. Durability performance of concrete made with fine recycled concrete aggregates. Cem. Concr. Compos. 2010. 32. Pp. 9–14. https://doi.org/10.1016/j.cemconcomp.2009.09.005
6. Poon, C., Shui, Z., Lam, L. Effect of microstructure of ITZ on compressive strength of concrete prepared with recycled aggregates. Constr. Build. Mater. 2004. 18. Pp. 461–468. https://doi.org/10.1016/j.conbuildmat.2004.03.005
7. Buyle-Bodin, R.H.Z.F. Influence of industrially produced recycled aggregates on flow properties of concrete. Mater. Struct. 35 (2002) 504–509. https://doi.org/10.1007/BF02483138
8. Kosmatka, S.H., Kerkhoff, B., Panarese, W.C. Design and control of concrete mixtures, 14th Edition, Portland Cement Association. 2002.
9. Chakradhara Rao, M., Bhattacharyya, S.K., Barai, S.V. Influence of field recycled coarse aggregate on properties of concrete. Mater. Struct. 2010. 44. Pp. 205–220. https://doi.org/10.1617/s11527-010-9620-x
10. de Juan, M.S., Gutiérrez, P.A. Influence of attached mortar contento n the properties of recycled concrete aggregate. International RILEM Conference on the Use of Recycled Materials in Building and Structures, Editor(s): E. Vázquez, Ch.F. Hendriks and G.M.T. Janssen. 2004. Pp. 536–544. DOI: 10.1617/2912143756.059
11. Etxeberria, M., Vázquez, E., Marí, A., Barra, M. Influence of amount of recycled coarse aggregates and production process on properties of recycled aggregate concrete. Cem. Concr. Res. 2007. 37. Pp. 735–742. DOI: 10.1016/j.cemconres.2007.02.002
12. Nagataki, S., Gokce, A., Saeki, T., Hisada, M. Assessment of recycling process induced damage sensitivity of recycled concrete aggregates, Cem. Concr. Res. 2004. 34. Pp. 965–971. https://doi.org/10.1016/j.cemconres.2003.11.008
13. Padmini, A.K., Ramamurthy, K., Mathews, M.S. Influence of parent concrete on the properties of recycled aggregate concrete. Constr. Build. Mater. 2009. 23. Pp. 829–836. https://doi.org/10.1016/j.conbuildmat.2008.03.006
14. Gómez-Soberón, J.M. Porosity of recycled concrete with substitution of recycled concrete aggregate: An experimental study. Cem. Concr. Res. 2002. 32. Pp. 1301–1311. https://doi.org/10.1016/S0008-8846(02)00795-0
15. Katz, A. Properties of concrete made with recycled aggregate from partially hydrated old concrete. Cem. Concr. Res. 2003. 33. Pp. 703–711. https://doi.org/10.1016/S0008-8846(02)01033-5
16. Rao, A., Jha, K.N., Misra, S. Use of aggregates from recycled construction and demolition waste in concrete. Resour. Conserv. Recycl. 2007. 50. Pp. 71–81. https://doi.org/10.1016/j.resconrec.2006.05.010

17. Barbudo, A., de Brito, J., Evangelista, L., Bravo, M., Agrela, F. Influence of water-reducing admixtures on the mechanical performance of recycled concrete. J. Clean. Prod. 2007. 59. Pp. 93–98. https://doi.org/10.1016/j.jclepro.2013.06.022
18. Pereira, P., Evangelista, L., de Brito, J. The effect of superplasticisers on the workability and compressive strength of concrete made with fine recycled concrete aggregates. Constr. Build. Mater. 2012. 28. Pp. 722–729. https://doi.org/10.1016/j.conbuildmat.2011.10.050
19. NF-EN 1097-6. Essais pour déterminer les caractéristiques mécaniques et physiques des granulats – Partie 6 : détermination de la masse volumique réelle et du coefficient d'absorption d'eau. 2014.
20. ASTM C 1202-97. Standard Test Method for Electrical Indication of Concrete's Ability to Resist Chloride Ion Penetration. 2003.
21. Bágel', L., Živica, V. Relationship between pore structure and permeability of hardened cement mortars: On the choice of effective pore structure parameter. Cem. Concr. Res. 1997. 27. Pp. 1225–1235. https://doi.org/10.1016/S00088846(97)-00111-7
22. Arya, C., Buenfeld, N.R., Newman, J.B. Factors influencing chloride-binding in concrete. Cem. Concr. Res. 1990. 20. Pp. 291–300. https://doi.org/10.1016/0008-8846(90)90083-A
23. Alonso, C., Andrade, C., Castellote, M., Castro, P. Chloride threshold values to depassivate reinforcing bars embedded in a standardized OPC mortar. Cem. Concr. Res. 2000. 30. Pp. 1047–1055. https://doi.org/10.1016/S0008-8846(00)00265-9
24. Deby, F., Carcassès, M., Sellier, A. Probabilistic approach for durability design of reinforced concrete in marine environment. Cem. Concr. Res. 2009. 39. Pp. 466–471. https://doi.org/10.1016/j.cemconres.2009.03.003
25. Theissing, E.M., de Larr, T.M., De Wind, G. . The combining of sodium chloride and calcium chloride by the hardened portland cement compounds C3S, C3A and C4AF, In 8th Int. Symposium on Chemistry of Cement. 1986. Pp. 823–828.
26. Suryavanshi, A., Scantlebury, J.D. Mechanism of friedel's salt formation in cements rich in tri-calcium aluminate. Cem. Concr. Res. 1996. 26. Pp. 717–727. https://doi.org/10.1016/S0008-8846(96)85009-5
27. Rasheeduzzafar, S., Ehtesham Hussain, S., Al-Saadoun, S.S. Effect of cement composition on chloride binding and corrosion of reinforcing steel in concrete. Cem. Concr. Res. 1991. 21. Pp. 777–794. https://doi.org/10.1016/0008-8846(91)90173-F
28. Luping, T., Nilsson, L.O. Chloride binding capacity and binding isotherms of OPC pastes and mortars. Cem. Concr. Res. 1993. 23. Pp. 247–253. https://doi.org/10.1016/0008-8846(93)90089-R

Contacts:

Zine El Abidine Tahar, zine-el-abidine.tahar@u-cergy.fr
El Hadj Kadri, el-hadj.kadri@u-cergy.fr
Benchaa Benabed, b.benchaa@lagh-univ.dz
Tien-Tung Ngo, tien-tung.ngo@u-cergy.fr

Magazine of Civil Engineering. 2022. 109(1). Article No. 10909

Magazine of Civil Engineering

ISSN 2712-8172

journal homepage: http://engstroy.spbstu.ru/

DOI: 10.34910/MCE.109.9

Effect of ferronickel slag in concrete and mortar

R. Suryaningrat Edwin*, M. Kimsan, B. Pramono, F. Masud, R. Sriyani

Department of Civil Engineering, Halu Oleo University, Anduonou Kendari, Indonesia

**E-mail: romy.edwin@uho.ac.id*

Keywords: ferronickel slag, compressive strength, fine aggregate, cement replacement, heat treatment, pozzolanic activity

Abstract. Cement and nickel mining industries are facing challenges such as the depletion of natural resources and insufficient landfill disposals of ferronickel slag. These problems can be solved by upgrading the ferronickel slag in concrete production without loss of quality. In this research, the use of ferronickel slag as fine aggregate and cement replacement in concrete and mortar was investigated. The ferronickel slag was ground using a ball mill to achieve two levels of fineness. The performance of mortar was assessed under heat treatment at 75 °C as a comparison to that of the normal curing. The pozzolanic activity of ferronickel slag was determined by the Frattini test. The results showed that the strength of concretes increased with increasing of ferronickel slag content in the concrete mixture up to 40 %, beyond that the strength of concrete decreased. A positive effect on the compressive strength of mortar was achieved by using the slag with a higher fineness. The use of heat treatment at 75 °C enhanced the compressive strength of mortar. Assessment of the pozzolanic activity by means of the Frattini test indicates the non-pozzolanic reaction of the slag after 28 days. The use of heat treatment partially hydrated unhydrated cement grains.

1. Introduction

In recent decades, concrete has become the main building material in construction projects throughout the world. In comparison to steel structure, concrete is easier to produce and relatively low cost, since the raw materials such as fine aggregate (sand) and coarse aggregate (stone and gravel) can be easily found near the project location and it does not require a high technology in its production. Besides the aggregates, cement is the essential “binder” which occupies about 15 % in the concrete matrix. Since the estimation of concrete production achieves about 25 billion tons worldwide annually [1], which will also demand about 6.25 billion tons of fine aggregate [2] and 2.8-4 billion tons of cement [3]. These numbers imply that massive exploitation of natural resources is on-going, leading to environmental degradation in the near future. In addition, the production of Portland cement consumes an enormous amount of energy from fossil fuels such as petroleum, coal, and natural gas, which will not be replenished for millions of years. Hence, burning fossil fuels for clinker calcination and grinding in cement manufacturing release a huge amount of CO_2 into the atmosphere, which directly upsets Earth’s balance carbon budget, leading to faster global warming. At the same time, the mining industry is facing challenges such as insufficient landfill disposal of waste material and the danger of heavy metals and other harmful elements from waste material on water quality and environment. Therefore, upgrading the waste material in concrete production is key to solve these problems regarding environmental degradation.

The primary source of ferronickel in Indonesia is saprolite nickel ore. After excavation and stockpile, the ore is then treated in the rotary dryer and rotary reduction kiln for sulfurization. Afterward, the treated ore is transferred to the smelting process for extracting and purification. In the final stage, the ferronickel which contains about 80 % iron and 20 % nickel is generated, followed by its by-product or slag. In

Suryaningrat Edwin, R., Kimsan, M., Pramono, B., Masud, F., Sriyani, R. Effect of ferronickel slag in concrete and mortar. Magazine of Civil Engineering. 2022. 109(1). Article No. 10909. DOI: 10.34910/MCE.109.9

Indonesia, approximately 4 million tons of ferronickel slag is produced yearly, which needs a large landfill for storage the slag. Besides, ferronickel slag is still categorized as a hazardous and toxic material which contains harmful elements such as Pb, Zn, As, Cd, Co, and Cu [4], which can affect human health. Hence, a possible breakthrough to solve such problems is utilizing the ferronickel slag as a raw material (fine aggregate or cement replacement) within the concrete production without loss of quality. Looking into literature, ferronickel slag was investigated by several researchers as fine aggregate replacement in concrete and mortar [5–7]. The use of ferronickel slag as partial cement replacement was also studied by [4, 8, 9]. While applying heat curing to mortar mixture containing ferronickel slag was only reported by Li et al. [10].

In the current research, the effect of ferronickel slag as fine aggregate replacement in strength and workability of concrete was studied. The influence of heat treatment on the compressive strength of mortar containing ferronickel slag as the supplementary was also evaluated.

2. Materials and methods

2.1. Aggregates

Aggregates used in this study were purchased from Indonesian Stone Crusher Manufacturer. In Indonesia, aggregates that are used in concrete production are generally natural aggregates. The fine aggregate can be found in the river basin with a round texture and smooth surface. The gravel used in this study is obtained from the erosion of rocks, which is crushed using a stone crusher to obtain the desired gradation. The particle size distribution (PSD) and physical properties of aggregates are shown in Fig. 1 and Table 2.

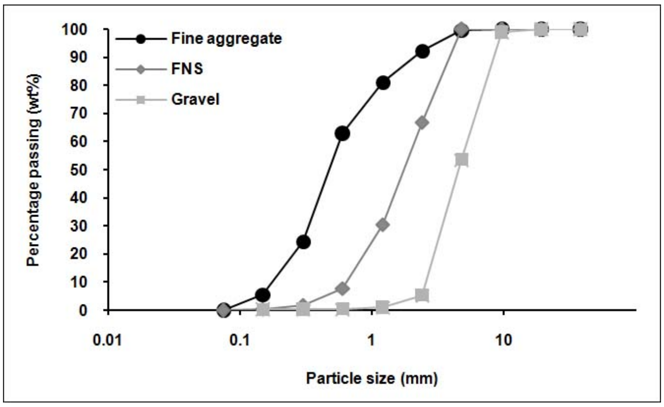

Figure 1. Particle size distribution of aggregates and FNS determined by sieving.

2.2. Ferronickel slag and cement

Ferronickel slag (FNS) used in this study is a by-product obtained from FeNi-IV Smelter Plant of one nickel mining company in Indonesia. This plant generates nickel ore and solid-granulated FNS. The slag has an angular particle with varying sizes and less porosity. As cement, an Ordinary Portland Cement I (OPC I) was used throughout all experiments. The physical properties and chemical compositions of OPC I and FNS are given in Fig. 1, Table 1 and 2.

Table 1. Physical characteristics of aggregates, OPC and FNS.

Test	Fine aggregate	Gravel	OPC	FNS
Specific gravity (g/cm3)	2.62	2.37	3.15	2.93
Water absorption (%)	1.43	0.89	–	0.50

Table 2. Chemical compositions and fineness of OPC and FNS.

Constituents	OPC	FNS
SiO_2	19.9	53.6
Al_2O_3	5.3	5.5
CaO	64.1	5.2
Fe_2O_3	3.0	12.7
MgO	2.4	20.9
SO_3	1.9	0.2
MnO	ND	0.5
K_2O	0.6	0.1
Na_2O	0.2	ND
Cr_2O_3	ND	1.2
Blaine permeability (cm^2/g)	3350	-

2.3. Grinding process and particle size distribution

Before using the FNS as a cement replacement, the slag has to be ground to reduce the size within the micron meter. In this study, at first, the FNS was ground for one hour in a ball mill machine using 12 balls. Afterward, the FNS was sieved using a sieve with a size of 1.18 mm. The sieved FNS was then ground using a ball mill machine with 24 balls for 1 hour and 2 hours to achieve two levels of fineness. The FNS finer 1 (FNS_F1) and the FNS finer 2 (FNS_F2) is the ground FNS for 1 hour and 2 hours, respectively.

After the grinding process, the FNS and OPC were measured their fineness using laser diffraction (LD). A wet method was chosen to measure the PSD of binders. As a dispersant, isopropanol was used instead of water in order to confirm that no hydration occurred during this measurement between binder and dispersant. An outline of the optical parameters used in this study is presented in Table 3.

Table 3. Outline of the optical parameters used to determine the PSD of binders by LD.

Optical parameters	OPC	FNS_F1	FNS_F2
Absorption coefficient [–]	0.003	0.500	0.500
Refractive index [–]	1.730	1.530	1.530
Dispersant [–]	1.390	1.390	1.390
Obscuration [%]	12.990	12.570	12.690
Stirrer rate [rpm]	1500	1500	1500
Sonication times (minutes]	5	5	5

2.4. Superplasticizer

In this research, a new generation of modified polycarboxylic ether (PCE) based superplasticizer (MasterGlenium Sky 8851) was used throughout all experiments. This superplasticizer has long side chains, which initiatives some electrostatic dispersion mechanism at the beginning of the mixing process to separate the cement particles. In this mechanism, the slump life and the desired workability at a low water-to-cement ratio is obtained.

2.5. Mixtures proportions and mixing procedure

In this study, the mix design of high strength concrete (HSC) is based on Indonesian Standard [11]. This standard can be used for concrete mix design with a water-to-cement ratio of less than 0.5. In the current research, a water-to-cement ratio of 0.35 was chosen. FNS was used as a fine aggregate replacement with the proportions of 0 %, 10 %, 20 %, 30 %, 40 %, 50 % and 60 % by weight. Due to the different specific gravity between fine aggregate and FNS, in which FNS is heavier than fine aggregate, the total volume of concrete containing FNS will decrease. Therefore, other materials such as cement, coarse aggregate, and water will compensate to obtain 1 m^3 of the total volume of concrete containing FNS. The detail of concrete composition is shown in Table 4.

To study the effect of FNS as cement replacement, the mix design of high strength mortar (HSM) was prepared with FNS contents from 0 to 20 wt% in steps of 5 wt%. Similar to concrete, a water-to-cement ratio of 0.35 was also chosen for HSM in this study. The mortar compositions used in this study is shown in Table 5.

In the mixing process of concrete, a 70 liter intensive mixer with two stirring plates and a speed of 30 rpm was used in this study. The mixing process of concrete was seen in Fig. 2. For mortar mixing, a 5 liter intensive mixer with 5 speeds was used. The mixing procedure of mortar used in this study was based on [12].

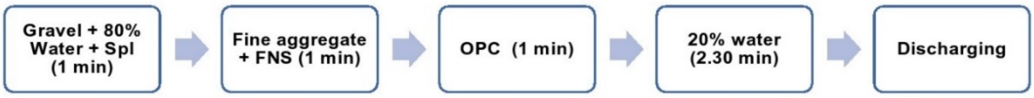

Figure 2. Mixing procedure of concrete.

Table 4. Mix composition of concrete with FNS as fine aggregate replacement (kg/m^3).

Material	Ref	10%	20%	30%	40%	50%	60%
OPC	449.0	449.1	449.2	449.3	449.4	449.5	449.6
Fine aggregate	576.0	518.6	461.1	403.6	346.1	288.5	230.8
FNS	0.0	57.6	115.2	172.9	230.6	288.4	346.1
Coarse aggregate	1117.0	1117.5	1117.9	1118.4	1118.9	1119.4	1119.8
Water	157.0	157.4	157.7	158.1	158.5	158.9	159.2
Superplasticizer	9.9	9.9	9.9	9.9	9.9	9.9	9.9

Table 5. Mix composition of mortar with FNS as cement replacement (kg/m^3).

Material	Ref	5%	10%	15%	20%
OPC	864.2	821.0	777.8	734.6	691.3
FNS	0.0	43.2	86.4	129.6	172.8
Fine aggregate	1108.9	1108.9	1108.9	1108.9	1108.9
Water	302.3	302.2	302.1	302.1	302.0
Superplasticizer	4.3	4.3	4.3	4.3	4.3

2.6. Heat treatment

In this study, after curing in room temperature for 24 h, the mortar samples were demolded and placed on the grid in the concrete curing box. The maximum temperature was set at 75 °C with a heating rate of 0.2 °C/min. Based on the literature, heat curing accelerates the hydration heat and simultaneously lead the porosity [13, 14]. The latter is due to the difference in the coefficient of thermal expansion of mortar ingredients [15]. Other literature reported that heat curing at higher temperatures also gives temporary-relaxation effect on strength at 28 days, which would again increase after longer curing periods as reported by [16]. So that, in this study a 75 °C was chosen to prevent the negative effect on the porosity and strength of mortar.

2.7. Frattini test

The Frattini test was used in this study to evaluate the pozzolanic activity of FNS. The procedure of this test was based on [17]. 20 grams of binder (cement + FNS) and 100 ml of distilled-decarbonized water were mixed in a polyethylene container. The carbonized water was prepared by boiling the distilled water to remove the carbon dioxide. Similar to the mortar composition as shown in Table 5, the FNS content varied from 0 wt% to 20 wt% of the binder in steps of 5 wt%. After curing in an oven at (40 ± 2) °C for 8 days and 28 days, the solution was then vacuum-filtered using Whatman filter paper. To analyze the filtered solution, the acid-base titration was performed to determine the hydroxyl ion [OH^-] concentration and calcium oxide concentration [Ca^{++}]. The pozzolanic activity of FNS can be assessed if they are below the lime saturation curve [18].

2.8. Workability and compressive strength

The workability of fresh concrete was determined using an Abrams cone with the following dimensions: diameter of the base (200 ± 2 mm); diameter of the top (100 ± 2 mm), and height (300 ± 2 mm) according to [19]. For fresh mortar, the flowability was measured using a mini-slump flow based on [20]. The slump test was conducted in a triplicate to evaluate the workability of concrete and mortar containing FNS as fine aggregate and cement replacement, respectively.

After curing in a water bath with a temperature of 25 ± 2 °C, the concrete cylinder (100 mm diameter × 200 mm length) and mortar cylinder (55 mm diameter × 110 mm length) were taken out and then left at ambient temperature for two hours. The cylinders were tested in triplicate to evaluate the compressive strength. A compression machine with a capacity of 150 tons-force was used.

3. Results and Discussion

3.1. Particle size distribution of different binders

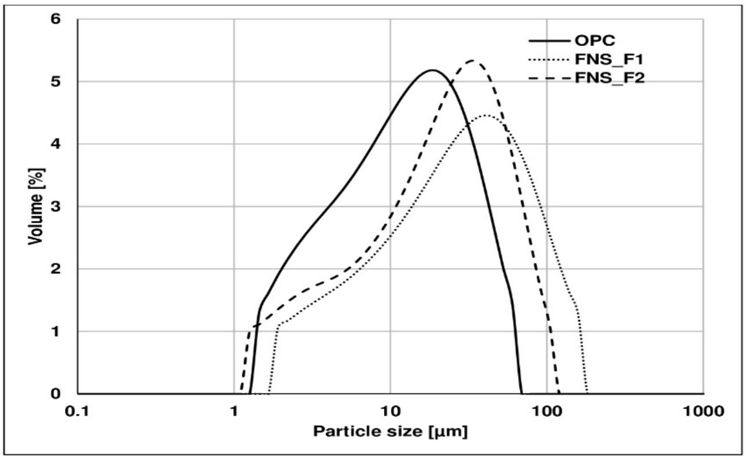

Figure 3. Particle size distribution of OPC and FNS.

Table 6. Specific gravity and d_{50} of the different binders.

Materials	OPC	FNS_F1	FNS_F2
Specific gravity (g/cm^3)	3.151	3.107	3.107
Particle size d_{50} (µm)	11.392	23.713	18.703

The results of the PSD of OPC and FNS determined by the wet method using laser diffraction was shown in Fig. 3. It seemed that the PSD of OPC was finer than FNS_F1 and FNS_F2. Meanwhile, the grain size distribution of FNS_F2 was finer than FNS_F1. By comparing the d_{50} of FNS as seen in Table 6, the FNS_F2 which was ground for the longer time obtained finer particle size (18.703 µm) compared to FNS_F1 (23.713 µm).

3.2. Workability

The results of the workability of concrete and mortar are shown in Fig. 4. It can be seen that the slump of fresh concrete and mortar increased as the increase of the FNS content. For concrete, it can be explained by the fact that the FNS has a low water absorption compared to fine aggregate, as seen in Table 1. This different water absorption could lead to surplus water content in fresh FNS concrete. In addition to the water absorption, the differences in physical properties such as particle size and particle shape of materials composing concrete also influence the workability of fresh concrete [7]. In the current research, the particle size of FNS is coarser than fine aggregate as shown in Fig. 1, also resulting in lower the specific surface area of FNS than fine aggregate, therefore it will lead to less amount of un-wetting area in the FNS concrete matrix. This phenomenon can increase the amount of water trap, generating in enhancement the excess water in the fresh concrete matrix, and in the end, the workability of fresh FNS-concrete rises.

The flowability of mortar containing FNS coarser is higher than FNS finer as shown in Fig. 4b. This result corresponds with the result obtained of concrete workability as mentioned above. Since the FNS_F2 has a higher specific surface area than FNS_F1, in the mixing process, the air cavities of fresh mortar significantly decreased, which was effectively filled by the fine particles of FNS_F2. So that, the higher viscosity of fresh mortar is obtained and reducing the flowability of fresh-FNS_F2 mortar compared to mortar containing FNS_F1. This result is in accordance with the finding of Humad et al. [21], who also found a decrease in the flowability of mortar using finer slags due to the effect of higher specific surface area.

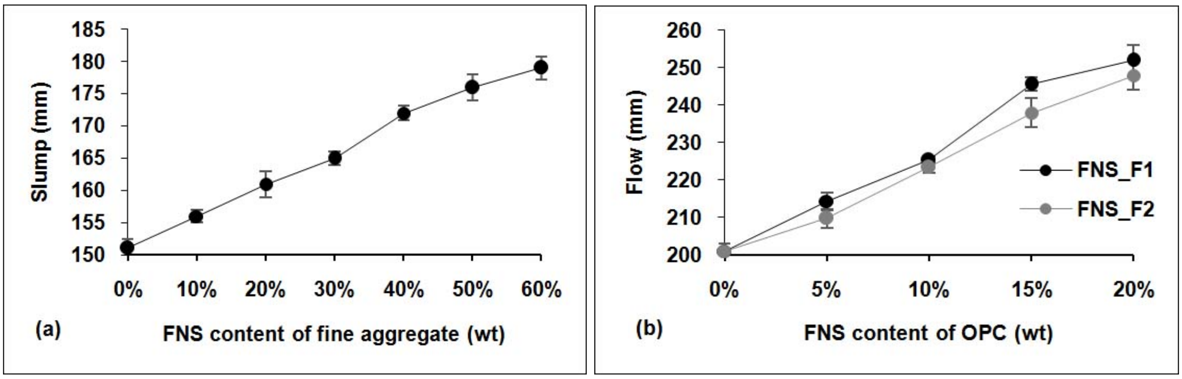

Figure 4. Workability of: (a) concrete and (b) mortar (error bars represent standard errors; the average values represent three replicates).

3.3. Compressive strength of concrete

The development of strength of concrete containing FNS as fine aggregate replacement is seen in Figure 5. It can be seen that the strength of concrete increased with the increasing FNS content in the concrete mixture up to 40 %, beyond that the strength of concrete decreased. The highest compressive strength was achieved for 40 % FNS at later ages, which increased by about 16 % compared to the reference mixture, as shown in Fig. 5. This finding is in accordance with the finding of Saha and Sarker [7], who also found in an increase the compressive strength up to 50 % FNS and then decrease at a higher replacement level of FNS. This result can be explained by the fact that FNS has sharp angular edges and rough surfaces, which can improve cohesion and slip resistance between aggregate and paste. Besides, it is mentioned in the literature that fine aggregate has good abrasion properties due to its irregular surface [22]. However, this irregular surface will change with time to have a round surface due to the physical weathering. Since the hardness of FNS is similar to copper slag [23] and higher than the fine aggregate [24], a good abrasion of FNS is still obtained even though they are exposed in the open area for many years. Another reason is that the grain size of FNS is bigger than fine aggregate as seen in Fig. 1, which cannot effectively fill the concrete pores. Otherwise, the filler effect is obtained from the finer grain size of fine aggregate. So that, the combined fine aggregate-FNS grading at 40 % FNS gives the optimal packing fraction in the concrete matrix. For higher replacement level, the optimum packing fraction does not obtain due to the reduced the finer fraction from the fine aggregate which cannot be compensated by the grain size of FNS. This is the reason for the decreased compressive strength of concrete at 50 % and 60 % FNS substitution, as shown in Fig. 5 and Fig. 6.

Concerning the influence of water absorption on strength development, Sun et al. [6] noticed that the use of FNS as a sand replacement with higher water absorption gives a positive effect on the compressive strength of concrete. Regarding this, it seems that this current finding is in contrast with the findings of Sun et al. [6] since the water absorption of FNS is lower than the fine aggregate. However, it should be noted that the higher strength of concrete obtained in this study is only achieved at a lower replacement level. In addition, the excess of water in the fresh concrete matrix due to lower water absorption of FNS will leave more air cavities. This weakness might be compensated by the packing effect of FNS.

From Fig. 6, it can be observed that for early curing days (7 days), the concrete containing 10 % and 50 % FNS achieved slightly lower or similar strength compared to the control mixture, respectively. Compared to the result obtained of compressive strength at 7 days for 10 % and 50 % FNS, better results were achieved at longer curing periods (28 and 56 days), which was similar and slightly higher compared to the reference mixture, as seen in Fig. 6. It also can be observed that the strength enhancement for mixes 20 %, 30 %, and 40 % increased in the function of curing time as seen in Fig. 6. From these results, it can be noticed that strength enhancement of concrete up to 50 % FNS tends to be low at early curing periods (7 days) but relatively high at longer curing periods (28 and 56 days). This higher strength development at the later ages might be due to the increased interlocking of the aggregates combined with the filled porosity by the gel calcium-silicate-hydrate (CSH gel) generated during the hydration process.

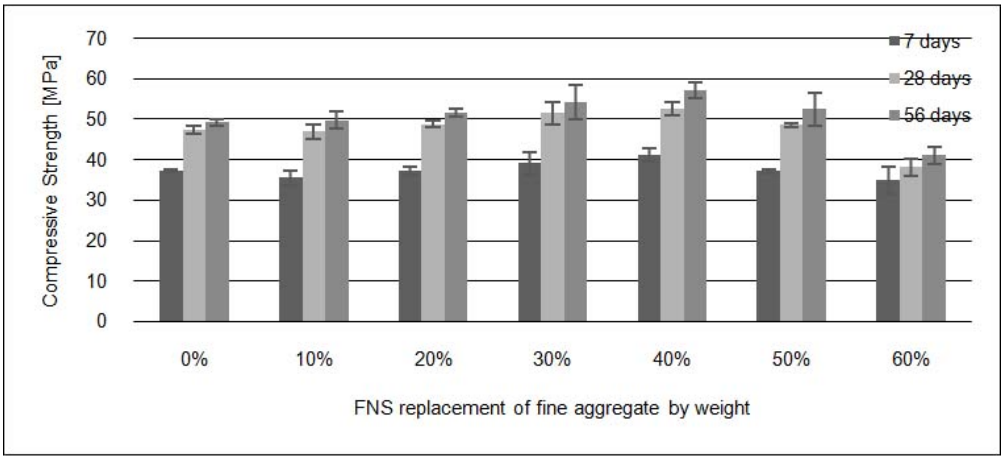

Figure 5. The strength evolution of concrete containing FNS as sand replacement (error bars represent standard errors; the average values represent three replicates).

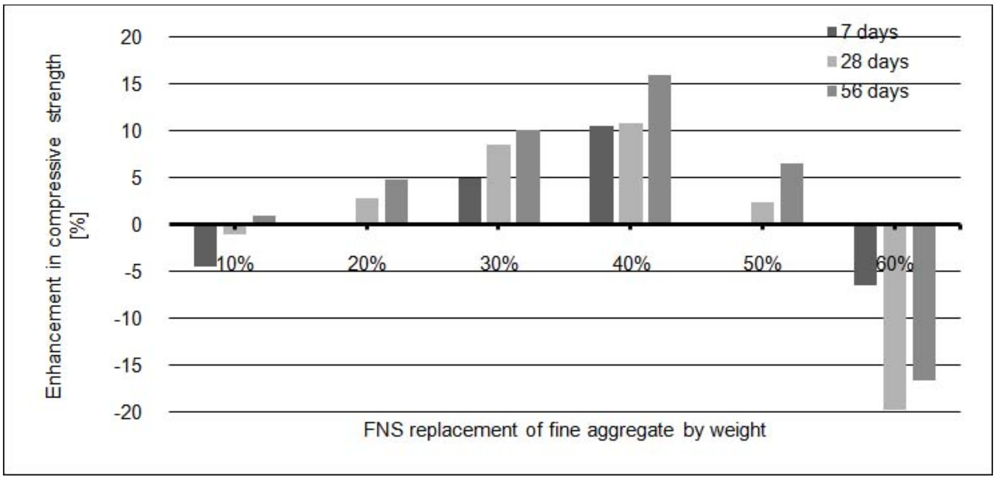

Figure 6. Enhancement in strength (concrete containing FNS versus reference) at 7, 28, and 56 days.

3.4. Compressive strength of mortar

In Fig. 7, the results of the compressive strength of mortar are presented. It is clear that the strength of mortar decreased as increasing the FNS content for all curing periods. At 3 days of normal curing, the compressive strength of mortar containing the lower replacement level of FNS_F1 decreased by about 14 % compared to reference mixture, whereas the mortar mixture with 5 % FNS_F2 showed a decrease by about 11 %. For normal curing at 90 days, it can be observed that the reduction of the compressive strength of mortar containing 5 % of FNS_F2 and FNS_F1 was about 3 % and 8 %, respectively compared to the reference mixture. These phenomena also occurred for the compressive strength of mortar after applying heat treatment at 75 °C. It can be seen in Fig. 7(c) and (d) that the mortar mixture with FNS_F2 gave a smaller reduction in compressive strength in comparison to that of mortar with FNS_F1 for both early and later curing periods. From these results, it can be concluded that the use of FNS as cementitious material gives a negative effect on the compressive strength of mortar. However, it should be noted that the relative strength enhancement of mortars mixed with FNS at later curing periods is higher than that of mortar FNS at early curing periods, indicating a gradually reducing the gap in strength between reference and mortar FNS. These phenomena were also reported by other researchers [4, 9]. The low reactivity of FNS is due to the low amount of Calcium content and inadequate fineness which does not speed up the reaction degree of cement hydration in the short period. The pozzolanic reactivity of FNS starts relatively late which will gradually consume the excess of $Ca(OH)_2$ from cement hydration to generate CSH gel.

According to the methods explained above, the FNS was ground intensively to achieve two levels of fineness. Besides this, the heat treatment was applied to the specimens. So that, these aspects will be emphasized in the next sections.

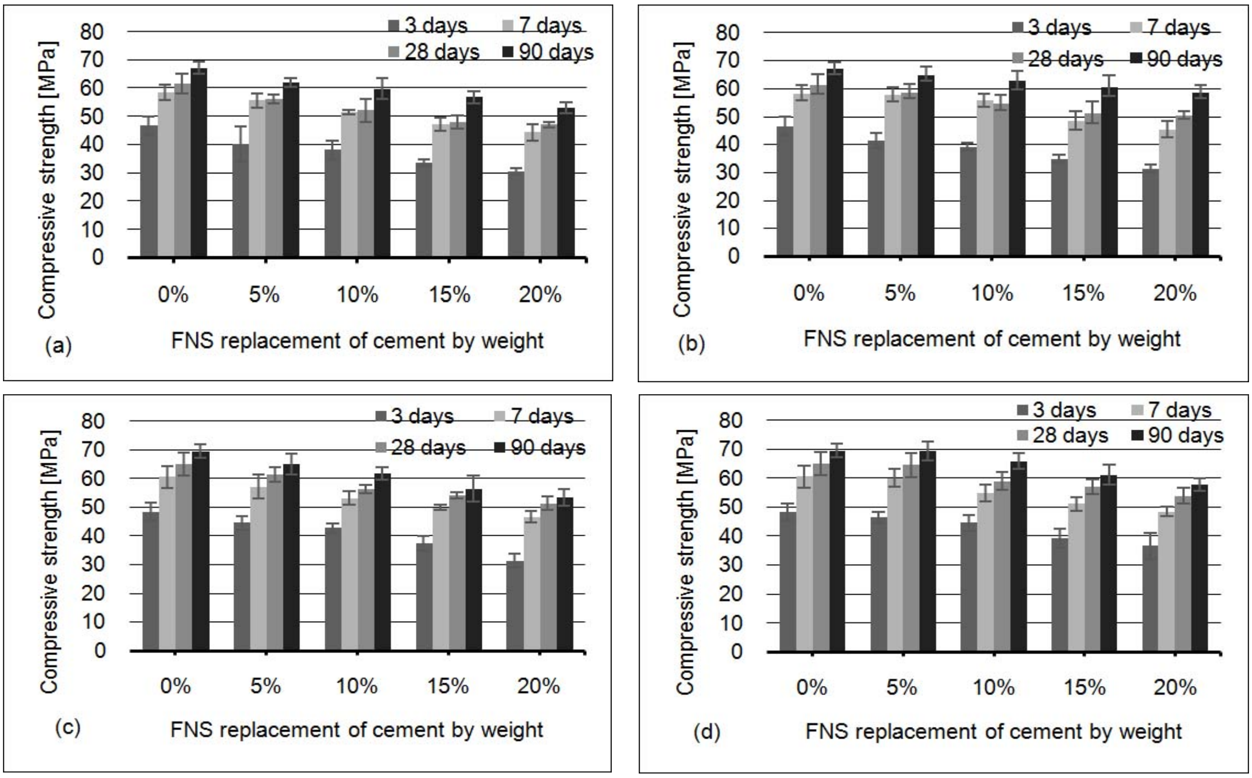

Figure 7. Mortar compressive strength results of difference fineness and treatment: (a) FNS_F1 + NC, (b) FNS_F2 + NC, (c) FNS_F1 + HT, (d) FNS_F2 + HT (error bars represent standard errors, the average values represent three replicates).

3.4.1. Effect of fineness of FNS as cement replacement

The influence of the fineness of FNS as cement replacement on the compressive strength of mortar is shown in Fig. 8. It can be seen that the use of finer slag (FNS_F2) enhanced the compressive strength of mortar for both NC and HT compared to coarser slag (FNS_F1). It seems that a positive effect on the compressive strength of mortar is achieved by using the FNS with a higher fineness. These observations are in accordance with the findings of Kim et al. [8], who also found the positive effect of the finer FNS on the compressive strength of concrete. These results also confirm the finding of other researchers [25–29] even though they used different SCMs. This achievement might be due to the filler effect of finer FNS, which enhances the heterogeneous nucleation of cement hydration products. In addition to the filler effect, the higher fineness of FNS promotes the pozzolanic reactivity, which consumes more portlandite compared to the coarser FNS.

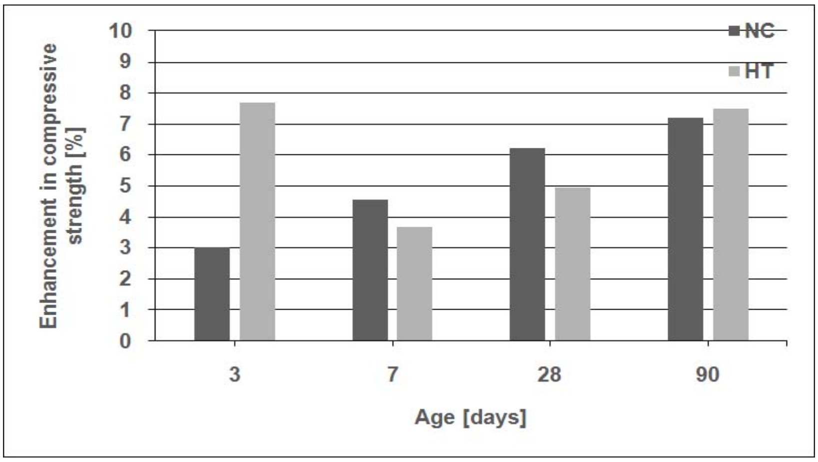

Figure 8. The change in strength development of mortar by increasing the fineness of FNS for NC and HT (The values represent the average of all replacement levels of FNS).

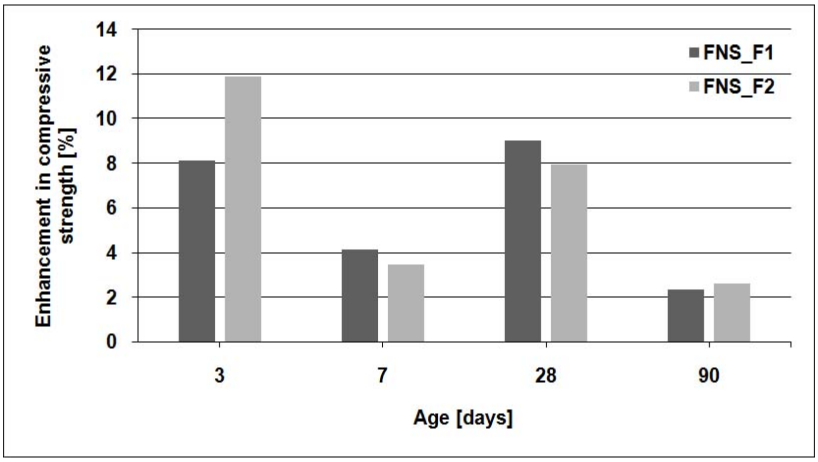

Figure 9. Enhancement in strength of mortar (HT versus NC) for FNS_F1 and FNS_F2 (The values represent the average of all replacement levels of FNS).

3.4.2. Effect of heat curing

The effect of heat curing on the strength enhancement of mortar for FNS_1 and FNS_2 is shown in Fig. 9. In general, the use of heat curing at 75 °C enhanced the compressive strength of mortar compared to that of normal curing for all curing days and both FNS_F1 and FNS_F2. It can be observed that a significant improvement of mortar strength with FNS_F2 after applying heat curing was obtained at early curing days (3 days), which increased almost 12 % compared to mortar strength applied normal curing. The latter result is not the case for mortar with FNS_F1, which achieved a higher strength development at later curing days (28 days) after applying heat treatment. For later curing periods (90 days), the use of heat curing seems beneficial in strength enhancement for both mortar FNS_F1 and FNS_F2 although this achievement is lower than for early curing periods as shown in Fig. 9. The positive effect of heat curing was also reported by other researchers [30–32]. They also found that heat treatment has a significant contribution to compressive strength at early age, which also corresponds to the result presented for mortar mixed with FNS_F2. It seems that heat curing speeds up the hydraulic and pozzolanic reactivity of binders (cement + FNS_F2) in the early curing periods, which force the FNS_F2 to release more amount of hydroxyl ion (OH^-) to consume calcium ion (Ca^{2+}) from cement. In the case of FNS_F1, a significant contribution of heat treatment in the reaction rate between a pozzolan and Ca^{2+} does not obtain due to the lower fineness of FNS_F1.

3.5. Frattini test

Fig. 10 depicts the results of the Frattini test for 8 days and 28 days. From Figure 10(a), it can be seen that all of the samples cured for 8 days are above the non-pozzolanic zone. For longer curing times, all of the data are still located in the non-pozzolanic zone. The results obtained for 8 days and 28 days indicated non-pozzolanic activity of both FNS_F1 and FNS_F2. However, it can be observed that all of the data of FNS_F2 at 28 days of curing move further and near the lime saturation curve as seen in Fig. 10(b). So that, it can be estimated that the pozzolanic activity of FNS determined by the Frattini test at 40 °C will be obtained for a curing day longer than 28 days. In literature, it is often mentioned that besides the chemical composition and the active phase content, a higher fineness also influences the rate of the pozzolanic reaction [33, 34]. This is the reason why the finer FNS used in this study consumed more amount of calcium ion (Ca^{2+}) than the coarser FNS, which led all of the plotted data of FNS_F2 to approach the saturation curve of lime as seen in Fig. 10(b). Hence, for future research, a longer grinding time combined with increasing the number of balls for FNS should be considered to behave as a pozzolan in a shorter period.

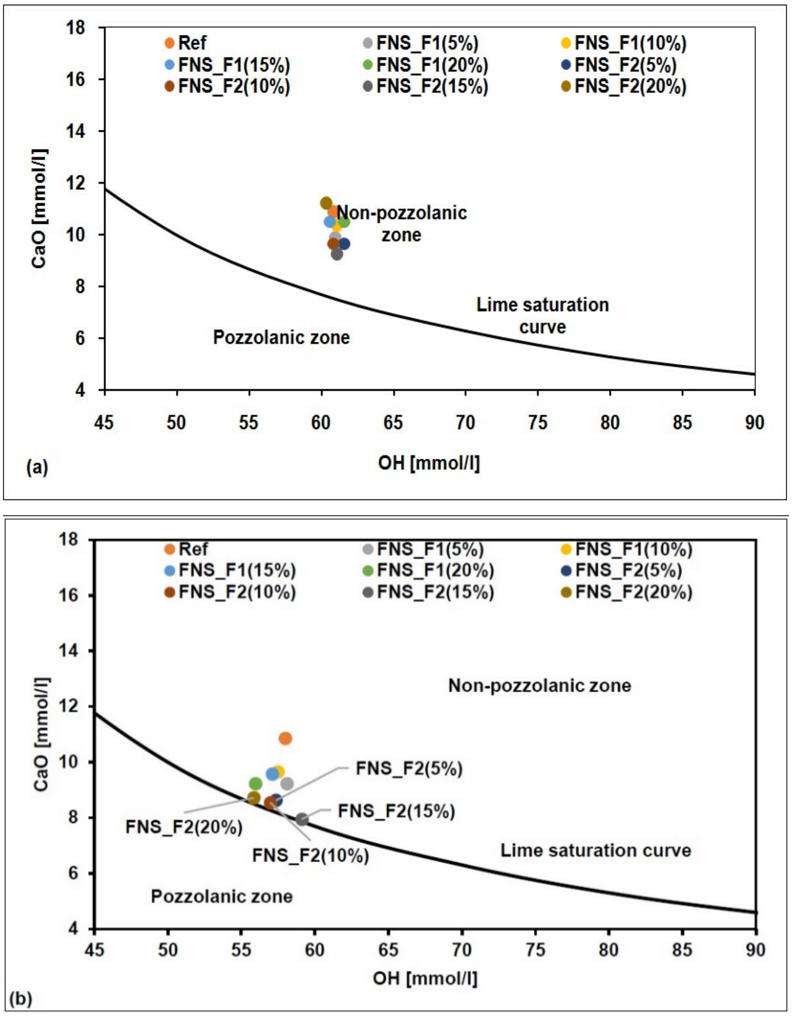

Figure 10. Frattini test results of FNS_F1 and FNS_F2 at: (a) 8 days and (b) 28 days.

3.6. Microstructure observation

To study the microstructure of mortar containing FNS, observation from literature is needed. According to [35–37], during hydration reaction, anhydrous cement grain reacts with water to generate hydration products such as CSH gel, ettringite, and calcium hydroxide (CH). While unhydrated cement grains (UCG) and pores still exist in the cementitious system in white and black parts, respectively. The UCG and pores can be clearly detected in this observation at a magnification of 100x as seen in Fig. 11, while CH and CSH need a microscope with a higher magnification (i.e. 350x).

For 10 % FNS_F2 + NC at 28 days, hydration reaction continued in which UCG with the particle size lower than 20 µm were encircled by thick rims of CSH and CH. The UCG with higher particle size tends to agglomerate and appearing between aggregates or surrounding aggregates as seen in Fig. 11(a). After applying heat treatment, UCG was partially hydrated, reducing the amount of UCG as visualized in Fig. 11(b). At young ages during the period of heat treatment, the UCG was partially hydrated to form the lighter CSH, while the darker CSH was gradually formed during the period of curing in water. At this phase, the amount of pore was reduced, filled by CSH, generating a denser paste.

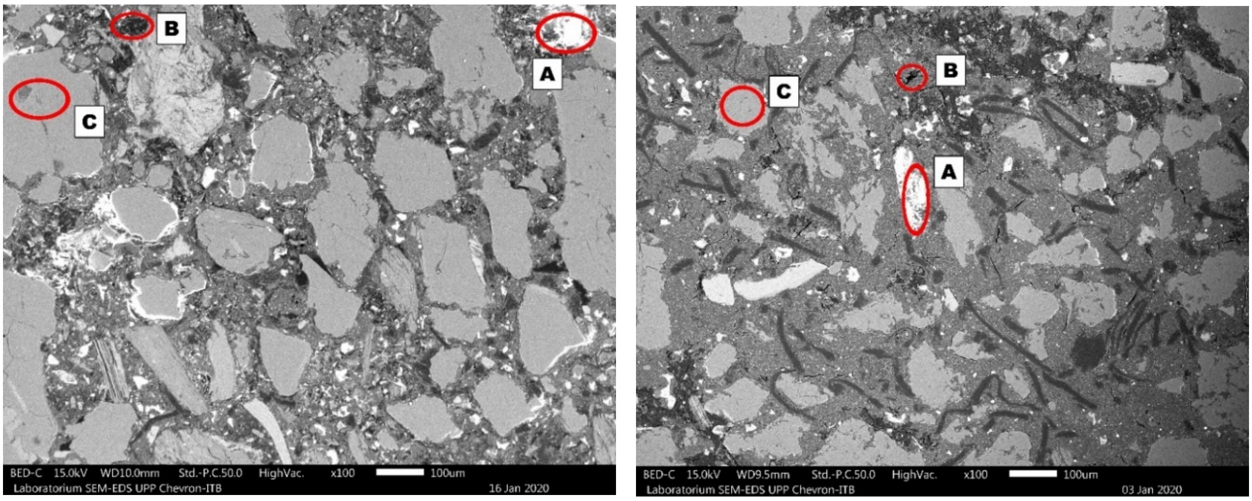

Figure 11. Visualization of the selected mortar mixture at 28 days by SEM-BSE: 10 % FNS_F2 + NC (left) and 10 % FNS_F2 + HT (right) (A = unhydrated cement grain; B = pore; C = fine aggregate).

4. Conclusions

In this study, the use of ferronickel slag (FNS) as a fine aggregate replacement and cement replacement was investigated. The following conclusions can be drawn based on the results obtained:

- The workability of fresh concrete and mortar increased as the increase of the FNS content. The higher specific area of FNS decreased the flowability of mortar. This is due to the filling effect of FNS finer in the air cavities, which increases the viscosity of fresh mortar.
- The use of FNS for up to 40 % fine aggregate replacement enhanced the compressive strength of concrete, beyond that the strength of concrete decreased.
- By increasing the fineness of the FNS, a higher compressive strength of mortar can be achieved for both normal curing and heat treatment.
- The use of heat treatment gives a positive effect on the strength development of mortar containing finer FNS or coarser FNS for all curing ages. However, for early curing days, a significant effect of heat treatment is only achieved for mortar containing FNS finer, while the effect of heat treatment is limited for mortar containing FNS coarser.
- The results of the pozzolanic activity assessed by the Frattini test show that all of the mixtures with FNS indicate no pozzolanic activity after 28 days of curing. However, the FNS finer consumes more portlandite than the FNS coarser.
- Based on the microscope observation, the use of heat treatment partially hydrated unhydrated cement grains.

5. Acknowledgements

The authors would like to thank the Ministry of Research, Technology and Higher Education of the Republic of Indonesia for providing the financial support to this research project (National Competitive Grant 2019-2021 with contract number: 171/SP2H/LT/DRPM/2019). The authors would also like to acknowledge Research and Development Strengthening Agency of the Ministry of Research, Technology and Higher Education of the Republic of Indonesia for Grant for participation in a conference abroad with contract number: B/2795/E5.3/KI.03.01/2019. Special thanks are addressed to the Construction and Material Laboratory at Halu Oleo University (staff and student) for their contribution to this research.

References

1. Klee, H. The Cement Sustainability Initiative: Recycling Concrete. World Business Council for Sustainable Development. 2009. (July).
2. Edwin, R.S., Ngii, E., Talanipa, R., Masud, F., Sriyani, R. Effect of nickel slag as a sand replacement in strength and workability of concrete. IOP Conference Series: Materials Science and Engineering. 2019. 615(1). DOI: 10.1088/1757-899X/615/1/01-2014
3. Schneider, M., Romer, M., Tschudin, M., Bolio, H. Sustainable cement production-present and future. Cement and Concrete Research. 2011. 41 (7). Pp. 642–650. DOI: 10.1016/j.cemconres.2011.03.019.

4. Katsiotis, N.S., Tsakiridis, P.E., Velissariou, D., Katsiotis, M.S., Alhassan, S.M., Beazi, M. Utilization of Ferronickel Slag as Additive in Portland Cement: A Hydration Leaching Study. Waste and Biomass Valorization. 2015. 6 (2). Pp. 177–189. DOI: 10.1007/s12649-015-9346-7
5. Saha, A.K., Sarker, P.K. Expansion due to alkali-silica reaction of ferronickel slag fine aggregate in OPC and blended cement mortars. Construction and Building Materials. 2016. 123. Pp. 135–142. DOI: 10.1016/j.conbuildmat.2016.06.144.
6. Sun, J., Feng, J., Chen, Z. Effect of ferronickel slag as fine aggregate on properties of concrete. Construction and Building Materials. 2019. 206. Pp. 201–209. DOI: 10.1016/j.conbuildmat.2019.01.187.
7. Saha, A.K., Sarker, P.K. Sustainable use of ferronickel slag fine aggregate and fly ash in structural concrete: Mechanical properties and leaching study. Journal of Cleaner Production. 2017. 162. Pp. 438–448. DOI: 10.1016/j.jclepro.2017.06.035.
8. Kim, H., Hong, C., Yong, K. Feasibility of ferronickel slag powder for cementitious binder in concrete mix. Construction and Building Materials. 2019. 207. Pp. 693–705. DOI: 10.1016/j.conbuildmat.2019.02.166.
9. Huang, Y., Wang, Q., Shi, M. Characteristics and reactivity of ferronickel slag powder. Construction and Building Materials. 2017. 156. Pp. 773–789. DOI: 10.1016/j.conbuildmat.2017.09.038.
10. Li, B., Huo, B., Cao, R., Wang, S., Zhang, Y. Sulfate resistance of steam cured ferronickel slag blended cement mortar. Cement and Concrete Composites. 2019. 96 (December 2018). Pp. 204–211. DOI: 10.1016/j.cemconcomp.2018.12.001.
11. BSN. SNI-03-2834-2000. Indonesia Standard for Mix Design of Normal Concrete 2000.
12. EN-196-1, Methods of testing cement – Part 1: Determination of strength. 2005, CEN: Brussels, Belgium. Work. 2007. (april). Pp. 0–90.
13. Kjellsen, K.O., Detwiler, R.J., Gjørv, O.E. Pore structure of plain cement pastes hydrated at different temperatures. Cement and Concrete Research. 1990. 20 (6). Pp. 927–933. DOI: 10.1016/0008-8846(90)90055-3
14. Edwin, R.S., Gruyaert, E., Dils, J., De Belie, N. Influence of Vacuum Mixing on the Carbonation Resistance and Microstructure of Reactive Powder Concrete Containing Secondary Copper Slag as Supplementary Cementitious Material (SCM). Procedia Engineering. 2017. 171. DOI: 10.1016/j.proeng.2017.01.367
15. Kjellsen, K.O. Heat curing and post-heat curing regimes of high-performance concrete: influence of microstructure and C-S-H compositions. Cement and Concrete Research. 1996. 2. Pp. 295–307.
16. Heinz, D., Ludwig, H.M. Heat treatment and the risk of DEF delayed ettringite formation in UHPC. International symposium on ultra high performance concrete. 2004. Pp. 717–730.
17. EN-196-5, Methods of testing cement – Part 5: Pozzolanic test for pozzolanic cement. 2005, CEN: Brussels, Belgium. 2005.
18. Donatello, S., Tyrer, M., Cheeseman, C.R. Comparison of test methods to assess pozzolanic activity. Cement and Concrete Composites. 2010. 32. Pp. 121–127.
19. BSN. SNI-1972-2008. Indonesia Standard for Slump Test of Concrete 2008.
20. EN-1015-3, Methods of test for mortar for masonry – Part 3: Determination of consistence of fresh mortar (by flow table).2006, CEN: Brussels, Belgium.2006.
21. Humad, A.M., Habermehl-Cwirzen, K., Cwirzen, A. Effects of fineness and chemical composition of blast furnace slag on properties of Alkali-Activated Binder. Materials. 2019. 12 (20). Pp. 1–16. DOI: 10.3390/ma12203447
22. Al-Jabri, K.S., Al-Saidy, A.H., Taha, R. Effect of copper slag as a fine aggregate on the properties of cement mortars and concrete. Construction and Building Materials. 2011. 25 (2). Pp. 933–938. DOI: 10.1016/j.conbuildmat.2010.06.090.
23. U.S. Department of Transportation – Federal Highway Administration Research and Technology. User Guidelines for Waste and Byproduct Materials in Pavement Construction, Publication Number: FHWA-RD-97-148. (1) 2016.
24. OBE, R.K.D., Brito, J. De, Mangabhai, R., Lye, C.Q. Sustainable construction materials: Copper slag. Woodhead Publisihing, 2016.
25. Edwin, R.S., De Schepper, M., Gruyaert, E., De Belie, N. Effect of secondary copper slag as cementitious material in ultra-high performance mortar. Construction and Building Materials. 2016. 119. DOI: 10.1016/j.conbuildmat.2016.05.007
26. Sajedi, F. Mechanical activation of cement-slag mortars. Construction and Building Materials. 2012. 26 (1). Pp. 41–48. DOI: 10.1016/j.conbuildmat.2011.05.001
27. Khan, K., Amin, M.N. Influence of fineness of volcanic ash and its blends with quarry dust and slag on compressive strength of mortar under different curing temperatures. Construction and Building Materials. 2017. 154. Pp. 514–528. DOI: 10.1016/j.conbuildmat.2017.07.214
28. Liu, S., Zhang, T., Guo, Y., Wei, J., Yu, Q. Effects of SCMs particles on the compressive strength of micro-structurally designed cement paste: Inherent characteristic effect, particle size refinement effect, and hydration effect. Powder Technology. 2018. 330. Pp. 1–11. DOI: 10.1016/j.powtec.2018.01.087
29. Mirzahosseini, M., Riding, K.A. Influence of different particle sizes on reactivity of finely ground glass as supplementary cementitious material (SCM). Cement and Concrete Composites. 2015. 56. Pp. 95–105. DOI: 10.1016/j.cemconcomp.2014.10.004
30. Zdeb, T. An analysis of the steam curing and autoclaving process parameters for reactive powder concretes. Construction and Building Materials. 2017. 131. Pp. 758–766. DOI: 10.1016/j.conbuildmat.2016.11.026
31. Urbonas, L., Heinz, D., Gerlicher, T. Ultra-High Performance Concrete Mixes with Reduced Portland Cement Content. Journal of Sustainable Architecture and Civil Engineering. 2013. 3 (4). DOI: 10.5755/j01.sace.3.4.4569
32. Helmi, M., Hall, M.R., Stevens, L.A., Rigby, S.P. Effects of high-pressure/temperature curing on reactive powder concrete microstructure formation. Construction and Building Materials. 2016. 105. Pp. 554–562. DOI: 10.1016/j.conbuildmat.2015.12.147
33. Snellings, R., Scrivener, K.L. Rapid screening tests for supplementary cementitious materials: past and future. Materials and Structures/Materiaux et Constructions. 2016. 49 (8). Pp. 3265–3279. DOI: 10.1617/s11527-015-0718-z
34. Mertens, G., Snellings, R., Van Balen, K., Bicer-Simsir, B., Verlooy, P., Elsen, J. Pozzolanic reactions of common natural zeolites with lime and parameters affecting their reactivity. Cement and Concrete Research. 2009. 39 (3). Pp. 233–240. DOI: 10.1016/j.cemconres.2008.11.008. URL: http://dx.doi.org/10.1016/j.cemconres.2008.11.008
35. Famy, C., Scrivener, K.L., Atkinson, A., Brough, A.R. Effects of an early or a late heat treatment on the microstructure and composition of inner C-S-H products of Portland cement mortars. Cement and Concrete Research. 2002. 32 (2). Pp. 269–278. DOI: 10.1016/S0008-8846(01)00670-6

36. Gallucci, E., Zhang, X., Scrivener, K.L. Effect of temperature on the microstructure of calcium silicate hydrate (C-S-H). Cement and Concrete Research. 2013. 53. Pp. 185–195. DOI: 10.1016/j.cemconres.2013.06.008.

37. Scrivener, K.L. Backscattered electron imaging of cementitious microstructures: Understanding and quantification. Cement and Concrete Composites. 2004. 26 (8). Pp. 935–945. DOI: 10.1016/j.cemconcomp.2004.02.029

Contacts:

Romy Suryaningrat Edwin, romy.edwin@uho.ac.id
Masykur Kimsan, masykur.kimsan@uho.ac.id
Bambang Pramono, Bambang.pramono@uho.ac.id
Fitriah Masud, fitriah.ecek@uho.ac.id
Rini Sriyani, rini.sriyani@uho.ac.id

Magazine of Civil Engineering. 2022. 109(1). Article No. 10910

Magazine of Civil Engineering

ISSN
2712-8172

journal homepage: http://engstroy.spbstu.ru/

DOI: 10.34910/MCE.109.10

Algorithm for building structures optimization based on Lagrangian functions

T.L. Dmitrieva*[a], Kh. Ulambayar[b]

[a] *Irkutsk National Research Technical University, Irkutsk, Russia*

[b] *Mongolian University of Science and Technology, Mongolia*

**E-mail: dmitrievat@list.ru*

Keywords: modified Lagrangian multiplier method, building structures, optimum design, steel beam, truss structure, finite element model

Abstract. A review of modern algorithms and optimization programs is presented, based on which it is concluded that there is no application software in the field of optimal design of building structures. As part of solving this problem, the authors proposed numerical optimization algorithms based on conditionally extreme methods of mathematical programming. The problem of conditional minimization is reduced to a problem of an unconditional extreme using two modified Lagrange functions. The advantage of the proposed methodology is a wide range of convergence, the absence of requirements for convexity of functions on an admissible set of variation parameters, as well as high convergence, which can be achieved by adjusting the parameters of the objective and constraint functions. Verification of the developed methodology was carried out by solving a well-known example of ten-bar truss optimization. A comparison of the results obtained by other sources with the copyright ones confirmed the effectiveness of the presented algorithms. As an example, the problems of optimizing the cross-section of a steel beam have also been solved. Automation of the algorithms is performed in mathematical package *MathCAD*, which allows you to visually trace the sequence of commands, as well as obtain graphs that reflect the state of the task at each iteration. Thus, the authors obtained an original methodology for solving the optimization problem of flat bar structures, which can be extended to solve the problem of optimal design of general structures, where the optimality criterion is defined as material consumption, and the given structural requirements are presented as constraint functions.

1. Introduction

Most of these problems are formulated in the form of a nonlinear programming problem and were solved using gradient methods of the 1st or 2nd order or direct (zero order) methods of constrain and unconstrain minimization [1].

For the first time, the most general statement of the optimization problem was proposed by L. Schmitt [2], where he indicated the admissibility of the application of structural analysis using the finite element model and the nonlinear programming method in the presence of various forms of constraints. In 1979, a monograph was published by American scientists E. Haug (Edward J. Haug) and J. S. Arora (Jasbir S. Arora) [3]. This work gave a serious impetus to the development of the applied direction of optimization. It outlined general approaches to solving the problems of analysis and synthesis of mechanical systems. The 70-80s of the last century also accounted for numerous software implementations of optimization algorithms.

Note that the nonlinear programming methods embedded in these algorithms have a rigorous mathematical justification of the convergence conditions, but are rather laborious in solving large-

Dmitrieva, T.L., Ulambayar, Kh. Algorithm for building structures optimization based on Lagrangian functions. 2022. 109(1). Article No. 10910. DOI: 10.34910/MCE.109.10

dimensional problems when it is necessary to optimize, for example, the topology of plane and spatial objects, explore dynami processes, etc.

Nevertheless, these algorithms still find application in applied optimization problems, as well as in their software implementations [4, 5]. Wherein, the problem of static and dynamic analysis of structural is performed using the finite element method algorithm, which over the past decades has been developed for tasks of a special kind [6, 7].

Since the 90s, a large number of studies have appeared in the field of optimization of engineering systems that use metaheuristics. Metaheuristic algorithms explore the search space using probabilistic transition rules [8-10]. Here, a possible solution is sought by random selection, combination and variation of the desired parameters with the implementation of mechanisms resembling biological evolution, or physical processes occurring in nature. Here are just some examples of heuristic algorithms: genetic algorithm (GA) [11], ant colony algorithm (ACO) [12], artificial bee colony algorithm (ABC) [13], particle swarm optimization (PSO) [14], firefly algorithm (FA) [15], raven search algorithm (CSA) [16], gray wolf algorithm (AGW) [17], bat algorithm (BA) [18], annealing simulation algorithm (SA) [19] and others [20–22]. In [23–28], practical problems of optimizing building structures using metaheuristic algorithms are presented.

Most theoretical research in the field of numerical optimization of structures was accompanied by their software implementation. Among the leading software systems, including optimization modules, the “heavy” multipurpose universal software packages “MSC Nastran”, “ANSYS” and “ABAQUS” should be noted first of all. At the same time, in spite of many approaches, the problem of solving the problems of optimizing complex technical objects in an acceptable time and with a given degree of error still remains relevant. Over the past decade, a new direction has emerged related to the construction of optimization models based on the use of neural networks, where the search process is controlled by intelligent systems [29].

In the Russian design, the most fully automated calculations related to structural optimization are implemented in the field of aircraft manufacturing (just call the “IOSO NM” software package). A sufficient number of publications are devoted to the issues of optimizing building structures, which describe algorithms and software developments [30], however, these programs are of a research or narrow applied nature. In general, it should be noted that the optimization of construction projects is not yet widely used in real design.

This is due to the fact that the designer, on the one hand, does not have to possess the intricacies of optimization algorithms, and at the same time, such calculations require concomitant “manual” control, which is expressed, for example, in setting some parameters that significantly affect the convergence in tracking local extremes, etc. Thus, the problem of constructing universal optimization algorithms with a wide area of convergence, and at the same time not requiring serious “tuning” to the task, is quite demanded, significantly determining the implementation of these algorithms in design practice.

2. Methods

In this paper, we propose an algorithm for the numerical optimization of flat rod systems. In its most general form, this problem can be formalized as a conditionally-extremal nonlinear programming problem (NLP) [31–34].

minimize $$f\left(x\right), \quad x \in E^{nx}, \tag{1}$$

subject to: $$g_j\left(x\right) \le 0, \quad j = 1, 2 \ldots m, \tag{2}$$

$$x_i^L \le x_i \le x_i^U, \; i = 1, 2 \ldots nx, \tag{3}$$

where $f(x)$ and $\{x\}$ are the objective function of variable parameters and the vector of these parameters on the interval $\{x^L\} - \{x^U\}$, and $g(x)$ is the constraint functions in the form of equalities and inequalities.

The problem of constrain minimization of the function of many variables (1-3) can be reduced to the problem of unconstrain minimization using the Lagrangian function F_L

$$F_L = f\left(x\right) + \left\{Y\right\}^T \left\{g\right\}, \tag{4}$$

where $\{Y\}$ is the Lagrange multiplier vector. In this case, the solution of problem (1-3) coincides with the saddle point of the Lagrangian function, for the determination of which the condition of its stationarity of this function with respect to x and y is used:

$$\frac{\partial F_L}{\partial x_i} = 0, \tag{5}$$

$$\frac{\partial F_L}{\partial y_j} = 0, \qquad j = 1, 2, \ldots m.$$

These conditions were obtained for the convex optimization problem by Kuhn and Tucker, and can serve as a check of a reliable optimum.

Since the problem is solved in the space of two vectors $\{X\}$ and $\{Y\}$, the vector $\{X\}$ is usually defined as a vector of direct variables, and the elements of the vector $\{Y\}$ are called dual variables.

One of the significant drawbacks of the Lagrangian function is that it is applicable to a limited class of convex, separable programming problems. To construct methods with a wider region of convergence and applicable for finding a local extremum in non-convex problems, it is necessary to introduce additional terms into the structure of the function, which lead to an optimum shift in the search iterations, thus modifying the standard Lagrangian function. Various versions of the methods of a modified Lagrangian function are described in [35–39].

The purpose of this article is to illustrate the effectiveness of the methods of a modified Lagrangian functions and algorithms based on them in solving problems of optimizing geometric parameters of flat bar structures by the criterion of the minimum of their volume when fulfilling the standard requirements for strength and rigidity. The stated goal involves solving the following tasks:

- investigation of the properties of a modified Lagrangian functions;
- development of numerical algorithms based on these functions;
- solving problems using the proposed methods;
- comparison of the efficiency of algorithms for the rate of convergence and error in the results.

We introduce two modified Lagrangian function F_P and F_M

$$F_P = k_f F_L + 0.5\{g\}^T [\delta][k]\{g\} + 0.5k_f \{Y\}^T ([\delta]-[I])\{\Delta Z\}, \tag{6}$$

$$F_M = k_f F_L (1-\tau) - 0.5\tau \left\{\frac{\partial F_L}{\partial x}\right\}^T \left\{\frac{\partial F_L}{\partial x}\right\}. \tag{7}$$

Here, $[I]$ is identity matrix; $[k]$ is diagonal matrix of penalty coefficient; k_f is normalization factor introduced to increase computational stability; τ is convergence control constant; ΔZ_j is constraint shear amount to an allowable area; $[\delta]$ is diagonal matrix of Boolean variables whose elements are determined from the condition:

if $g_j + \Delta Z_j > 0,$ then $\delta_{jj} = 1,$ otherwise $\delta_{jj} = 0.$

Thus, the function F_P can be interpreted as the sum consisting of the Lagrangian function and the penalty for violation of restrictions, shifted by an amount ΔZ to an allowable area.

The function F_M is the sum of the Lagrangian function and the penalty for not fulfilling the stationarity conditions at the point $\{X^t\}$. If $\{X^*\}$, $\{Y^*\}$ are solution of the problem (1-3), then the ratio is true:

$$\frac{1}{k_f^t} F_M \left(X^*, Y\right) \le F_L \left(X^*, Y^*\right) \le \frac{1}{k_f^t} F_P \left(X, Y^*\right).$$

An equal sign in this expression is possible only with $X = X^*$; $Y = Y^*$, since at the same time penal additives turn into zero.

Consider iterative algorithms using a modified Lagrangian functions, which at each iteration in turn include two main procedures:

- determination of the vector of direct variables $\{X^{t+1}\}$;
- definition of a vector of dual variables $\{Y^{t+1}\}$.

The iterative process terminated by the condition of convergence:

$$\left|\left\{X^{t+1}\right\}-\left\{X^{t}\right\}\right| \le \varepsilon_x \left|\left\{X^{t}\right\}\right|, \qquad \bar{g}_j \le \varepsilon_g, \quad j=1,...m^*, \tag{8}$$

or if the specified limit number of iterations is exceeded *it_lim*.

In expression (8), $\left\{\bar{g}\right\}$ is a vector of potentially active constraints of dimension m^*; ε_x, ε_g are predetermined calculation error; t is iteration number.

2.1. Direct method for solving the problem NLP

Consider an iterative algorithm for solving problem (1-3), which operates only with a function $F_P\,(x, y)$ and reduces to finding the saddle point of this function from the condition

$$\max_{y\in E^m} \quad \min_{x\in E^{nx}} \quad F_P\left(x, y\right).$$

The most stable version of this algorithm is when direct variables are determined from the condition of minimizing the function F_P

$$\begin{gathered}\left\{X\right\} \in Arg\min F_P\left(X^t, Y^t\right)\\ \left\{X^L\right\} \le \left\{X\right\} \le \left\{X^U\right\},\end{gathered} \tag{9}$$

and the dual conditions from the equality of stationarity with respect to X are the Lagrangian functions F_L (expression (4)) F_P and functions (expression (6)), which after the corresponding transformations has the form:

$$y_j^{t+1} = \max\left(y_j^t + \frac{k_{jj}^t}{k_f^t} g\left(x^{t+1}\right)\right).$$

This algorithm is investigated in [30]. In a comparative analysis with another algorithm, we designate it as “direct”, since the search for an extremum at iteration t here is carried out only by direct variables $\{X\}$.

3. Results and Discussion

Based on the foregoing, the authors propose a numerical algorithm to solve problems (1-3) using two modified Lagrangian functions – function (6) and function (7).

3.1. Combined method for solving the problem NLP

At each iteration of the algorithm, to find the vector $\{X^{t+1}\}$, the function F_P in X (6) is also minimized, and dual variables are determined directly through straight lines by maximizing the function F_M.

$$\begin{gathered}\left\{Y^{t+1}\right\} \in Arg\max F_M\left(X^t, Y^t\right)\\ Y \in E^m.\end{gathered} \tag{10}$$

Expression (10) is more convenient to obtain explicitly. For this, we substitute the expression of the Lagrangian function F_L in function F_M (7). To maximize the function F_M with respect to y, we perform differentiation with respect to this variable and equate the result to zero:

$$\left\{\frac{\partial F_M}{\partial y}\right\} = k_f\left(1-\tau\right)\left[\delta\right]\left\{g\left(x\right)\right\} -$$

$$-0.5\tau\left[\left(2\left[\delta\right]\left[\frac{\partial g\left(x\right)}{\partial x}\right]^T\left\{\frac{\partial f\left(x\right)}{\partial x}\right\} + 2\left[\delta\right]\left[\frac{\partial g\left(x\right)}{\partial x}\right]^T\left\{\frac{\partial g\left(x\right)}{\partial x}\right\}\left[\delta\right]\left\{Y\right\}\right)\right] = 0.$$

Expand the brackets and simplify this expression:

$$k_f\left(1-\tau\right)\left[\delta\right]\left\{g\left(x\right)\right\}-$$
$$-\tau\left[\delta\right]\left[\frac{\partial g\left(x\right)}{\partial x}\right]^T\left\{\frac{\partial f\left(x\right)}{\partial x}\right\}-\tau\left[\delta\right]\left[\frac{\partial g\left(x\right)}{\partial x}\right]^T\left\{\frac{\partial g\left(x\right)}{\partial x}\right\}\left[\delta\right]\left\{Y\right\}=0. \quad (11)$$

Since the function F_M is quadratic, expression (11) is reduced to a symmetric system of linear algebraic equations:

$$\left[W\right]\left\{\overline{Y}\right\}=\left\{P\right\}, \quad (12)$$

where $[W]$ is a matrix whose dimension is equal to the number of active constraints ($m^* \times m^*$), $\{\bar{Y}\}$ is vector of dual variables reduced to dimension m^*. Each element of this matrix is determined by the product of vectors:

$$W_{ij}=\left\{\frac{\partial \overline{g}_i}{\partial x}\right\}^T\left\{\frac{\partial \overline{g}_j}{\partial x}\right\}. \quad (13)$$

In expression (13) a dash sign indicates that derivatives are taken only by active restrictions. Matrix dimension $\left[\frac{\partial \overline{g}}{\partial x}\right]$ – $nx \times m^*$.

The element i of the vector P is formed by the expression:

$$P_i=-k_f\left\{\frac{\partial \overline{g}_i}{\partial x}\right\}^T\left\{\frac{\partial f}{\partial x}\right\}+\frac{\left(1-\tau\right)}{\tau}g_i. \quad (14)$$

In (14) vectors $\left\{\frac{\partial \overline{g_i}}{\partial x}\right\},\left\{\frac{\partial f}{\partial x}\right\}$ have dimension nx, where nx is the number of variable parameters that belong to an admissible region ($x_i^L \le x_i \le x_i^U$).

A distinctive feature of the combined algorithm is that when solving a conditionally extremal problem on its basis, there is no requirement for accuracy in the search for direct variables, i.e. their calculation at the iteration may have an error, and reflect only a certain movement towards the optimum.

A mixed form of these algorithms is possible when, at the first iteration, if a good initial approximation of the variables $\{X^0\}$ is known and there are no recommendations for the assignment of dual variables, a combined approach is used, and at subsequent iterations, the dual variables are recalculated using the direct method.

3.2. Algorithm for solving conditional-extreme problems for NLP using the combined method

The sequence of operations of the above algorithms differs only in the calculation of dual variables.

Since in the combined method this procedure is much more complicated, we present here a flowchart of the algorithm of the combined method (Fig. 1).

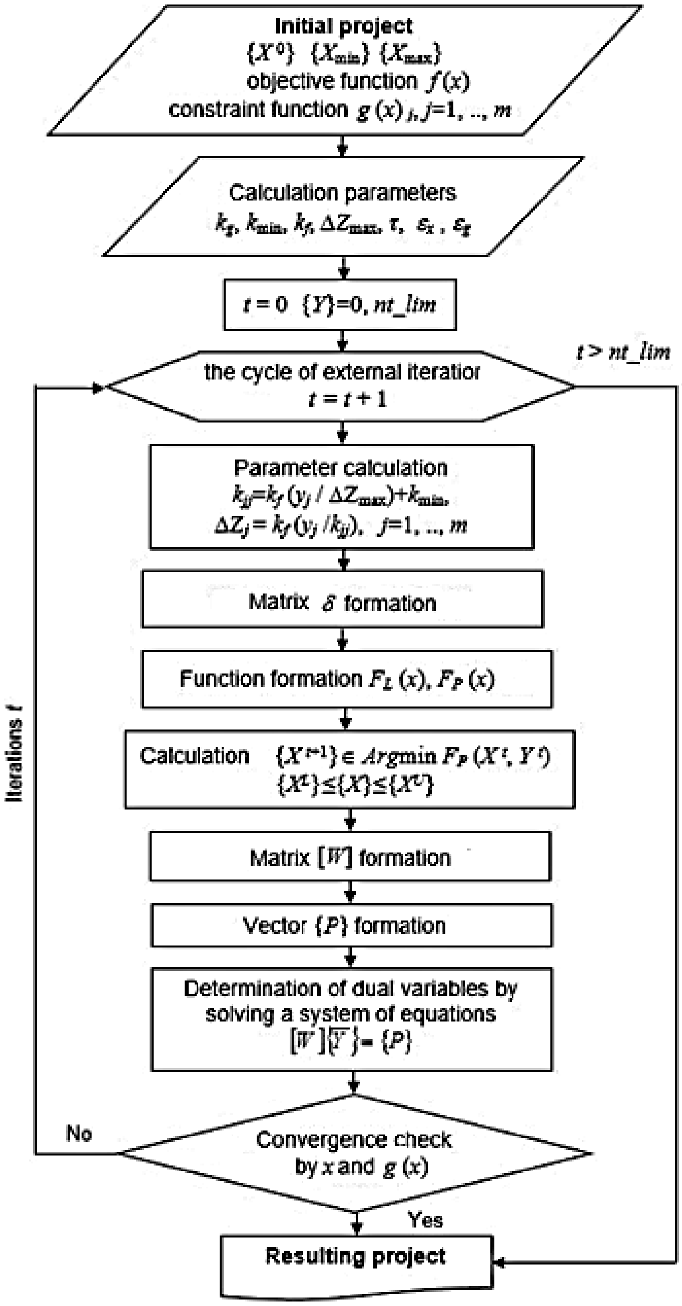

Figure 1. The flowchart of the algorithm for solving the conditional problem NLP.

3.3. Illustration of the proposed algorithm

Let us illustrate the operation of the algorithm by the example of the problem of optimal design of flat web steel I-beam, working on bending (Fig. 2).

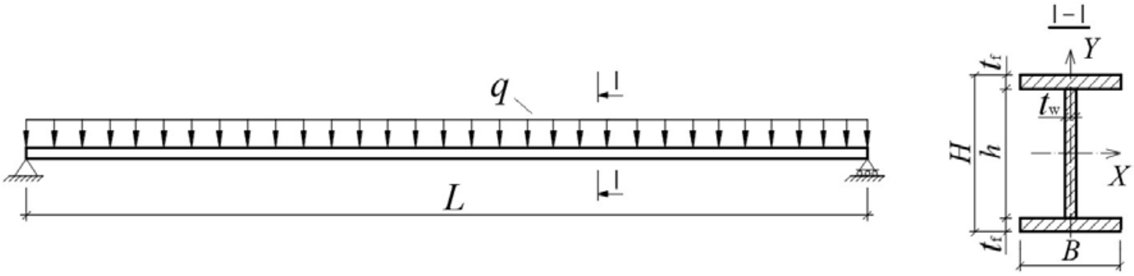

Figure 2. Calculation scheme of beam.

Initial data: L = 9 m; q = 0.08 MN/m.

Physical characteristics of the beam material: the modulus of elasticity E = 2.06·10^5 MPa; the stress restrictions R_u = 230 MPa; R_s = 133 MPa.

Problem statement

It is required to select the parameters of the beam section at a given interval by minimizing its volume, provided that the regulatory requirements for strength and rigidity are met.

3 parameters of the cross section of the composite I-beam vary (Table 1).

Table 1. Variable parameters.

Parameter number	Designation	Description
X_1	h	Web depth
X_2	B	Flange width
X_3	t_f; t_w	Flange and Web thickness

The initial value of the varied parameters and the limits of their change:

$X_1 = h$ = 0.50 m [0.20÷1.20 m]; $X_2 = B$ = 0.1 m [0.07÷0.60 m]; $X_3 = t_f = t_w$ = 0.03 m [0.0008÷0.08 m].

The objective function $f(x)$ represents the volume of the beam:

$$f(x) = (X_1 X_3 + 2X_2 X_3)L.$$

The restrictions used in the task are checks for strength and stability, and are set in accordance with the sections of Russian Construction Rules SP 16.13330.2001 "Steel structures". All restrictions reduced to dimensionless form are listed below.

The condition that ensures the local stability of the wall, in accordance with paragraph 8.5.1. the above Russian Construction Rules SP:

$$g_1 = \frac{h}{3.5t_f}\sqrt{\frac{R_u}{E}} - 1 \le 0,$$

where R_u is the calculated resistance by yield strength.

The check on the strength by normal stress:

$$g_2 = \frac{M}{W_{n,\min} R_u} - 1 \le 0,$$

where M and $W_{n,\min}$ are the calculated value of bending moment and the minimum moment of resistance.

The check on the strength by shear stress:

$$g_3 = \frac{QS}{Jt_f R_s} - 1 \le 0,$$

where Q and R_s are the calculated value of shear force and the calculated resistance by shear, J is moment of inertia and S is the static moment of inertia.

The check by rigidity:

$$g_4 = \frac{\Delta_{\max}}{[\Delta]} - 1 \le 0,$$

where $\Delta_{\max}$ and $[\Delta]$ are the maximum value of displacement in the beam and the maximum permissible value of displacement ($[\Delta] = L/500$ = 0.018 m).

Thus, the number of variables is nx = 3, and the number of constraints is m = 4.

The parameters of the optimization algorithm in the direct method were adopted as follows:

- minimum value of coefficient penalty ($k_{\min}$) - 80;

- maximum value of shear ($\Delta Z_{\max}$) - 0.2;
- normalization coefficient of the objective function (k_f) - $3\cdot10^6$;
- normalization coefficient of constraint functions (k_g) - 50.

Since the beam is statically determinable, the calculated forces do not change during the variation of the dimensions of the cross section.

For numerical solution, 2 iterative algorithms of modified Lagrangian function were applied – direct and combined.

Here is the sequence of operations of the direct method with the notation used in the MathCAD program:

1. Input of initial data:

1.1. Assignment of deterministic geometric (L) and physical (E, R_u, R_s) parameters of the problem, the value of the intensity of the uniformly distributed load q, as well as the limiting value of the displacement Δlim.

1.2. The purpose of the optimization algorithm parameters: the number of components of the constraint vector m; normalization coefficients of the objective function and the constraint vector k_f, k_g; the minimum value of the penalty coefficient k_{min} and the maximum value of the shift value outside the permissible range ΔZ_{max}.

1.3. Assignment of initial parameters of variation (vector X) and range of variation (vectors X_{min} and X_{max}).

1.4. The appointment of the initial values of the components of the vector of dual variables y_i (i = 1…m).

2. Formalization of the objective function $f(X)$ and the vector of the constraint function $g(X)$ through variable parameters:

2.1. Formation of the objective function $f(X)$ through variable parameters.

2.2. Writing a subroutine for calculating the moment of inertia of the I-section $\boldsymbol{J}(\boldsymbol{X})$.

2.3. Writing a subroutine for calculating the static moment of the I-section $\boldsymbol{S}(\boldsymbol{X})$.

2.4. Formation of expressions of constraints g_1–g_4 by substituting in them the calculated values of the bending moment and shear force, which are expressed through variable parameters.

2.5. Formation of the constraint vector $g(X)$, where its components g_1–g_4 are multiplied by the normalization factor k_g.

3. Organization of a cycle where iterations of the search optimization algorithm are performed:

3.1. Assigning an it iteration counter.

3.2. Formation of a diagonal matrix of penalty coefficients by assigning its diagonal elements $k_{i,i}$ (i = 1…m).

3.3. Formation of the elements of the shift vector of the admissible region of restrictions ΔZ_i (I = 1..m).

3.4. Formation of a diagonal matrix is a matrix of Boolean variables by assigning its elements $\delta_{i,i}$.

3.5. Formation of the Lagrange function $F_L(X)$, as well as the modified Lagrange function $F_p(X)$.

3.6. Formation of the block for finding the minimum of the function $F_p(X)$ by X on the interval X_{min} and X_{max}, where 2 search methods of unconstrained minimization are included: Conjugate Gradient method and Quasi-Newton method. When testing each of these, a practical coincidence of results was obtained.

3.7. Formation of the vector of values of the objective function at iterations F.

3.8. Identifying the maximum value in the vector of constraints on iterations it and entering it into the vector G.

3.9. Finding the ordinal number of the maximum element in the vector of constraints on iterations it and entering it into the vector k_k.

3.10. Calculation of the elements of the vector of dual variables y_i $(i = 1...m)$.

4. Output of results:

4.1. Numerical values of the vectors of change in the target and maximum values of the restrictive functions at iterations.

4.2. The values of the optimal parameters of the section of the beam X.

4.3. Values of residual constraints without taking into account the coefficient kg.

4.4. Graphs of changes in the target and maximum values of the restrictive functions at iterations.

4.5. Rounding of the beam section parameters to the required bit depth.

The solution was carried out in universal mathematical package *MathCAD*. *MathCAD* program listings are shown in Fig. 3–13.

The results of comparative calculations for the two methods are given in Table 2.

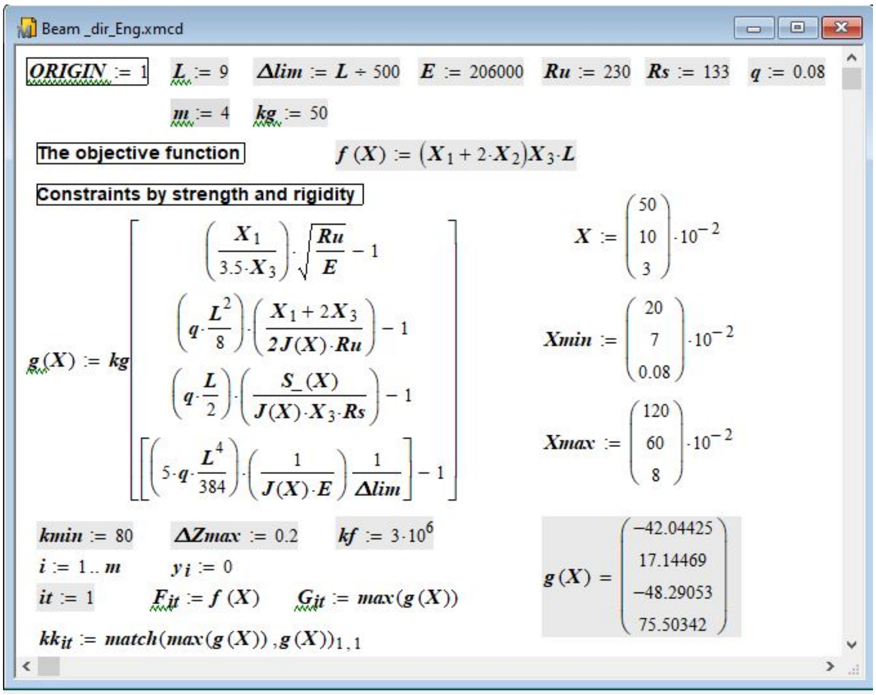

Figure 3. Implementing of numerical methods in mathematical package *MathCAD*: initial data of the task.

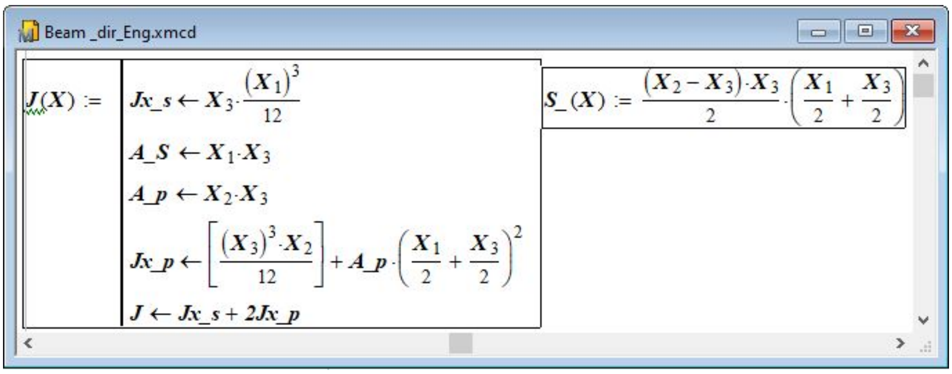

Figure 4. Subroutines used in the algorithm.

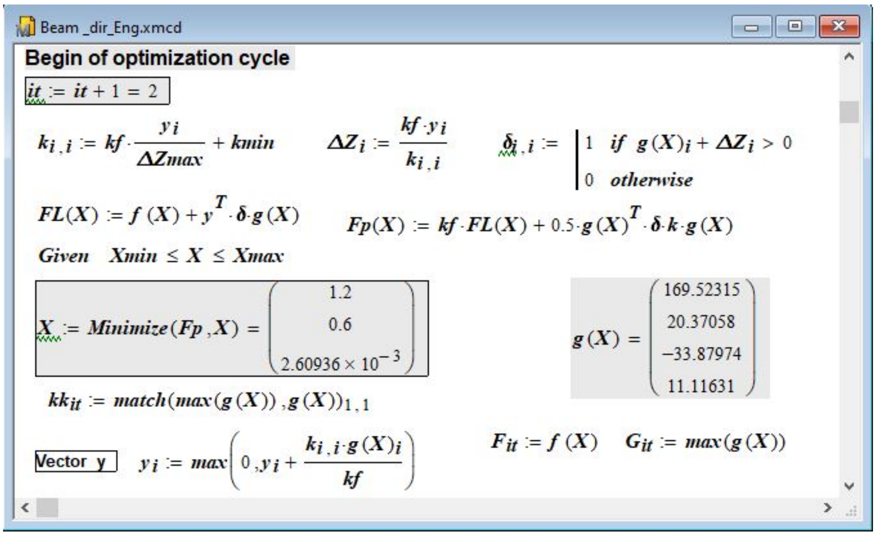

Figure 5. Begin of optimization cycle.

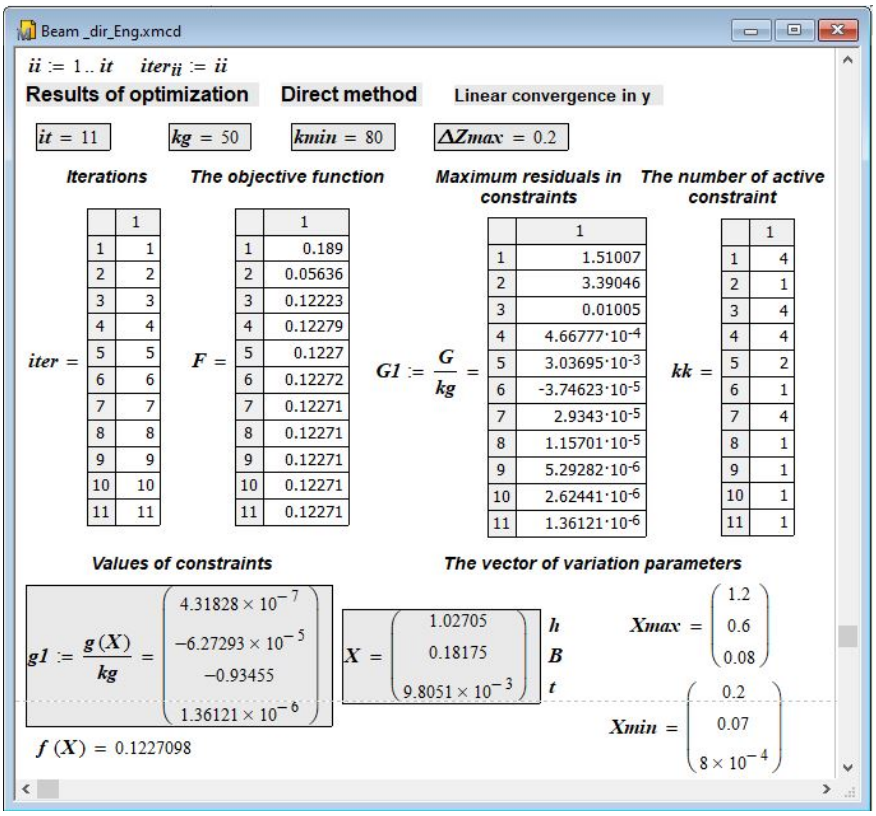

Figure 6. Optimization results.

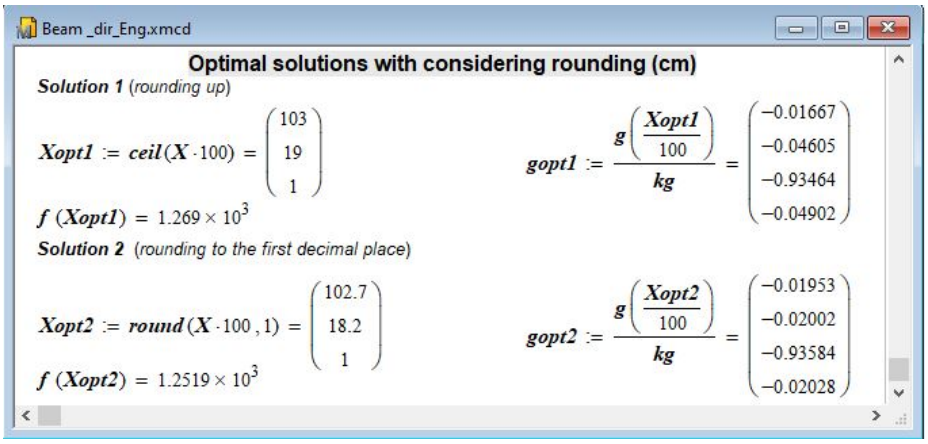

Figure 7. Optimal solutions with considering rounding.

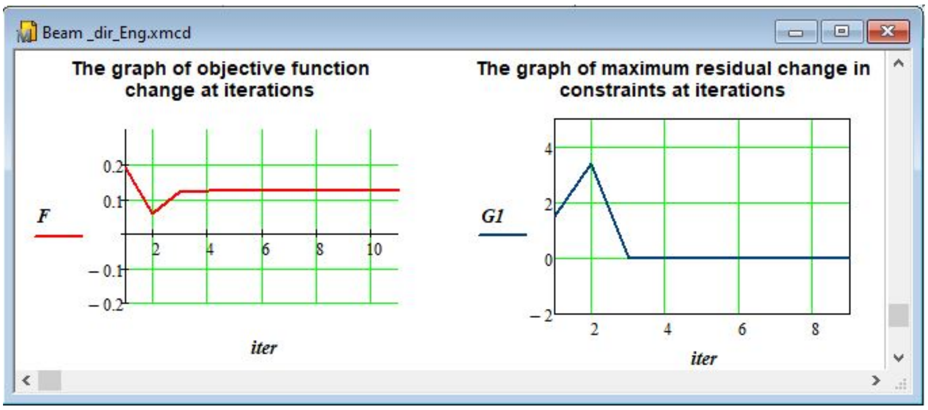

Figure 8. Graphs of changes in the objective function and maximum residuals of constraints at iterations.

The combined method algorithm differs in the following paragraphs:

P.1.2, where the parameters of the optimization algorithm are assigned, the assignment of the parameter τ is added, which is included in expression (14).

P.3.10, where the vector of dual variables $\{Y\}$ is formed, includes the solution of the system of equations (12). For this, the matrix $[W]$ and the vector $\{P\}$ are formed in the optimization cycle. This requires writing subroutines: dr_f (formation of the vector of derivatives of the objective function with respect to the varied parameters X) and dr_g (the formation of a matrix of derivatives of the functions of constraints with respect to the varied parameters X). In these subroutines, the input parameter Δ specifies the step of the offset from the current point in the numerical determination of derivatives.

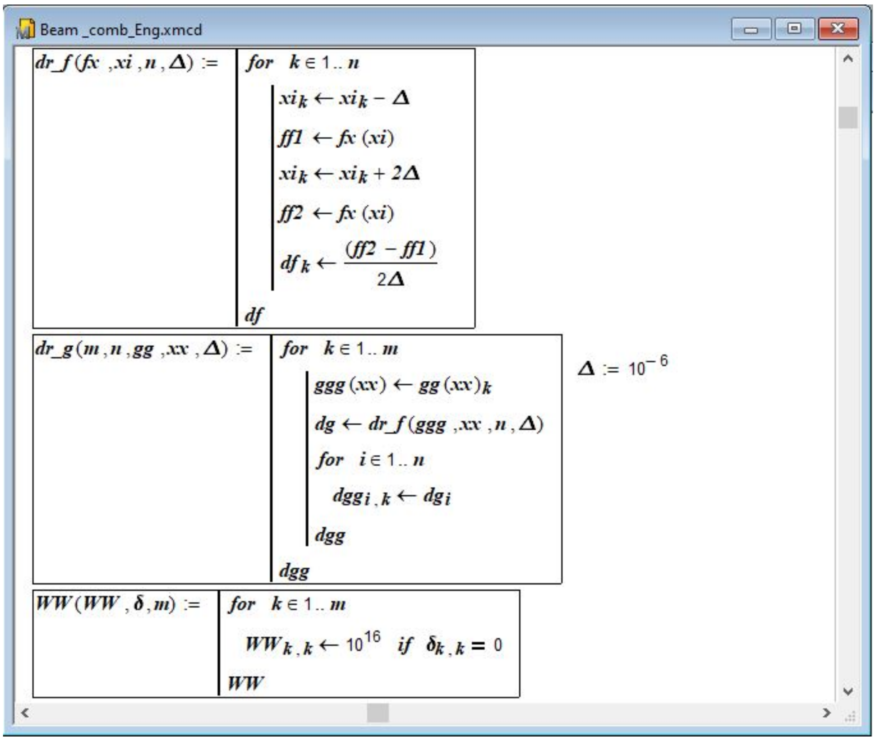

Figure 9. Subroutines used in the algorithm.

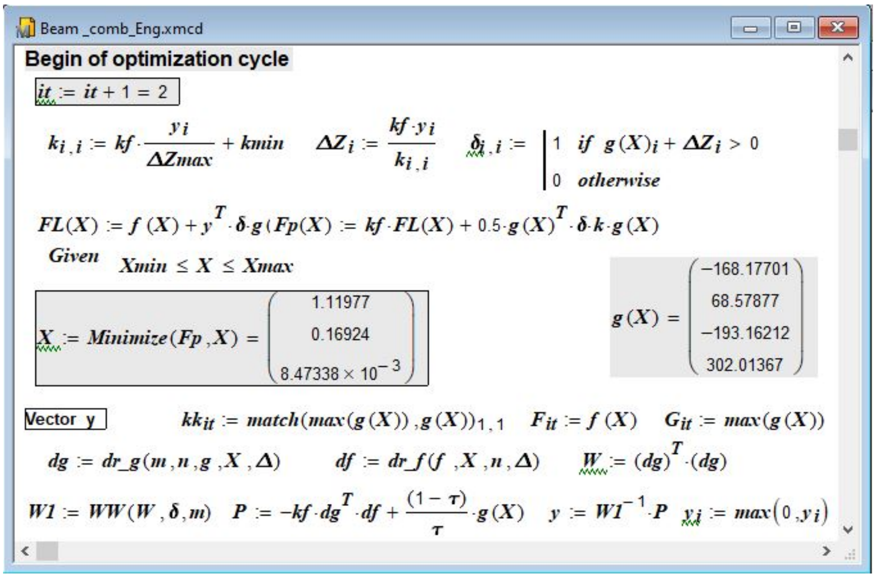

Figure 10. Begin of optimization cycle.

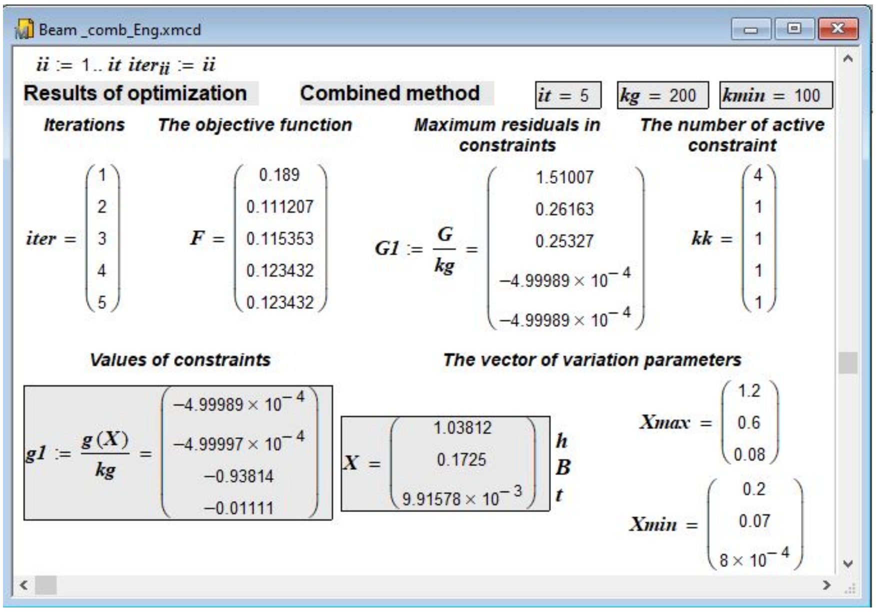

Figure 11. Optimization results.

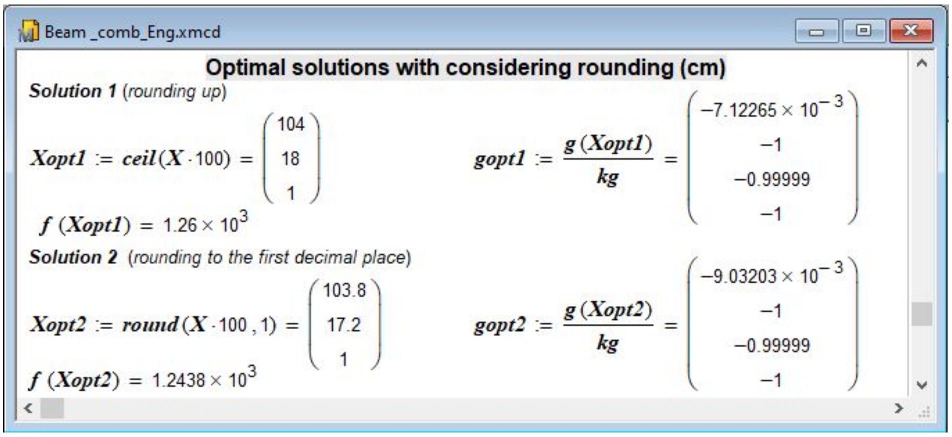

Figure 12. Optimal solutions with considering rounding.

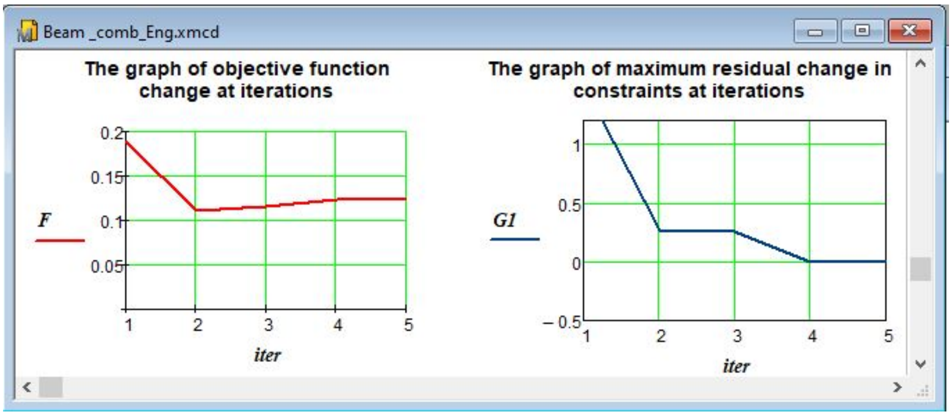

Figure 13. Graphs of changes in the objective function and maximum residuals of constraints at iterations.

Table 2. Comparative results of calculations.

№	Name	Numerical methods	
		Direct method	Combined method
1	Iteration number	11	5
2	Value of the objective function, m^3	$f(x)$ = 0.122791	$f(x)$ = 0.123432
3	Discrepancies in active constraints	$g_1 = 0.431828 \cdot 10^{-6}$ $g_2 = -0.627293 \cdot 10^{-4}$ $g_4 = 0.136121 \cdot 10^{-5}$	$g_1 = -0.499989 \cdot 10^{-3}$ $g_2 = -0.499989 \cdot 10^{-3}$
4	X_1, m	1.02705	1.03812
5	X_2, m	0.18175	0.1725
6	X_3, m	$9.8051 \cdot 10^{-3}$	$9.91578 \cdot 10^{-3}$

The combined method showed better convergence with lower accuracy in constraint residuals, which does not change on subsequent iterations. It should be noted that the value of the objective function here is 0.6% higher than in the direct method.

The conditions for achieving the optimal solution at iterations, according to expression (8), were as follows:

a) equality of variable parameters at 2 adjacent iterations;

b) not exceeding the limits of the allowable area, taking into account the accepted errors for the constraint functions.

Thus, the accuracy of the solution was consistent with the accuracy in the calculation of potentially active constraints. The resulting solutions can be rounded to the required bit depth, which is reflected in the program listings.

4.1 Testing the proposed algorithm

The ten-bar truss optimization design problem is presented as verification of the proposed methodology. Let us consider a variant of this problem, set forth in the monograph [3] and article [40]. The geometry and loading conditions of ten-bar truss are shown in Fig. 14.

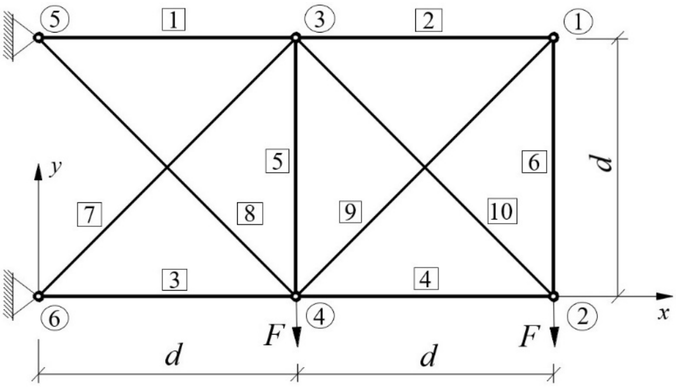

Figure 14. The geometry and applied loads for a ten-bar truss.

Initial data: d = 9.144 m (360 in); F = 444.822 kN (100 kips). All the members were constructed from a material with the modulus of elastic E = 6.89476·10^7 kPa (10^4 ksi); the stress restrictions are R_u = ± 1.72369·10^5 kPa (±25.0 ksi). The displacements for all nodes in all directions had to be less than [Δ] = ±0.0508 m (±2.00 in).

Problem statement. It is required to select the cross-sectional area of the truss at a given interval by minimizing its volume, provided that regulatory requirements for strength and stiffness are met.

The range of the available cross-sectional areas for each member in the truss vary between $A_{\min}$ = 6.4516·10^{-5} m^2 (0.1 in^2) and $A_{\max}$ = 0.02258 m^2 (35 in^2). Initial areas values A_0 = 3.2258·10^{-3} m^2 (5 in^2).

The objective function $f(x)$ represents the weight of the truss.

The constraints are as follows:

The check on the strength in i element of the truss:

$$g_i = \frac{|N_i|}{R_u A_i} - 1 \le 0, \quad i = 1, 2...10.$$

In the test examples given in various sources, the calculation is performed without taking into account the buckling loss of compressed rods.

The constraint on vertical movement at joint 2:

$$g_{11} = \frac{\Delta_2}{[\Delta]} - 1 \le 0.$$

Thus, the number of variables is nx = 10 and the number of constraints is m = 11.

Were applied 2 iterative algorithms of modified Lagrangian function – direct and combined.

A feature of the implementation of the algorithms as applied to this problem was as follows:

1. Given that the truss is statically indeterminate, the analysis task was performed using the algorithm of the finite element method in displacements (*FEA* subroutine).

2. The functions of constraints on strength and stiffness contain state parameters (stress and displacement). Thus, the task of FE analysis, taking into account the changes in areas in the elements of the truss in this task, was recounted at each iteration.

Here is the sequence of operations of the direct method with the notation used in the MathCAD program:

1. Input of initial data:

11.1. Assignment of deterministic geometric (d) and physical (E, R_u) parameters of the problem, as well as the limiting value of displacements of nodes Δ_lim.

11.2. Assignment of truss geometry:

• setting the constants: ne (the number of members), np (the number of nodes), nop (the number of support reactions);

• setting vectors xp, yp (coordinates of nodes along the x and y axes);

• setting an array ni, which lists the connections of jointes for each members;

• specifying the vector iop, which lists the ordinal numbers of zero degrees of freedom connected by supports.

11.3. The purpose of the optimization algorithm parameters: the number of components of the constraint vector m; normalization coefficients of the objective function and the constraint vector k_f, k_g; the minimum value of the penalty coefficient k_{min} and the maximum value of the shift value outside the permissible range ΔZ_{max}.

1.8. Assignment of initial parameters of variation (vector X) and range of variation (vectors X_{min} and X_{max}).

1.9. The appointment of the initial values of the components of the vector of dual variables y_i $(i = 1 \ldots m)$.

2. Formalization of the objective function $f(X)$ and the vector of the constraint function $g(X)$ through variable parameters:

2.1. Writing the $FEA\ (X)$ subroutine that implements a finite element calculation of the truss. The output parameters of this subroutine are contained in an array, which includes three vectors – Z (nodal displacements), $Nabs$ (values of the internal forces in absolute value), L (lengths of elements).

Thus, the indices 1, 2, 3 that occur when calling this subroutine indicate which of these three arrays is being evaluated. Nodal displacements and internal forces are functions of variable parameters X (areas of sections of elements), therefore, they are defined as $Z(X)$ and $Nabs(X)$. The length of the elements L does not change in the course of optimization, therefore, it is calculated once.

2.6. Formation of the objective function $f(X)$ through variable parameters.

2.7. Formation of the constraint vector $g_1\ (X)$, which contains 10 strength checks for each truss element, multiplied by the normalization factor k_g.

2.8. Formation of the stiffness constraint $g_2\ (X)$, which contains a check for the vertical displacement of the truss node 2 (this displacement has index 4 in the general vector of nodal displacements Z). The constraint is also multiplied by the normalization factor k_g.

2.9. Formation of the complete constraint vector $g\ (X)$ by connecting the vectors $g_1\ (X)$ and $g_2\ (X)$.

This vector has 11 elements, where 10 corresponds to strength constraints and 11 corresponds to stiffness constraints.

3. Organization of a cycle where iterations of the search optimization algorithm are performed:

3.1. Assigning an it iteration counter.

3.2. Formation of a diagonal matrix of penalty coefficients by assigning its diagonal elements $k_{i,\,i}$ $(i = 1 \ldots m)$.

3.3. Formation of the elements of the shift vector of the admissible region of restrictions ΔZ_i $(I = 1..m)$.

3.4. Formation of a diagonal matrix is a matrix of Boolean variables by assigning its elements $\delta_{i,i}$.

3.5. Formation of the Lagrange function $F_L\ (X)$, as well as the modified Lagrange function $F_p(X)$.

3.6. Formation of the block for finding the minimum of the function $F_p(X)$ by X on the interval X_{min} and X_{max}; The main difference in solving this problem is that each time the constraint function is accessed, the internal forces and displacements in the elements are recalculated, since function call $g\ (X)$ assumes calling in subroutine $FEA\ (X)$.

3.7. Formation of the vector of values of the objective function at iterations F.

3.8. Identifying the maximum value in the vector of constraints on iterations it and entering it into the vector G_i.

3.9. Finding the ordinal number of the maximum element in the vector of constraints on iterations it and entering it into the vector k_k.

3.10. Calculation of the elements of the vector of dual variables y_i $(i = 1...m)$.

4. Output of results:

4.1. Numerical values of the vectors of change in the target and maximum values of the restrictive functions at iterations.

4.6. Values of optimal areas of the truss elements (vector X).

4.7. Values of residual constraints without taking into account the coefficient kg.

4.8. Graphs of changes in the target and maximum values of the restrictive functions at iterations.

The results of the calculations are shown in Fig. 15-20. A comparison of solutions from sources [3, 40] with solutions obtained by authors is given in Table 3.

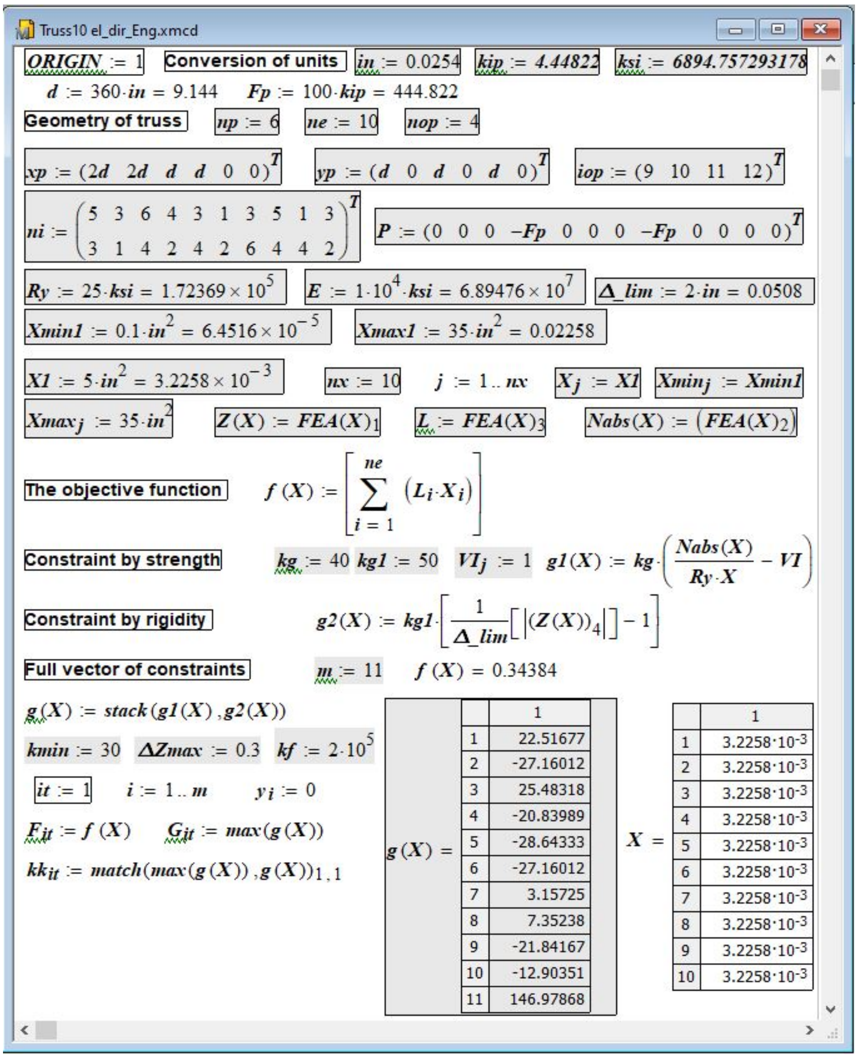

Figure 15. Implementing of numerical methods in mathematical package *MathCAD*: initial data of the task.

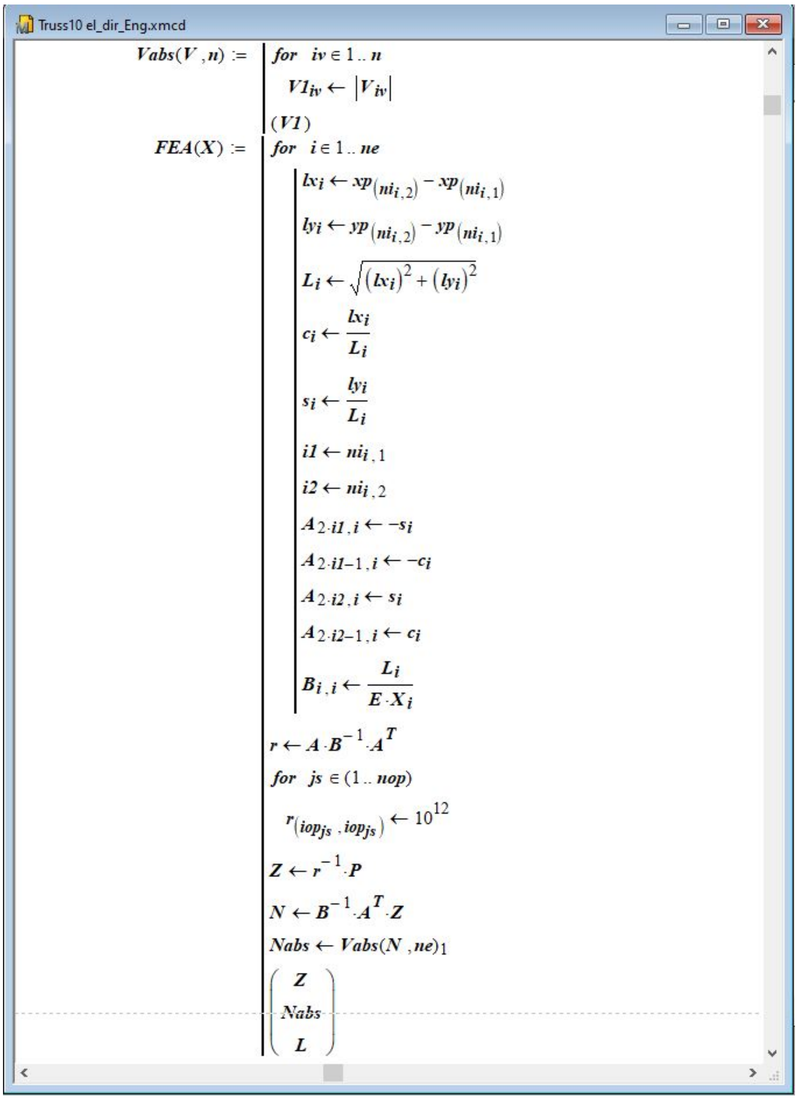

Figure 16. Subroutine *FEA*.

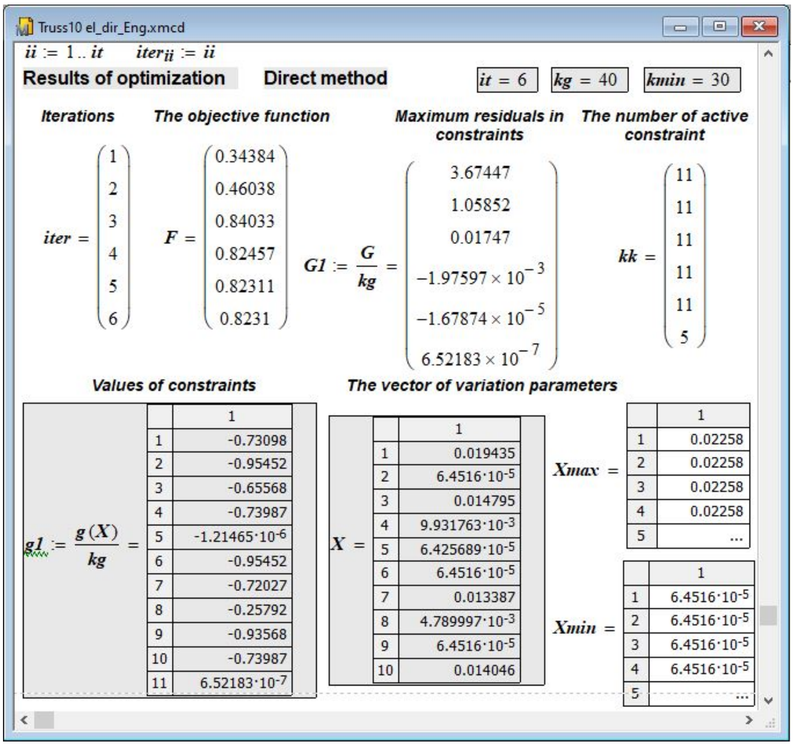

Figure 17. Optimization results.

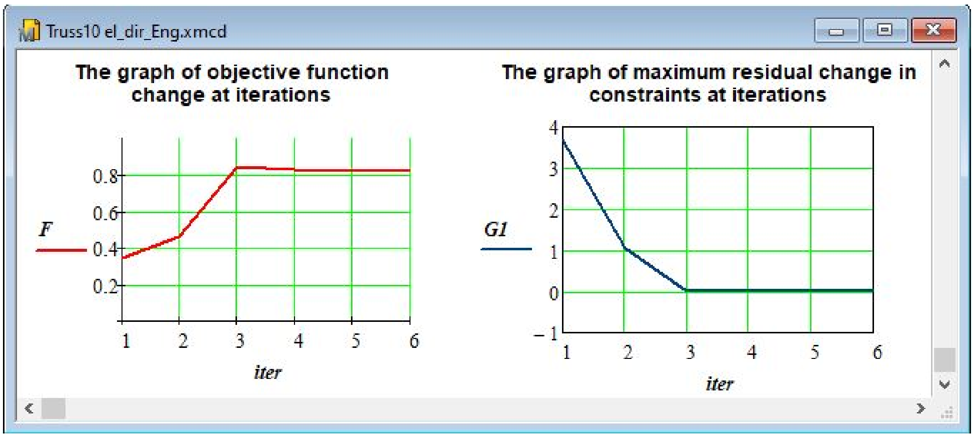

Figure 18. Graphs of changes in the objective function and maximum residuals of constraints at iterations.

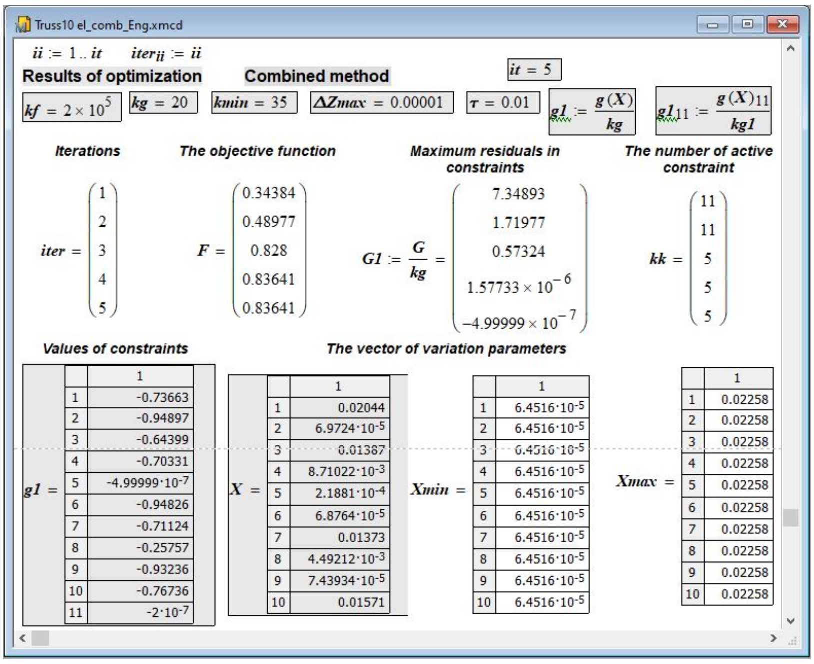

	g1	X	Xmin	Xmax
1	-0.73663	0.02044	6.4516·10-5	0.02258
2	-0.94897	6.9724·10-5	6.4516·10-5	0.02258
3	-0.64399	0.01387	6.4516·10-5	0.02258
4	-0.70331	8.71022·10-3	6.4516·10-5	0.02258
5	-4.99999·10-7	2.1881·10-4	6.4516·10-5	0.02258
6	-0.94826	6.8764·10-5	6.4516·10-5	0.02258
7	-0.71124	0.01373	6.4516·10-5	0.02258
8	-0.25757	4.49212·10-3	6.4516·10-5	0.02258
9	-0.93236	7.43934·10-5	6.4516·10-5	0.02258
10	-0.76736	0.01571	6.4516·10-5	0.02258
11	-2·10-7			

Figure 19. Optimization results.

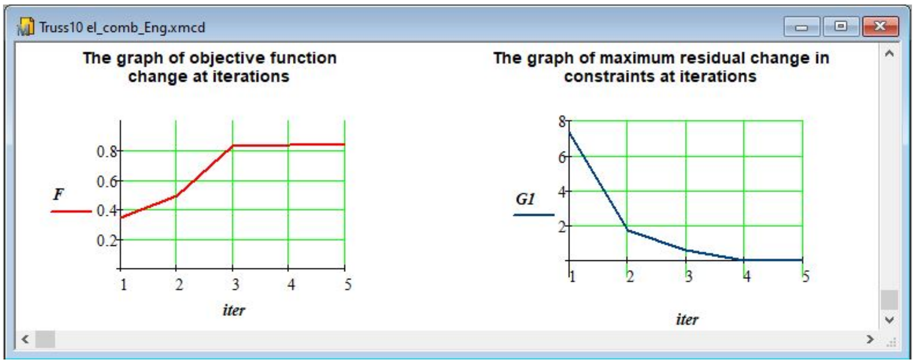

Figure 20. Graphs of changes in the objective function and maximum residuals of constraints at iterations.

Table 3. Comparative results of calculations.

№	Name	Numerical methods			
		Edward J. Haug [3]	B. Farchi [40]	Direct method	Combined method
1	Iteration number	15	–	6	5
2	Value of the objective function, $f(x)$, m³	0.8294574	0.8294187	0.82312	0.83641
3	Discrepancies in active constraints, g_5; g_{11}	-0.322×10^{-4}; -0.425×10^{-4}	-0.9067×10^{-4}; -0.4315×10^{-4}	-0.1215×10^{-5}; 0.6522×10^{-6}	-0.4999×10^{-6}; -0.2×10^{-6}
4	X_1 (A_1), m²	$0.19374\cdot10^{-1}$	$0.19691\cdot10^{-1}$	$0.19435\cdot10^{-1}$	$0.2044\cdot10^{-1}$
5	X_2 (A_2), m²	$0.64516\cdot10^{-4}$	$0.64516\cdot10^{-4}$	$0.64516\cdot10^{-4}$	$0.69724\cdot10^{-4}$
6	X_3 (A_3), m²	$0.15015\cdot10^{-1}$	$0.14970\cdot10^{-1}$	$0.14795\cdot10^{-1}$	$0.13870\cdot10^{-1}$
7	X_4 (A_4), m²	$0.98619\cdot10^{-2}$	$0.98212\cdot10^{-2}$	$0.99318\cdot10^{-2}$	$0.87102\cdot10^{-2}$
8	X_5 (A_5), m²	$0.64516\cdot10^{-4}$	$0.64516\cdot10^{-4}$	$0.64516\cdot10^{-4}$	$0.21881\cdot10^{-3}$
9	X_6 (A_6), m²	$0.35903\cdot10^{-3}$	$0.35612\cdot10^{-3}$	$0.64516\cdot10^{-4}$	$0.68764\cdot10^{-4}$
10	X_7 (A_7), m²	$0.13676\cdot10^{-1}$	$0.13570\cdot10^{-1}$	$0.13387\cdot10^{-1}$	$0.13730\cdot10^{-1}$
11	X_8 (A_8), m²	$0.48182\cdot10^{-2}$	$0.48174\cdot10^{-2}$	$0.47899\cdot10^{-2}$	$0.44921\cdot10^{-2}$
12	X_9 (A_9), m²	$0.64516\cdot10^{-4}$	$0.64516\cdot10^{-4}$	$0.64516\cdot10^{-4}$	0.7439410^{-4}
13	X_{10} (A_{10}), m²	$0.13947\cdot10^{-1}$	$0.13890\cdot10^{-1}$	$0.14046\cdot10^{-1}$	$0.15710\cdot10^{-1}$

The solution of the problem by the direct and combined method gave close results in terms of the number of iterations, the accuracy of the results and the nature of convergence, although in the combined method an overestimated value of the objective function was obtained by 0.8 %. Solutions close to optimal, were obtained already at the 3rd iteration with refinement at subsequent iterations to the required degree of accuracy. When comparing with the results obtained in two other sources, it should also be noted that the values in the areas are close with greater accuracy in the residuals of constraints (by 3-4 orders of magnitude).

In general, the results shown in the table show the high efficiency of the proposed algorithms, which give the best performance in almost all parameters compared with the results given in [3, 40].

The main difficulties in implementing the above examples were related to their adjustment to the task, which was carried out by setting optimization parameters, such as normalization coefficients of the target and restrictive functions, and the penalty coefficient. Guided by the experience of solving examples, we can relate the influence of these parameters on the convergence of the algorithm with the structure of the modified Lagrange function F_P. In the allowable region, this function coincides with the target, and outside the allowable values, the parameters k_g and k_{min} affect its curvature. It is revealed that the algorithm gives the most stable convergence if the values of the objective function are in the same order as the penalty additives.

4. Conclusions

In conclusion, we give the following conclusions:

1. The solution of practical examples of optimization of flat rod systems showed the effectiveness of the presented algorithms for searching for a constrain extremum. It was revealed that the solutions obtained using 2 algorithms of a modified Lagrangian functions in the first example gave a complete match, and in the second some discrepancy, which hindicates the presence in the tasks of this class of several extremes.

2. Some difficulties associated with tuning algorithms to stable convergence are noted. If the objective function has a low order (volume in m3), and the constraints are normalized to unity, then it is necessary to increase the values of the objective function and penalty additions in the F_P function to a close order.

For this, the corresponding penalty and normalizing coefficients are introduced.

3. It is shown that the combined method for solving a conditionally extremal problem, although it has some complications in the definition of dual variables, can give better convergence. In addition, the

problems of searching for direct and dual variables in this algorithm are not interconnected. This is important when solving optimization problems of mechanics that have a complex formulation (for example, nonlinear problems, dynamics problems, etc.), when the problem of a conditional extremum in direct variables often becomes incompatible (especially in the initial iterations).

4. The study of the test problem of optimizing the ten-bar truss confirmed the efficiency of the developed algorithm. The results were obtained, giving the best indicators for the speed of convergence and accuracy compared with known solutions.

5. The optimization algorithm is presented in mathematical package *MathCAD*, which allows open access to its teams, confirms its adequacy and allows you to implement this algorithm to solve similar problems in design, scientific or educational activities.

6. In the software implementation of the practical problems of optimizing complex systems with a large number of variation parameters, it is more expedient to search for the unconditioned extremum using zero-order methods, such as the deformable polyhedron method, or based on metaheuristic algorithms.

7. Further research in the direction of optimization of planar and spatial rod systems can be effectively implemented by constructing optimization models based on neural networks.

References

1. David, M.H. Applied nonlinear programming. McGraw-Hill. Texas, 1972. 498 p.
2. Schmit, L.A. Structural Design by Systematic Synthesis. Proceedings, 2nd Conference on Electronic Computation, ASCE. 1960. Pp. 105–122.
3. Edward, J. Haug., Jasbir, S.A. Applied optimal design: mechanical and structural systems. A Wiley-Interscience. Michigan, 1979. 506 p.
4. Yamasaki, S., Kawamoto, A., Nomura, T., Fujita, K. A consistent grayscale-free topology optimization method using the level-set method and zero-level boundary tracking mesh. International Journal for Numerical Methods in Engineering. 2015. Vol. 101. Pp. 744–773. DOI: 10.1002/nme.4826
5. Chen, J., Xiao, Z., Zheng, Y., Zheng, J., Li, C., Liang, K. Automatic sizing functions for unstructured surface mesh generation. International Journal for Numerical Methods in Engineering. 2017. Vol. 109. Pp. 577–608. DOI: 10.1002/nme.5298
6. Lalin, V.V., Rybakov, V.A., Ivanov, S.S., Azarov, A.A. Mixed finite-element method in V.I. Slivker's semi-shear thin-walled bar theory. Magazine of Civil Engineering. 2019. 89 (5). Pp. 79–93. DOI: 10.18720/MCE.89.7
7. Lalin, V.V., Yavarov, A.V., Orlova, E.S., Gulov, A.R. Application of the Finite Element Method for the Solution of Stability Problems of the Timoshenko Beam with Exact Shape Functions. Power Technology and Engineering. 2019. No. 53 (4). Pp. 449–454. DOI: 10.1007/s10749-019-01098-6
8. Gandomi, A.H., Yang, X.S., Alavi, A.H. Cuckoo search algorithm: A metaheuristic approach to solve structural optimization problems. Engineering with Computers. 2013. No. 29 (1). Pp. 17–35. DOI: 10.1007/s00366-011-0241-y
9. Hasançebi, O., Çarbaş, S., Doğan, E., Erdal, F., Saka, M.P. Performance evaluation of metaheuristic search techniques in the optimum design of real size pin jointed structures. Computers and Structures. 2009. Vol. 87. Pp. 284–302. DOI: 10.1016/j.compstruc.2009.01.002
10. Saka, M.P., Hasançebi, O., Geem, Z.W. Metaheuristics in structural optimization and discussions on harmony search algorithm. Swarm and Evolutionary Computation. 2016. Vol. 28. Pp. 88–97. DOI: 10.1016/j.swevo.2016.01.005
11. Serpik, I.N., Alekseytsev, A.V. Optimization of flat steel frame and foundation posts system.
12. Kaveh, A., Ghafari, M.H. Plastic analysis of planar frames using CBO and ECBO algorithms. Iran University of Science & Technology. 2015. No. 5 (4). Pp. 479–492.
13. Aydın, D., Yavuz, G., Stützle, T. ABC-X: a generalized, automatically configurable artificial bee colony framework. Swarm Intelligence. 2017. No. 11 (1). Pp. 1–38. DOI: 10.1007/s11721-017-0131-z
14. Bonyadi, M.R., Michalewicz, Z. Particle swarm optimization for single objective continuous space problems: A review. 2017. No. 25 (1). Pp. 1–54. DOI: 10.1162/evco_r_00180
15. Nekouie, N., Yaghoobi, M. A new method in multimodal optimization based on firefly algorithm. Artificial Intelligence Review. 2016. No. 46 (2). Pp. 267–287. DOI: 10.1007/s10462-016-9463-0
16. Askarzadeh, A.A novel metaheuristic method for solving constrained engineering optimization problems: Crow search algorithm. Computers & Structures. 2016. Vol. 169. Pp. 1–12. DOI: 10.1016/j.compstruc.2016.03.001
17. Mirjalili, S., Mirjalili, S.M., Lewis, A. Grey Wolf Optimizer. Advances in Engineering Software. 2014. Vol. 69. Pp. 46–61. DOI: 10.1016/j.advengsoft.2013.12.007
18. Cai, X., Wang, H., Cui, Z., Cai, J., Xue, Y., Wang, L. Bat algorithm with triangle-flipping strategy for numerical optimization. International Journal of Machine Learning and Cybernetics. 2017. No. 9 (2). Pp. 199–215. DOI: 10.1007/s13042-017-0739-8
19. Samma, H., Mohamad-Saleh, J., Suandi, S.A., Lahasan, B. Q-learning-based simulated annealing algorithm for constrained engineering design problems. Neural Computing and Applications. 2019. Pp. 1–15. DOI: 10.1007/s00521-019-04008-z
20. Cheng, M.-Y., Prayogo, D., Wu, Y.-W., Lukito, M.M. A Hybrid Harmony Search algorithm for discrete sizing optimization of truss structure. Automation in Construction. 2016. Vol. 69. Pp. 21–33. DOI: 10.1016/j.autcon.2016.05.023
21. Jalili, S., Talatahari, S. Optimum Design of Truss Structures Under Frequency Constraints using Hybrid CSS-MBLS Algorithm. KSCE Journal of Civil Engineering. 2017. No. 22 (5). Pp. 1840–1853. DOI: 10.1007/s12205-017-1407-y
22. Rao, R.V., Saroj, A. Multi-objective design optimization of heat exchangers using elitist-Jaya algorithm. Energy Systems. 2016. No. 9 (2). Pp. 305–341. DOI: 10.1007/s12667-016-0221-9
23. Lieu, Q.X., Do, D.T.T., Lee, J. An adaptive hybrid evolutionary firefly algorithm for shape and size optimization of truss structures with frequency constraints. Computers & Structures. 2018. Vol. 195. Pp. 99–112. DOI: 10.1016/j.compstruc.20-17.06.016

24. Degertekin, S.O., Hayalioglu, M.S. Optimum Design of Steel Space Frames: Tabu Search vs. Simulated Annealing and Genetic Algorithms. International Journal Of Engineering & Applied Sciences. 2009. No. 2 (1). Pp. 34–45.
25. Kaveh, A., Zakian, P. Improved GWO algorithm for optimal design of truss structures. Engineering with Computers. 2018. No. 34 (4). Pp. 685–707. DOI: 10.1007/s00366-017-0567-1
26. Jalili, S., Hosseinzadeh, Y. Combining Migration and Differential Evolution Strategies for Optimum Design of Truss Structures with Dynamic Constraints. Iranian Journal of Science and Technology - Transactions of Civil Engineering. 2019. No. 43 (1). Pp. 289–312. DOI: 10.1007/s40996-018-0165-5
27. Ho-Huu, V., Nguyen-Thoi, T., Vo-Duy, T., Nguyen-Trang, T. An adaptive elitist differential evolution for optimization of truss structures with discrete design variables. Computers and Structures. 2016. Vol. 165. Pp. 59–75. DOI: 10.1016/j.compstruc.2015.11.014
28. Khatibinia, M., Yazdani, H. Accelerated multi-gravitational search algorithm for size optimization of truss structures. Swarm and Evolutionary Computation. 2018. Vol. 38. Pp. 109–119. DOI: 10.1016/j.swevo.2017.07.001
29. Donskoy, V.I. Extraction of Optimization Models from Data: an Application of Neural Networks. Taurida Journal of Computer Science Theory and Mathematics. 2018. No. 39 (2). Pp. 71–89.
30. Dmitrieva, T.L. Parametricheskaya optimizatsiya v proektirovanii konstruktsii, podverzhennykh staticheskomu i dinamicheskomu vozdeistviiu [Parametric optimization in the design of structures subject to static and dynamic effects]. Izd-vo IrGTU. Irkutsk, 2010. 176 p. (rus)
31. Fiacco, A.V., McCormick, G.P. Computational Algorithm for the Sequential Unconstrained Minimization Technique for Nonlinear Programming. Management Science. 1964. No. 10 (4). Pp. 601–617. DOI: 10.1287/mnsc.10.4.601
32. Allaire, G., Dapogny, C., Estevez, R., Faure, A., Michailidis, G. Structural optimization under overhang constraints imposed by additive manufacturing technologies. Journal of Computational Physics. 2017. Vol. 351. Pp. 295–328. DOI: 10.1016/j.jcp.2017.09.041
33. Chou, J.S., Ngo, N.T. Modified firefly algorithm for multidimensional optimization in structural design problems. Structural and Multidisciplinary Optimization. 2017. No. 55 (6). Pp. 2013–2028. DOI: 10.1007/s00158-016-1624-x
34. Golshtein, E.G., Tretyakov, N.V. Modified Lagrangians and Monotone Maps in Optimization. Wiley&Sons Publ. Co. New York, 1996. 438 p.
35. Bertsekas, D.P. Constrained Optimization and Lagrange Multiplier Methods. 1rd ed. Athena Scientific. New York, 1996. 410 p.
36. 36. Andreani, R., Birgin, E.G., Martínez, J.M., Schuverdt, M.L. On augmented Lagrangian methods with general lower-level constraints. SIAM Journal on Optimization. 2007. No. 18 (4). Pp. 1286–1309. DOI: 10.1137/060654797
37. Wang, X., Zhang, H. An augmented Lagrangian affine scaling method for nonlinear programming. Optimization Methods and Software. 2015. No. 30 (5). Pp. 934–964. DOI: 10.1080/10556788.2015.1004332
38. Bertsekas, D.P. Nonlinear Programming. 3rd ed. Athena Scientific. New York, 2016. 861 p.
39. Long, W., Liang, X., Huang, Y., Chen, Y. A hybrid differential evolution augmented Lagrangian method for constrained numerical and engineering optimization. CAD Computer Aided Design. 2013. No. 45 (12). Pp. 1562–1574. DOI: 10.1016/j.cad.2013.07.007
40. Farshi, B., Alinia-Ziazi, A. Sizing optimization of truss structures by method of centers and force formulation. International Journal of Solids and Structures. 2010. No. 47 (18–19). Pp. 2508–2524. DOI: 10.1016/j.ijsolstr.2010.05.009

Contacts:

Tatiana Dmitrieva, dmitrievat@list.ru

Khukhuudei Ulambayar, Ulambayar_kh@yahoo.com

Magazine of Civil Engineering. 2022. 109(1). Article No. 10911

Magazine of Civil Engineering

journal homepage: http://engstroy.spbstu.ru/

ISSN 2712-8172

DOI: 10.34910/MCE.109.11

The strength of fly ash concrete of experimental design

T.T.N. Nguyen[a], A.T. Nguyen[a], Q.V. Vu[b], V.T. Ngo[c], T.Q.K. Lam*[c]

[a] *University of Transport Technology, Hanoi, Vietnam*

[b] *Thuy Loi University, Hanoi, Vietnam*

[c] *Mien Tay Construction University, Vinh Long, Vietnam*

**E-mail: lamthanhquangkhai@gmail.com*

Keywords: concrete grade, fly ash, compressive strength, DOE, Cement concrete.

Abstract. Cement concrete has always played an essential role in the general development of the construction industry. Many studies improve the properties and durability of cement concrete by adding chemical additives and mineral additives. One of them, fly ash, is one of the most preferred applied mineral additives. Currently, the demand for fly ash is becoming an urgent problem, as it is also can reduce environmental pollution from by-products of thermal power plants not only in Vietnam but also all around the world. To evaluate the factors affecting compressive strength of concrete, such as fly ash, type of cement used, date and designed concrete grade, we based our study on the design of experiment (DOE). The influencing variables have different levels of investigation, which are based on previous studies. With the useful statistical analysis tools, the number of experiments, and the results of the experimental analysis, we can see the influence of each element and their interaction on the compressive strength of the concrete. On that basis, it is possible to choose the option with reasonably selected ingredients to achieve the expected optimal compressive strength.

1. Introduction

1.1. Overview of fly ash and fly ash concrete in the world

Thermoelectric fly ash was discovered to be active as a pozzolan additive in the early 20th century. It was officially used as an additive in concrete production since the mid-20th century, beginning with the study of fly ash applications in concrete of the University of California, Berkely, the USA in 1937. For more than half a century, the application of fly ash as an additive for concrete production, especially in countries with a large coal power output, increasingly popular and increasing volumes.

The scientific basis of mixing mineral additives into the mixed composition of concrete is based on the following aspects. In the first phase, fly ash (FA) is almost inactive but acts as an inert material filling the mixed voids [1–3]. Over time, the hydration process continues to increase the alkaline environment (the concentration of OH- ions increases), thereby activating the potential hydraulic properties in fly ash to create the pozzolanic reaction. The result of the process of the puzzolanic reaction has transformed the $Ca(OH)_2$ component into stable C-S-H ($C_3S_2H_3$, C_4ASH_{12}, C_4AH_{13}) products, which increase the ability to resist waterproof, corrosion, temperature and adds strength to the concrete. So that many types of cement concrete, when using reasonable fly ash, can improve the mechanical properties better than conventional cement concrete. Due to the pozzolanic reaction, the fly ash particles lose their original spherical shape and are gradually covered with a new product layer and, after six months, no longer determine the actual

Nguyen, T.T.N., Nguyen, A.T., Vu, Q.V., Ngo, V.T., Lam, T.Q.K. The strength of fly ash concrete of experimental design. Magazine of Civil Engineering. 2022. 109(1). Article No. 10911. DOI: 10.34910/MCE.109.11

condition [4]. The cement hydration process consists of complex reaction chains, with the addition of fly ash, the more complex the reaction processes. The only activity of fly ash particles affects the hydration of the cement, but not all fly ash particles are involved. The micro-aggregates fill the space between the cement particles, contribute to reducing the voids of the cement stone, while also helping to significantly improve the structure of the transition zone between the cement stone and the aggregate. Besides, the presence of mineral additives in the transition area together with the gradual increase of C-S-H products from the pozzolanic reaction increasing the density of the hydration products, the formation of C-S-H takes place in a narrow environment, solidifies the structure of the concrete, increasing the strength of the concrete. The filling effect of mineral additives is highly dependent on their fineness.

There are many scientific works in the world that have partly demonstrated that the properties of concrete are significantly improved when mineral additives are added.

According to ACI 232R [5], fly ash cement concrete (FC) is understood as Portland cement concrete (PC), which uses fly ash with a specific content to partially binder replace the Portland cement binder. According to Michael [6], in the history of development, fly ash is used in cement concrete with varying levels, depending on the purpose of the use of the goal of projects. Typically, to meet the requirements of structural strength, the fly ash ratio is from 15 % – 30 % of the volume of adhesive, at a higher concentration of 30 % – 50 % used for hydropower and dams to control the temperature in mass concrete structures. In recent years, the concrete with a very high fly ash content of more than 50 % has been developed for structural works requiring high strength. Currently, for high-performance concrete (HPC), the use of fly ash is 10 % – 30 % of the adhesive content. In the cement concrete, the amount of fly ash added is equal or higher than the amount of cementless, because fly ash has a smaller density than cement. The studies of Owen [7] by Jiang and associates [8] produce that with high-quality cement concrete depending on the fly ash quality and the amount of cement to be replaced. The level of loss of fly ash cement concrete is usually smaller, which is very suitable for high-temperature construction conditions in our country [9]. According to Mehta [10], using fly ash in high-quality concrete also has the effect of reducing shrinkage, reducing heat cracking, and increasing water resistance. The authors also have researched on the application of fly ash, clearly seeing the advantages of this mineral additive [11–15]. According to research by Konstantin Sobolev and colleagues [16], has obtained significant results on fly ash mortar and fly ash concrete strength at different age dates with two types of class C and F fly ash. Photo The effect of fly ash type and quantity is specifically assessed in the properties such as time and intensity. In particular, the effect of fly ash is assessed specifically by the strength of the mortar at the age of 1, 7 and 28. It is found that the effect of mineral additives is very clear and brings many benefits. Moreover, the results obtained concrete strength of all types achieved results above the standard of 20 Mps at 7 days of age and best at 365 days up to 47.7 MPa when mixed 15 % simultaneously. In the study of Anjali Yadav and Nikhi Kumar Yadav [17] also about the use of flying in concrete pavement, the amount of fly ash used ranged from 0 % to 60 %. The compressive strength of concrete was determined at 7 and 28 days of age, showing that if the content increases, the strength of the concrete decreases, it is safe to use fly ash up to 40 %, and more the strength of the concrete is not satisfactory. Analysis and design of fly ash concrete used for road foundations, research by A. Hilmi Lav et al [18] with the main reason for this research is to want to reduce costs and use industrial waste. Level F fly ash content is added to make up 2 %, 4 %, 8 % and 10 % by total weight. Test batches were performed to adjust the fly ash appropriately. The mechanical properties are then checked to obtain the basic properties of the cement stabilizer, thereby analyzing the pavement texture. In the study of Jin Huang, Huayou Su [19] used shows that the workability of fly ash concrete can significantly improve, and the compressive strength is similar with ordinary concrete after 28 days. In research of Uma Maguesvari Muthaiyan and Sundararajan Thirumalai [20], showed the result of some main characteristics of fly ash concrete with differential level of class C fly ash ranging from 0 % to 20 %, their suggestion should use minimum cement content 250 kg/m^3 and with 10 and 20 % of replacement of cement by fly ash. Besides, the increasing content of fly ash, the reducing compress strengthen of concrete.

The selection of the appropriate ratio of fly ash in concrete is based on the purpose of the survey to fabricate concrete with a certain replacement flight content while still ensuring the necessary features for the application of the concrete type. This concrete is in construction of high-grade road foundations, pavement for traffic and for prefabricated structures. Therefore, in the research scope of the paper, some concrete grades selected for specific survey are the following: C20, C30, C40. The ratio of fly ash/binder has a great influence on the strength of concrete, depending on the purpose of the strength to be achieved to choose the appropriate ratio. According to the recommendations of ACI 211.4R [21] for concrete with strength greater than 35 MPa, the ratio of 15 % – 25 % (type F) and 20 % – 35 % (type C) should be used. As recommended by EN206 [22] standard, use the ratio from 15 % – 33 % (type F) and 15 % – 35 % (type C). In this paper, the authors' research only compressive the strengthen of fly ash concrete basing on some key factors namely concrete of grade, percentage of fly ash in cementitious, and type of cement by DOE approach.

2. Materials and methods

2.1. Design of experiment

Experimental Design mathematical methodology is a branch of applied statistics, used to plan and conduct experiments as well as to analyze and interpret data which is obtained from experiments. Over the past two decades, the design of experiment (DOE) has expanded across a wide range of industries. It is a handy tool often that is used to improve product quality and reliability [23]. Since the 1920s, Ronald A. Fisher has conducted a study in agriculture to increase productivity growth in England. After giving an experimental design and the official was the first to start using DOE. By 1935, his book about DOE was written for the first time, which explains how valid conclusions can be drawn from experiments with nuisance factors. In which he analyzed the presence of objective factors subject to the fluctuation of weather conditions such as temperature, precipitation. Then, the experimental design process to optimize the process, the Feedback Surface Method (RSM) was also mentioned by George Box, who is also from the UK. In the 1550s, W. Edwards Deming was interested in experimental design as well as statistical methods. Genichi Taguchi is a Japanese statistician interested in quality improvement methods, by introducing the Loss function and extensive experiments with "external arrays" in DOE as an advanced approach in Six SIGMA initiatives [24].

Suppose there are two factors A, B affect the output variable Y, then the relational equation is as follows (equation 1):

$$Y_{\mathrm{ij}k} = \mu + \tau_i + \delta_j + (\tau\delta)_{\mathrm{ij}} + \varepsilon_{\mathrm{ij}k} \tag{1}$$

where:

μ represents the overall mean effect;

τ_i is the effect of the $\mathrm{i_{th}}$ level of factor A $(i = 1, 2, \ldots, n_a)$;

δ_j is the effect of the $\mathrm{j_{th}}$ level of factor B $(j = 1, 2, \ldots, n_b)$;

$(\tau\delta)_{ij}$ represents the interaction effect between A and B;

$\in_{ijk}$ represents the random error terms (which are assumed to be normally distributed with a mean of zero and variance of σ^2) and the subscript k denotes the m replicates ($k = 1, 2, \ldots, m$).

Since the effects τ_i , δ_j and $(\tau\delta)_{ij}$ represent deviations from the overall mean, the following constraints exist (equation 2):

$$\sum_{i=1}^{n_a} \tau_i = 0; \sum_{j=1}^{n_b} \delta_j = 0; \sum_{i=1}^{n_a} (\tau\delta)_{ij} = 0;\ \sum_{j=1}^{n_b} (\tau\delta)_{ij} = 0 \tag{2}$$

Hypothesis Tests in General Factorial Experiments

Furthermore, in addition to the two factors A, B, and the interaction between them AB, after building the relationship model (equation 1), it is necessary to check the hypotheses to evaluate their significance in the following aspects.

1. H0: $\tau_1 = \tau_2 = \ldots = \tau_{na} = 0$ (Main effect of A is absent)

   H1: $\tau_I \neq 0$ for at least one i

2. H0: $\delta_1 = \delta_2 = \ldots = \delta_{nb} = 0$ (Main effect of B is absent)

   H1: $\delta_j \neq 0$ for at least one j

3. H0: $(\tau\delta)_{11} = (\tau\delta)_{12} = \ldots = (\tau\delta)_{nanb} = 0$ (Main effect of AB is absent)

   H1: $(\tau\delta)_{Ij} \neq 0$ for at least one ij

The sum of squares of the factors is as follows (equation 3):

$$SS_{TR} = SS_A + SS_B + SS_{AB} \tag{3}$$

where SS_{TR} represents the model sum of squares, SS_A represents the sequential sum of squares due to factor A, SS_B represents the sequential sum of squares due to factor and SS_{AB} represents the sequential sum of squares due to the interaction AB. The mean squares are obtained by dividing the sum of squares by the associated degrees of freedom. Once the mean squares are known the test statistics can be calculated. For example, the test statistic to test the significance of factor A (or the hypothesis H0: $\tau_1 = 0$) can then be obtained as (equation 4):

$$(F_0)_A = \frac{MS_A}{MS_E} = \frac{SS_A / dof(SS_A)}{SS_E / dof(SS_E)} \tag{4}$$

Similarly, the test statistic to test significance of factor B and the interaction AB can be respectively obtained as (equation 5 and equation 6):

$$(F_0)_B = \frac{MS_B}{MS_E} = \frac{SS_B / dof(SS_B)}{SS_E / dof(SS_E)} \tag{5}$$

$$(F_0)_{AB} = \frac{MS_{AB}}{MS_E} = \frac{SS_{AB} / dof(SS_{AB})}{SS_E / dof(SS_E)} \tag{6}$$

where MS_A is the mean square for factor A and MS_E is the error mean square, MS_B is the mean square for factor B and MS_E is the error mean square, MS_{AB} is the mean square for interaction AB and MS_E is the error mean square.

It is recommended to conduct the test for interactions before conducting the test for the main effects. This is because, if an interaction is present, then the main effect of the factor depends on the level of the other factors and looking at the main effect is of little value. However, if the interaction is absent then the main effects become important.

2.2. Experimental materials

PC (Portland cement) is crushed from clinker with a certain amount of gypsum (accounting for 4 % – 5 %). Meanwhile, PCB (Portland blended cement) is a mixture of Portland cement produced from grinding a mixture of clinker, gypsum, and additives (the amount of additives including gypsum does not exceed 40 % of which the full additive does not exceed 20 %). PC40 (type 1) and PCB40 (type 2) is one of the common types of cement, with the physical and chemical components that meet the requirements, and both of them having equal strength of 40 Mpa at 28 days of age.

River sand: Natural sand has the largest nominal particle size of 2.5 mm with a density of 2.62 g/cm^3. Although natural sand has mechanical indicators meeting the requirements, but the modulus of size and particle composition shows that this is fine sand leading to the amount of mixed water increasing, so it is necessary to consider mixing with other sands to adjust the modulus of size and particle composition.

Crushed sand produced from rock originated from sedimentary rock. Crushed sand with particles larger than 2.5 mm and 5.0 mm is quite large, with a density of 2.62 g/cm^3, which needs to be mixed with fine sand to have a mixture of small aggregates with large modulus and reasonable grain composition.

Coarse aggregate produced from andesite stone has a particle size of 5 mm – 20 mm, has the largest nominal particle size of 20 mm with a density of 2.72 g/cm^3. Fly ash taken from the silo, and the physical-mechanical properties of fly ash Vung Ang I are in line with the technical requirements of fly ash Type F as prescribed of ASTM C618 [25], which is qualified for use as construction materials.

Superplasticizer additive from O-Basf MasterGlenium® SKY 8735, with a composition consisting of ether polycarboxylates (PCE).

Water meets the standards for concrete production.

2.3. Mix design

Select the percentage of the ratio of crushed sand and river sand is 40:60 used to make concrete to optimizing the amount of binder used. The rate of mixing is commonly used at commercial concrete stations in Vietnam. A small aggregate mixture of 40 % crushed sand and 60 % natural sand has physical-mechanical properties, size modulus, and particle composition suitable for use in the manufacture of concrete.

Research and design of concrete components have a level of strength from 20 MPa to 40 MPa with the workability of 120 mm – 160 mm.

Designing the method of concrete mix, according to the ACI 211.4R [21]. The required average strength is used to select the concrete composition. In the design of materials for the manufacture of concrete mixes, the mineral additives have an essential role that is regulated to use as silica fume or fly ash. Fly ash can be type F or type C. In which, the recommended fly ash content a substitute for cement is class F fly ash about 15 % – 25 %, and fly ash type C about 20 % – 35 %. The amount of water in the mixture is reduced by using a superplasticizer. The concrete mix composition is summarized, as shown in Table 1.

Table 1. Component concrete mix.

No	Concrete of Grade	FA (%)	Type of cement	Cement (kg)	FA (kg)	CA (kg)	RS (kg)	CS (kg)	W (lít)	SP (lít)	W/B
1	20	0	1	260	0	1050	531	354	192	2.86	0.74
2	20	0	2	290	0	1045	531	342	191	3.19	0.66
3	20	5	1	247	13	1050	531	354	191	2.86	0.73
4	20	5	2	275.5	14.5	1045	513	342	191	3.15	0.66
5	20	10	1	234	26	1045	531	354	191	2.84	0.73
6	20	10	2	261	29	1040	513	342	190	3.12	0.66
7	20	15	1	221	39	1045	531	354	190	2.82	0.73
8	20	15	2	246.5	43.5	1040	513	342	190	3.07	0.66
9	20	20	1	208	52	1045	528	352	190	2.82	0.73
10	20	20	2	232.0	58	1040	510	340	189	3.02	0.65
11	30	0	1	360	0	1025	507	338	184	3.96	0.51
12	30	0	2	365	0	1025	498	332	183	4.02	0.50
13	30	5	1	342	18	1020	505	337	184	3.94	0.51
14	30	5	2	346.7	18.3	1020	498	332	183	4.00	0.50
15	30	10	1	324	36	1020	504	336	183	3.92	0.51
16	30	10	2	328.5	36.5	1020	497	331	182	3.98	0.50
17	30	15	1	306	54	1015	504	336	182	3.90	0.51
18	30	15	2	310.2	54.8	1015	497	331	182	3.95	0.50
19	30	20	1	288	72	1010	504	336	182	3.88	0.51
20	30	20	2	292.0	73	1015	495	330	181	3.92	0.50
21	40	0	1	440	0	1005	480	320	180	4.84	0.41
22	40	0	2	455	0	1005	470	313	177	5.01	0.39
23	40	5	1	418	22	1002	480	320	179	4.82	0.41
24	40	5	2	432.3	22.8	1000	470	313	177	4.00	0.39
25	40	10	1	396	44	1000	477	318	179	4.80	0.41
26	40	10	2	409.5	45.5	1000	468	312	176	3.98	0.39
27	40	15	1	374	66	1000	475	317	178	4.78	0.40
28	40	15	2	386.8	68.3	995	468	312	176	3.95	0.39
29	40	20	1	352	88	995	474	316	178	4.75	0.40
30	40	20	2	364	91	990	468	312	175	3.92	0.38

While: FA – Fly Ash; RS – River Sand; CS – Crush Sand; CA – Coarse Aggregate; W – Water; SP – superplasticizer; B – Binder.

2.4. Experiment

The experiment is conducted at the sample ages, as shown in Table 2. The experiment method of compressive strength of concrete was performed according to ASTM C39 [26]. For each concrete at a certain age, an experiment was conducted with three cylindrical prototypes (diameter 150 mm, height 300 mm). The mixture was fabricated by the ASTM C192 [27] and the European standard [22]. The sample is compacted on an automatic vibrator until all air bubbles are released, and the cement paste floats evenly, using a flattened model.

The samples are flattened the contact surface to ensure the compression plate is in contact with the sample surface during the experiment. The compressive intensity experiments of concrete were performed under ASTM C39 [26]. The cylindrical sample experiment with diameter D = 150 mm and height H = 300 mm; Carry out the force load at a maximum velocity of 0.15 – 0.35 MPa/s until sample failure. With each type of concrete conducting experiments, each group includes three compressed samples at the required ages, shown in Fig. 1.

a) Concrete mixer **b) Sample** **c) Moisturizing** **d) Sample compressor**

Figure 1. Some photos of the experiment.

3. Results and Discussion

Based on the Design of Experiments and statistical analysis with Minitab 19 software at 95 % confidence level, significance level α = 5 %. The number of test samples: 3 samples/group ensure to detect the difference within ± 3α. A general full factorial design was used to plan the experiment and analyze the results achieved.

3.1. Experimental results

Using Minitab19 software to design General full factorial design and analyze the results. The input variables of the experimental design: 3 variables

- Concrete grade: There are 3 types: C20, C30, C40.
- Date of age: There are 9 days: 1, 3, 7, 14, 28, 56, 90, 180, 360.
- Fly ash: There are 5 ratios: 0 % (control); 5 %; 10 %; 15 %; 20 %.
- Type of cement: There are 2 types of PC40 (type 1) and PCB40 (type 2).
- Each mixture consists of three specimens.

The output results need statistical analysis of one criterion is the compressive strength R_n. Total number of experiments: 3 × 9 × 5 × 2 × 3 = 810 (specimen), the results are summarized in Table 2.

Table 2. Results of compressive strength.

No	FA(%)	Type of cement	Days	Concrete grade 20			Concrete grade 30			Concrete grade 40		
				1st	2nd	3rd	1st	2nd	3rd	1st	2nd	3rd
1	0	1	1	0	0	0	7.3	7.8	8	11	11.5	10.8
2	0	1	3	15.2	16	15.3	23.3	23.8	23.1	26.4	26.9	26.2
3	0	1	7	22	22.5	21.8	32.4	32.9	32.2	36.9	37	37
4	0	1	14	26	26.5	26.2	38.1	38.6	37.9	45.2	45.7	45
5	0	1	28	30.3	31	31	45.6	46	45.3	55.1	55.6	54.9
6	0	1	56	33.6	34.3	33.8	50.6	51.1	50.4	60.1	60	60
7	0	1	90	35.4	36.2	35.1	52.9	53.4	52.7	62.3	62.8	62.1
8	0	1	180	36.9	37.4	36.7	54.7	55.2	54.5	64.5	65	64.3
9	0	1	360	37	37.5	37.6	55.6	56.1	55.6	66.1	66.6	65.9
10	0	2	1	6.9	7.4	6.7	9	9	8.3	10.9	11.4	11
11	0	2	3	13.7	14.2	13.5	22.7	23.2	22.5	26.2	26.7	26
12	0	2	7	20.3	20.8	20.1	31.7	32.2	31.7	36.6	37.1	36.4
13	0	2	14	24.7	25.2	24.5	37.2	37.7	37	44.8	45	45

No	FA(%)	Type of cement	Days	Concrete grade 20			Concrete grade 30			Concrete grade 40		
				1st	2nd	3rd	1st	2nd	3rd	1st	2nd	3rd
14	0	2	28	29.8	30.3	30	44.6	45.1	44.4	54.6	55.1	54.4
15	0	2	56	32.2	32.7	32	49.1	49.6	48.9	59.5	60	59.3
16	0	2	90	33.1	33.6	33.3	51.3	51.8	51.1	61.7	62.2	61.5
17	0	2	180	34	34.5	33.8	53.5	54	54	63.9	64.4	63.7
18	0	2	360	35.2	35.7	35	55.3	55.8	55.1	65.5	66	65.3
19	5	1	1	0	0	0	6.4	6.9	6.2	10.8	11.3	10.6
20	5	1	3	13.2	13.7	13.2	22.1	22.6	21.9	25.8	26.3	25.6
21	5	1	7	20	20.5	19.8	31.4	31.9	32	36	36.5	36
22	5	1	14	24	24.5	23.8	36.8	36.1	37	44.1	44.6	43.9
23	5	1	28	28.9	29.4	28.7	44.1	44.6	45	53.8	54.3	53.6
24	5	1	56	32.2	32.7	32	49.4	49.9	49.2	59.2	59.7	59
25	5	1	90	33.8	34.3	33.8	51.8	52.3	52	61	61.5	61.8
26	5	1	180	35.6	36.1	35.4	53.8	54.3	53.6	63.2	63.7	63
27	5	1	360	36.2	36.7	36.5	54.4	54.9	54.2	65	65	64.6
28	5	2	1	6.6	7.1	6.4	8.3	8	8.5	10.6	11.1	10.4
29	5	2	3	13.7	14.2	13.5	22.2	22	21.8	25.5	26	25.3
30	5	2	7	19.4	19.9	19.2	30.9	31.4	30.7	35.6	36.1	35.4
31	5	2	14	23.7	24.2	23.5	36.3	36	36.5	43.2	44	43.5
32	5	2	28	28.5	29	28.3	43.5	44	43.5	53.1	53.6	52.9
33	5	2	56	31.1	31.6	30.9	47.9	48.4	47.7	58.4	58.4	59
34	5	2	90	31.9	32.4	31.7	50.2	50.7	51	60.5	61	60.3
35	5	2	180	31.4	32.1	31.9	52.2	52.7	52	62.4	62	62
36	5	2	360	31.9	32.4	31.7	54	54.5	53.8	64	64	63.7
37	10	1	1	0	0	0	5.5	6	5.3	10.4	10.9	10.2
38	10	1	3	10.2	10.7	10	21.6	22.1	21.4	24.9	25.4	25
39	10	1	7	18	18.5	17.8	30.2	30.7	30	34.8	34.5	35
40	10	1	14	22	22.5	21.8	35.4	35.9	35.2	42.6	43	43
41	10	1	28	26.8	27.3	26.6	42.4	42.9	42.2	51.9	52.4	51.7
42	10	1	56	30.2	30.7	30	47.5	48	47.3	58.2	58	57.9
43	10	1	90	31.9	32	32	50	50	49.3	59.9	60.4	59.7
44	10	1	180	33.4	33.9	33.2	52	52.5	51.8	61.8	62.3	61.6
45	10	1	360	34.9	35.4	34.7	52.5	53	52.3	63.3	63.8	63.1
46	10	2	1	6.3	7	6.5	7.6	8.1	7.4	10.4	10.9	10.2
47	10	2	3	12.6	13	12.3	21.4	21.9	21.2	24.9	25.4	24.7
48	10	2	7	18.6	19.1	18.5	30	30.5	29.8	34.7	35.2	35
49	10	2	14	22.7	23.2	22.5	35.2	35.7	35	42.5	43	42.3
50	10	2	28	27.3	27.8	27.1	42.1	42.6	41.9	51.8	52	52
51	10	2	56	29.9	30.4	29.7	46.3	46.8	46.1	57.7	58.2	57.5
52	10	2	90	30.8	31.3	30.6	48.7	49.2	48.5	59.8	60.3	59.6
53	10	2	180	31.7	32.2	31.5	50.5	51	50.3	61.6	62	61.6
54	10	2	360	32.8	33.3	32.6	52.3	52.8	52.1	63.2	63.7	63
55	15	1	1	0	0	0	4.6	5.1	4.4	10	10.5	9.8
56	15	1	3	8.5	9	8.3	20.8	21.3	20.6	24	24.5	23.8
57	15	1	7	16	16.5	15.8	29.2	29.7	29	33.5	34	33.3
58	15	1	14	20	20.5	19.8	34.3	34.8	34.1	41	41.5	40.8
59	15	1	28	24.5	25	24.3	41	41.5	40.8	50	50.5	49.8
60	15	1	56	28.4	28.9	28.2	46.1	46.6	47	56	56.5	56.6
61	15	1	90	30.2	30.7	30	48.8	49.3	49	58.3	58.5	59
62	15	1	180	31.8	32.3	31.6	50.3	50.8	51	60.5	61	60.3

No	FA(%)	Type of cement	Days	Concrete grade 20			Concrete grade 30			Concrete grade 40		
				1st	2nd	3rd	1st	2nd	3rd	1st	2nd	3rd
63	15	1	360	33	33.5	33.2	50.8	51.3	50.6	62.4	62	62.7
64	15	2	1	6	6.5	5.8	6.9	7.4	6.7	9.9	10.4	9.7
65	15	2	3	12	12	11.8	20.5	21	20.3	23.8	24.3	3.6
66	15	2	7	17.7	18.2	17.5	28.7	29.2	28.5	33.2	33.7	33
67	15	2	14	21.4	22	21.6	33.7	33.7	33	41	40.8	41
68	15	2	28	26	26.5	25.8	40.3	40.8	40.1	49.6	50	50
69	15	2	56	28.8	29.3	29	44.3	44.8	44.1	56	56.2	56.6
70	15	2	90	29.9	30.4	29.7	46.7	46.7	47	58.5	59	58.3
71	15	2	180	30.4	30.9	30.2	48.8	49.3	48.6	60.5	61	60.3
72	15	2	360	31.5	32	31.3	50.2	50.7	50	61.9	61.6	61
73	20	1	1	0	0	0	3.7	4.2	3.5	9.7	10	10
74	20	1	3	7	7.5	6.8	20.1	20.6	20	23.3	23.8	24
75	20	1	7	14	14.5	13.8	28.3	28.5	29	32.5	33	32.3
76	20	1	14	18	18.5	17.8	33.1	33	33.5	39.8	40	40
77	20	1	28	22.1	22.6	21.9	39.6	40.1	39.4	48.5	49	48.3
78	20	1	56	26.2	26.7	27	44.7	45.2	44.5	55	54.2	54.8
79	20	1	90	28.6	29.1	28.4	47.1	46.5	45.8	57.1	57.6	56.9
80	20	1	180	30.5	31	30.3	49	49	48.7	60	60.5	59.2
81	20	1	360	31.5	32	31.3	49.1	49	49.3	61.5	62	61.3
82	20	2	1	5.7	6.2	5.5	6.2	6.7	6	9.6	10.1	9.4
83	20	2	3	11.4	11.9	11.2	19.5	20	19.3	23	23.5	22.8
84	20	2	7	16.9	17.4	16.7	27.5	28	27.3	32.1	32.6	33
85	20	2	14	20.6	21.1	20.4	32.2	32.7	32	39.3	39.8	39.1
86	20	2	28	24.8	25.3	24.6	38.5	39	38.3	47.9	48.4	47.7
87	20	2	56	28	28.5	27.8	42.4	42.9	42.2	55	54.6	54.4
88	20	2	90	29	29.5	28.8	44.7	44	43.3	57	57.5	56.8
89	20	2	180	29.5	30	29.3	47	47.5	46.8	58.9	59.4	58.7
90	20	2	360	31	31.5	30.8	48.1	48.6	47.9	61	60.7	60.4

3.2. Discuss the results

The results of the analysis of all variables and interaction between each other affected the compressive strength with statistical significance, shown in Fig. 2.

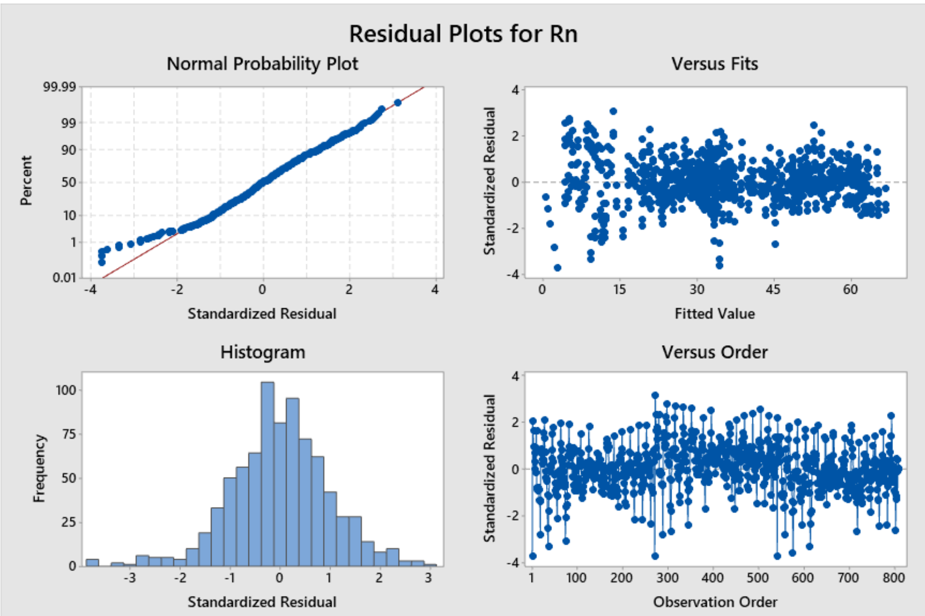

Figure 2. Residual Plots for R_n.

From Fig. 3, The chart evaluating the residuals shows that the normal distribution graph is showing the residuals very close to the normal distribution, and distributed on both sides via the "0" line so satisfying conditions for applying experimental statistical methods.

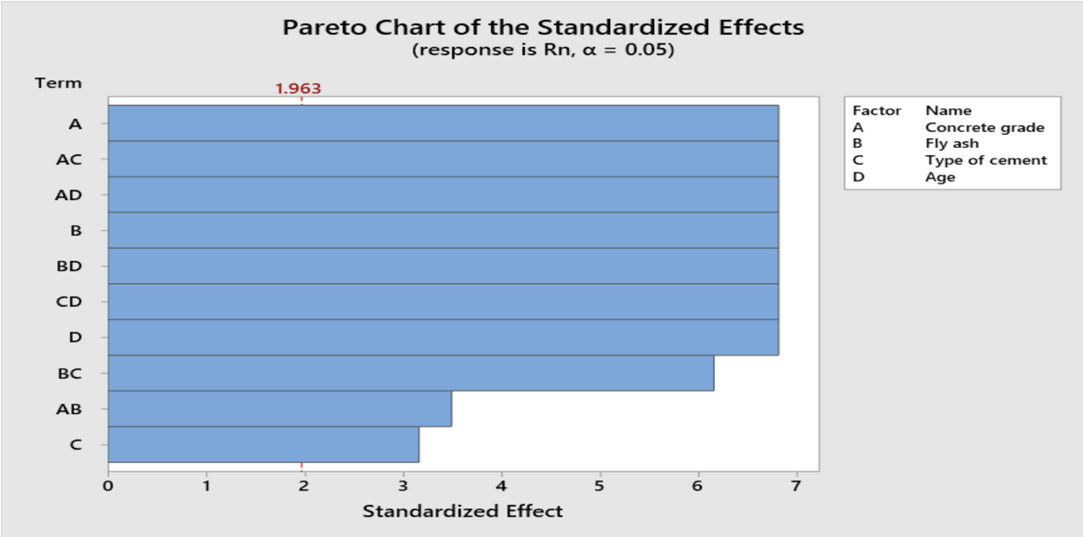

Figure 3. Pareto chart of the factors influencing R_n.

The Pareto chart in Fig. 3 shows that all variables and interactions between variables affect R_n with statistical significance. Cement type (C) has the least impact compared to other factors. Analysis of the variance of factors affecting compressive strength, the relationship model between them is built from Table 3 to Table 5 as follows:

Table 3. Analysis of variance factors and regression model.

Source	DF	Adj SS	Adj MS	F-Value	P-Value
Model	85	235257	2767.7	4597.05	0.000
Linear	15	226674	15111.6	25099.52	0.000
Concrete grade	2	65398	32698.8	54310.95	0.000
Fly ash	4	2543	635.8	1056.09	0.000
Type of cement	1	6	6.0	9.99	0.002
Age	8	158727	19840.9	32954.58	0.000
2-Way Interactions	70	8583	122.6	203.66	0.000
Concrete grade*Fly ash	8	17	2.1	3.53	0.001
Concrete grade*Type of cement	2	50	25.2	41.84	0.000
Concrete grade*Age	16	8013	500.8	831.80	0.000
Fly ash*Type of cement	4	29	7.4	12.25	0.000
Fly ash*Age	32	193	6.0	10.04	0.000
Type of cement*Age	8	280	35.0	58.13	0.000
Error	724	436	0.6		
Lack-of-Fit	184	370	2.0	16.56	0.000
Pure Error	540	66	0.1		
Total	809	235693			

Table 4. Model Summary.

S	R-sq	R-sq(adj)	R-sq(pred)
0.775930	99.82%	99.79%	99.77%

Table 5. Regression Table.

Term	Coef	SE Coef	T-Value	P-Value	VIF
Constant	35.3156	0.0273	1295.35	0.000	
Concrete grade					
20	–11.8611	0.0386	–307.63	0.000	1.33
30	1.9819	0.0386	51.40	0.000	1.33
Fly ash					
0	2.4530	0.0545	44.99	0.000	1.60
5	1.2807	0.0545	23.49	0.000	1.60
10	0.0715	0.0545	1.31	0.190	1.60
15	–1.2711	0.0545	–23.31	0.000	1.60
Type of cement					
1	0.0862	0.0273	3.16	0.002	1.00
Age					
1	–28.5478	0.0771	–370.21	0.000	1.78
3	–15.8878	0.0771	–206.03	0.000	1.78
7	–7.5456	0.0771	–97.85	0.000	1.78
14	–1.9222	0.0771	–24.93	0.000	1.78
28	5.0533	0.0771	65.53	0.000	1.78
56	9.5933	0.0771	124.41	0.000	1.78
90	11.5311	0.0771	149.54	0.000	1.78
180	13.2644	0.0771	172.01	0.000	1.78
Concrete grade*Fly ash					
20 0	0.1759	0.0771	2.28	0.023	2.13
30 5	0.1904	0.0771	2.47	0.014	2.13
Concrete grade*Type of cement					
20 1	-0.3414	0.0386	-8.85	0.000	1.33
30 1	0.2475	0.0386	6.42	0.000	1.33
Concrete grade*Age					
20 1	8.313	0.109	76.23	0.000	2.37
20 3	4.303	0.109	39.46	0.000	2.37
20 7	2.484	0.109	22.78	0.000	2.37
20 14	0.908	0.109	8.32	0.000	2.37
20 28	–1.458	0.109	–13.37	0.000	2.37
20 56	–2.821	0.109	–25.87	0.000	2.37
20 90	–3.402	0.109	–31.20	0.000	2.37
20 180	–4.069	0.109	–37.31	0.000	2.37
30 1	–2.116	0.109	–19.41	0.000	2.37
30 7	0.431	0.109	3.96	0.000	2.37
30 90	0.365	0.109	3.35	0.001	2.37
30 180	0.751	0.109	6.89	0.000	2.37
Fly ash*Type of cement					
0 1	0.2354	0.0545	4.32	0.000	1.60
5 1	0.2274	0.0545	4.17	0.000	1.60
10 1	-0.1251	0.0545	–2.29	0.022	1.60
15 1	-0.1356	0.0545	–2.49	0.013	1.60
Fly ash*Age					
0 1	-1.610	0.154	–10.44	0.000	2.84
0 3	-0.497	0.154	–3.23	0.001	2.84
0 28	0.684	0.154	4.43	0.000	2.84

Term	Coef	SE Coef	T-Value	P-Value	VIF
0 180	0.356	0.154	2.31	0.021	2.84
5 1	–0.871	0.154	–5.65	0.000	2.84
5 28	0.506	0.154	3.28	0.001	2.84
5 90	0.317	0.154	2.06	0.040	2.84
15 28	–0.403	0.154	–2.62	0.009	2.84
Type of cement*Age					
1 1	–1.4673	0.0771	–19.03	0.000	1.78
1 3	–0.2740	0.0771	–3.55	0.000	1.78
1 56	0.2849	0.0771	3.70	0.000	1.78
1 90	0.4294	0.0771	5.57	0.000	1.78
1 180	0.6272	0.0771	8.13	0.000	1.78

ANOVA analysis results adjusted determination coefficient R-sq(adj) = 99.79 %, all variables and combinations have P-value coefficient < 0.05. The regression table shows the relationship between compressive strength and factors. In which the model takes into account the interaction between the factors. Values that guarantee a significance level with P-value < = 0.05 are retained, while effects that do not guarantee statistical significance are removed in the regression table.

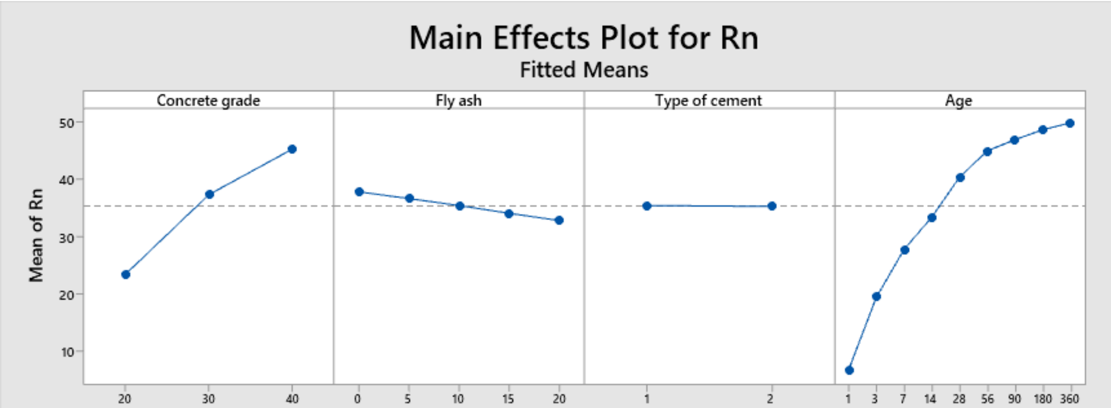

Figure 4. Factors that mainly influence R_n.

Fig. 4 shows the main factors that affect the compressive strength of concrete and their degree of influence. The grade of concrete will affect the design of the components in concrete with the higher the level, the correspondingly high strength. The impact of fly ash tends to the opposite. The more using fly ash, the intensity tends to decrease, while the type of cement has no significant effect between two kinds of cement PC and PCB at the same level. The most significant impact is the age of the concrete. The longer the time, then increasing the intensity of the concrete, the most robust increase in the period from 1 day to 56 days (very steep graph). However, after this period, the uptrend gradually slows down, and from 180 days to 360 days, the level of increase is negligible, the intensity remains at a stable level.

Observed Fig. 5 shows the interaction between the factors affecting the compressive strength of the concrete. The graphs related to the interaction effect between age and other factors have the most apparent change.

The graph in Fig. 6 shows the strength development of fly ash concrete over time; similar to previous studies [16–20], the compressive strength of concrete tends to decrease with increasing content used fly ash. Especially when studying the effect of time on the compress strengthen of fly ash concrete, Tukey's post-deterministic analysis shows very clear subgroups shown in Table 6 and Fig. 7.

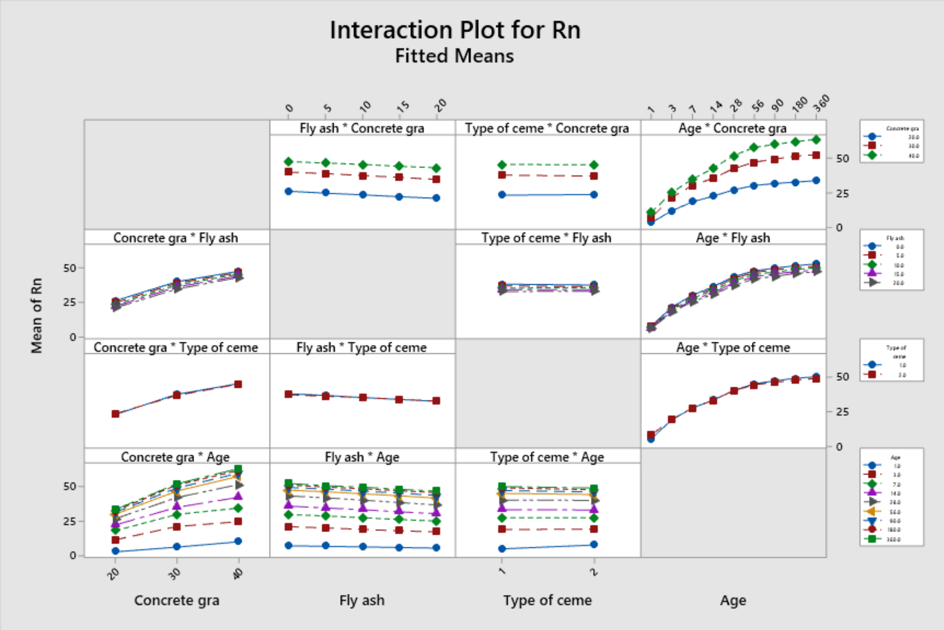

Figure 5. Interaction Plot for R_n.

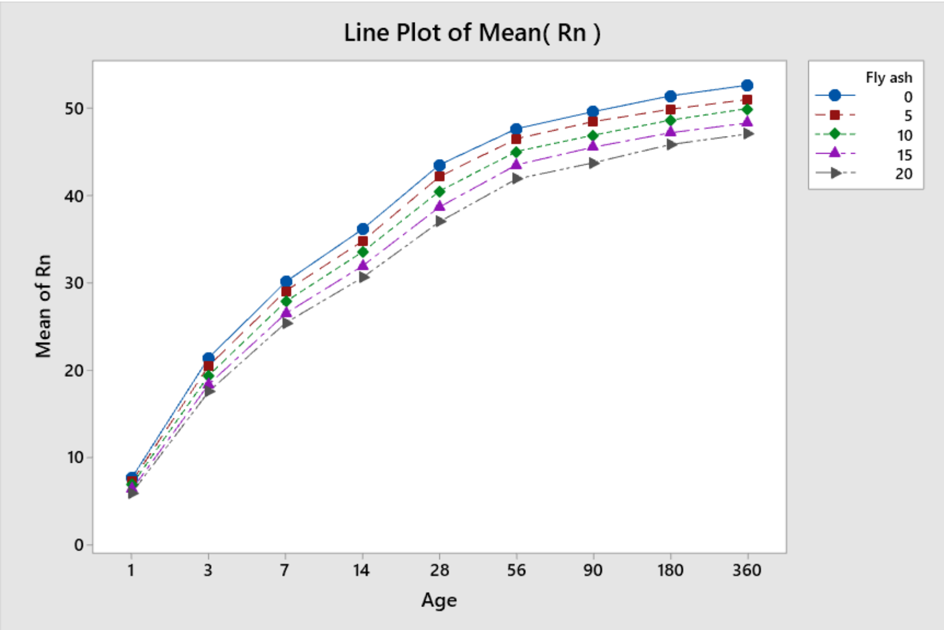

Figure 6. Compression strength development over time.

Table 6. Tukey Pairwise Comparisons between age of fly ash concrete.

Grouping Information Using the Tukey Method and 95 % Confidence

Age	N	Mean	Grouping
360	90	49.78	A
180	90	48.58	A B
90	90	46.85	A B
56	90	44.91	B
28	90	40.37	C
14	90	33.393	D
7	90	27.770	E
3	90	19.428	F
1	90	6.768	G

Means that do not share a letter are significantly different.

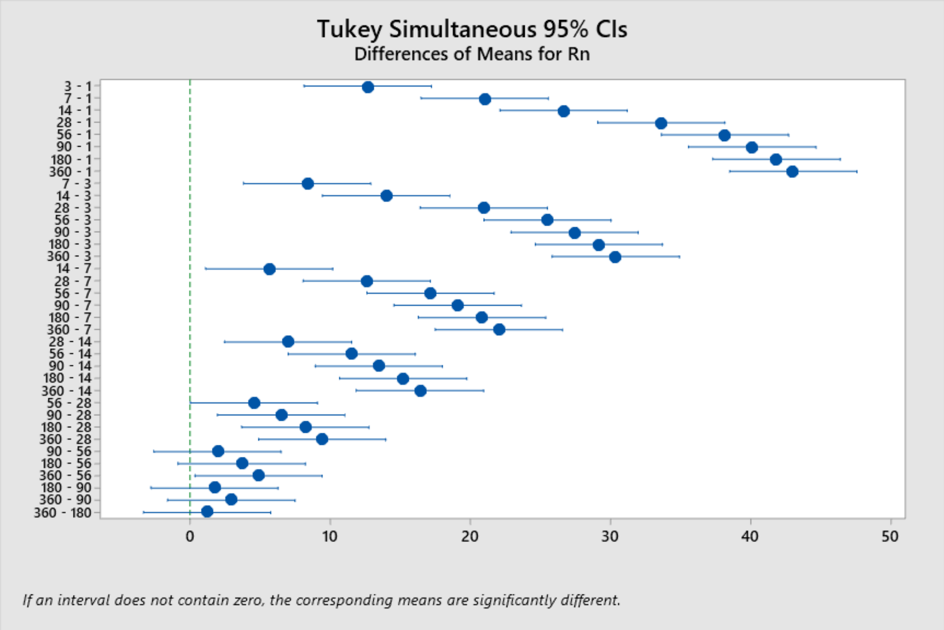

Figure 7. Compression strength development over time.

The difference is most pronounced in the 1, 3, 7, 14, and 28 years old, when they are classified into different groups, G, F, E, D, C, respectively. This marked difference partly reflects the cement's hydration and the reaction of fly ash and the cement's hydration product in the concrete mix. That process simultaneously increases the concrete's consistency, making the concrete's compressive strength increase rapidly, especially after seven days of age. Whereas the 56,90 and 180,360 of the remaining days, the difference between the age dates is classified into two groups A and B, meaning that the change in intensity between the age dates is not significant. These partly explain the intensity stability after the reaction equations occurred; in other words, the intensity developed slowly after 90 days and gradually stabilized at the age of 360 when the increase was not significant.

3.3. Response optimization to determine the best possible combinations for each grade of concrete

The most apparent difference between the methods using the experimental DOE planning and linear regression is to give predictive options when there are input parameters and output requirements for the problem.

To satisfy each concrete level has the best-guaranteed intensity at 28 days, the options are selected as Table 7 and Fig.8 below.

Table 7. The optimal options for each concrete grade.

No	Solution	Concrete grade	Fly Ash (%)	Type of cement	Age	Rn Fit	Composite Desirability
1	1	20	10	2	28	27.4690	0.412448
2	2	20	10	1	28	26.7006	0.400910
3	3	20	15	2	28	25.7110	0.386051
4	1	30	10	1	28	42.6328	0.640133
5	2	30	10	2	28	42.2235	0.633986
6	3	30	15	1	28	40.8149	0.612837
7	1	40	10	1	28	52.0047	0.780851
8	2	40	10	2	28	51.9027	0.779320
9	3	40	15	1	28	50.1868	0.753555

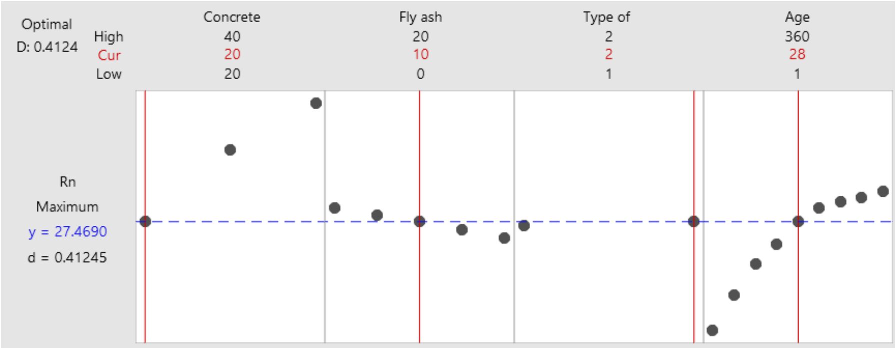

a) Optimal D: 0.4124

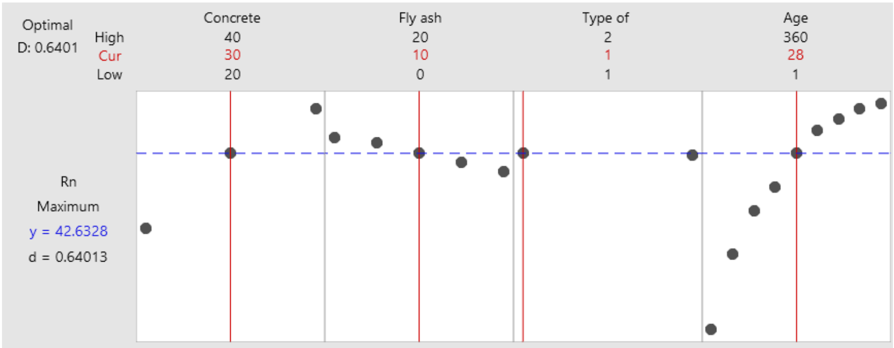

b) Optimal D: 0.6401

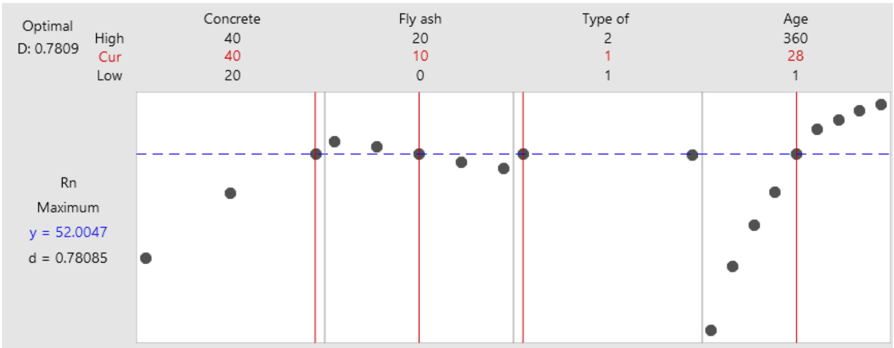

c) Optimal D: 0.7809

Figure 8. The images show the optimal solutions for the respective concrete grades.

For each concrete grade, there are three options, which have been proposed with the amount of fly ash and type of cement, based on ensuring the compressive strength of fly ash concrete at the best level at 28 days. Furthermore, for all three grades of concrete with proposed options for the optimal solution, fly ash content is usually selected at 10 % and 15 %, although in experimental planning, fly ash is considered up to 5 levels ranging from 0 % to 20 %.

4. Conclusions

1. Fly ash cement concrete has been applied in many countries to take advantage of waste from thermal power plants, which improves both the properties of concrete, such as workability, consistency, strength, and increase the intensity remaining to solve problems of environmental pollution. There are many factors to consider affecting the properties of concrete, especially the compressive strength, which is the most fundamental parameter specific to each concrete grade. The covered factors in the paper include the level of concrete, the type of used cement, the percentage of fly ash is used with the total amount of binder, and the time factor.

2. Based on previous studies and the authors' group, fluctuation of selected elements, to meet the current needs of reality. The results show that all factors have an apparent influence on the compressive strength of the concrete, especially the time factor. Over time the vigorous development process is for the first time (from 1 to 56 days). After this period, the process slows down and does not seem to change after one-year-old. At the same time, the conventional and mixed PC cement does not show the difference in the compressive strength of concrete.

3. Besides, the most useful fly ash content for concrete grades to achieve the best compressive strength at 28 days ranges from 10% to 15%. This research result is also consistent with some other studies in the world. Thus, with the influencing factors, depending on the grade of concrete used, the most appropriate coordination options can be selected.

5. Conflict of interests

The authors declare that there is no conflict of interests regarding the publication of this paper.

References

1. Berry, E.E., Hemmings, R.T., Cornelius, B.J. Mechanism of Hydration Reactions in High Volume Fly Ash Pastes and Mortars. Cem Concr Compos. 1990. 12.
2. Gordana, S. Hydration of Mechanically Activated Mixtures of Portland Cement and Fly ash, Faculty of Mechanical Engineering, Republic of Serbia. 2007.
3. Lam, L., Wong, Y.L., Poon, C.S. Degree of Hydration and Gel/space Ratio of High-Volume Fly Ash/Cement Systems. Cement and Concrete Research. 2000. 30.
4. Pacheco-Torgal, F., Castro-Gomes, J., Jalali, S. Alkali-activated binders: a review part I, historical background, terminology, reaction mechanisms and hydration products, J. Constr. Build. Mater., 2008. 22, Pp. 1305–1314.
5. American Concrete Institute. ACI 232R-11, Fly Ash in Concrete. American. 2011.
6. Michael, T. Optimizing the Use of Fly Ash in Concrete. University of New Brunswick. 2012.
7. Owen, P.L. Fly Ash and Its Usage in Concrete. Journal of Concrete Society. 1979. 13.
8. Jiang, L.H., Malhotra, V.M. Reduction in Water Demand of Non Air-Entrained Concrete Incorporating Large Volume of Fly Ash. Cement and Concrete Research. 2000. 30.
9. Thai, D.S. Report on the results of research and application of high quality concrete. Institute of Building Materials. 2006.
10. Kumar, M.P. High Performance, High-Volume Fly Ash Concrete for Sustainable Development. 2009.
11. Nguyen, T.T.N. Research of some main properties of roller compacted concrete for motorways and airports. Doctoral Thesis. University of Transport and Communications. 2016.
12. Nguyen, T.T.N. Research of using by-products of Vung Ang I Thermal power plant to make construction material for rural road. Vietnam Road and Bridge Magazine. 2018. 9.
13. Usanova, K., Barabanshchikov, Y.G. Cold-bonded fly ash aggregate concrete. Magazine of Civil Engineering. 2020. 95 (3). Pp. 104–118. DOI: 10.18720/MCE.95.10
14. Ngo, V.T., Lam, T.Q.K., Do, T.M.D., Nguyen, T.C. Increased plasticity of nano concrete with steel fibers. Magazine of Civil Engineering. 2020. 93 (1). Pp. 27–34. DOI: 10.18720/MCE.93.3
15. Do, T.M.D., Lam, T.Q.K. Design parameters of steel fiber concrete beams. Magazine of Civil Engineering. 2021. 102 (2).
16. Konstantin, S., Mohamadreza, M., Habib, T., Hani, T. Class F Fly Ash Assessment for Use in Concrete Pavements, Technical Report. 2017. 1.
17. Anjali Yadav, Nikhil Kumar Yadav. Study of Fly Ash Cement Concrete Pavement, International Journal of Civil Engineering. 2017. 4 (2).
18. Hilmi, L.A., Aysen, L.M., Burak, G.A. Analysis and Design of a Stabilized Fly Ash as Pavement Base Material. World of Coal Ash, Lexington, Kentucky, USA. 4/2005.
19. Jin, H., Huayou, S. Application for Fly Ash Concrete in Pavement Engineering. Advanced Materials Research. 2012. 510. Pp. 817–821.
20. Uma, M.M., Sundararajan, T. Studies on the properties of previous fly ash – cement concrete as a pavement material, Cogent Engineering, 4/2017.
21. ACI Committee 214. Guide to evaluation of strength test results of concrete, ACI 214-11. American Concrete Institute, Farmington Hills, Michigan. 2011.
22. European Committee for Standardization, EN206, Concrete. Specification, Performance, Production and Conformity, European. 2013.
23. Pacheco, T.F., Castro, G.J., Jalali, S. Alkali-activated binders: a review part I, historical background, terminology, reaction mechanisms and hydration products. J. Constr. Build. Mater. 2008. 22, Pp. 1305–1314.
24. Duraković, B., Bašić, H. Continuous Quality Improvement in Textile Processing by Statistical Process Control Tools: A Case Study of Medium-Sized Company. Periodicals of Engineering and Natural Sciences. 2013. 1 (1), Pp. 36–46.
25. ASTM C618 – 19 Standard Specification for Coal Fly Ash and Raw or Calcined Natural Pozzolan for Use in Concrete.
26. American Society for Testing and Materials, ASTM C39, Standard Test Method for Compressive Strength of Cylindrical Concrete Specimens, American. 2014.
27. American Society for Testing and Materials, ASTM C192, Standard Practice for Making and Curing Concrete Test Specimens in the Laboratory, American. 2014.

Contacts:

Thi Thu Nga Nguyen, ngantt@utt.edu.vn

Anh Tuan Nguyen, tuanna@utt.edu.vn

Quoc Vuong Vu, vuongvlxd@tlu.edu.vn

Van Thuc Ngo, nvthuc34@gmail.com

Thanh Quang Khai Lam, lamthanhquangkhai@gmail.com

Magazine of Civil Engineering. 2022. 109(1). Article No. 10912

Magazine of Civil Engineering

ISSN 2712-8172

journal homepage: http://engstroy.spbstu.ru/

DOI: 10.34910/MCE.109.12

Target reliability of alternative fundamental combinations in Eurocode EN1990

P. Croce*, P. Formichi, F. Landi

Department of Civil and Industrial Engineering – University of Pisa, Pisa, Italy

**E-mail: p.croce@ing.unipi.it*

Keywords: structural reliability; failure reliability; reliability index, reliability analysis, reliability assessment, random variable, structural analysis, probability function, design optimization, reliability optimization

Abstract. In Eurocode EN1990 action effects in persistent and transient design situations for ULS checks are derived according to three different alternative expressions for combinations of actions, to be chosen in the National Annex for use in a country. The three formulations, ([6.10], or [6.10a] and [6.10b], or [6.10a modified] and [6.10b]), which are substantially confirmed in the draft version of the new EN1990 (prEN1990:2019), are not completely equivalent in terms of structural reliability. In the present study, the reliability levels associated with each of them are compared in some relevant examples considering permanent and imposed loads for different buildings categories. In the analyses, the structural reliability indexes derived using level 2 and 3 methods are discussed considering the influences of different assumptions about statistical distributions and parameters of material resistances and action effects. The results of the sensitivity analyses confirm that the reliability level for ULS checks is also strongly dependent upon the statistical models adopted. The target reliability level recommended for use in EN 1990 (and in prEN1990:2019) is commonly reached using expression [6.10], while the adoption of expressions [6.10a] and [6.10b] can lead to lower values, especially when the coefficient of variation (COV) of the material resistance is high. Expressions [6.10a modified] and [6.10b] generally lead to very significant reductions of the reliability levels in all the investigated cases, especially when permanent loads dominate the structural design.

1. Introduction

EN1990 is the head code in the Eurocode suite and establishes the principles and requirements for safety and serviceability for all the Structural Eurocodes [1]. EN1990 provides the basis for structural design and verifications, introducing the limit state design concept to be used in conjunction with the partial factor method. In the limit state design, also known as load and resistance factor design [2], it should be verified that the design load effect does not exceed the design resistance of the structure in ultimate limit states. Design load effects are determined for each limit state considering a representative load combination defined to take into account the probability of the simultaneous application of the various load types. Load combination rules, with the associated partial and combination factors, should be defined with the final aim to guarantee a minimum target reliability level for the designed structural members for all construction materials. In this study, load combinations in the structural Eurocodes are discussed evaluating the resulting reliability levels for different building structures and considering the relevant influences of different assumptions about statistical distributions and parameters of material resistances and action effects.

Combination of actions, which are given in Section 6 of Eurocode EN 1990:2002 [3], are substantially confirmed in Section 8 of new draft of prEN1990:2019 [4]. The choice of the format to be adopted in a country is transferred to National authorities, according to clause 6.4.3.1(1) P of [1], which states that "*for*

Croce, P., Formichi, P., Landi, F. Target reliability of alternative fundamental combinations in Eurocode EN1990. Magazine of Civil Engineering. 2022. 109(1). Article No. 10912. DOI: 10.34910/MCE.109.12

each critical load case, the design values of the effects of actions $\left(E_d\right)$ *shall be determined by combining the values of actions that are considered to occur simultaneously*".

The Ultimate Limit States (ULS) verifications in EN1990 regard the loss of static equilibrium (EQU), internal failure or excessive deformation of the structure (STR), failure or excessive deformation of the ground (GEO) and fatigue failure (FAT). The occurrence of any ULS is prevented by checking the fundamental inequality

$$E_d \leq R_d, \tag{1}$$

where E_d is the design value of action effects and R_d the design value of the resistance.

Following clause §6.4.3.2 of EN 1990, design values of the action effects in persistent and transient design situations can be derived adopting three alternative and mutually exclusive sets of fundamental combinations of actions. These sets, given below, are formally identified by expression [6.10] of EN1990 (Eq. (2)); or by the most adverse between expressions [6.10a] (Eq. (3.a)) and [6.10b] (Eq. (3.b)); or by the most adverse between expressions [6.10a modified] (Eq. (4)) and [6.10b] (Eq. (3.b)). Although in prEN1990:2019, ULS are no more formally distinct in EQU, STR and GEO, the sets of mutually exclusive combinations remain substantially unchanged: in fact, the "new" combination [8.12] corresponds to the "old" combination [6.10]; the "new" combination [8.13.a] to the "old" [6.10.a], the "new" combination [8.13.b] to the "old" [6.10.b] and, finally, the "new" combination [8.14] to the "old" combination [6.10.a modified]:

$$\sum_{j\geq 1} \gamma_{G,j} G_{k,j} \text{"+"} \gamma_P P \text{"+"} \gamma_{Q,1} Q_{k,1} \text{"+"} \sum_{i>1} \gamma_{Q,i} \psi_{0,i} Q_{k,i}; \tag{2}$$

$$\sum_{j\geq 1} \gamma_{G,j} G_{k,j} \text{"+"} \gamma_P P \text{"+"} \gamma_{Q,1} \psi_{0,1} Q_{k,1} \text{"+"} \sum_{i>1} \gamma_{Q,i} \psi_{0,i} Q_{k,i}; \tag{3a}$$

$$\sum_{j\geq 1} \xi \gamma_{G,j} G_{k,j} \text{"+"} \gamma_P P \text{"+"} \gamma_{Q,1} Q_{k,1} \text{"+"} \sum_{i>1} \gamma_{Q,i} \psi_{0,i} Q_{k,i}; \tag{3b}$$

$$\sum_{j\geq 1} \gamma_{G,j} G_{k,j} \text{"+"} \gamma_P P. \tag{4}$$

In expressions (2), (3.a), (3,b) and (4), $G_{k,j}$ is the nominal or characteristic values of the j-th *permanent actions*, P is the relevant representative value of prestressing action, $Q_{k,1}$ is the characteristic value of the *leading variable action*, $\psi_{0,i} Q_{k,i}$ is the combination value of the i-th accompanying variable action, acting simultaneously with the leading one, $\gamma_{G,j}$, $\gamma_{Q,i}$ and γ_P are the partial factors for permanent, variable and prestressing actions, respectively, and ξ, considered as a combination factor, is a reduction factor for permanent actions in expression [6.10b], or [8.13.b], for which the recommended value is 0.85.

Considering that combinations in EN1990:2002 and in prEN1990:2019 coincide, in the following reference is made to the EN1990 nomenclature.

EN1990, the choice among the above formulations for use in a country is left to the National Annex, prepared by the National Standard Body.

The rationale of the alternative sets is evident, In fact, in expression [6.10a] the unfavourable part of permanent actions is assumed as leading action and all variable actions are considered as accompanying actions; in expression [6.10b] unfavourable permanent actions are also considered as accompanying ones; finally, in the third alternative, expression [6.10a modified] only includes permanent actions.

Typical argument in support of the alternative formulation [6.10a] and [6.10b] is that in this way it is possible to weaken the dependence of the reliability index β on the parameter χ, better described in he following, which is the ratio between the effects of variable actions and the total actions [1, 5], arriving to a more uniform distribution of β values over χ. Truly, very sound arguments can be also claimed endorsing adoption of the recommended formulation [6, 10]; among them, particularly relevant is the observation that the fraction of the design life, during which the minimum reliability should be assured, depends on the nature of the actions governing the design. In fact, the total duration of that fraction of the design life, which is very significant in case the structural design is governed by permanent actions, when the required minimum reliability is little varying over time, reduces as soon as the influence of variable actions increases.

Evidently, in case the variable actions predominate, the minimum reliability is required only occasionally, however, for a small amount of the life of the construction.

Finally, use of alternative [6.10a mod] and [6.10b] is supported only by merely economic arguments. In the Authors opinion, these arguments are very week, since they lead, when permanent loads are governing the design, i.e. χ is small, to inacceptable reduction of β.

Load combinations in the Eurocodes were first discussed in [1] to formulate general recommendations for the BSI National Annex to EN1990. Simple examples for generic structural members showed that expression [6.10] leads to the most reliable structures, expressions [6.10a] and [6.10b] provide a lower but comparatively most uniform reliability level for all load ratios, while the use of modified expression [6.10a] and expression [6.10b] is not recommended since leads to rather low reliability level.

In any case, till now there are no logical reasons strong enough to clearly identify the most appropriate formulation, In fact, examining 24 National Annexes available to the Authors, it resulted that: 13 countries adopted expression [6.10]; 5 countries adopted expressions [6.10a] and [6.10b]; 5 countries allowed the designer to choose between [6.10], or [6.10a] and [6.10b]; and only one country adopted expressions [6.10a mod] and [6.10b].

An in deep evaluation about the Nationally Determined Parameter (NDPs) selected by each Member State and the reliability of structural members designed accordingly can be found in [5].

In the recent years, a discussion about reliability levels of structural members designed according to the partial factor method given in the Eurocodes has been initiated and it is currently ongoing also in view of the second generation of Eurocodes [6, 7] The discussion is mainly focused on target reliability levels [8–12] and the calibration of load factors to minimize variability of reliability levels [13, 14].

In this context, it is important to remind that the evaluation of reliability indexes and the calibration of partial factors is characterized by several uncertainties concerning for example, the assumptions on the distribution functions for loads and material resistances, the methods adopted to evaluate reliability [15–17], and not least the combination rule adopted for structural design.

Since the three formulations given in EN1990 are not equivalent in terms of structural reliability [1], aim of the present study is to compare the reliability levels associated with each expression in some significant case studies. In the examples, residential, commercial and storage buildings are considered, varying the representative parameters of the permanent and variable actions, as well as of the resistances of building materials, assuming different statistical distributions.

In the investigation, the reliability indexes β [15–17] were initially calculated according to level 2 approach; successively, a supplementary level 3 sensitivity analysis was carried out. The latter allowed to investigate the influence of different hypotheses, regarding statistical distributions of mechanical properties for structural materials and actions, on the structural reliability index β and to compare the results with the target reliability levels [9–12].

2. Methods

The study is articulated in three subsequent steps, increasing the level of deepening and complexity.

In a first phase (case 1) [18] the distribution of actions' effect (E_d) is derived, in turn, as the result of the combination of permanent and variable actions, according to one of the three alternative formulations, so focusing on their influence on the reliability. Briefly, that preliminary study aims to assess the sensitivity of the calculated reliability indexes on the adopted formulation.

In the second phase (case 2) [18], the actual distribution of effects of actions has been theoretically derived, taking also into account the influence of model uncertainties.

The outcomes of these first two phases confirmed, once again, that the reliability index β is a relative measure of the structural safety, strongly dependent on the starting assumptions.

Also aiming to clarify whether and how much level 2 simplifications influence the results, a more refined study (phase 3 – case 3) has been finally carried out, determining the actual probabilities of failure, by means of direct numerical integration of the relevant limit state functions.

The investigated case studies are referred to structural steel and reinforced concrete members in different building categories. Aiming to cover the most significant cases occurring in current design practice, they were considered residential buildings (categories A and B of EN 1991-1-1 [19]), commercial buildings (categories C and D) and storage buildings (category E1). Besides the unfavourable permanent action G, only one unfavourable variable action Q, the imposed load, was considered, but the investigation could be easily extended to a greater number of actions.

The relative effects of permanent and variable actions were taken into account by means of the already cited parameter χ, defined as the ratio between the characteristic value of the variable action, Q_k, and the characteristic value of the global action, sum of the characteristic value of permanent and variable actions, $G_k + Q_k$:

$$\chi = \frac{Q_k}{G_k + Q_k}. \tag{5}$$

The χ values were assumed varying in the range $0 \le \chi \le 0.67$, being the upper limit approximately corresponding to a ratio $Q_k / G_k = 2.0$. Evidently, smaller values of χ correspond to heavy structures, where permanent load is governing the design, while $\chi \ge 0.5$ correspond to lighter structures, where imposed load is leading.

Failure in reinforced concrete structures was associated, in turn, to concrete crushing, like in compressed columns or in beams with high reinforcement ratio, or to yielding of reinforcing steel.

In each example, and for each given χ value, the structure was designed in the most economical way, thus equalizing design effects and design resistance in Eq. (1), i.e. setting $E_d = R_d = R_k / \gamma_M$, being γ_M the partial factor for resistance.

Design effects E_d were calculated adopting recommended values of partial and combination factors provided in EN1990: $\gamma_G = 1.35$; $\gamma_Q = 1.50$; $\xi = 0.85$; $\psi_0 = 0.70$ for residential and commercial buildings; $\psi_0 = 1.00$ for storage buildings, In must be remarked that, for storage buildings, the group [6.10a modified+6.10b] is the unique alternative to [6.10], since in that case the group [6.10a +6.10b] coincides with expression [6.10].

Of course, for a given value of χ, adoption of expression [6.10] leads to the maximum required design strength, $R_{d\max}(\chi)$, $R_{d\max}(\chi) = R_{d[6.10]}(\chi)$. Adopting alternative expressions [6.10a+6.10b] or [6.10a modified+6.10b], the required strength reduces to $R_{d[6.10a+b]}(\chi)$ or to $R_{d[6.10a\,\mathrm{mod}+b]}(\chi)$, where the index indicates the expressions used in designing the structures. With obvious symbolism [18, 19], the characteristic resistances required by the various alternative expressions can be easily obtained as a function of $R_{d[6.10]}(\chi)$, in the forms:

$$R_{k[6.10]}(\chi) = \gamma_M R_{d[6.10]}(\chi) = \gamma_M R_{d\max}(\chi); \tag{6.a}$$

$$R_{k[6.10a+b]}(\chi) = \gamma_M R_{d[6.10a+b]}(\chi) = \\ = \gamma_M R_{d[6.10]}(\chi) \frac{\max\left(1 + \gamma_Q \gamma_G^{-1} \psi_0 \frac{\chi}{1-\chi}; \xi + \gamma_Q \gamma_G^{-1} \frac{\chi}{1-\chi}\right)}{1 + \gamma_Q \gamma_G^{-1} \frac{\chi}{1-\chi}}; \tag{6.b}$$

$$R_{k[6.10a\,\mathrm{mod}+b]}(\chi) = \gamma_M R_{d[6.10a\,\mathrm{mod}+b]}(\chi) = \\ = \gamma_M R_{d[6.10]}(\chi) \frac{\max\left(1; \xi + \gamma_Q \gamma_G^{-1} \frac{\chi}{1-\chi}\right)}{1 + \gamma_Q \gamma_G^{-1} \frac{\chi}{1-\chi}}. \tag{6.c}$$

In the first two phases of the study, for the resistance and actions effects they were considered the statistical parameters, mean, μ, and coefficient of variation (COV), V, summarized in Table 1, assuming normal or log-normal probability density functions.

Table 1. Statistical properties of relevant actions and strengths.

Strength/Action	Symbol	Mean μ	COV (V)	γ_M
Steel (yield stress)	R	$R_k + 1.64\ \sigma_R$	0.07	1.00
Rebars (yield stress)	R	$R_k + 1.64\ \sigma_R$	0.07	1.15
Concrete compressive strength	R	$R_k + 1.64\ \sigma_R$	0.15	1.50
Concrete compressive strength (1)	R	$R_k + 1.64\ \sigma_R$	0.20	1.50
Permanent action (case 1)	G	$G_k - 1.64\ \sigma_G$	0.10	
Permanent action (case 2)	G	G_k	0.10	
Imposed load (residential etc.)	Q	~ 0.3 Q_k	1.42	
Imposed load (shopping etc.)	Q	~ 0.6 Q_k	0.35	
Imposed load (storage etc.)	Q	~ 0.8 Q_k	0.15	

(1) Cast in situ, no special control

In the following sections, the reliability levels will be assessed for different categories of imposed loads (residential, shopping and storage). Climatic actions can be easily added in the analysis; however, the obtained reliability levels will be influenced also by the considered locations. For example, for snow loads different climatic zones can be characterized by significantly different values of the coefficient of variation [20]. The reliability of roof structures designed according to the Eurocodes and subjected to snow loads have been already discussed in [21, 22] and by the authors in [23, 24] and [25] considering also climate change influence. The results highlighted lower values than the target ones for lightweight roof structures; however, it must be recalled that often additional safety margins are intentionally introduced in codes, increasing the characteristic ground snow loads resulting from the statistical analysis of data in the adopted snow load maps, as observed by the authors in [26].

Concerning wind loads, the evaluation of structural reliability levels involves a complete probabilistic description of all the relevant parameters in the wind load chain (shape, roughness and gust factor, together with the basic wind velocity). An example of reliability assessment is carried out with reference to the benchmark two-storey steel frame defined in the example applications of the JCSS model code [27]. The benchmark structure is subjected to permanent (G), imposed (Q) and wind load (W) and designed adopting the expression [6.10] in EN1990 [3]. Adopting the probabilistic models given by the JCSS [27], the variation of reliability levels with load ratio $\chi = W_k / (G_k + Q_k)$ is evaluated considering different probability density function (pdf) for the wind velocity, Gumbel, Weibull and Generalized Pareto Distribution (GPD). The results are shown in Fig. 1 and highlight the sensitivity of the reliability measure to the adopted pdf for the wind velocity. The heavy tail of the GPD leads to significantly lower values of reliability than those obtained adopting Gumbel and Weibull pdf. Beside the high sensitivity of the outcomes on the adopted extreme value distribution, we can notice the relevant decrease of reliability when the COV of the wind action is increased: in fact, looking at the Fig. 1, it clearly emerges that reliability indexes obtained assuming COV = 0.1 (solid lines), are significantly higher than those pertaining to COV = 0.2 (dashed lines).

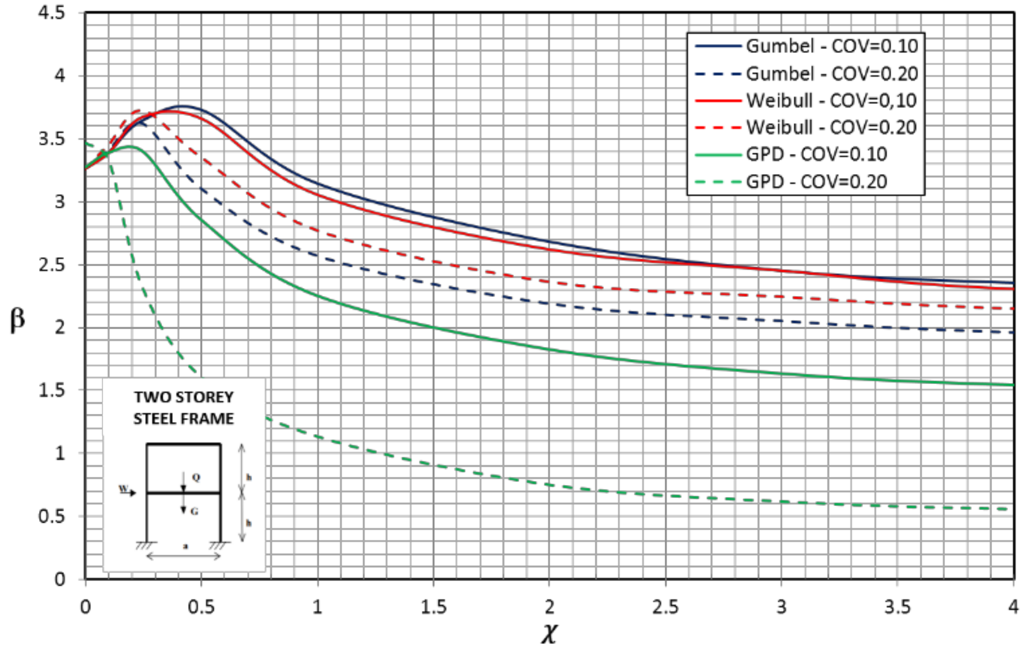

Figure 1. $\beta-\chi$ reliability curves for the benchmark two-storey steel frame described in [27].

Values in table 1 are consistent with those recommended by the *Joint Committee on Structural Safety* (JCSS) [27] and currently adopted in literature [5, 28–33]. As better described in §3.1, in the first two phases of the research, the statistical parameters of the imposed load where obtained fitting the upper tail of the extreme values distribution with the upper tail of a normal distribution, according the JCSS recommendations. Furthermore, in order to adequately cover the whole range of current design applications, the coefficient of variation of imposed loads was selected close to its upper bound, is case of residential buildings, and close to its lower bound, in the other cases.

The resistance R was modelled as the product of three independent log-normally distributed variables,

$$R = Azf, \tag{7}$$

where A and z are suitable geometrical properties, for instance an area and an inner lever arm, and f an appropriate strength, namely yield stress f_y for steel, and compressive strength f_c for concrete.

The *COV*s for the geometrical properties (V_A and V_z) were taken equal to 6 % for r.c. sections and to 3 % for steel ones. Regarding the strength of building materials, the *COV*s were adopted according to Table 1. More into detail, for concrete, beside the usual value $V = 0.20$, it was also explored the reduced value $V = 0.15$, which is consistent with a more stringent quality control during execution. Whence, recalling eq. (7), the COV of R results 17.3 % for high quality control concrete ($V = 0.15$), 21.8 % for concrete cast in situ with normal quality control $(V = 0.20)$, and 8.19 % for structural steel and reinforcing steel $(V = 0.07)$.

It must be underlined that results pertaining to different materials or to different failure modes cannot be directly compared, since the assessment formulae currently provided in Eurocodes, or in other structural standards, frequently contain additional safety, although not explicitly declared.

2.1. Evaluation of statistical parameters for imposed loads

Live loads on building floors are induced by the weight of furniture, equipment, stored items and occupants; they depend on building's category and vary in time and space. In a first approximation, spatial variations of live loads can be assumed to be homogeneous, while time variations can be represented by two components, the sustained load and the intermittent load [27, 34, 35].

The sustained load includes the weight of furniture and heavy equipment; its short-term variations are generally included in uncertainties. The intermittent load, characterized by usually short relative duration, represents all other kinds of live loads not covered by the sustained load, like gathering of people, or stacking of furniture during maintenance, as well as, when load-structure interaction is negligible, the dynamic magnification.

The equivalent uniformly distributed load q of the sustained load part is characterized by its overall mean intensity, μ_q, and by its standard deviation σ_q, expressed by [27].

$$\sigma_q = \sqrt{\sigma_y^2 + k\sigma_u^2 \min\left(1;\frac{A_0}{A}\right)}; \tag{8}$$

being σ_y is the standard deviation of the effects of a zero mean normal variable Y; σ_u the standard deviation of the effects of a zero mean random field $U(x,y)$ with a specific skewness to the right; A the tributary area of the considered element, A_0 the reference area and k an adjustment factor depending on the shape of the influence surface. Generally, k varies in the range 1.0 – 2.4 [27, 35]. In the present study it has been assumed $k = 2.0$, which is a typical value for bending moments on beams or axial forces in columns.

If the time between load changes is exponentially distributed, the number of load changes is Poisson distributed and the process is a Poisson pulse process. The cumulative distribution function (CDF) of the arbitrary point in time value q of a rectangular pulse process is expressed by

$$F_q(x) = (1-d)H(x) + dF_{q'}(x), \tag{9}$$

where $H(x)$ is the Heaviside unit step function, $F_q(x)$ is the CDF of q' and d is the fraction of time the process is non-zero. For the sustained load, obviously, it is $d = 1.0$.

From equation (9), the CDF of the life-time maximum value $q_{\max}$ results

$$F_{q_{\max}}(x) = \left[(1-d)H(x) + dF_{q'}(x)\right]\exp\left[-\lambda T\left(1-F_{q'}(x)\right)\right], \tag{10}$$

where T is a suitable time interval linked with the expected life of the building and λ the rate of the process, i.e. the number of pulses in the time unit. For high values of x it is $F_{q'}(x) \approx 1.0$, therefore (10) reduces to

$$F_{q_{\max}}(x) \approx \left[(1-d)H(x) + d\right]\exp\left[-\lambda T\left(1-F_{q'}(x)\right)\right]. \tag{11}$$

The equivalent uniformly distributed load (EUDL) p of the intermittent load part can be represented by the same stochastic field as the sustained load, whose representative parameters, mean intensity, μ_p, and standard deviation σ_p, depend on the building's category. The intermittent load maxima occur as a Poisson rectangular pulse process characterized by a mean occurrence rate v, and by an average duration of each pulse, d_p, depending on the imposed load classification.

The extreme values of EUDL, p, in the reference time interval T are again expressed by equations like (10) and (11).

Adopting input data parameters for live load distributions consistent with table 2.2.1 of JCSS Code [27] and assuming that q and p are stochastically independent and described by appropriate gamma distributions, the following parameters of the extreme value distributions of the maxima of imposed loads can be found: $\mu_{q,\max} \approx 0.39$ kN/m^2, COV ≈ 1.30, $Q_k = 2.00$ kN/m^2 in residential buildings; $\mu_{q,\max} \approx 2.19$ kN/m^2, COV ≈ 0.50, $Q_k = 5.00$ kN/m^2 in commercial buildings and $\mu_{q,\max} \approx 4.15$ kN/m^2, COV ≈ 0.30, $Q_k = 7.50$ kN/m^2 in storage buildings. Obviously, in storage buildings intermittent loads are not significant.

Since characteristic values of imposed loads are extremely sensitive to input data variations, the parameters in Table 1 were adopted for the analyses, in order to appropriately cover the possible range of variations.

3. Results and Discussion

In the following sub-sections, the results in terms of reliability curves are presented and discussed for the three case studies described in the Introduction:

- Case 1: effects of actions represented by alternative expressions of load combinations given in EN1990;
- Case 2: effects of actions represented by the theoretical combination, taking into account also the influence of model uncertainties;
- Case 3: Level 3 sensitivity analysis determining the actual probabilities of failure, by means of direct numerical integration of the relevant limit state functions.

3.1. Case 1: distribution of effects represented by alternative load combinations

In the first phase of the analysis (case 1), effects of the actions were evaluated considering all the three EN1990 alternative formulations, already recalled in §1, setting the characteristic value of permanent actions as the 95 % fractile.

To make easier the analytical treatment, two limit state functions were analyzed: the safety margin, S, in case of normal variables,

$$S = R - E \tag{12}$$

and the safety factor, Z, for log-normal variables,

$$Z = \frac{R}{E}. \tag{13}$$

The probability of failure is then given by

$$P_f = P\left[\left(R - E\right) < 0\right] = \Phi\left(-\beta\right) \quad \text{(a)} \qquad \text{or by} \qquad P_f = P\left[\left(\frac{R}{E}\right) < 1\right] = \Phi\left(-\beta\right) \quad \text{(b)}, \tag{14}$$

being Φ the normal cumulative distribution function and β the associated reliability index. To estimate (14.b), the right tail of the sum of two independent log-normal variables G and Q was fitted with a log-normal tail using the Fenton and Wilkinson approximation [36, 37].

It must be underlined that, at the level 2, expressions (14.a) and (14,b) lead to different β values, despite from the theoretical point of view they are absolutely equivalent. However, these different outcomes can be easily explained, recalling that, in the aforementioned cases, the tails of the actual distributions of R and E have been fitted with different *pdf*s: normal distributions referring to safety margin, Eq. (14.a), log-normal distributions referring to safety factor, Eq. (14.a). That is a further reason to emphasize that β values cannot be directly compared, as their significance is largely conventional [38].

It is worth to note that in EN 1990 characteristic values of variable actions are defined as those characterized by 2 % of exceedance on annual basis (roughly corresponding to 50 years return period), and the target value of β for 50 years reference period is fixed to 3.8 for Consequence Class 2 structures (i.e. “normal” consequences), corresponding to an accepted failure probability $P_f \approx 7.23 \cdot 10^{-5}$ in 50 years.

3.1.1. Evaluation of β reliability index for normal variables

If R and E are normally distributed, the reliability index β is given by [1, 39, 40–42]:

$$\beta = \frac{\mu_R - \mu_E}{\sqrt{\sigma_R^2 - 2\rho_{RE}\sigma_R\sigma_E + \sigma_E^2}}; \tag{15}$$

being μ_R and μ_E the mean values of variables, σ_R and σ_E their standard deviations, and ρ_{RE} the correlation coefficient, which is zero for uncorrelated variables, like assumed in the present investigation.

As remarked in the introduction, the Eurocode does not give a unique expression to evaluate actions' effects E_d, leaving the choice among the three alternatives (2–4) to the National Annex. Clearly, since the intent of the fundamental combination is to represent, as close as possible, the design values of the actual actions' effects, none of the three alternatives is unanimously recognized as the one able to represent in the most effective way the design load combination.

As better explained in the following §3.3, it is possible to directly compare alternative load combination rules, in terms of structural reliability, only when the reliability is calculated with reference to the effective joint probability distribution of actions, to which the structure will be subjected during its design life.

Evidently, being at least $R_d = E_d$ (see Eqs. (6)), the design depends on the choice of the expression for the fundamental combination. Once designed the structure, its reliability will be a function of the effective distribution of actions' effects. In the spirit of the sensitivity analysis, to investigate how different choices on combination rules influence the structural reliability, each structural element was designed according to one of the given expressions (e.g. [6.10]; or [6.10a] and [6.10b]; or [6.10a mod] and [6.10b]) and the β values, associated to each set of the alternative load combinations, were calculated. Each combination rule is assumed to be, in turn, the one best representing the actual situation, which is denoted with the prefix "act" in the following: in that way, nine $\beta-\chi$ reliability curves are obtained, three for each set of expressions. Each curve represents the reliability curve associated to a structural element designed using one of the tree alternative sets of load combinations, depending on the load combination best representing the actual situation.

Let Ξ the load combination used for the design, Ξ = ([6.10]; [6.10a+b]; [6.10a mod+b]). Manifestly, for each value of χ, the reliability index β satisfies the following inequalities:

$$\beta\left(\chi,\Xi,\left[\text{act } 6.10\right]\right) \le \beta\left(\chi,\Xi,\left[\text{act } 6.10a+b\right]\right) \le \beta\left(\chi,\Xi,\left[\text{act } 6.10a\,\text{mod}+b\right]\right), \quad (16)$$

where, as said, terms in square brackets indicate the combination of actions assumed to be the best representation of the real situation.

Significant outcomes of the analysis are shown in Fig. 2 and 3. To make easier their interpretation, and according to what previously said, in the legends the nine $\beta-\chi$ reliability curves are labelled in such a way that the term in brackets indicates the expression better representing the actual situation and the first term indicates the expression adopted to design the element.

The case illustrated in Fig. 2 refers to steel members' failure in a commercial building. Reliability curves are characterized by different trends:

– Let consider structures designed according to [6.10]:
  i. if the actual combination is represented by [6.10], reliability increases in the interval $\chi = 0-0.3,$ and decreases for $\chi > 0.3,$ when the quota of variable imposed loads becomes more relevant;
  ii. if the actual combination is represented by [6.10a+b] or by [6.10a mod+b], the calculated reliability further increases, since designing with [6.10] introduces overstrength. Again, an increasing trend is shown when permanent action predominates and χ is up to 0.3.

- Let consider structures designed according to [6.10a+b]:
  iii. if the actual combination is represented by [6.10a+b], the trend of the $\beta-\chi$ curve is similar to that described in the previous case I;
  iv. if the actual combination is represented by [6.10] a decreasing reliability trend is observed when [6.10a] governs the design, the trend is inverted when [6.10b] dominates;

v. if the actual combination is represented by [6.10a mod+b] the structure results overdesigned and the behavior of the $\beta-\chi$ curve is similar to that described in previous case ii.

- Let, finally, consider structures designed according to [6.10a mod+b]:

vi. if the actual combination is represented by [6.10a mod+b] an almost constant reliability is observed as soon as [6.10a mod] governs;

vii. if the actual combination is represented by [6.10] the $\beta-\chi$ curve is significantly decreasing in the range where [6.10a mod] governs. A similar trend is observed if the actual combination is represented by [6.10a+b].

Similar trends characterize curves in the following Fig. 3, 4 and 5.

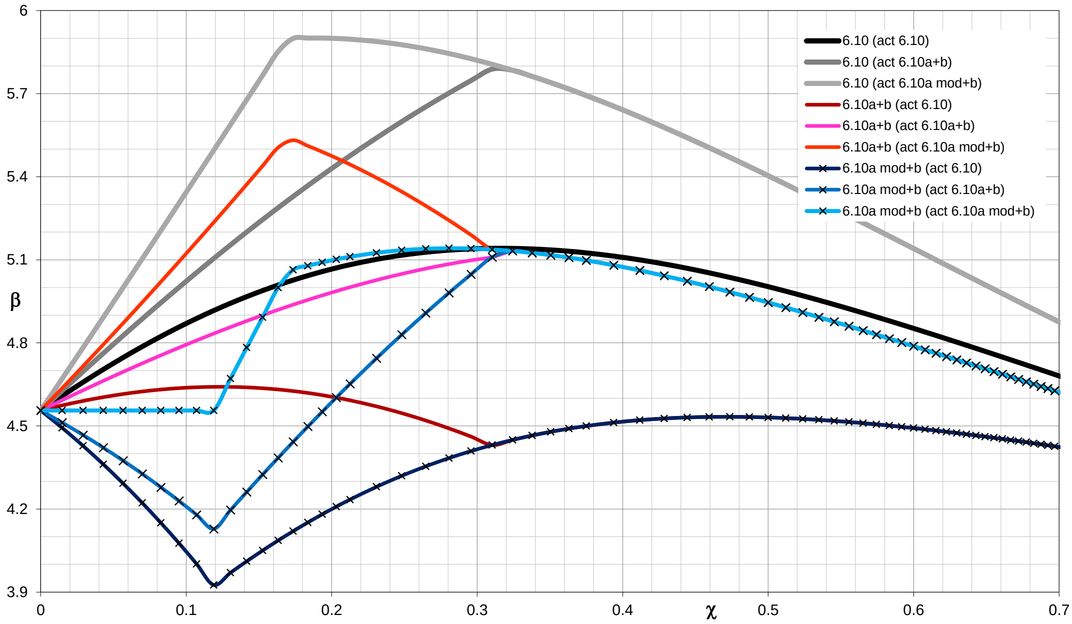

Figure 2. $\beta-\chi$ reliability curves for steel member in commercial buildings – normal variables.

For the resistance of reinforced concrete structures, they are considered two relevant cases, according as yielding of steel rebars or crushing of concrete governs. In the following cases indicated as “rebars” correspond to yielding of steel reinforcement, cases indicated as “concrete” correspond to crushing of concrete.

The diagrams in Fig. 3 refer to compressed concrete failure of reinforced concrete members in a residential building.

The two complete sets of curves refer to different coefficient of variations of concrete strength: V = 0.20, corresponding to “normal” quality control level, and V = 0.15, corresponding to improved quality control level. The results are of particular interest, as they refer to an extreme case, where small variations of input data are associated to relevant variations of the reliability index. The phenomenon is so evident that the two sets of curves do not overlap.

In a previous work [18], similar results were reported more extensively, considering also the effects of material over-strength, drawing the following conclusions:

– although, as explained later, reliability indexes calculated here are overestimated, since the incidence of model uncertainties is disregarded, β values sems often smaller than the target value, 3.8, especially in r.c. residential buildings, when concrete crushing governs the failure and no special quality control measures are adopted for the material itself (V = 0.2);

– in case of over-strength [18], the reliability indexes increase; the increment is more relevant for steel members than for reinforced concrete members;

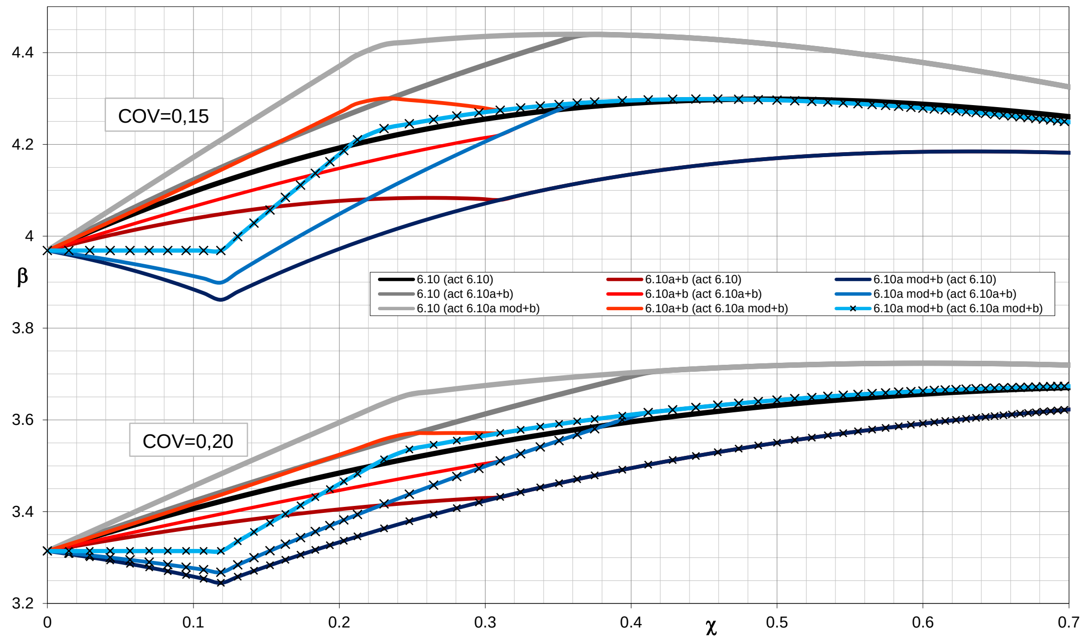

Figure 3. $\beta-\chi$ **reliability curves for concrete failure of r.c. members in residential buildings (different quality control level for concrete) – normal variables.**

- in all the investigated cases, structures designed using [6.10] exhibit higher β values than those designed using alternative expressions, with peaks in the range $0.1<\chi<0.35$; the gain is particularly relevant when the actual situation is best fitted by alternative expressions;
- values associated with [6.10a] and [6.10b] can be significantly smaller than those associated with [6.10], mainly in vicinity of $\chi=0.35$, which is quite often the case in current design; moreover, in r.c. residential buildings β values are often below the target;
- expressions [6.10 a modified] and [6.10b] lead in all considered cases to significant reduction of β, especially in the range $0<\chi<0.25$, where local minima of $\beta-\chi$ curves are very low; since this range corresponds to heavy structures, like r.c. massive ones, this behaviour seems to be in contrast with the inspiring criterion of such an expression, which is based on permanent loads primacy;
- the lowest β curve associated to [6.10] practically always envelopes alternative curves.

Since the influence of the model uncertainty factors is disregarded, β values evaluated up to now appear generally overestimated. Actually, the design value of the capacity demand E_d [1],

$$E_d=\gamma_f \gamma_{Sd} E_k=\gamma_F E_k, \tag{17}$$

is higher than that strictly required by reliability analysis. In equation (17) E_k is the characteristic value of the effect of the load combination, γ_f the partial factor for uncertainty in representative values of the effect, γ_{Sd} the model uncertainty factor and γ_F the partial factor for actions.

Hence, despite of the relative meaning of β and regardless of the disturbance caused by the model uncertainty factors, an accurate calculation requires to consider, instead of γ_F, only its quota γ_f. To check the sensitivity of β on model uncertainty factors, the above-mentioned commercial building were re-examined considering the contribution of the γ_{Sd} factors on the action side, and updating the $\beta-\chi$ reliability curves for steel members' failure. The uncertainty factor γ_{Sd} has been hypothesized only depending on the nature of the action, and, according to recommendations in EN1990, it has been assumed 1.06 for permanent loads and 1.15 for variable loads.

Since the study aimed to compare different $\beta-\chi$ reliability curves, derived under homogeneous hypotheses, model uncertainty factors were disregarded on the resistance side, leaving unchanged the partial factors γ_M, since they do not affect the comparison.

Diagrams in in Fig. 4, compared to the corresponding ones in Fig. 2, show the influence of γ_{Sd} on the evaluation of the reliability index β.

3.1.2. Evaluation of β reliability index for log-normal variables

In case of log-normal variables, the expression for the reliability index β is [39–41]

$$\beta=\frac{\ln\left(m_R\right)-\ln\left(m_E\right)}{\sqrt{\ln\left(1+V_R^2\right)+\ln\left(1+V_E^2\right)-2\rho_{RE}\sqrt{\ln\left(1+V_R^2\right)\ln\left(1+V_E^2\right)}}}; \tag{18}$$

where m_R and m_E are the medians of R and E, V_R and V_E are the corresponding coefficients of variation and ρ_{RE} is the correlation coefficient, which is again assumed to be zero under the hypothesis of uncorrelated variables.

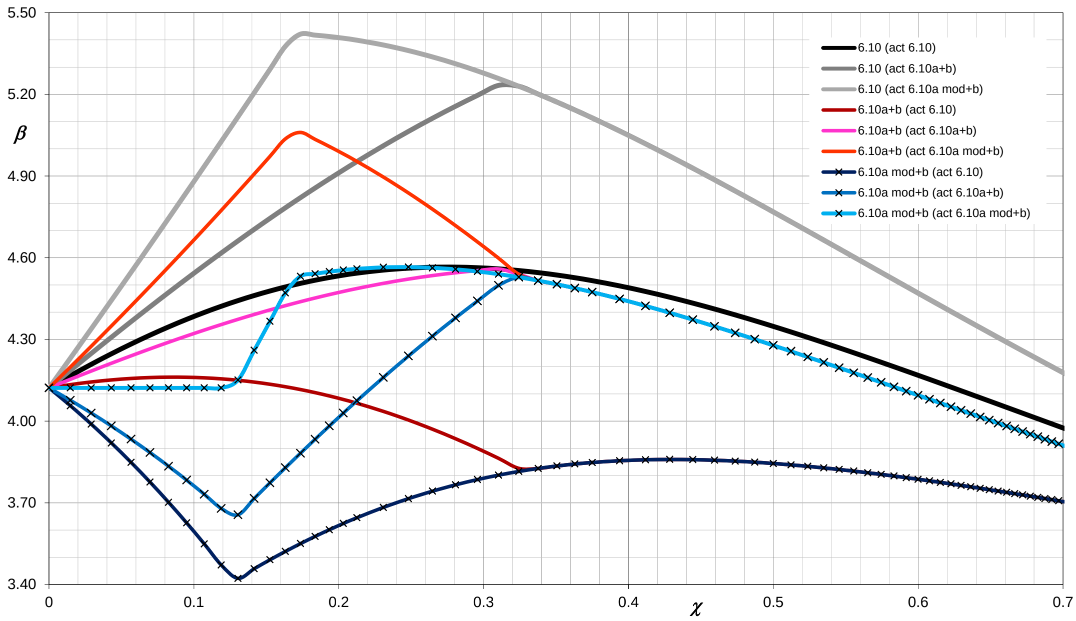

Figure 4. $\beta-\chi$ reliability curves for steel members in commercial buildings – normal variables, model uncertainty factors on actions considered.

Fig. 5 shows the outcomes of the analysis developed for the same case as in Fig. 2. Comparing diagrams in Fig. 2 and 5, it is evident that the shape of the curves and their trends are similar, so that the analysis of the diagram in Fig. 5 leads to analogous conclusions to those expressed in §3.1. At the same time, it must be highlighted that β values evaluated considering safety factor Z and log-normal variables are different, and in some cases rather significantly, than those calculated considering safety margin S and normal variables. These discrepancies, due to the inaccuracies of level 2 approach and to the errors of the Fenton and Wilkinson approximation, confirm once again that β is a relative measure of the reliability. In other words, the reliability index β fully represents structural reliability only if it is calculated exactly matching the assumptions adopted to evaluate the target values.

3.2. Case 2: effects of actions represented by the theoretical combination

When G and Q are both normal variables, their joint *pdf* can be derived theoretically. In this case, the appropriateness of the three normative sets of load combinations can be directly checked, comparing the design capacity associated with each of them with the effective design capacity derived by the theoretical joint *pdf*. This is the aim of the second phase of the present study (case 2) [18], where permanent actions have been assumed not to significantly vary during the design working life of the structure.

To emphasize the comparison, the characteristic value of permanent actions has been set to $G_K = \mu_G$ (see table 1), assuming again COV = 0.1, which is upper limit justifying the assumption $G_K = \mu_G$.

The design value of the effect E of a single normally distributed action, considered alone, is (17)

$$E_d = \gamma_{Sd}\left(\mu_E + \alpha_E \beta \sigma_E\right) = \gamma_{Sd}\left(\mu_E + 2.66\beta\sigma_E\right) = \gamma_f \gamma_{Sd} E_k = \gamma_F E_k; \tag{19}$$

where μ_E and σ_E are the mean and the standard deviation of E, respectively, β =3.8 is the target reliability index for a 50-year reference period and a CC2 structure [3], and $\alpha_E = 0.7$ is the FORM [16] [42] sensitivity factor. Hence, from (19) it follows

$$\gamma_{Sd} = \frac{\gamma_F E_k}{\mu_E + 2.66\sigma_E}, \tag{20}$$

which, applied separately on G and Q, gives partial factors γ_g and γ_q to be introduced in formulae (2), (3.a), (3.b) and (4) to cut off the model uncertainties.

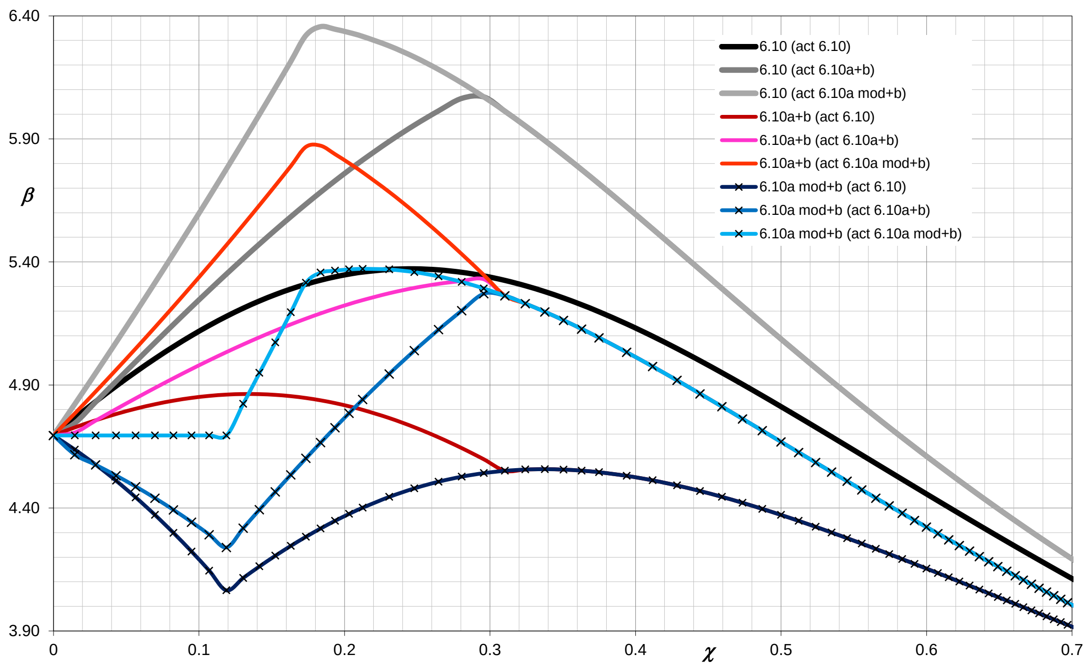

Figure 5. $\beta - \chi$ reliability curves for steel members in commercial buildings – log-normal variables.

Since G and Q are assumed to be normally distributed, and $G_K = \mu_G$, the theoretical design value $(G+Q)_d$ results

$$(G+Q)_d = \mu_G \left[1 + \frac{\chi}{1-\chi}\left(1+1.645V_Q\right)^{-1} + 2.66\sqrt{V_G^2 + \left(\frac{\chi}{1-\chi}\right)^2 V_Q^2 \left(1+1.645V_Q\right)^{-2}}\right], \tag{20}$$

where V_G and V_Q are the coefficients of variation of G and Q, respectively, and χ is defined by (5).

3.2.1. Evaluation of β reliability index

The influence of the model uncertainties γ_{Sd} can be easily evaluated adopting, in eqs. (2), (3) and (4), γ_g and γ_q instead of γ_G and γ_Q. For each case study, assuming G and Q normally distributed, it is possible to evaluate the reliability index β by means of (15), excluding the effects of model uncertainty factors γ_{Sd}. In accordance with §3.1.1, weighted values of γ_{Sd} depend on the ratio χ.

Fig. 6 shows the results obtained for the case of commercial buildings, with reference to the alternative sets of load combinations in case of structural steel, re-bars, and concrete with different levels of quality control (V = 0.15 and V = 0.20).

Results for residential or storage building categories look similar, both in terms of curves' shapes and values, to those illustrated in Fig. 6, and the following remarks can be drawn:

- Eq. [6.10] guarantees almost constant reliability, independently on structural material and on χ, while alternative sets lead to considerable reduction of β; particularly when $0 < \chi < 0.25$ or failure is governed by steel (either re-bars or structural steel);
- r.c. structures are particularly sensitive to the level of quality control measures adopted during concrete preparation and casting; beside that, when yielding of steel re-bars govern the failure, they are more reliable than the other structures examined in the present study;
- β values seem to be above the target value only for steel reinforcement; nevertheless this conclusion should be carefully considered: since β increases considerably whenever the material's strength increases or its coefficient of variation decreases, this phenomenon is consequence of the adoption of γ_M values for rebars (γ_M = 1.15) sensibly higher than for structural steel (γ_M = 1.00).

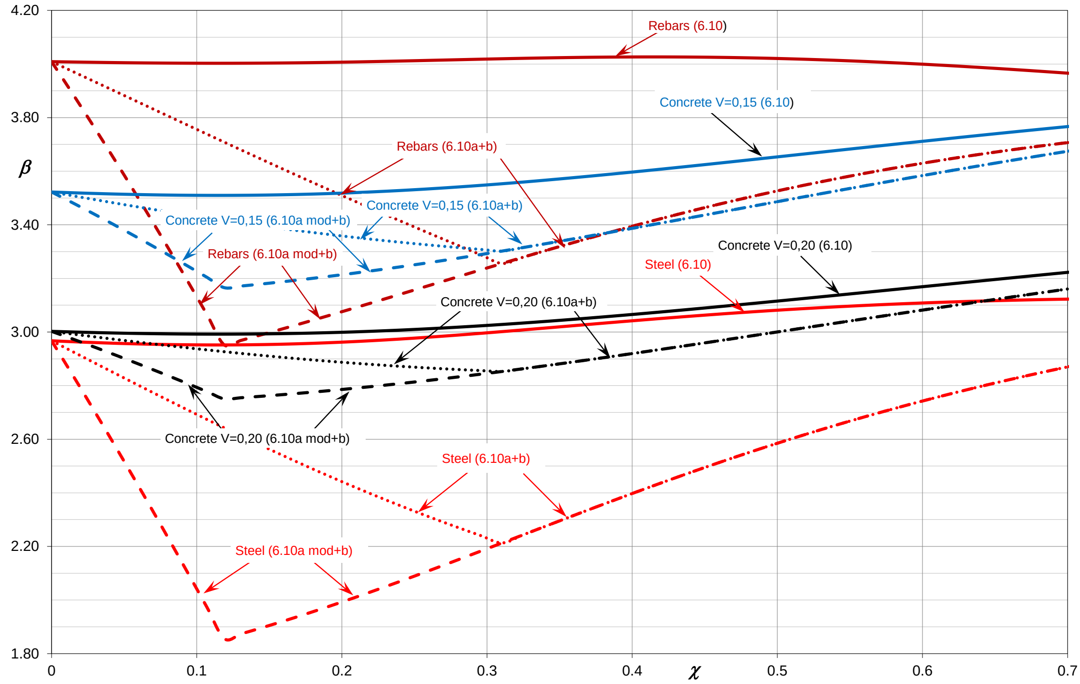

Figure 6. $\beta - \chi$ **reliability curves for commercial buildings –** $G_K = \mu_G$.

In addition, the influence of the replacement of $G_K = \mu_G$, with $G_K = \mu_G + 1.645\,\sigma_G$ has been investigated. An example of these analyses is illustrated in Fig. 7, which refers as well as Fig. 6, to building categories C and D.

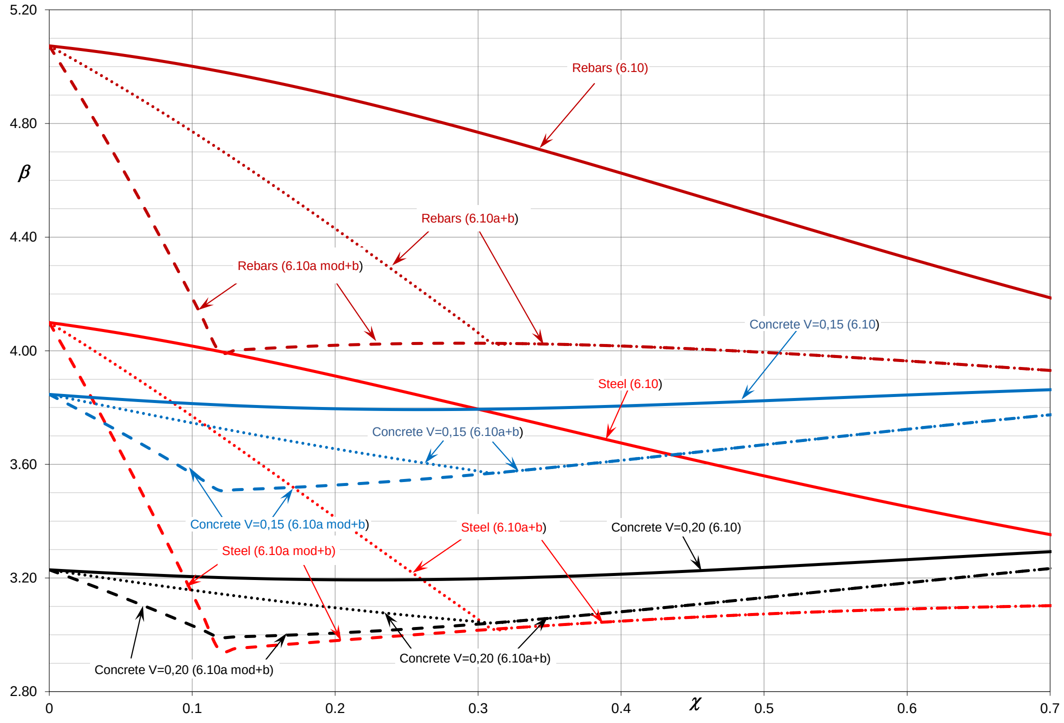

Figure 7. $\beta - \chi$ **reliability curves for commercial buildings –** $G_K = \mu_G + 1.645\,\sigma_G$

The curves in Fig. 7 demonstrate that β values strongly depend on the definition of G_K, in effect, if compared with the previous ones (Fig. 6) all the curves are considerably up-shifted, in particular those pertaining to structural steel and to concrete failure of r.c. elements subjected to strict quality controls.

3.3. Case 3: Level 3 sensitivity analysis

The results discussed above, and particularly the circumstance that β values depend on the initial assumptions, suggested the need of more refined investigation to separate the intrinsic variations of β, effectively influenced by the assumptions, from those pertinent to level 2 approximations. For that reason, a more advanced sensitivity analysis (case 3), aiming to calculate the exact probability of failure, P_f, by means of a level 3 reliability approach has been undertaken.

The present subsection illustrates the comparison between reliability levels reached by applying expression [6.10] (Eq. (2)) and the reliability levels obtained with expressions [6.10a] and [6.10b] (Eqs. (3.a) and (3.b)).

Owing the fact that, as remarked before, expression [6.10a modified] (Eq. (4)) leads to probably excessive, reduction of the reliability index in a particularly relevant interval of the parameter χ, it will be not further considered.

To investigate the influence on structural reliability of the variable action models, the extreme values of imposed loads have been hypothesized described, in turn, by a normal, a log-normal, or a gamma distribution, often adopted in current practice. Obviously, the parameters describing these three distributions have been calibrated to attain the same characteristic values and similar upper tails.

Varying load combinations and building materials, the following cases were investigated:

– variable (imposed) loads described by normal, log-normal or gamma distributions;
– characteristic value of permanent load expressed by $G_K = \mu_G$ or by $G_K = \mu_G + 1.645\,\sigma_G$;
– partial factors for permanent and variable actions γ_G and γ_Q or γ_g and γ_q, according if the model uncertainty factors γ_{Sd} is considered or not, as previously discussed in §3.1.2.

Assuming resistances R log-normally distributed, and permanent loads G normally distributed with V = 0.1(see §2), once assigned the actual *pdf* of each random variable, the P_f associated to each case study was calculated, by means of a full probabilistic procedure, via numerical integration of the limit state function. To make easier the interpretation of results, the probability of failure P_f was converted into the corresponding β value, using the inverse of the Φ function.

Fig. 8, 9, 1 and 11 summarize some particularly relevant results.

In Fig. 8 the plotted reliability curves refer to the concrete failure of r.c. members in storage buildings.

The curves are grouped into families, derived according to expression [6.10], consisting of three curves each. The curves of each family are associated to different *pdf*s (normal, log-normal or gamma) for imposed loads, as indicated in the figure.

Concerning concrete strength, in Fig. 8 three different families of curves are plotted for each examined case, V = 0.15 and V = 0.20. These families correspond to the cases: $G_K = \mu_G$ and partial factors γ_g and γ_q, i.e. disregarding the model uncertainty factors γ_{Sd}; $G_K = \mu_G$ and partial factors γ_G and γ_Q, i.e. including the model uncertainty factors γ_{Sd}; and $G_K = \mu_G + 1.645\,\sigma_G$; and partial factors γ_G and γ_Q, respectively, characterized by increasing values of reliability index.

Investigating diagrams in Fig. 8, we can observe that:

- the level of quality controls influences considerably the reliability; in fact, the reduction of scattering of concrete strength, associated with more stringent controls leads to significant increases of β values, especially for lightweight structures ($\chi > 0.5$);
- in the present example, the reliability is slightly influenced by the *pdf* of variable actions. That is not surprising since the COVs of live loads in storage buildings are comparable with the COVs of concrete strength and partial factor for concrete is relatively high $(\gamma_C = 1.50)$;
- the values of β are always well above the target value for all the considered cases; therefore, a sufficient safety margin exists to cover also the model uncertainty on the resistance side.

Fig. 9, built up according to the same criteria followed for Fig. 8, refers to concrete failure of a r.c. member in a residential building, which is the case study previously considered in Fig. 3.

For the sake of clarity, in the figure curves referred to expressions [6.10a] and [6.10b], which lead in some cases to considerable reductions of the reliability index, are omitted.

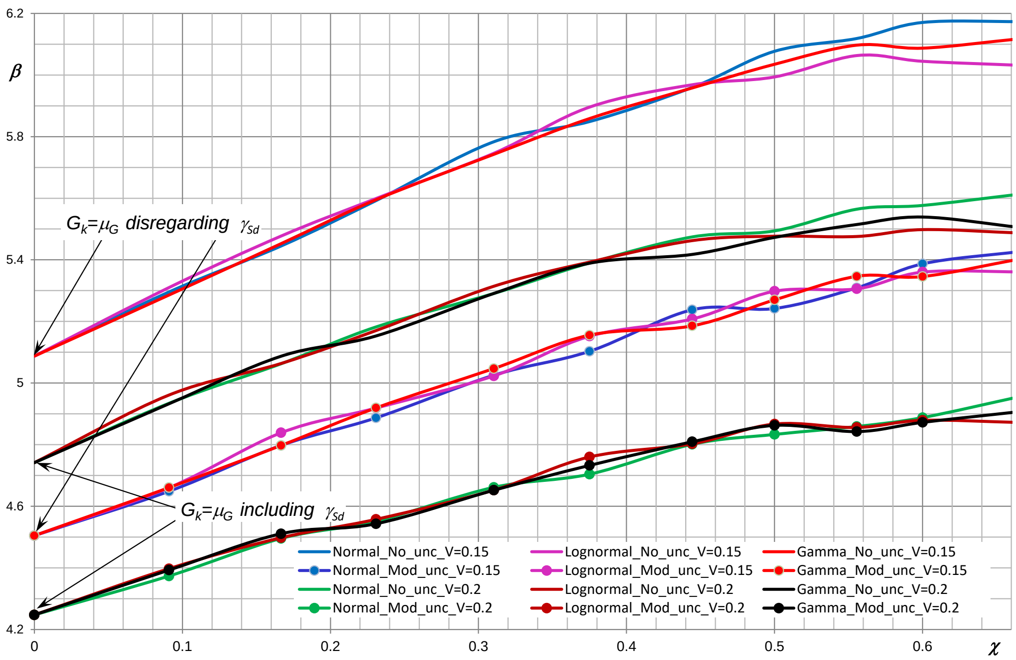

(a)

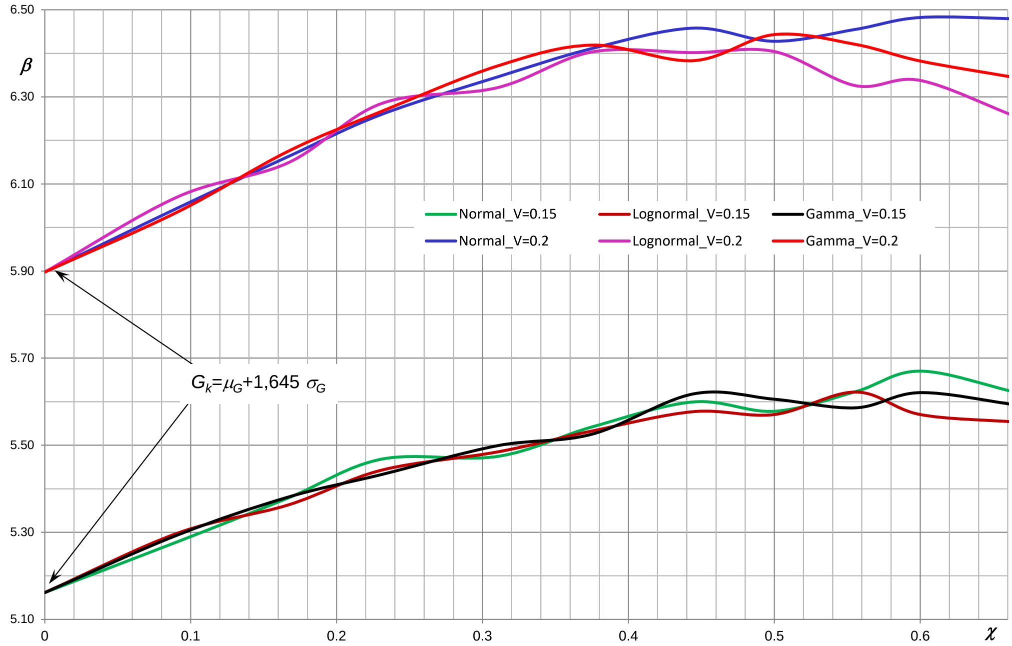

(b)

Figure 8. Sensitivity analysis of $\beta-\chi$ curves considering normal, lognormal, and gamma distributions for imposed loads, expression [6.10]: concrete failure of r.c. members in storage buildings (50 years ref. period): a) Case $G_K=\mu_G$, including or disregarding the model uncertainty factors γ_{Sd}; b) Case $G_K=\mu_G+1.645\,\sigma_G$, disregarding the model uncertainty factor γ_{Sd}.

Examining curves in Fig. 9, we can highlight that:

– influence of concrete quality controls is still relevant even if it decreases for lightweight structures ($\chi>0.45$);

– the reliability significantly depends on the statistical distribution of actions. When gamma and log-normal distributions are adopted, β value decreases as χ increases: this effect is more pronounced in log-normal case, where, for $\chi>0.3$, β values are well below the target value.

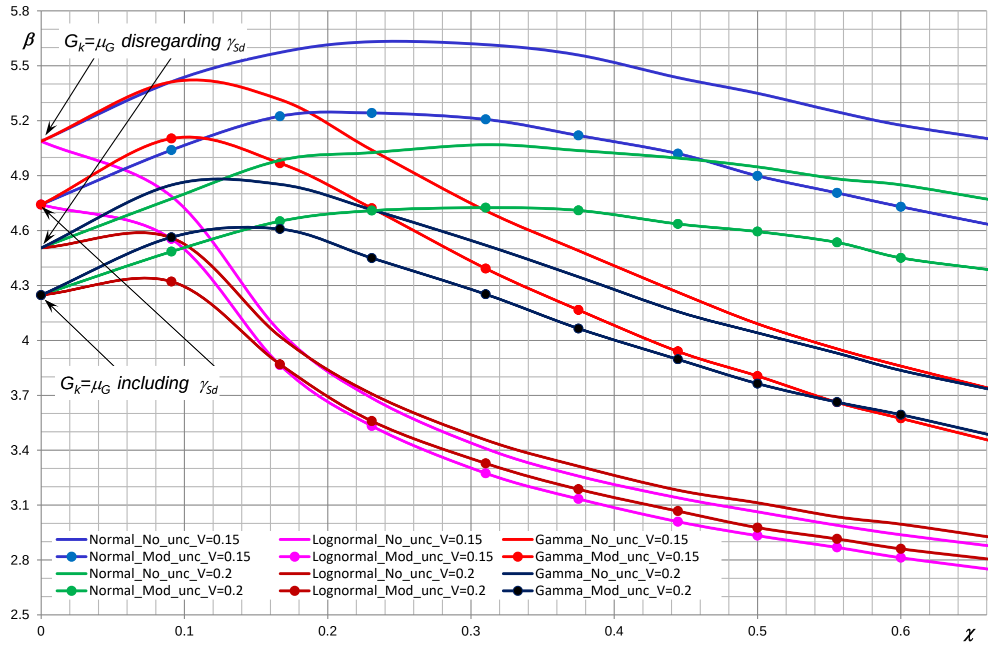

(a)

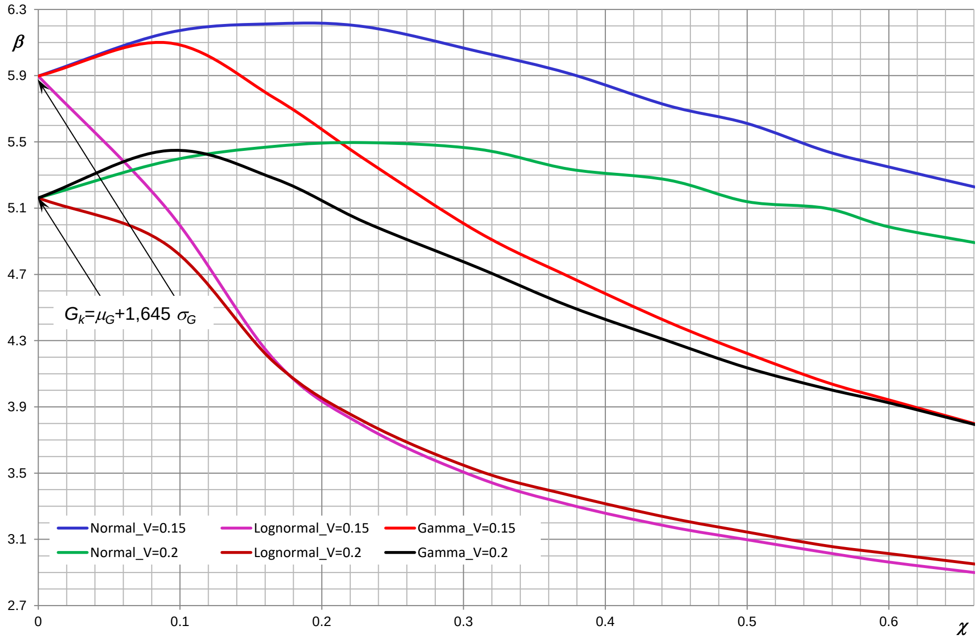

(b)

Figure 9. Sensitivity analysis of $\beta-\chi$ curves considering normal, lognormal, and gamma distributions for imposed loads, expression [6.10]: concrete failure of r.c. members in residential buildings (50 years ref. period): a) Case $G_K=\mu_G$, including or disregarding the model uncertainty factors γ_{Sd}. b) Case $G_K=\mu_G+1.645\,\sigma_G$, disregarding model uncertainty factors γ_{Sd}.

Since the imposed loads are highly scattered and the results are extremely sensitive on the *pdf*s, in residential buildings level 2 approximations seems to be unacceptable, leading to questionable results.

Fig. 10, correlated with previous Fig. 2 and 5, concerns steel members in a commercial building.

Inspecting the curves pertaining to this example, the following remarks can be formulated:

– β values depend on the statistical distribution, and they do not always reach the target value;

– as the partial factor for steel resistance is small, $\gamma_M=1.0$, β depends on model uncertainty factors as well as on the definition of characteristic value of permanent loads;

– expressions [6.10a+b] can lead, as already observed, to severe reductions of the reliability;

– comparison with Fig. 2 and 5 shows that, adopting combination [6.10], level 2 analysis gives acceptable estimates of the reliability indexes.

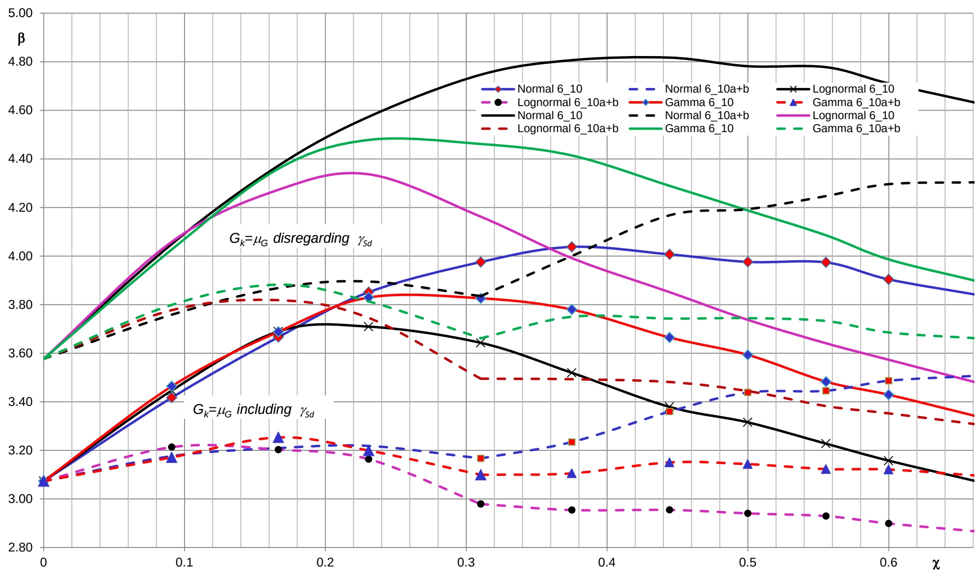

(a)

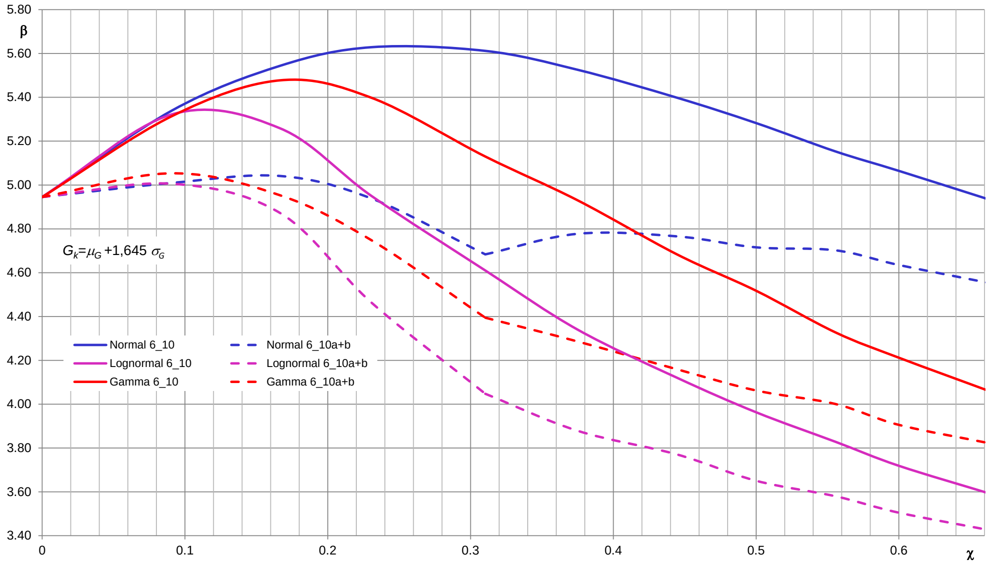

(b)

Figure 10. Sensitivity analysis of $\beta-\chi$ curves considering normal, lognormal, and gamma distributions for imposed loads, expressions [6.10] and [6.10a+b]: steel members in commercial buildings (50 years ref. period): a) Case $G_K=\mu_G$, including or disregarding the model uncertainty factors γ_{Sd}; b) Case $G_K=\mu_G+1.645\,\sigma_G$, disregarding model uncertainty factors γ_{Sd}.

Examining Fig. 11, which refers to steel members and rebar's failure in r.c. members of storage buildings, we can finally remark that:

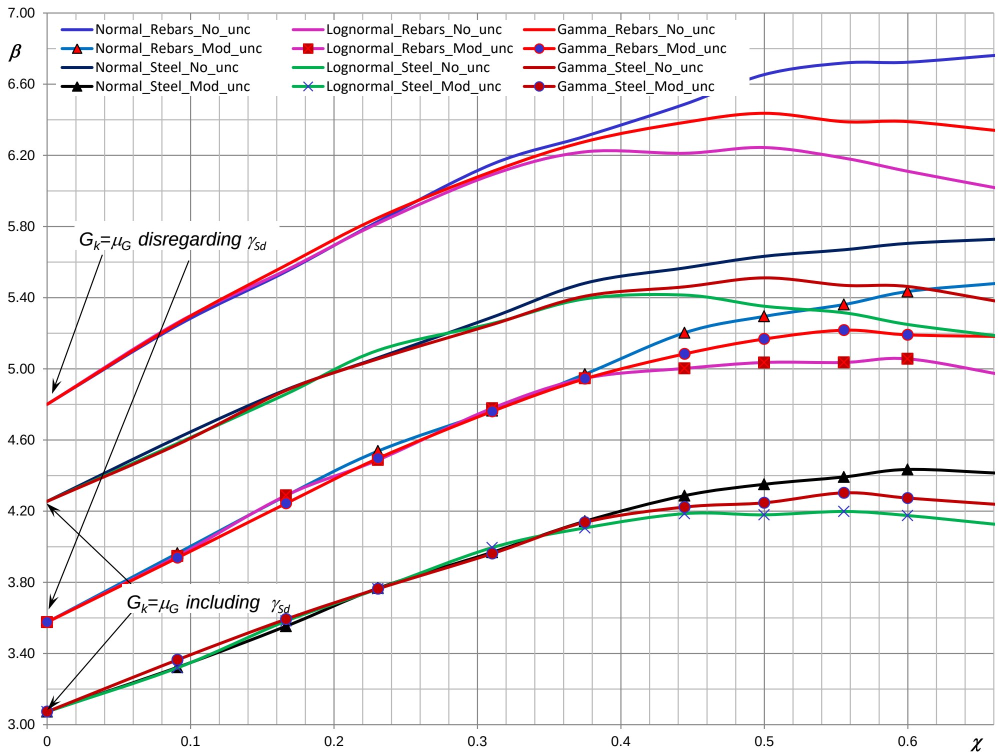

(a)

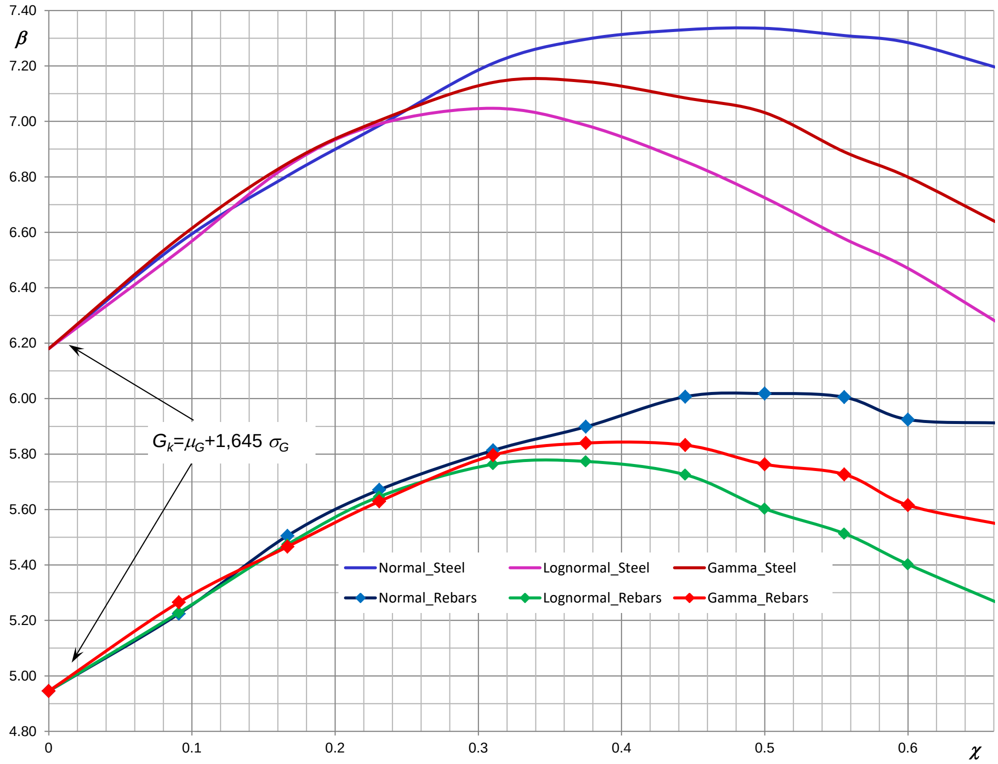

(b)

Figure 11. Sensitivity analysis of $\beta-\chi$ curves considering normal, lognormal, and gamma distributions for imposed loads, expression [6.10]: steel members and reinforcement failure of r.c. members in storage buildings (50 years ref. period): a) Case $G_K=\mu_G$, including or disregarding the model uncertainty factors γ_{Sd}; b) Case $G_K=\mu_G+1.645\,\sigma_G$, disregarding model uncertainty factors γ_{Sd}.

- since the strength distributions of structural steel and reinforcing steel are described by the same statistical parameters, reliability index raises when the partial factor γ_M increases from $\gamma_M=1.0$, as for structural steel, to $\gamma_M=1.15$, as for reinforcing steel.
- heavier structures reveal smaller reliability indexes, while *pdf* of imposed loads influences the results mainly for lightweight structures, where imposed loads predominate;
- independently on χ-value, structural steel members, affected by a smaller partial factor γ_M, exhibit lower reliability than reinforcing steel members.

4. Conclusions

The present study discusses the reliability levels associated with the three mutually exclusive expressions provided in EN1990:2002 [3] and in prEN1990:2019 [4] for ULS combination of actions, taking into account the effect of the ratio χ between imposed loads and the total acting loads (permanent and imposed loads), in some significant case studies.

In each example, resorting both to level 2 and level 3 approaches, the reliability index β pertaining to each set of load combinations has been derived, assuming that extreme values of imposed loads are described, in turn, by a normal, a log-normal, or a gamma distribution.

The following general conclusions can be drawn:

- the reliability index β is extremely sensitive to the coefficient of variation of the strength's distribution, to partial factors and to the assumptions on the type and the relevant parameters of the *pdf* adopted to model extreme values;
- in principle, adoption of partial factors for actions and strengths adequately calibrated according to the actual statistical distribution could allow to reduce the above variability, but the adoption of the

appropriate distribution is a still open question, since the upper tails of the distributions of variable actions are largely unknown, lacking sound enough data. Moreover, despite of its effectiveness, this approach would significantly complicate the application of the code, since level 3 analyses would be systematically required;

- the study confirms that the reliability index is not an univocal property of the structure (or the structural element), on the contrary, it is a function of the method adopted to evaluate the reliability itself. For that reason, as already pointed out, the reliability index β is to be regarded as a relative measure of safety, which strongly depends on the assumptions, and its use should be limited to compare, adopting consistent approaches, the reliability of structures designed under the same hypotheses, and built with the same material;
- since a quota of the reliability index β is spent to cover model uncertainties, actual values of β could result sensibly smaller than the calculated ones, in particular when the tails of the actual distributions of actions deviate, or are not adequately fitted, by the assumed distributions;
- the target reliability level indicated in the Eurocodes (EN1990) for a 50-year reference period and for structures belonging to Consequence Class 2, i.e. "normal" consequences in case of failure, is generally achieved using expression [6.10];
- adoption of alternative expressions [6.10 a] and [6.10b] leads in some cases to reliability indexes smaller than the target, while use of [6.10.a modified] plus [6.10.b] leads to reliability indexes often unacceptably below the target for massive structures, whose design is governed by the self-weight.

Although not a direct consequence of the study, it should be also considered that, to cover failure modes occurring without significant warnings, like in case of buckling in steel members or shear failure in concrete, verification formulae provided in structural codes can intentionally include often not explicitly declared additional safety. That aspect should be duly taken into account comparing reliability levels pertaining to different limit state functions.

Further investigations are in progress, based on level 3 analyses, mainly focusing on the refinement of the partial factors, avoiding the, often controversial, introduction of sensitivity factors α, required by FORM or SORM [16][43][44], as well as and a more precise estimate of uncertainty factors for actions and resistance.

References

1. Gulvanessian, H., Holicky, M. Eurocodes: using reliability analysis to combine action effects. Proceedings of the Institution of Civil Engineers – Structures and Buildings. 2005. 158 (4). Pp. 243–252. DOI: https://doi.org/10.1680/stbu.2005.158.4.243
2. Galambos, T.V., Ravindra, M.K. The basis for load and resistance factor design criteria of steel building structures. Canadian Journal of Civil Engineering. 1977. 144 (2). Pp. 178–189. DOI: https://doi.org/10.1139/l77-023
3. EN1990. Eurocode: Basis of structural design. Brussels: CEN, 2002.
4. prEN1990:2019. Eurocode: Basis of structural design, CEN/TC 250/SC10 Document, 2019.
5. Markova, J., Sousa, M.L., Dimova, S., Athanasopoulou, A., Iannaccone, S., Reliability of structural members designed with the Eurocodes NDPs selected by EU and EFTA Member States, EUR 29410 EN, Publications Office of the European Union, Luxembourg, 2018. 98 p. ISBN 978-92-79-96815-0. DOI: 10.2760/426349
6. European Commission. M/515 EN—Mandate for Amending Existing Eurocodes and Extending the Scope of Structural Eurocodes. European Commission. Brussels, 2012. 8 p.
7. CEN/TC250. Response to Mandate M/515–Towards a Second-Generation of Eurocodes; CEN-TC250–N 993. Brussels, 2013. 138 p.
8. Meinen, N.E., Steenbergen, R.D.J.M. Reliability levels obtained by Eurocode partial factor design – A discussion on current and future reliability levels. HERON. 2018. 63 (3). Pp. 243–302.
9. Diamantidis, D. Current safety acceptance criteria in codes and standards – A critical review. Proceedings of the 2008 Structures Congress – Structures Congress 2008: Crossing the Borders. Vancouver, 2008. DOI: https://doi.org/10.10-61/41016(314)76
10. Holicky, M., Markova, J., Sykora, M. Target reliability levels in present standards. Transactions of the VŠB – Technical University of Ostrava. 2014, 14 (2). DOI: https://doi.org/10.2478/tvsb-2014-0018
11. Holicky, M., Diamantidis, D., Sykora, M. Reliability levels related to different reference periods and consequence classes. Beton- und Stahlbetonbau Spezial. 2018. 113 (S2). Pp. 22–26. DOI: https://doi.org/10.1002/best.201800039
12. Holicky, M. Target reliability of civil engineering structures. IOP Conf. Series: Materials Science and Engineering. 2018. 365. 052002. DOI: https://doi.org/10.1088/1757-899X/365/5/052002.
13. Baravalle, M., Köhler, J. A risk-based approach for calibration of design codes. Structural Safety. 2019. 78. Pp. 63–75. DOI: https://doi.org/10.1016/j.strusafe.2018.12.003
14. Köhler, J., Sørensen, J.D., Baravalle, M. Calibration of existing semi-probabilistic design codes. Proceedings 13th International Conference on Applications of Statistics and Probability in Civil Engineering, ICASP13. Seoul, 2019.
15. Hasofer, A., Lind, N. An exact and invariant first-order reliability format, Journal of Engineering Mechanics Division. 1974. 100. Pp. 111–121.
16. Rackwitz, R., Fiessler, B. Structural reliability under combined random load sequences. Computers and Structures. 1978. 9 (5). Pp. 489–94. DOI: https://doi.org/10.1016/0045-7949(78)90046-9
17. Ditlevsen, O., Madsen, H.O. Structural Reliability Methods. John Wiley & Sons Ltd. Chichester, 1996. 361p.

18. Croce, P., Formichi, P., Gulvanessian, H. Reliability differentiation in ULS checks according to EN1990. Proceedings IABSE Symposium "Large Structures and Infrastructures for Environmentally Constrained and Urbanised Areas". Venice, 2010. DOI: https://doi.org/10.2749/222137810796024880
19. EN1991-1-1. Eurocode: Actions on structures Part 1-1: General actions – Densities, self-weight, imposed loads for buildings. Brussels: CEN, 2002.
20. Sanpaolesi, L., Del Corso, R., Formichi, P., Currie, D., Sims, P., Sacré, C., Stiefel, U., Lozza, S., Eiselt, B., Peckham, R., Solomos, G., Holand, I., Sandvik, R., Gränzer, M., König, G., Sukohv, D. Phase 1 Final Report to the European Commission, Scientific Support Activity in the Field of Structural Stability of Civil Engineering Works: Snow Loads, Department of Structural Engineering, University of Pisa, 1998. available at: http://www2.ing.unipi.it/dic/snowloads/Final%20Report%20I.pdf (last access: 18 January 2021).
21. Holicky, M. Safety design of lightweight roofs exposed to snow load. Eng. Sci. 2007. 58. Pp. 51–57. DOI: https://doi.org/10.2495/EN070
22. Holický, M., Sýkora, M., Failures of Roofs under Snow Load: Causes and Reliability Analysis. Fifth Forensic Engineering Congress November 11-14, 2009. DOI: https://doi.org/10.1061/41082(362)45
23. Croce, P., Formichi, P., Landi, F. Reliability of roof structures subjected to snow loads. Proceedings of the 30th European Safety and Reliability Conference and the 15th Probabilistic Safety Assessment and Management Conference, Edited by Piero Baraldi, Francesco Di Maio and Enrico Zio. DOI: https://doi.org/10.3850/978-981-14-8593-0
24. Croce, P., Formichi, P., Landi, F. Probabilistic Assessment of Roof Snow Load and the Calibration of Shape Coefficients in the Eurocodes. Applied Science. 2021. 11. Art. No. 2984. DOI: https://doi.org/10.3390/app11072984
25. Croce, P., Formichi, P., Landi, F. Climate Change: Impacts on Climatic Actions and Structural Reliability. Applied Science. 2019. 9. Art. No. 5416. DOI: https://doi.org/10.3390/app9245416
26. Croce, P., Formichi, P., Landi, F., Marsili, F. Harmonized European ground snow load map: Analysis and comparison of national provisions. Cold Reg. Sci. Technol. 2019. 168. Art. No. 102875. DOI: 10.1016/j.coldregions.2019.102875
27. Joint Committee on Structural Safety. Probabilistic Model Code [online]. URL: https://www.jcss-lc.org/jcss-probabilistic-model-code/
28. Sýkora, M., Holický, M. Comparison of load combination models for probabilistic calibrations. Applications of Statistics and Probability in Civil Engineering -Proceedings of the 11th International Conference on Applications of Statistics and Probability in Civil Engineering., Zurich, 2011. DOI: https://doi.org/10.1201/b11332-147
29. Croce P, Cecconi A, Salvatore W, Sensitivity of partial safety factors m to production standards. Journal of Constructional Steel Research. 1998. 46 (1-3). Pp. 134–135. DOI: https://doi.org/10.1016/S0143-974X(98)00029-7
30. Hueste, M.B.D., Chompreda, P., Trejo, D., Cline, D.B.H., Keating, P.B. Mechanical properties of high-strength concrete for prestressed members, ACI Struct Journal. 2004. 101 (4). Pp. 457–466. DOI: https://doi.org/10.14359/13331
31. Croce, P., Formichi, P., Landi, F., Marsili, F., Puccini, B., Zotti, V. Statistical Parameters of Steel Rebars of Reinforced Concrete Existing Structures. Proceedings of the 30th European Safety and Reliability Conference and the 15th Probabilistic Safety Assessment and Management Conference, Edited by Piero Baraldi, Francesco Di Maio and Enrico Zio. DOI: https://doi.org/10.3850/978-981-14-8593-0
32. Croce, P., Formichi, P., Landi, F. Influence of Reinforcing Steel Corrosion on Life Cycle Reliability Assessment of Existing R.C. Buildings. Buildings. 2020. 10(6). 99. DOI: https://doi.org/10.3390/BUILDINGS10060099
33. Croce, P., Marsili, F., Klawonn, F., Formichi, P., Landi, F. Evaluation of statistical parameters of concrete strength from secondary experimental test data. Construction and Building Materials. 2018. 163. Pp. 343–359. DOI: https://doi.org/10.1016/j.conbuildmat.2017.11.001
34. Wen, Y.K. Structural load modelling and combination for performance and safety evaluation. Elsevier Science Publisher Company. New York, 1990. 219 p.
35. Madsen, H.O., Krenk, S., Lind, N.C. Methods of structural safety. Prentice-Hall. Englewood Cliffs, 1986. 407 p.
36. Fenton, L. The sum of lognormal probability distributions in scatter transmission systems, IRE Transactions on Com-munications Systems. 1960. 8 (1). Pp. 57–67. DOI: 10.1109/TCOM.1960.1097606
37. Gao, X., Xu, H., Ye, D. Asymptotic Behaviour of Tail Density for Sum of Correlated Lognormal Variables. International Journal of Mathematics and Mathematical Sciences. 2009. 200. Article ID 630857. DOI: https://doi.org/10.1155/2009/630857
38. Christopher, D.E., Bulakorn, C. Reliability estimation of complex numerical problems using modified conditional expectation method. Computers and Structures. 2011. 89 (1-2). Pp. 181–188.
39. Kottegoda, N.T., Rosso, R. Statistics, probability and reliability for civil and environmental engineers. McGraw-Hill. New York, 1997. 735 p.
40. Ang, A.H.S., Tang, W.H. Probability concepts in Engineering planning and design. Vol. 2 Decision, risk and reliability. John Wiley & Sons. New York, 1984. 574 p.
41. Gulvanessian, H., Calgaro, J.A., Holicky, M. Designers' Guide to EN 1990 Eurocode: Basis of structural design. Thomas Telford Ltd. London, 2002. 192 p.
42. Sedlacek, G., Kraus, O. Use of safety factors for the design of steel structures according to the Eurocodes. Engineering Failure Analysis. 2007. 14. Pp. 434–441. DOI: https://doi.org/10.1016/j.engfailanal.2005.08.002
43. Breitung, K. 40 years FORM: Some new aspects?. Probabilistic Engineering Mechanics. 2015. 42. Pp. 71–77. DOI: https://doi.org/10.1016/j.probengmech.2015.09.012
44. Breitung, K. Asymptotic approximations for multinormal integrals. Journal of Engineering Mechanics. 1984. 110 (3). Pp. 357–366.

Contacts:

Pietro Croce, p.croce@ing.unipi.it

Paolo Formichi, p.formichi@ing.unipi.it

Filippo Landi, filippo.landi@ing.unipi.it

Magazine of Civil Engineering. 2022. 109(1). Article No. 10913

Magazine of Civil Engineering

ISSN 2712-8172

journal homepage: http://engstroy.spbstu.ru/

DOI: 10.34910/MCE.109.13

Different types of basalt fibers for disperse reinforcing of fine-grained concrete

***A.S. Rassokhin*[a], *A.N. Ponomarev*[b], *S.L. Shambina*[*b], *A.I. Karlina*[c]**

[a] *Peter the Great St. Petersburg Polytechnic University, St. Petersburg, Russia*

[b] *Peoples' Friendship University of Russia, Moscow, Russia*

[c] *Moscow State University of Civil Engineering, Moscow, Russia*

**E-mail: shambina_sl@mail.ru*

Keywords: concretes, basalt fiber, fiber reinforcement, compressive strength, flexural strength

Abstract. The paper concentrates on the experimental research of basalt fibers presented at Russian market with eight samples of fibers selected for this research. Five of them are chopped basalt roving (manufactured by LUKE, Rusbazalt Inc, Kamenny Vek Ltd, Armastek), one of them is chopped polymer-basalt wire (manufactured by SK Ltd), two of them are basalt microfibers (manufactured by NTC of Applied Nanotechnologies Inc.). Each of the fibers was added to fine-grained concrete at concentrations of 0.25 vol.-%, 0.5 vol.-%, and 1 vol.-%. Changes in density, compressive strength, and flexural strength were investigated. The density of fine-grained concrete increased proportionally to the quantity of chopped basalt roving. Concrete's density decreased proportionally with the fiber percentage when using chopped polymer-basalt wire and basalt microfiber. The highest compression strength enhancement (9.8 %) of fine-grained concrete was achieved when using fibers manufactured by SK Ltd and Kamenny Vek Ltd. The highest flexural strength enhancement was achieved when using polymer-basalt fiber manufactured by SK LLC (68.6 %) and modified basalt microfiber manufactured by NTC of Applied Nanotechnologies Inc (52.9 %).

1. Introduction

It is widely known that concrete perceives the compression load better than bending, and concrete reinforcement is used to improve the load-bearing capacity of concrete for bending. Traditionally, the reinforcement is steel bars and wire, depending on the type of structure. However, alternative methods of reinforced concrete structures, as various types of fibers, are now used [1–4]. This is mainly used as additional reinforcement. Also, fiber reinforcement is used as the main one in concrete 3D printing [5, 6].

Fibers in concrete have been widely used over the past decades [7, 8]. Even in antiquity, horsehair was sometimes used in Roman concrete [9]. However, in modern construction, fibers returned in the form of cut metal wire, as well as anchor fiber [10–12].

Initially, fibers were used in special concrete in unique buildings and structures, as well as in special regions with extreme natural conditions, for example, in areas with increased seismic activity [13].

However, the development of fiber reinforced concrete industry has led to higher use of fibers in various construction industries. Alternatives to steel fibers have also appeared, as steel fibers and steel reinforcing bars do not have a long service life, as they can corrode fairly quickly [14, 15]. As a result, the ability to increase the durability of reinforced concrete structures is not fully used. Therefore, various types of non-metallic fibers have appeared on the construction market, specifically: mineral (basalt, glass, carbon,

Rassokhin, A.S., Ponomarev, A.N., Shambina, S.L., Karlina, A.I. Different types of basalt fibers for disperse reinforcing of fine-grained concrete. Magazine of Civil Engineering. 2022. 109(1). Article No. 10913. DOI: 10.34910/MCE.109.13

etc.) [16], polymer (polypropylene, polyvinyl alcohol, polyaramid, etc.), as well as organic (viscose, hemp, bamboo, etc.) [17, 18].

Fibers are used to improve the characteristics of the liquid concrete mixture, for example, to prevent separation, as well as to increase the mobility of the concrete mixture [19]. Also, it is possible to reduce the amount of cement with the current mechanical and operational characteristics. Moreover, fibers more significantly affect the properties of hardened concrete, specifically the flexural and compression strength enhancement [20], freeze-thaw resistance [21], durability [22], abrasion resistance [23], crack resistance [24], etc.

The comparative analyses of the different kinds of fibers are shown in Table 1 where the main characteristics of some known kinds of fibers used for the disperse reinforcement of concrete structures are provided [25–30].

Table 1. Comparative properties of different materials for fiber production.

Characteristic	Basalt	Polypropylene	Glass	Steel	Carbon	Polyaramid
Material	Basalt	Polypropylene	E-Glass/ S-Glass	Steel	Carbon	Polyaramid
Tensile strength, MPa	3100–3500	150–600	1500–3500	600–1500	2000–7000	4500–5500
Modulus of elasticity, GPa	Not less than 75	16–35	51–88	190–210	200–800	140–180
Coefficient of elongation, %	3.1	20–150	4.5	3–4	2–3	2–3
Temperature resistance, ^{O}C	–260 + 700	–10 + 160	–60 + 350	–40 + 450	–260 + 2000	–260 + 400
Resistance to alkalis and to acid corrosion	High	High	Only S-Glass	Low	High	High
Density, g/cm^3	2.60	0.91	2.60	7.80	1.7–1.9	1.4–1.5

Table 1 shows that basalt fibers are in the top three in terms of basic technical characteristics. At the same time, from the economic point of view, they are several times cheaper. So low cost and high technical characteristics of basalt fibers provide increased interest in this material for manufacturers of high-performance concrete [31].

The distinctive properties of basalt fiber are high mechanical strength, chemical resistance [32], relative cheapness, as well as high-temperature resistance [33]. Basalt fibers are used in modern construction in reinforced concrete structures, hollow concrete [34], cement floor screed [35], industrial floors, small architectural forms [36], etc. Also, one of the upcoming sectors for the use of basalt fiber is 3D printing [37–39]. With mechanical characteristics comparable to carbon fiber, the cost of basalt fiber is lower several times, and sometimes tens of times.

Therefore, basalt fibers have been widely used in construction in Russia and there are a significant number of companies manufacturing basalt fibers. Moreover, there is an almost unlimited amount of raw materials for the production of basalt fibers, because they are produced from the melt of natural basalt stone. The final fibers are produced by chopping of basalt roving for segments of the necessary length.

This makes basalt fiber one of the most promising fibers on the market. In turn, the study of the use of basalt fiber in concrete is becoming a relevant research task.

Based on the above, the following research tasks have been set:

- selection of the most available mass-produced basalt fibers on the Russian market;
- manufacture and testing of concrete samples with different dosage of basalt fiber;
- analysis of experimental data and conclusions.

2. Methods

For this research, eight fibers presented on the Russian market were selected. Five of them are chopped basalt roving (LUKE, Rusbazalt Inc, Kamenny Vek Ltd, Armastek), one of them is chopped polymer-basalt wire (SK Ltd), two of them are basalt microfibers (NTC of Applied Nanotechnologies Inc. NTC of AN Inc).

Two types of basalt microfibers produced by NTC of Applied Nanotechnologies Inc have indicated in the following way: the actual row basalt microfibers have a MB index. And the modified basalt fibers which contain carbon toroidal nanoparticles “Astralene” deposited on the surface of each filament have a MBM index. In this case, short basalt fibers serve as carriers of carbon nanoparticles in concrete and are added to the concrete using the known method of "successive dilution". This method allows to distribute of the micro-quantity of any additives (in this case it is carbon nanoparticles) in a large volume (mass) of the substance uniformly.

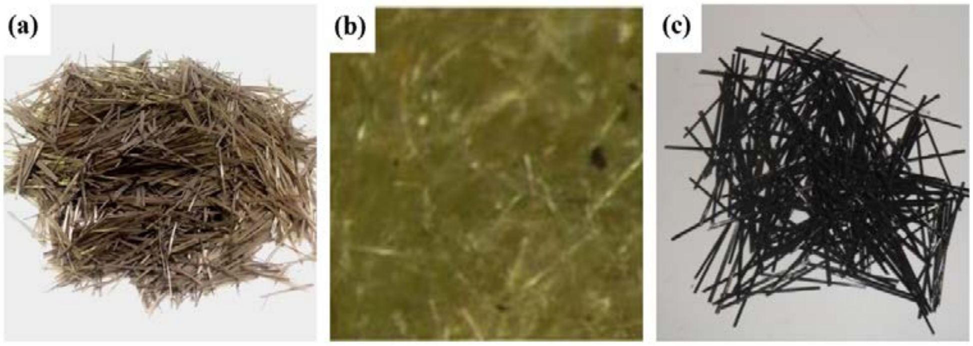

Figure 1. Basalt fibers produced by “Armplast” group (www.arm-plast.ru) – a; modified basalt microfiber produced by “NTC of Applied Nanotechnologies Inc.” (www. ntc-pn.ru) – b; basalt-polymer fiber produced by “SK Ltd.” – c.

Table 2 shows the properties of basalt fibers that have been declared by manufacturers in their certificates.

Table 2. Basalt fiber properties claimed by manufacturers.

Properties	LUKE	Rusbazalt Inc	Kamenny Vek Ltd	Armastek	SK Ltd	MB and MBM, NTC “AN Inc”
City and country of manufacture	Shandong, China	Chelyabinsk, Russia	Dubna, Russia	Perm, Russia	St. Petersburg, Russia	St. Petersburg, Russia
Density, (linear density)	2.8 kg/m^3	2.6 – 2.8 kg/m^3	2.8 kg/m^3	2.8 kg/m^3	1.9 kg/m^3	2.8 kg/m^3
Young's modulus of elasticity	93 – 110 GPa	~80 GPa	85 – 95 GPa	N/A	N/A	N/A
Tensile stress (force) at break	2800 – 3800 MPa	~3100 GPa	2700 – 3200 Mpa	N/A	N/A	N/A
Elongation at break	≤ 3.1%	2.0 – 4.5%	3.1%	3.1%	3.1%	3.1%
Operating temperature	–260+ 400 °C	–260+700 °C	–260+460 °C	–260+600°C	–70+600°C	–250+530 °C
Alkali resistance	≥ 75%	N/A	≥ 93	High	High	High
Diameter of a filament	5 – 26 µm	13 – 17 µm	23 – 25 µm	17 – 19 µm	80 150 µm	10 – 14 µm
Fiber length	6 mm	6 mm	6 mm	6 mm	6 mm	1 – 6 mm

Fine-grained concrete cubes with dimensions of 100×100×100 mm in a quantity of 3 pieces, and prisms of dimensions of 40×40×160 mm in a quantity of 3 pieces, were made from each batch according to Russian State Standard GOST 10180-2012.

The control samples were prepared according to the following fine-grained concrete recipe with the same water-cement ratio which was equal to 0.35:

1. Portland cement PP 500-D0-H produced by Oskolcement Inc…..29 %
2. Gabrodiabasic sand of fraction 0-5 mm …………………………………….………………..…23.5 %
3. River washed sand according to Russian State Standard GOST 8736-2014……………….37.3 %

4. Water according to Russian State Standard GOST 23732-2011………………………………10.2 %

The concrete samples were prepared in moulds and removed from the moulds after 1-day curing at room temperature. All the samples (and also the control samples) have been hardened in thermo-humidity conditions for 28 days according to Russian State Standard GOST 10180-2012.

Fiber-reinforced fine-grained concrete cubes were made with a fiber dosage of 0.25 vol.-%, 0.5 vol.-%, and 1 vol.-%.

The density of fine-grained concrete was determined according to Russian State Standard GOST 10180-2012.

The compressive strength test of concrete cubes with dimensions of 100x100x100 mm and the flexural strength tests (by the method of 3-point bending) of concrete prisms with dimensions of 40×40×160 mm was carried out on the hydraulic laboratory testing machine WK-18 ZARZAD SPRZETU (Poland) according to Russian State Standard GOST 10180-2012.

3. Results and Discussion

During this research, experimental data have been obtained on the changes in density and strength of concrete depending on the fiber's dosage. Experimental data are presented in Tables 3, 4 and Fig. 2–5.

Table 3. Density of concrete with basalt fiber of various manufacturers with different fiber dosage.

Manufacturer of fibers	Density of fiber-reinforced concrete, kg/dm³			
	without fiber	0.25 %	0.5 %	1 %
LUKE Inc.	2.312	2.319	2.338	2.354
Rusbazalt Inc.		2.329	2.342	2.362
Kamenny Vek Ltd.		2.315	2.327	2.351
NTC of Applied Nanotechnologies Inc. (MB)		2.294	2.271	2.254
Armastek Inc.		2.322	2.341	2.349
NTC of Applied Nanotechnologies Inc. (MBM)		2.303	2.291	2.272
SK Ltd.		2.309	2.302	2.293
Armplast group		2.314	2.317	2.321

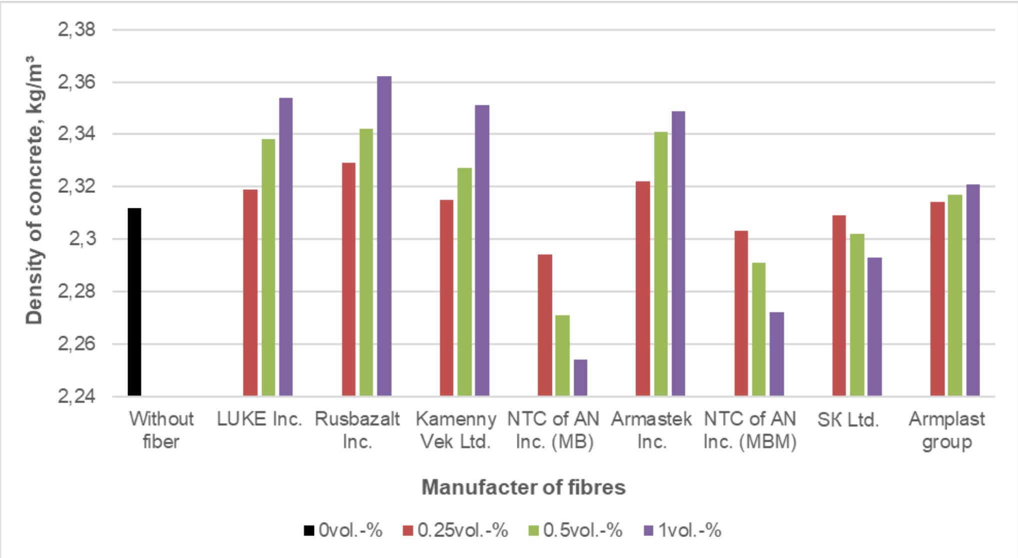

Figure 2. Density of fiber-reinforced concrete, Kg/dm³.

Table 3 and Fig. 2 show concrete density depending on fibers dosage. Fibers that are made from chopped basalt roving (manufactured by LUKE, Rusbazalt Inc, Kamenny Vek Ltd, Armastek) result in a proportional increase in density as the fiber content increases. On one hand, this is since the fibers improve the structure of concrete and reduce air entrainment. On the other hand, this because the density of the fibers (2.6 – 2.8 kg/dm³) is higher than the density of fine-grained concrete (2.3 kg/dm³), as confirmed by the results of other researchers [40].

The density of concrete with chopped polymer-basalt wire fiber (manufactured by SK Ltd) decreases proportionally as the amount of fiber increases. This is primarily due to the lower density of this fiber (1.9 kg/dm³) relative to the density of fine-grained concrete (2.3 kg/dm³).

The density of microfibers (manufactured by NTC of AN Inc.) reinforced concrete decreases proportionally with increasing fibers dosage. This is since microfibers involve additional air in the concrete. However, in the case of the modified basalt microfiber (MBM), the density reduction is slower, which is most likely because nanoparticles lead to the structuring of cement rock, which confirms the previously obtained results [41].

Table 4. Strength of basalt fiber-reinforced fine-grained concrete.

Manufacturer of fibers	Compressive strength of fiber-reinforced concrete after 28 days, MPa			Flexural strength of fiber-reinforced concrete after 28 days, MPa		
	0.25 vol.-%	0.5 vol.-%	1 vol.-%	0.25 vol.-%	0.5 vol.-%	1 vol.-%
Without fibers	51.7	51.7	51.7	5.1	5.1	5.1
LUKE Inc.	52.7	53.9	54.8	5.9	6.8	7.3
Rusbazalt Inc.	53.3	54.6	55.7	6.0	7.1	7.6
Kamenny Vek Ltd.	52.9	55.4	56.7	6.2	7.0	7.7
NTC of Applied Nanotechnologies Inc. (MB)	52.5	53.1	54.3	5.4	6.3	7.1
Armastek Inc.	52.9	53.8	54.9	5.9	6.7	7.5
NTC of Applied Nanotechnologies Inc. (MBM)	53.5	55.2	56.3	6.1	7.3	7.8
SK Ltd.	53.7	54.9	56.8	5.7	7.4	8.6
Armplast group	53.4	54.5	56.5	5.9	6.6	7.4

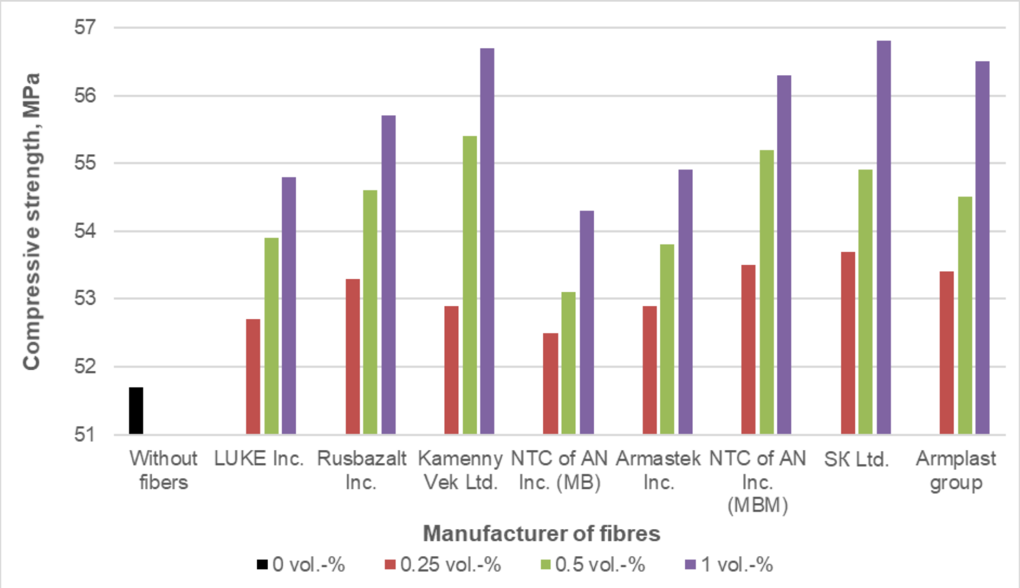

Figure 3. Compressive strength of concrete reinforced with basalt fibers of various manufacturers.

Table 4 and Fig. 3 show the effect of basalt fibers on fine-grained concrete properties. The compressive strength enhancement when using each of the fibers occurs proportionally to the increase in fibers dosage in concrete. Maximum strength enhancement was obtained for each type of fibers at the fiber dosage of 1 vol.-%.

The maximum compressive strength enhancement (9.8%) was achieved using fibers manufactured by SK Ltd (from 51.7 MPa to 56.8 MPa) and by Kamenny Vek Ltd (from 51.7 MPa to 56.7 MPa). It is worth to remark that the fibers manufactured by Kamenny Vek Ltd are chopped basalt roving, and the fibers manufactured by SK Ltd are cut polymer-basalt wire.

The minimum compressive strength enhancement (6%) from fibers from chopped basalt roving was achieved using fibers manufactured by Luke Ink (China). This is most likely due to a lower quality raw material for the production of this fibers compared to other fibers or due to the difference in production technology. Other fibers also made of chopped basalt roving gave the following compressive strength enhancement values: maximum strength enhancement using basalt fibers of Rusbasalt Inc was 7.7% (from 51.7 MPa to 55.7 MPa), maximum strength enhancement using basalt fibers of Armastek Inc was 6.2% (from 51.7 MPa to 54.9 MPa), maximum strength enhancement using basalt fibers of Armplast group was 9.3% (from 51.7 MPa to 56.5 MPa).

The compressive strength enhancement using basalt microfibers produced by NTC of AN Inc was 4.1% (from 51.7 MPa to 54.3 MPa), and using modified basalt fibers was 6.7% (from 51.7 MPa to 56.3 MPa) since carbon toroidal nanoparticles "Astralene" were used for medication of the basalt microfibers. It led to the structuring of the concrete matrix, as well as to an increase in adhesion between concrete and basalt microfibers. This can be seen in Fig. 5.

The obtained results are consistent with the results of other researchers. For example, these papers also note an increase in the compression strength of concrete using basalt fiber [33], [37]. In this paper [37], a 10% increase in the compressive strength of concrete was obtained using basalt fiber. In the paper [42], it was also obtained a compression strength increase of 8–11%. However, this was achieved using a dosage of 2-3 vol.-% of the fiber.

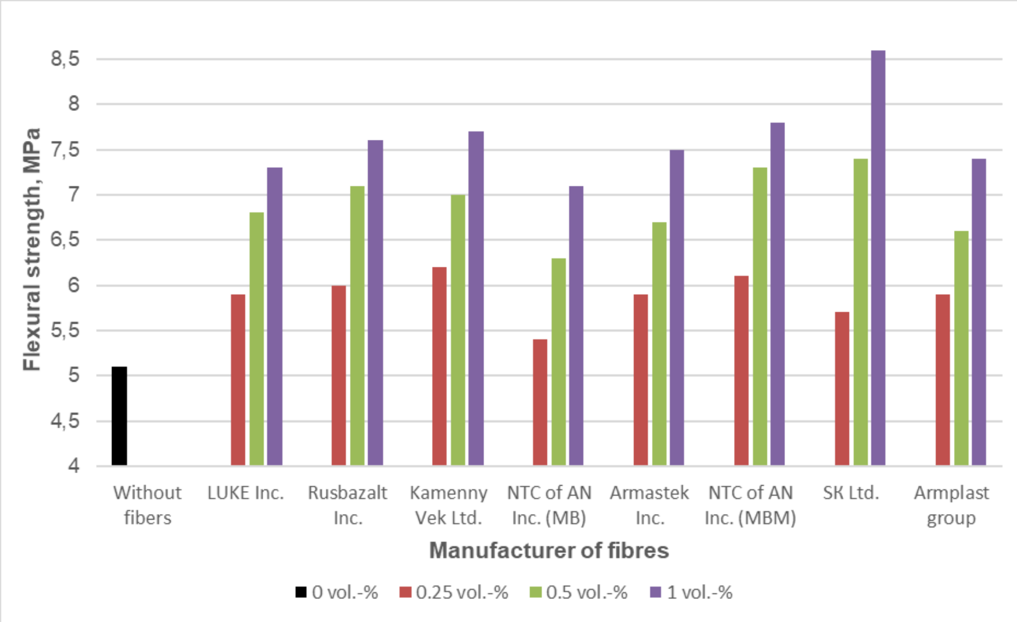

Figure 4. Flexural strength of concrete reinforced with basalt fiber of various manufacturers.

Table 3 and Fig. 4 show that all the used fibers result in a significant flexural strength enhancement. The highest flexural strength enhancement was achieved using fiber manufactured by SK Ltd (68.6%, from 5.1 MPa to 8.6 MPa), NTC of AN Inc (52.9%, from 5.1 MPa to 7.8 MPa) and Kamenny Vek Ltd (50.9%, from 5.1 MPa to 7.7 MPa).

The highest flexural strength enhancement of basalt fibers reinforced fine-grained concrete is due to the fact that the fibers produced by SK Ltd are a chopped polymer-basalt wire, which allows large agglomerates of basalt fibers to work together.

The other type of fiber also made of chopped basalt roving gave the following flexural strength enhancement values: maximum strength enhancement using basalt fibers from Rusbasalt Inc was 49% (from 5.1 MPa to 7.6 MPa), maximum strength enhancement using basalt fibers from Armastek Inc was 47.1% (from 5.1 MPa to 7.5 MPa), maximum strength enhancement using basalt fibers from Armplast group was 45.1% (from 5.1 MPa to 7.4 MPa).

The difference between the increase in strength of concrete reinforced with basalt microfibers (39.2%, from 5.1 MPa to 7.1 MPa) and modified basalt fibers is explained by the fact that carbon toroidal nanoparticles "Astralene" were used to modify the basalt microfibers (52.9%, from 5.1 MPa to 7.8 MPa). It led to the structuring of the concrete matrix and an increase in adhesion between concrete and basalt microfiber. This can be seen in Fig. 5.

The results obtained differ for the better from the results obtained in the paper [42] where an increase in strength of 2–26% was obtained depending on the dosage of the fiber. However, the results obtained are quite well consistent with the results obtained in this paper [43]. Here, the increase in flexural strength was also about 30–40 %. It has also been found that the use of 6 mm long fiber results in a superior increase in concrete strength than 12 mm long fiber.

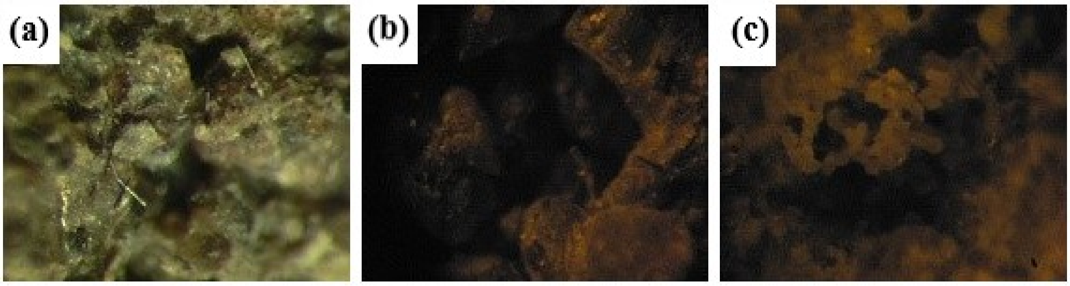

Figure 5. Structure of the fiber-reinforced concrete with MFM at the maturity period of: (a) – 1 day; (b) – 28 days; (c) – 6 months.

In Fig. 5 one can see the elongated outgrowths on the surface of basalt fibers, which were formed during the maturation of concrete. During the maturing process, the elongated outgrowths formed on the surface of basalt fibers are transformed into "druses" from the dicalcium silicate, and they increase thereby the effect of dispersed reinforcement. This is an unexpected and important effect of using nanoparticles “Astralene” for obtaining a new type of nano-modified high-strength concrete.

4. Conclusions

1. Each of the used fibers showed a significant compression and flexural strength enhancement of fine-grained concrete.

2. The maximum compressive strength enhancement (9.8%) was achieved using fibers manufactured by SK Ltd and Kamenny Vek Ltd. It is worth remarking that fibers manufactured by Kamenny Vek Ltd are chopped basalt roving, and fibers manufactured by SK Ltd are a cut polymer-basalt wire. When dispersing basalt fiber is used, the maximum strength values are slightly lower. This increase in strength was about 7%.

3. The highest flexural strength enhancement was achieved using fibers manufactured by SK Ltd (68.6%), NTC of AN Inc (52.9%) and Kamenny Vek Ltd (50.9%). The highest flexural strength enhancement fine-grained concrete reinforced with basalt fibers was due to the fact that fibers produced by SK Ltd are a cut polymer-basalt wire, which allows large agglomerates of basalt fibers to work together.

4. Basalt fiber improves the structure of concrete and reduces its porosity, which is one of the reasons for the strength and operational properties enhancement of concrete.

5. Basalt microfiber manufactured by NTC of Applied Nanotechnologies Inc modified with carbon toroidal nanoparticles "Astralene" leads to an additional strength enhancement compared to basalt microfiber without modification due to the additional reinforcement with elongated outgrows that appeared in the concrete during its maturation.

References

1. Afroughsabet, V., Biolzi, L., Ozbakkaloglu, T. High-performance fiber-reinforced concrete: a review. 51 (14). Springer US, 2016.
2. Monaldo, E., Nerilli, F., Vairo, G. Basalt-based fiber-reinforced materials and structural applications in civil engineering. Composite Structures. 2019. 214. Pp. 246–263. DOI: 10.1016/j.compstruct.2019.02.002
3. Pakravan, H.R., Ozbakkaloglu, T. Synthetic fibers for cementitious composites: A critical and in-depth review of recent advances. Construction and Building Materials. 2019. 207. Pp. 491–518. DOI: 10.1016/j.conbuildmat.2019.02.078
4. Murali, G., Amran, M., Fediuk, R., Vatin, N., Raman, S.N., Maithreyi, G., Sumathi, A. Structural behavior of fibrous-ferrocement panel subjected to flexural and impact loads. Materials. 2020. 13 (24). Pp. 1–22. DOI: 10.3390/ma13245648
5. Asprone, D., Auricchio, F., Menna, C., Mercuri, V. 3D printing of reinforced concrete elements: Technology and design approach. Construction and Building Materials. 2018. 165. Pp. 218–231. DOI: 10.1016/j.conbuildmat.2018.01.018
6. Matthäus, C., Kofler, N., Kränkel, T., Weger, D., Gehlen, C. Interlayer reinforcement combined with fiber reinforcement for extruded lightweight mortar elements. Materials. 2020. 13 (21). Pp. 1–17. DOI: 10.3390/ma13214778
7. Batson, G. Steel fiber reinforced concrete. Materials Science and Engineering. 1976. Vol. 25. Pp. 53–56. DOI: 10.1016/0025-5416(76)90051-3
8. Afroughsabet, V., Ozbakkaloglu, T. Mechanical and durability properties of high-strength concrete containing steel and polypropylene fibers. Construction and Building Materials. 2015. Vol. 34. Pp. 73–82. DOI: 10.1016/j.conbuildmat.2015.06.051
9. Mumenya, S.W. Development of textiles customized as reinforcement to cementitious matrices. Textiles: Types, Uses and Production Methods. Nova Science Publishers. New York, 2012. 639 p.
10. Song, P.S., Hwang, S. Mechanical properties of high-strength steel fiber-reinforced concrete. Construction and Building Materials. 2004. 18 (9). Pp. 669–673. DOI: 10.1016/j.conbuildmat.2004.04.027

11. Yazici, Ş., Inan, G., Tabak, V. Effect of aspect ratio and volume fraction of steel fiber on the mechanical properties of SFRC. Construction and Building Materials. 2007. 21 (6). Pp. 1250–1253. DOI: 10.1016/j.conbuildmat.2006.05.025
12. Klyuev, S.V., Klyuev, A.V., Abakarov, A.D., Shorstova, E.S., Gafarova, N.G. The effect of particulate reinforcement on strength and deformation characteristics of fine-grained concrete. Magazine of Civil Engineering. 2017. 75 (7). Pp. 66–75. DOI: 10.18720/MCE.75.6
13. Saghafi, M. hossein, Shariatmadar, H. Enhancement of seismic performance of beam-column joint connections using high performance fiber reinforced cementitious composites. Construction and Building Materials. 2018. 180. Pp. 665–680. DOI: 10.1016/j.conbuildmat.2018.05.221
14. Marcos-Meson, V., Michel, A., Solgaard, A., Fischer, G., Edvardsen, C., Skovhus, T.L. Corrosion resistance of steel fibre reinforced concrete – A literature review. Cement and Concrete Research. 2018. 103. Pp. 1–20. DOI: 10.1016/j.cemconres.20-17.05.016
15. Marcos-Meson, V., Fischer, G., Edvardsen, C., Skovhus, T.L., Michel, A. Durability of Steel Fibre Reinforced Concrete (SFRC) exposed to acid attack – A literature review. Construction and Building Materials. 2019. 200. Pp. 490–501. DOI: 10.1016/j.conbuildmat.2018.12.051
16. Larisa, U., Solbon, L., Sergei, B. Fiber-reinforced Concrete with Mineral Fibers and Nanosilica. Procedia Engineering. 2017. 195. Pp. 147–154. DOI: 10.1016/j.proeng.2017.04.537
17. Reis, J.M.L. Fracture and flexural characterization of natural fiber-reinforced polymer concrete. Construction and Building Materials. 2006. 20 (9). Pp. 673–678. DOI: 10.1016/j.conbuildmat.2005.02.008
18. Awwad, E., Mabsout, M., Hamad, B., Farran, M.T., Khatib, H. Studies on fiber-reinforced concrete using industrial hemp fibers. Construction and Building Materials. 2012. 35. Pp. 710–717. DOI: 10.1016/j.conbuildmat.2012.04.119
19. Corinaldesi, V., Moriconi, G. Durable fiber reinforced self-compacting concrete. Cement and Concrete Research. 2004. 34 (2). Pp. 249–254. DOI: 10.1016/j.cemconres.2003.07.005
20. Larsen, I.L., Thorstensen, R.T. The influence of steel fibres on compressive and tensile strength of ultra high performance concrete: A review. 2020. 256. Pp. 1–15. https://doi.org/10.1016/j.conbuildmat.2020.119459
21. Baricevic, A., Pezer, M., Jelcic Rukavina, M., Serdar, M., Stirmer, N. Effect of polymer fibers recycled from waste tires on properties of wet-sprayed concrete. Construction and Building Materials. 2018. 176. Pp. 135–144. DOI: 10.1016/j.conbuild-mat.2018.04.229
22. Fallah, S., Nematzadeh, M. Mechanical properties and durability of high-strength concrete containing macro-polymeric and polypropylene fibers with nano-silica and silica fume. Construction and Building Materials. 2017. 132. Pp. 170–187. https://doi.org/10.1016/j.conbuildmat.2016.11.100
23. Kabay, N. Abrasion resistance and fracture energy of concretes with basalt fiber. Construction and Building Materials. 2014. 50. Pp. 95–101. DOI: 10.1016/j.conbuildmat.2013.09.040
24. Banthia, N., Nandakumar, N. Crack growth resistance of hybrid fiber reinforced cement composites. Cement and Concrete Composites. 2003. 25 (1). Pp. 3–9. DOI: 10.1016/S0958-9465(01)00043-9
25. Frank, E., Hermanutz, F., Buchmeiser, M.R. Carbon fibers: Precursors, manufacturing, and properties. 2012. 297 (6). Pp. 493–501. https://doi.org/10.1002/mame.201100406.
26. Deák, T., Czigány, T. Chemical Composition and Mechanical Properties of Basalt and Glass Fibers: A Comparison. Textile Research Journal. 2009. 79 (7). Pp. 645–651. DOI: 10.1177/0040517508095597
27. Harvey, P. Engineering properties of steel. American society for metals. Ohio, 1982. 1634 p.
28. Huang, X. Fabrication and properties of carbon fibers. 2009. 2 (4). Pp. 2369–2403. DOI: 10.3390/ma2042369
29. Pusch, J., Wohlmann, B. Carbon Fibers. Inorganic and Composite Fibers: Production, Properties, and Applications. 2018. Pp. 31–51. https://doi.org/10.1016/B978-0-08-102228-3.00002-5
30. Pagnoncelli, M., Piroli, V., Romanzini, D., Pereira, I.M., Rodrigues Dias, R., Amico, S.C., Zattera, A.J. Mechanical and ballistic analysis of aramid/vinyl ester composites. Journal of Composite Materials. 2018. 52 (3). Pp. 289–299. DOI: 10.1177/0021998-317705976
31. Yoo, D.Y., Kim, M.J., Kim, S.W., Park, J.J. Development of cost effective ultra-high-performance fiber-reinforced concrete using single and hybrid steel fibers. Construction and Building Materials. 2017. 150. Pp. 383–394. DOI: 10.1016/j.conbuild-mat.2017.06.018
32. Urkhanova, L.A., Lkhasaranov, S.A., Buyantuev, S.L., Fediuk, R.S., Taskin, A. V. Reducing alkaline corrosion of basalt fiber in concrete. Magazine of Civil Engineering. 2019. 91 (7). Pp. 112–120. DOI: 10.18720/MCE.91.10
33. High, C., Seliem, H.M., El-Safty, A., Rizkalla, S.H. Use of basalt fibers for concrete structures. Construction and Building Materials. 2015. 96. Pp. 37–46. DOI: 10.1016/j.conbuildmat.2015.07.138
34. Awang, H., Ahmad, M.H. Durability properties of foamed concrete with fiber inclusion. International Journal of Civil, Structural, Construction and Architectural Engineering. 2014. 8. Pp. 273–273. doi.org/10.5281/zenodo.1091440
35. Chakartnarodom, P., Prakaypan, W., Ineure, P., Kongkajun, N., Chuankrerkkul, N. Feasibility study of using basalt fibers as the reinforcement phase in fiber-cement products. Key Engineering Materials. 2018. 766. Pp. 252–257. DOI: 10.4028/www.sci-entific.net/KEM.766.252
36. Baranova, A., Badenikova, M., Shustov, P., Rudykh, C., Bobrova, A. Light fine-grained fibrous concrete for small architectural forms. MATEC Web of Conferences, 2018. 6 p. DOI: 10.1051/matecconf/201821201008
37. Hambach, M., Volkmer, D. Properties of 3D-printed fiber-reinforced Portland cement paste. Cement and Concrete Composites. 2017. 79. Pp. 62–70. DOI: 10.1016/j.cemconcomp.2017.02.001
38. Yu, S., Hwang, Y.H., Hwang, J.Y., Hong, S.H. Analytical study on the 3D-printed structure and mechanical properties of basalt fiber-reinforced PLA composites using X-ray microscopy. Composites Science and Technology. 2019. 175. Pp. 18–27. DOI: 10.1016/j.compscitech.2019.03.005
39. Ma, G., Li, Z., Wang, L., Wang, F., Sanjayan, J. Mechanical anisotropy of aligned fiber reinforced composite for extrusion-based 3D printing. Construction and Building Materials. 2019. 202. Pp. 770–783. DOI: 10.1016/j.conbuildmat.2019.01.008
40. Branston, J., Das, S., Kenno, S.Y., Taylor, C. Mechanical behaviour of basalt fibre reinforced concrete. Construction and Building Materials. 2016. 124. Pp. 878–886. DOI: 10.1016/j.conbuildmat.2016.08.009
41. Ponomarev, A., Knezević, M., Vatin, N., Kiski, S., Ageev, I. Nanosize scale additives mix influence on the properties of the high performance concretes. Journal of Applied Engineering Science. 2014. 12 (3). Pp. 227–232. DOI: 10.5937/jaes12-6161

42. Ma, J., Qiu, X., Cheng, L., Wang, Y. Experimental research on the fundamental mechanical properties of presoaked basalt fiber concrete. Advances in FRP Composites in Civil Engineering. 2011. Pp. 85–88. DOI: doi.org/10.1007/978-3-642-17487-2_16
43. Wang, X., He, J., Mosallam, A., Li C., Xin, H. The effects of fiber length and volume on material properties and crack resistance of basalt fiber reinforced concrete (BFRC). Advances in Materials Science and Engineering. 2019. 2019 (4). Article ID 7520549. DOI: doi.org/10.1155/2019/7520549

Contacts:

Aleksandr Rassokhin, rassokhinaleksandr@gmail.com
Andrey Ponomarev, 9293522@gmail.com
Svetlana Shambina, shambina_sl@mail.ru
Antonina Karlina, karlinat@mail.ru

Magazine of Civil Engineering

ISSN 2712-8172

journal homepage: http://engstroy.spbstu.ru/

DOI: 10.34910/MCE.109.14

Fibers reinforcement of the fissured clayey soil by desiccation

M. Jamei*, Y. Alassaf, A. Ahmed, A. Mabrouk

Northern Border University, Engineering College, Arar, Kingdom Saudi Arabia (KSA)

**E-mail: mehjamei@yahoo.fr*

Keywords: desiccation, cracks, fibers, tensile strength, modeling

Abstract. The cracks caused by desiccation induce rapid failures as rapid shallow landslides in stiff and fragile clayey soils. Several environmental structures such as landfill liners and road embankments are often constructed by compaction of a series of soil layers. These works suffered in many cases of disorders due to desiccation. One of the potential valuable techniques to reduce these disorders is the short fibers reinforcement. Fibers reduce the cracks propagation and the geometric cracks characteristics such as the length, depth and opening. The paper presents an experimental characterization of the crack pattern observed in compacted samples at optimum water content (OMC) with and without fibers reinforcement. 2D Image Analysis has been used to investigate the characteristics of the geometric cracks. Alfa natural short fibers used to assure the reinforcement, reduced the carks' propagation by stopping the propagation and reducing their 3D opening (surface opening and depth growth). The role of fibers to improve the tensile strength and reduce the growth of the crack has been well-highlighted. At this stage, a simple model was calibrated to predict the tensile strength for reinforced soil specimens with short fibers considering various fibers contents and fiber's geometrical characteristics.

1. Introduction

The unsaturated soil mechanics offers a convenient framework for understanding several disorders due to the collapse, swelling, and shrinkage by saturation changes. This paper focuses on the constrained shrinkage role in developing cracks in soils. In order to reduce the developed cracks, micro-reinforcement is often helpful. So, the use of short fibers is one of the recommended techniques. This paper investigates this role and presents experimental evidence to prove fibers' role. It also presents a simple model to predict the tensile strength as a key parameter governing the cracks' appearance and propagation.

Otherwise, several engineering works suffer from the disorders caused by the wetting-drying environmental cycles. The long drying path affected the geotechnical works built in fine soils as embankments, slopes, shallow foundations, and landfill liner cover, which causes cracks development. Cracks reduce mechanical properties such as stiffness, cohesion, and shear resistance. It significantly increases permeability, which permits a high seepage and infiltration of rainwater. Many disorders were previously studied concerning seepage and cracks [1–3]. For example, in the case of landfill liners, [4] affirmed that cracks deteriorate the liner containment function leading to accentuated leachate migration into surrounding soils and groundwater. On the other hand, several researchers were concerned by the behavior of compacted intact unsaturated clay samples and highlighted the role of the fabric on the macroscopic behavior (see, for instance, [5]). For example, it was shown that the tensile resistance depended on the fabric structure, which was conditioned by the compaction path. Depending on the fabric structure, this behavior is responsible for the cracks pattern type and cracks growth. Moreover, the effect of the wetting-drying cycles after compaction is crucial in the crack's development and cracks pattern characteristics evolution [6]. The paper [7] has shown that the crack intensity factor for wet-dry cycles was higher than those obtained for the compaction-dry cycle (samples were dried immediately after compaction

Jamei, M., Alassaf, Y., Ahmed, A., Mabrouk, A. Fibers reinforcement of the fissured clayey soil by desiccation. Magazine of Civil Engineering. 2022. 109(1). Article No. 10914. DOI: 10.34910/MCE.109.14

and then submitted to wetting-dry cycles). Studying the impact of wetting-drying cycles on the crack's development [6] showed that the growth of the cracks significantly affects both the unsaturated permeability of the studied fine soil and the water retention property. Well recently, [8] provided an overview of the desiccation process of fine soils, summarizing the experimental development in the laboratories and the field to investigate and characterize the cracks and the main models proposed to follow the development and propagation of the crack. The authors concluded that, although cracks in soils have been widely studied, there are still some aspects, principally: the establishment of reliable relationships between the cracking parameters and macroscopic engineering parameters; the investigation of the relation between the microstructure of fine soils and cracking parameters and particularly with its dynamic process. The engineering field's expectations of studying the geotechnical's stability investigate the cracked soils under desiccation process considering the effect of wetting-drying cycles.

On the other hand, few studies were interested in using the micro-reinforcement technique to improve the desiccated clays submitted to wetting-drying cycles (see, for instance, [9]). However, the use of short fibers for intact soils to reinforce the shear strength was more studied [10, 11]. In addition, fibers reinforcement concrete was well studied (see non-exhaustive works [12–14])

This paper presents the tensile feature and cracks development during the drying path of a typical fine soil characterized by a high percentage of fines based on experimental tests using a new tensile device with suction control. The data was required during the experience, and many sequential photos were taken at a fixed time interval. These photos have been exploited separately by the image analysis. Added to this first series of tests, samples were prepared by mixing the soil with natural Alfa short fibers. The mixing was conducted in a completely dry state, and the water was added progressively until reaching the optimum water content of the composite. In this paper, the role of the fibers on the cracks growing is investigated. Since the tensile strength is the main resistance material that governs the development of the cracks, this research determined water content variation by using a controlled-displacement direct tensile. A simple analytical model was calibrated to predict the tensile strength. Predicting the growth and propagation of cracks and the fiber's role in reducing and delaying the cracks is a challenge of this study.

2. Materials and Methods

2.1. Soil Properties

The selected soil was classified using Standard ASTM classification (USCS) as silty-clay soil with high plasticity. The physical properties are summarized in Table 1. Moreover, the soil exhibits high shrinkage potential [15]. The tested soils' physical and chemical propertiess are summarized in Table 1.

Table 1. Main physical characteristics of the studied soil.

Bulk Density (gr/cm^3)	LL (%)	PL (%)	PI (%)	SL (%)	VBS
2.65	60	35	25	13	7

The activity of the studied soil is defined by equation (1):

$$A = \frac{PI}{\%\,of\ \ fines \prec 2\mu m} = \frac{25}{32.5} = 0.77 \tag{1}$$

The activity of used soil is classified as normal, and it appears in the range of the Illite clays. However, as is shown in Figure 2, the smectite fraction is more dominant. A standard Proctor test have been performed, which gave the compaction curve. The maximum dry density was 1.52 gr/cm^3, and the optimum water content was 25 % (Figure1).

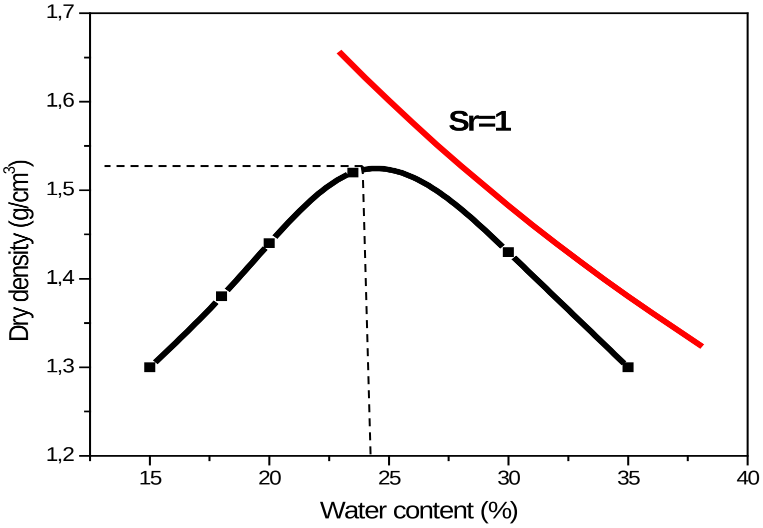

Figure 1. Compaction curve of the used soil (Sr= degree of saturation).

The grain size distribution (GSD) as provided by the laser technique is also summarized in Table 2. Since fine-grained soils are more susceptible to crack due to small pores [7], the compaction at the OMC is more convenient to investigate the crack pattern growth and its consequences on the fundamental hydromechanical properties of shear resistance and permeability. Figure 2 shows the XRD distribution, which indicates the dominant smectite component (see table 2, in which the clay fractions are summarized).

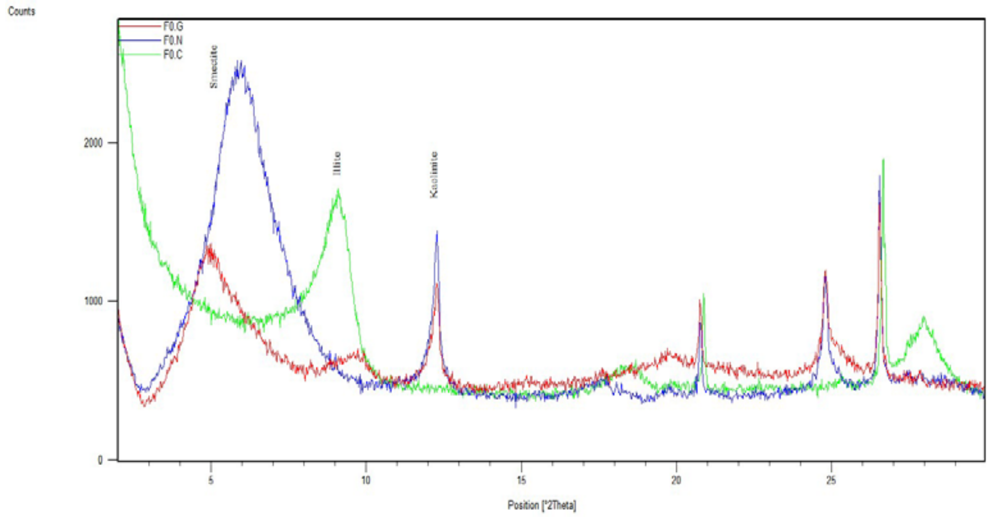

Figure 2. XRD results for the undistributed sample.

Table2. Grain Size and XRD Analysis.

Fraction of soil	Sand (15%)	Silt (50%)	Clay (35%)
Mineral component	Smectite (62 %)	Illite (22 %)	Kaolinite (16%)

In the unsaturated state, the water retention curves linking the water content (or saturation degree) to the suction are fundamental property. So, in this study, the water retention curves have been determined (Figure 3) using different techniques as the osmotic technique, the salt solutions, and the psychrometer [16]. The principal water retention curves were obtained for different paths. The first was obtained from slurry samples submitted to the drying path (D) and the compacted drying path (CD). The compacted samples are prepared at OMC state. A humidification path was applied from OMC to the saturation water content of 30%. A drying path was applied from 30% (CD) water content. According to the experimental results, the van-Genuchten model [17] was used to fit the experimental results (Eq. 2). As shown in Figure 3, the effect of the initial state of the soil has an essential effect on the water retention curve (WRC), where the WRC of slurry and dried soil is entirely different from WRC compacted and dried. This happened due to the microstructure change by mechanical compaction compared to the evolution of the slurry one, which is influenced by the only hydraulic drying path. It is evident that such hydraulic retention behavior affects both the tensile strength and soil microstructure (see for instance [5]) and consequently the cracks network growth and development.

$$\omega(s) = \left| \omega_r + \frac{(\omega_s - \omega_r)}{\left[1 + (\frac{s}{a})^n\right]^m} \right| \quad (2)$$

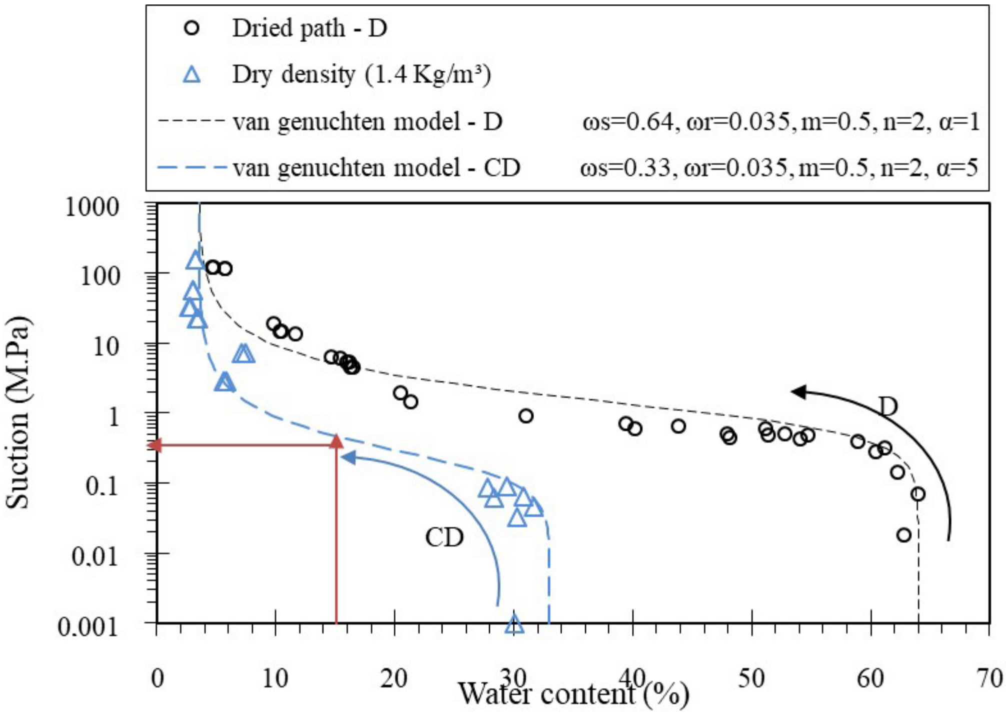

Figure 3. Principle Drying Water retention curves for compacted-drying (CD) and slurry-drying (D) samples.

2.2. Fibers Properties

Alfa fibers were selected as natural fibers to assure the micro-improvement of tensile strength of soil and then delay the rise and the growth of cracks and even affect their orientation and opening. Natural Alfa fibers were selected due to their abundance in Tunisia (especially in the west). In this study, Alfa fibers were treated using Sodium hydroxide. This chemical treatment was used to facilitate the extraction of fibers from the plants' branches and was developed to have a less aggressive extraction. It consists of degrading the non-cellulosic constituents of the plant, taking into account adequacy, rapidity, and preservation of the properties of the fibers, and respecting environmental requirements, of course [9]. This extraction was carried out by Alfa rods soaking in beakers with a soda solution (2N) and at a temperature of 100 °C. After the time determined for soaking (2h), the fibers were removed from the beakers and rinsed several times with distilled water to remove any trace of NaOH solution from the fibers. Figure 4 gives real and MEB photos of Alfa fibers.

Regarding international research [10, 18–20], some studies have been conducted using different natural fibers for tens of years. Among them, sisal fibers have equivalent physical, chemical, and mechanical properties. Table 3 summarizes the properties of Alfa fibers compared to those of Sisal fibers as also vegetal fibers mainly produced in Brazil and in some countries in the South of America.

Table 3. Physical and mechanical properties of Alfa and Sisal fibers.

Properties	Sisal [a]	Alfa[b]
Stiffness E_f (GPa)	11.8	13
Tensile Strength $\sigma_t (MPa)$	510	565
Breaking Deformation ε_f (%)	5.6	5.8
Density (gr/cm^3)	0.94	0.89
Average Diameter (mm)	0.3	0.3
Acid and alkali resistance	Very	good
Dispersibility	Normal	

[a][18], [b][21].

(a)

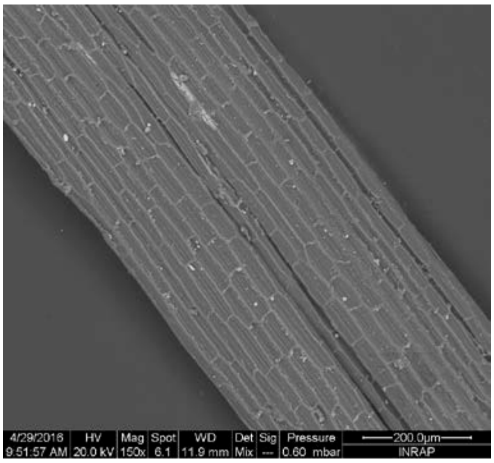

(b)

Figure 4. Alfa fibers (a) and the corresponding MEB observation (x150) (b).

Figure 5 gives the microscopic observation of Halfa fibers used as natural fibers to reduce the propagation of desiccation cracks. The microscopic observation shows the adhesion between the soil and the fibers, which contributes to developing more tensile deformation to composite soil during the developed tensile by the constrained shrinkage.

Figure 5. MEB observation (x150) of the Alfa fiber embedded in the used soil: a good adhesion between soil and fibers.

2.3. Tensile Experience

A new direct tensile device was developed based on the transformation of the shear box and using a specific mold to prepare the sample for the tensile action (Figure 6). This required a specific methodology to perform the compaction in the mold. In fact, firstly, the specimens were prepared by hand mixing to assure the homogeneity of dry soil and distilled water content concerning the amount of water to reach the

OMC value in each test. For the second set of reinforced specimens, a fixed volumetric rate (η_f) of fibers to dry soil and distilled water was added for each test. A test campaign was carried out with η_f =0.1%; η_f =0.3% and η_f =0.5%, as defined by Eq. 3.

$$\eta_f = \frac{m_f}{m_{sd}}, \tag{3}$$

where m_f and m_{sd} are respectively the masses of fibers and dry soil used to prepare the specimen.

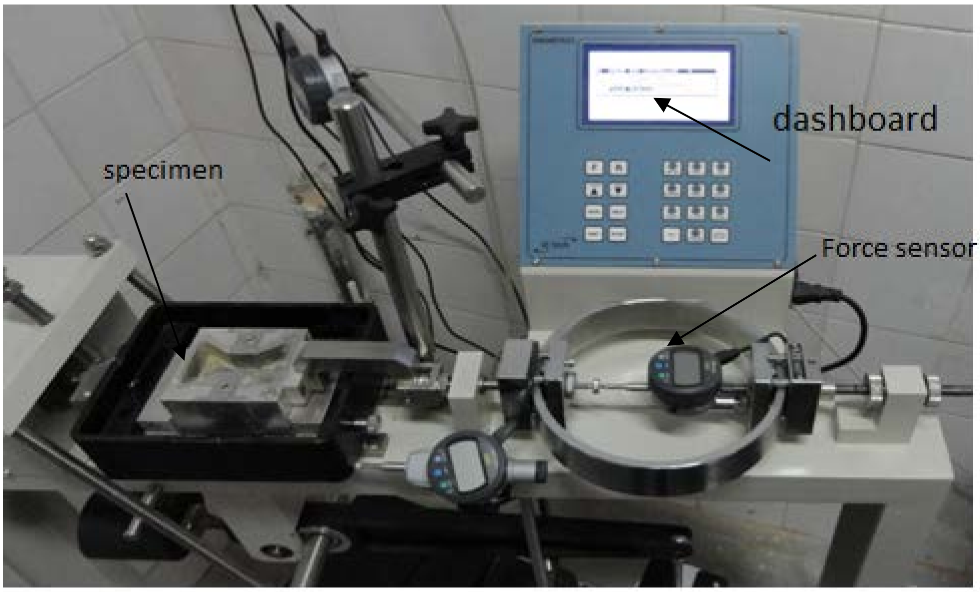

Figure 6. Photo of direct tensile test used in this study

2.4. Desiccation tests

Several authors recently studied desiccation-induced cracks using image analysis [22, 23]. New test setups and methodologies were developed, except that few have studied the 3D cracks growth [24]. According to a fixed time step, the crack patterns were quantitively determined by image analysis basing on the surface photos token progressively during the drying process. Different authors have used several parameters to characterize the crack pattern (see [25, 26]): crack spacing and depth and average crack width opening. This study characterized the cracks pattern principally by the Crack Intensity Factor (CIF). CIF is the area of cracks for the total area. The image analysis involved the conversion of the digital image from the original RGB (red-green-blue) color to gray-scale and then to a binary black and white image obtained by the principle of 'threshold gray-scale image.' After that, the binary image's black and white pixels were quantified. The white pixels correspond to the undamaged zone, while the black pixels correspond to the cracks. Each quantified number of pixels gave the corresponding density CIF [7, 25–27].

3. Results and Discussions

3.1. Tensile strength for nonreinforced soil: Effect of drying path

Figure 7 gives the tensile strength results against the compacted water content (more or less 6 tests were conducted for each path: Standard Proctor compaction and compaction-drying paths). As shown in this figure, the trend of the tensile strength against the water content depends on the followed path, particularly the compaction trend of tensile strength-suction has a similar to the Proctor compaction one [9–28]. The tensile strength of specimens prepared at a fixed initial water content of 80% OMC and dried increases and reaches a constant value of 120 kPa for suction of 60MPa.

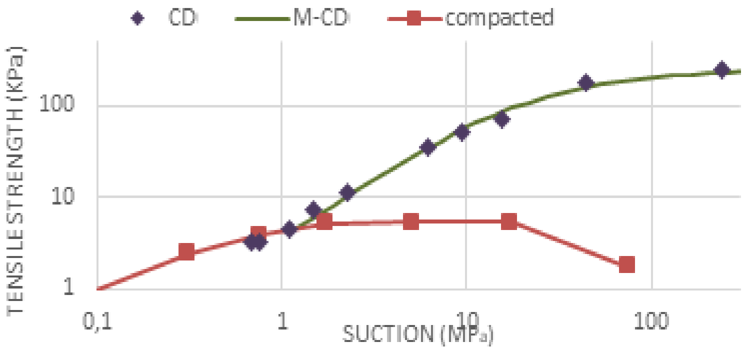

Figure 7. Tensile strength against suction for different paths (C: Compacted; CD: compacted and dried, M-CD modeled or fitted experimental results).

3.2. Experimental results of Tensile strength for reinforced soil

Figure 8 shows the typical tensile curves of specimens with different fibers rates (η_f = 0.1 %; η_f = 0.3 % and η_f = 0.5 %. The length of all used Alfa fibers was 30 mm). The specimens were compacted in the tensile box, where the dry density was fixed at 1.5 gr/cm^3. As expected, the tensile strength (the pick corresponding to the maximum of tensile stress) increases with fiber rate η_f and the delayed cracks initiation. After the reached pick value, the tensile stress decreased suddenly. Probably, the fibers played a weak role after they reached maximum tensile stress. Both phenomena were observed, the fiber's slippage and breaking of the rest.

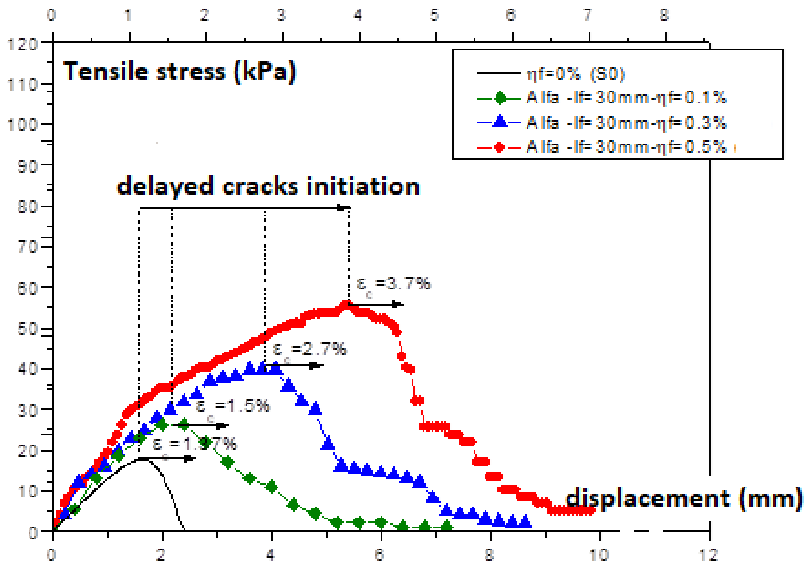

Figure 8. Tensile stress evolution with axial deformation for different fibers contents.

Several authors identified that the crack initiation is linked to the fact that the tensile stress developed by shrinkage (under drying) exceeded or equaled the tensile strength. Locally the failure was developed, and the crack growth is happened due to the tensile energy concentration [29–30]. In addition, when the fibers content increases, cracks initiation is more delayed. Appeared the first crack, with the same opening, by direct tensile force, was observed for 3.7% of tensile deformation with η_f = 0.5 %. However, it appears for 1.5 % of deformation for η_f = 0.1% (Figure 7). Consequently, the contribution of the fibers has been mainly noted for both mechanical properties, the increase of tensile resistance, and the delay of the fissure opening.

3.3. Modeling of the tensile strength of reinforced specimens

Because of the importance of developing modeling to predict the cracks, which first begins with predicting the tensile strength, we propose a simple model that can be considered in this section. As follow the tensile strength $\sigma_t(s)$ which depends on the suction (s) can be upper-estimated using the Coulomb criterion (Eq.4):

$$\sigma_t(suction,\eta_f) = \sigma_t(s,\eta_f) = \cot an(\varphi(s,\eta_f)).C(s,\eta_f) \tag{4}$$

where $\varphi(s,\eta_f)$ and $C(s,\eta_f)$ are respectively the friction angle and cohesion of the unreinforced soil, depending on both the suction (s) and fibers content (η_f).

Then, using the water retention curve, corresponding to the compacted and dried path (CD), one obtains the suction corresponding to the OMC (25 %), of 0.5MPa (Figure 3). Thus, the value of the measured tensile strength corresponding to the suction of 0.5MPawas deduced from the results in Figure 7. The tensile strength was of 8 kPa. However, from the direct compaction test (where) the compaction was done in the tensile device followed by a tensile test gives a tensile strength of 14 kPa. This difference is attributed to the compaction path with or without drying path. The 14 kPa value corresponds to the compaction at Standard Optimum Proctor without drying, and the experimental strength value was obtained from a direct test on the specimens at OMC (without a drying following the compaction).

Considering that determining the tensile strength using the model by equation (4) needs the triaxial tests under suction control on reinforced specimens. Therefore, we propose a model based on the direct tensile tests where the tensile strength $\sigma_{ts}(s,\eta_f)$ for reinforced specimen is given as follow (Eq. 5):

$$\sigma_{ts}(s,\eta_f) = \sigma_{ts}(s,\eta_f = 0) + \Delta\sigma_{ts}(s,\eta_f) \tag{5}$$

where

$$\Delta\sigma_{ts}(s,\eta_f) = \frac{\alpha\pi D_f \sum_{i=1}^{N_f}(\sigma_t(\varepsilon_f(s,\eta_f))(l_a)_i)}{A} \tag{6}$$

and

$$\alpha = \frac{\int_{-\frac{\theta}{2}}^{\frac{\theta}{2}}(d\theta)}{2\pi} \tag{7}$$

where D_f is the diameter of the fiber, $\sigma_t\left(\varepsilon_f(s,\eta_f)\right)$ is the tensile stress at the failure strain $\sigma_t\left(\varepsilon_f(s,\eta_f)\right)$ which obviously depends on the suction and fibers content. A is the section of the interest zone (20mmx30mm, see Figure 9). $(l_a)_i$ is the active length of fiber (i) under tensile. In general, it was assumed that this active length is in the range between L/4 and L/2. It is fixed in this model at L/4 for all the fibers in the zone's interest. Also, because only a part of the set of fibers is submitted to tension, a coefficient (α) defining an effective zone (see Figure 9), where fibers are submitted in tension, is introduced and defined by α (Eq. 7).

The number of fibers N_f is deduced from the volumetric fibers content given as follow (Eq. 8):

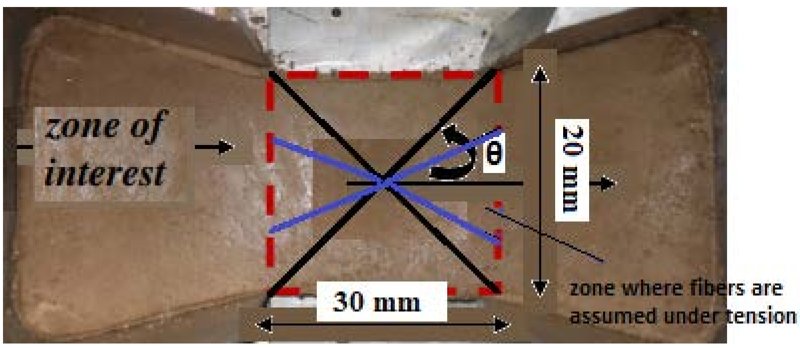

Figure 9. Shema of the interest of the specimen in tensile box.

$$N_f = N_v.V_{zI} \tag{8}$$

where V_{ZI} = volume of zone of interest =20 mm×30 mm×20 mm and N_V is the number of fibers per unit of volume. N_V is given as follow (Eq. 9), as it was shown in [10]:

$$N_v = \frac{C_f}{(1+C_f)L\pi r^2} \text{ where } C_f = \eta_f \frac{\gamma_d}{\gamma_f} \tag{9}$$

With γ_d is the maximum dry density of soil (at OMC) and γ_f is the density of Alfa fibers (see Table 3). The term corresponds to a coefficient indicating the part of a set of fibers assumed to be submitted to tensile. The fibers under tensile are elastically deformed, and the tensile stress developed by each fiber is as follow:

$$\sigma_t(\varepsilon_f(s,\eta_f)) = E_f\ \varepsilon_c(s,\eta_f) \tag{10}$$

where E_f is the stiffness of Alfa fiber (Table 3) and $\varepsilon_c(s,\eta_f)$ is the strain at maximum tensile stress of the reinforced specimen at given suction (s) and fiber content (η_f), (Figure 8).

Figure 9 gives the predicted tensile strength of the composite (reinforced soil) against measured tensile strength. This figure highlights a good agreement between the model and the experience's results (the correlation coefficient was 0.96).

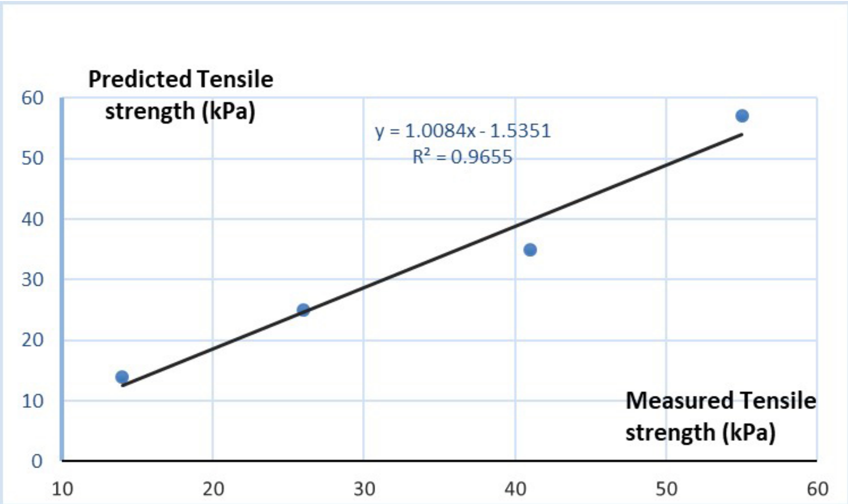

Figure 9. Predicted Tensile strength against the measured tensile strength.

3.4. Role of fibers in Cracks development

The Cracks Influence Factor (CIF) has been defined as the following (Eq. 11). CIF has been considered the main parameter to measure the cracks propagation by measuring the surface opening considered as the area of total cracks captured by the vertical camera that took the images sequentially. Figures 10.a, 10.b and 10.c give respectively the images of cracks patterns in three-time sequences (t = 48 h, t = 60 h and t = 72 h), for non-reinforced and reinforced specimens (η_f = 0.3 % and η_f = 0.5 %).

$$CIF(\%) = \frac{Fissure's\ Area}{Total\ Area\ of\ the\ specimen} \tag{11}$$

As shown in Figure 10.a, the opening of primary cracks reached its final state at 60 hours. However, secondary cracks continue to appear without a significant effect on the value of the area of the total fissure.

t = 48 h **t = 60 h** **t = 72 h**

Figure 10. a cracks pattern evolution by drying (nonreinforced specimen).

t = 48 h **t = 60 h** **t = 72 h**

Figure 10. b cracks pattern evolution by drying (reinforced specimen η_f = 0.3 %)

t=48h **t=60h** **t=42h**

Figure 10.c cracks pattern evolution by drying (reinforced specimen η_f = 0.5 %)

The formation and the morphology were well affected by the fibers. The same conclusion was given by [31]. Without fibers (nonreinforced clay), the cells tend to be more significant. Large opening and orthogonal and non-orthogonal carks have been observed. The orthogonal cracks were well-identified for the nonreinforced specimen. However, the fiber affects either the crack intensity by reducing the opening and the length of cracks and the morphology of patterns, which were developed with discontinues aspect and not necessarily perpendicular.

Figure 11 gives the variation of CIF during drying. Although the effect of fibers in cracks opening is well-demonstrated, where the role of fibers was to stop the opening, their growth was also well affected. The first fissure was happened at 2hours and was well larger for the nonreinforced specimen. However, with significantly smaller dimensions (width and length), the first one was better for the reinforced specimen (η_f = 0.5 %).

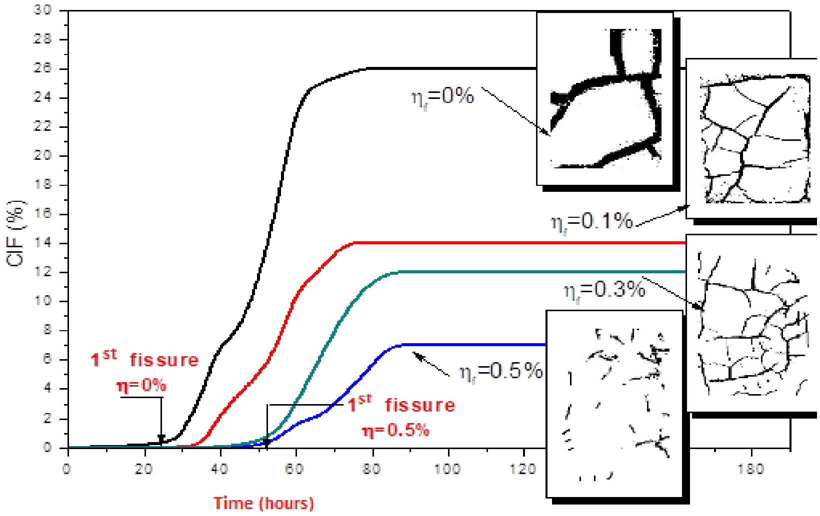

Figure 11. CIF evolution during drying time: Effect of fibers content.

The CIF was reduced from 26 % (non-reinforced clay) to 14 %, 12 % and 6 % for respectively η_f = 0.1 %, η_f = 0.3 % and η_f = 0.5 %. The fibers not only influenced the intensity factor, but also the formation and morphology of the cracks.

From the literature, the governing mechanism of desiccation of unreinforced soils (mainly silty soils) has been analyzed based on the experiments and image analysis [32–36]. As stated, the cracks birth arrived when strained shrinkage develops tensile stress that exceeds the tensile resistance of the material. Now regarding the role of fibers to globally increases the tensile strength and locally to develop a tensile force that opposes the forces developed by strained shrinkage, the fibers reduce the cracks growing and development and modify their orientation.

4. Conclusions

In this paper, the cracking patterns and morphology have been studied in the laboratory using rectangular specimens of plastic clayey-silty soil. The Digital Image Correlation (DIC) was used to quantify the cracks patterns (Length and Opening) parameters. The CIF parameter as a dimensionless parameter was retained in this study to quantify the cracks growing and development during the drying process. This study leads to the following results:

1. The tensile strength and its relation with the suction were obtained for this soil using direct tensile tests. The trends of tensile strength-suction were: (a) the same as the Proctor-compaction curve for the compacted specimens. However, for the compacted and dried specimens (b), the tensile strength against suction had a completely different trend. This indicated a monotonic increase of tensile strength with an increase of suction.

2. From DIC, the morphology of the pattern of the cracks was well-investigated. For nonreinforced specimens, the cells were large, and the opening of cracks was also significant. However, the cells vanished progressively with the increase of fibers content. The morphology of the crack pattern was significantly affected by the fibers. The presence of fibers omitted the perpendicular morphology.

3. Because the fibers improved the tensile strength, the cracks intensity (measured by CIF) was significantly decreased by adding the fibers.

4. From an environmental point of view, the use of natural short fibers seems to be a promising alternative for geotechnical works which suffer from desiccation by drying. In arid regions, such technical solutions will be envisaged and encouraged.

5. Although experimental results have been obtained for many soils by research, mainly in laboratories, the reinforced soils by fibers are still few studied. Some aspects still need more attention: (a) The quantitative relations between the fibers content, the fibers length, the fibers sections, and separately the tensile strength for soils with initial water contents and dry densities. (b) the same relations are still needed with the cracks parameters characteristics. (c) the modeling of each relation helps to obtain an efficiency model to predict the role of fibers by delaying the inevitable cracks and eventually stopping them from growth, which should be paid more attention.

References

1. Willden, R., Mabey, D.R. Giant desiccation fissures on the black rock and smoke creek deserts, Nevada. Science. 1961. Vol. 133. No. 3461. Pp. 1359–1360.
2. Morris, P.H., Graham, J., Williams, D.J. Cracking in drying soils. Canadian Geotechnical Journal. 1992. Vol. 29. No. 2. Pp. 262–277.
3. Tay, Y.Y., Stewart, D.I., Cousens, T.W. Shrinkage and desiccation cracking in bentonite-sand landfill liners. Engineering Geology. 2001. Vol. 60. No. 1–4. Pp. 263–274.
4. Miller, C.J., Mishra, M. Modeling of leakage through cracked clay liners — I: state of the art. Water Resources Bulletin. 1989. AWRA 25 (3). Pp. 551–555.
5. Trabelsi, H., Romero, E., Jamei, M. Tensile strength during drying of remolded and compacted clay: The role of fabric and water retention. Applied Clay Science. 2018. 162. Pp. 57–68.
6. Louati, F., Trabelsi, H., Jamei, M., Taibi, S. Impact of wetting-drying cycles and cracks on the permeability of compacted clayey soil. European Journal of Environmental and Civil Engineering. 2019. 1. Pp. 1–26. DOI: 10.1080/19648189.2018.1541144
7. Yessiller, N., Miller, C.J., Inci, G., Yaldo, K. Desiccation and cracking behavior of three compacted landfill liner soils. Engineering geology. 2000. Vol. 57. No. 1-2. Pp. 105–121.
8. Wei, X., Gao, C., Liu, K. A Review of Cracking Behavior and Mechanism in Clayey Soils Related to Desiccation. Advances in Civil Engineering. 2020. Vol. 2020. Pp. 1–12. Article ID 8880873. DOI: 10.1155/2020/8880873
9. Chebbi, M., Guiras, H., Jamei, M. Tensile behaviour analysis of compacted clayey soil reinforced with natural and synthetic fibers: effect of initial compaction conditions. European Journal of Environmental and Civil Engineering. 2017. 24:3. Pp. 354–380. DOI: 10.1080/19648189.2017.1384762
10. Jamei, M., Villard, P., Guiras, H. Shear Failure Criterion Based on Experimental and Modeling Results for Fiber-Reinforced Clay, International Journal of Geomechanics. 2013. December. Vol. 13. No. 6. Pp. 882–893.
11. Polyankin, A.G., Korolev, K.V.,Kuznetsov, A.O. Analysis of reinforced soil sustainability while tunnel construction. Magazine of Civil Engineering. 2020. 95(3). Pp. 80–89. DOI: 10.18720/MCE.95.8
12. Eberhardt, E., Stead, D., Stimpson, B., R.S. Read Identifying crack initiation and propagation thresholds in brittle rock. Can. Geotech. 1998. J. 35. Pp. 222–233.
13. Begich, Y.E., Klyuev, S.V., Jos, V.A., Cherkashin, A.V. Fine-grained concrete with various types of fibers. Magazine of Civil Engineering. 2020. 97(5). Article No. 9702. DOI: 10.18720/MCE.97.2
14. Gavrilov, T.A., Kolesnikov, G.N., Evolving crack influence on the strength of frozen sand soils. Magazine of Civil Engineering. 2020. 94(2). Pp. 54–64. DOI: 10.18720/MCE.94.5
15. Trabelsi, H., Jamei, M., Zenzri, H., Olivella, S. Crack patterns in clayey soils: Experiments and modeling, International Journal for Numerical and Analytical Methods in Geomechanics. 2012. Vol. 36. No. 11. Pp. 1410–1433.
16. Agus, S.S., Schanz, T. Swelling pressure and total suction of compacted bentonite sand mixtures. In: Bilsel, H., Nalbantoglu, Z. (Eds.), Proceedings of the International Conference on Problematic Soils. 2005. Vol. V1. North Cyprus. Pp. 61–70.
17. van-Genuchten, M.T. A closed form equation for predicting the hydraulic conductivity of unsaturated soils. Soil Science Society of America Journal. 1980. 44. Pp. 892–898.
18. Morel, J.C., Ghavami, K., Mesbah, A. Theoretical and experimental analysis of composite soil blocks reinforced with Sisal fibres subjected to shear. Masonry International. 2000. 13(2). Pp. 54–62.
19. Prabakara, J., Sridharb, R.S. Effect of random inclusion of sisal fibre on strength behaviour of soil. Construction and Building Materials. 2002. Vol. 16. No. 2. Pp. 123–131.
20. Zhang, C.-C., Zhu, H.-H., Shi, B., Wu, F.-D., Yin, J.-H. Experimental Investigation of Pullout Behavior of Fiber-Reinforced Polymer Reinforcements in Sand. Journal of Composites for Construction. 2015. 19. Pp. 11.
21. Bessadok, A., Roudesli, S., Marais, S., Follain, N., Lebrun, L. Alfa fibres for unsaturated polyester composites reinforcement: effects of chemical treatments on mechanical and permeation properties. Composites. 2009. Part A. Vol. 40. No. 2. Pp. 184–195.
22. Lakshmikantha, M.R., Prat, P.C., Ledesma, A. Image analysis for the quantification of a developing crack network on a drying soil. Geotechnical Testing Journal. 2009. 32(6). Pp. 505–515.
23. Lakshmikantha, M.R., Prat, P.C., Ledesma, A. Experimental evidence of size effect in soil cracking. Can. Geotech. 2012. J. Vol. 49. Pp. 264–284.
24. Sanchez, M., Atique, A., Kim, S., Romero, E., Zielinski, M. Exploring desiccation cracks in soils using a 2D profile laser device. Acta Geotechnica. 2013. 8. Pp. 583–596. DOI 10.1007/s11440-013-0272-.
25. Vogel HJ, Hofmann H, Roth K., Studies of crack dynamics in clay soil: I. Experimental methods, results, and morphological quantification. Geoderma. 2005. 125. Pp. 203–211.
26. Vogel, H.J., Hofmann, H., Leopold, A., Roth, K. Studies of crack dynamics in clay soil: II. A physically based model for crack formation. Geoderma. 2005. 125. Pp. 213–223.
27. Tang, C.-S., Shi, B., Liu, C., Suo, W.-B., Gao, L. Experimental characterization of shrinkage and desiccation cracking in thin clay layer, Applied Clay Science, 2011. Vol. 52. No. 1-2. 26. Pp. 69–77.
28. Tang, C.S., Pei, X.J., Wang, D.Y., Shi, B., Li, J. Tensile strength of compacted clayey soil. J. Geotech. Geoenviron. 2014. 141(4). 04014122.
29. Mazars, J., Bažant, Z.P. Cracking and damage: localization and size effect. 1989, Elsevier, New York.
30. Lima, L.A., Grismer, M.E. Application of fracture mechanics to cracking of saline soils. Soil Science. 1994. 158(2). Pp. 86–96. DOI: 10.1097/00010694-199408000-00002
31. Tang, C.-S., Shi, B., Cui, Y.-J., Liu, C., Gu, K. Desiccation cracking behavior of polypropylene fiber-reinforced clayey soil. Canadian Geotechnical Journal. 2012. Vol. 49. No. 9. 31. Pp. 1088–1101.
32. Wei, X., Hattab, M., Bompard, P., Fleureau, J.-M. Highlighting some mechanisms of crack formation and propagation in clays on drying path. Géotechnique. 2016. Vol. 66. No. 4. Pp. 287–300.
33. Zhang, Y., Ye, W.M., Chen, Y.G., Ye, B. Desiccation of Nacl-contaminated soil of earthen heritages in the site of Yar city, Northwest China. Applied Clay Science. 2017. Vol. 124-125. Pp. 1–10.

34. Péron, H., Hueckel, T., Laloui, L., Hu, L.B. Fundamentals of desiccation cracking of fine-grained soils: Experimental characterisation and mechanisms identification. Canadian Geotechnical Journal. 2009. Vol. 46. No. 10. Pp. 1177–1201.
35. Cordero, J.A., Useche, G., Prat, P.C., Ledesma, A., Santamarina, J.C. Soil desiccation cracks as a suction contraction process. Géotechnique Letters. 2017. Vol. 7. No. 4. Pp. 272–278.
36. Wang, L.-L., Tang, C.-S., Shi, B., Cui, Y.-J., Zhang, G.-Q., Hilary, I. Nucleation and propagation mechanisms of soil desiccation cracks. Engineering Geology. 2018. Vol. 238. Pp. 27–35.

Contacts:

Mehrez Jamei, mehjamei@yahoo.fr
Yahya Alassaf, ysalassaf@gmail.com
Anwar Ahmed, bokshe12@yahoo.com
Abdelkader Mabrouk, abdmabs@yahoo.fr

Magazine of Civil Engineering. 2022. 109(1). Article No. 10915

Magazine of Civil Engineering

ISSN 2712-8172

journal homepage: http://engstroy.spbstu.ru/

DOI: 10.34910/MCE.109.15

Lightweight concrete for 3D-printing with internal curing agent for Portland cement hydration

***A.S. Inozemtcev*[*a]*, E.V. Korolev*[b]*, T.Q. Duong*[a]**

[a] *National Research Moscow State Civil Engineering University, Moscow, Russia*

[b] *Saint Petersburg State University of Architecture and Civil Engineering, St. Petersburg, Russia*

**E-mail: InozemcevAS@mgsu.ru*

Keywords: concretes, extrusion, rheology, super absorbent polymers, curing, 3D printers, concrete additives, measurement, compressive strength, shrinkage

Abstract. The development of 3D printing technology requires solving material science problems to ensure the rheology of concrete mixtures with controlled mobility and high retention of volume after extrusion and also the creation of favorable conditions for the hardening of the binder. This paper investigates lightweight concretes on hollow microspheres. The rheological properties of concrete mixtures and the peculiarities of the structure formation of cement stone in the presence of a superabsorbent polymer (SAP) have been studied. The paper used standardized test methods following EN 1015-3-2007, EN 12390-1-2009, and employing modern equipment and tools (K100 KRUSS processor tensiometer, comparator, calorimeter). It was found that concrete mixtures on hollow microspheres with an average density of 1400 kg/m^3 have a high ability to retain volume (buildability) of more than 90 % after extrusion with mobility of not more than 135 mm of the spread diameter. It has been shown that the use of superabsorbent polymer solutions with controlled polymerization is an effective solution to provide internal curing for the hydration of Portland cement. Calorimetric analysis of cement stone showed a positive effect of SAP on the processes of structure formation of cement stone. This is expressed by an increase in the amount of hydration products, in particular portlandite. The number of SAP solution of 0.50–1.0 % of the mass of Portland cement in lightweight concrete provides the least reduction in strength. It was found that the flexural strength varies in the range of 5.5–5.8 MPa and the compressive strength – 45.3–47.8 MPa. An increase in the SAP content of more than 1.5 % of the mass of Portland cement is characterized by a decrease in compressive strength by 8.5 %. The permissible amount of SAP in concrete is limited to 1.0–1.5 % of the mass of Portland cement. The possibility of providing internal curing for the hydration of Portland cement in lightweight concrete through the use of SAP solution has been substantiated. The obtained results of the study of lightweight concrete show high printability of concrete mixtures on hollow microspheres for 3D printing. Moreover, the implemented soluble SAP composition instead of the granular SAP is capable of providing the function of internal curing for the hydration of cement with no loss in strength.

1. Introduction

Interest in 3D printing technology in construction is constantly growing. It is evident from the many publications [1–5]. World experience in the development of equipment for construction 3D printing shows that the mobility of the concrete mix is selected in a wide range of rheological properties, depending on the features of the extrusion nozzle of the printer [6–10]. The principal technological feature of the extrusion process is the presence or absence of direct formation of the layer. In the first case, the concrete mixture is supplied according to the principle of form-less molding (Fig. 1,a [6]) using a rectangular extrusion nozzle.

Inozemtcev, A.S., Korolev, E.V., Duong, T.Q. Lightweight concrete for 3D-printing with internal curing agent for Portland cement hydration. Magazine of Civil Engineering. 2022. 109(1). Article No. 10915. DOI: 10.34910/MCE.109.15

In the second case, the mixture just is supplied from a nozzle, usually of circular cross-section, without the formation of a layer (Fig. 1,b [6]). Requirements for the viscous-flow properties of the concrete mixture for each of the methods are significantly different.

a)  b) 

Figure 1. Extruded concrete layers produced using by forming (a) and non-forming (b) nozzle of printer.

As the main criteria for concrete mixtures in 3D printing technology, formability or extrudability, flowability, retention of volume (buildability), and retention of mobility (open time) are distinguished. The variability of these properties should ensure the continuity of the layer formation through the printer nozzle. And high mobility is necessary to ensure minimum deformation after extrusion of each layer and maximum storage time to improve interlayer adhesion [8].

The specificity of these properties and their interdependence complicates the universalization of their quantitative assessment using standard test methods. At the same time, various design features of 3D printers (including feeding and extrusion systems) require an individual approach to the selection of the "acceptable" suitability of the concrete mix for printing (printability).

Cement-based dispersion systems are usually considered to be thixotropic materials. That is, they can liquefy under mechanical stress and thicken when the load is removed. In this case, the description of the shear stress (τ) from the shear rate (γ) is carried out using the Herschel-Bulkley model:

$$\tau = \tau_0 + K \cdot \gamma^n, \tag{1}$$

where τ_0 is shear stress, K is consistency index, n is an indicator of non-Newtonian behavior.

In the process of 3D printing, the lower layers, in addition to their deformation, are subjected to additional influence from the upper layers. Due to the thixotropic dilution of the mixture, these influences can lead to plastic destruction of the structure (Fig. 2 [7, 11]). In this case, the limiting value depends on the density of the concrete (ρ) and the height of the structure (H) [12]:

$$A_{\text{tix}} \geq \frac{\rho g H}{\sqrt{3}}, \tag{2}$$

where g is gravitational constant.

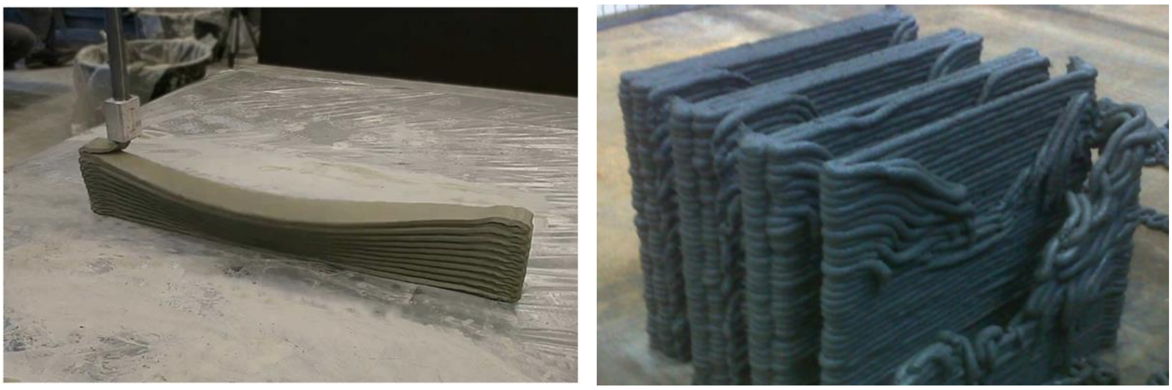

Figure 2. Plastic failures of 3D printed constructions.

Thus, it is natural to conclude that the use of lightweight concrete mixes is promising. Following (2) the lower average density of such compositions in comparison with heavy concrete will allow to increase the height of the extrusion layer with equal liquefaction or to increase this limit of liquefaction. Taking into account the positive experience of obtaining lightweight concrete with high strength [13, 14] one of the tasks can be formulated as the need to ensure the possibility of controlling the rheology of mixtures saturated by the gas phase. The object of research is lightweight concrete on hollow microspheres.

At the same time, the construction of concrete layers by extrusion at the construction site is associated with the emergence of a large open surface area of the finished product. The lack of external care in such conditions creates unfavorable preconditions for the hydration of Portland cement. Intense water loss due to evaporation leads to a lack of water for structure formation and a subsequent decrease in concrete density, shrinkage, cracking, and loss of strength.

The indicated disadvantages are less pronounced when providing a reserve of water in the particles of the porous aggregate, the so-called internal curing. This approach is known in the technology of lightweight concrete [15, 16] when the preparation of lightweight concrete is preliminarily performed by water saturation of the aggregate. A similar function can be performed by special polymer additives, the so-called superabsorbent polymers (SAP) [18–20]. As a rule, these are micrometer-sized granules or fibers capable of absorbing water up to 50 times the original volume. As a rule, these are micrometer-sized granules or fibers capable of absorbing water in an amount more than 50 times the original volume.

Currently, experience in the use of SAP in cement systems has been accumulated. There is a positive effect of SAP on reducing shrinkage and as a result, reducing the risk of cracking. However, there are several disadvantages. One of them, SAP polymer granules, require adjusting the water consumption in the mixtures to maintain their mobility [21, 22].

That is, the use of superabsorbent polymers in cement systems is characterized by both positive and negative effects [18, 23, 24].

On the one hand, SAP in the cement composite is the carrier of the water reserve to ensure the hydration of the binder. This has the positive effect of reducing shrinkage. On the other hand, the granular polymer component not only requires preliminary water saturation (up to 30 minutes) to ensure sufficient mobility of the mixture but also is a source of additional pores by reducing its volume, contributing to a decrease in mechanical properties.

Previously, the authors proposed a solution [25] which consists of using solutions of acrylate compositions with delayed polymerization for the internal curing of cement. Such solutions allow to form the polymer films at the right time, starting the process of retaining water in the volume (absorption) after extrusion of the mixtures. It is shown that the use of such a solution reduces the loss of strength of the cement stone during hardening in unfavorable conditions.

Thus, research aimed at solving the cumulative problems of ensuring the required rheology of concrete mixtures and proper care for the hydration of cement after molding is an actual direction for the development of effective compositions for 3D printing technology in construction. To achieve this goal, it is necessary to determine the mobility and buildability of the extruded volume of the concrete mixture of lightweight concrete, to establish the effect of the superabsorbent polymer solution on the mobility, strength, and shrinkage of the concretes, and to substantiate the effectiveness of such a solution to ensure the internal curing of cement hydration.

2. Methods

The object of study is lightweight concrete on hollow microspheres with an average density of 1400 kg/m^3. Concrete is made according to [26] using Portland cement CEM I 42.5 N Lipetskcement, microsilica MK-85 (NLMK) with a density of 2200–2350 kg/m^3, a particle size of 1...100 microns, and a SiO_2 content of more than 97.8 %, quartz sand 0.16–0.63 mm fraction, quartz sand flour with a specific surface of 700...800 m^2/kg, water and plasticizer Melflux 1641F. Hollow glass microspheres "Foresphere 3000" (average particle size 30 microns) were used as a lightweight aggregate to reduce the average concrete density. The subject of research is the rheological and physical-mechanical properties of concrete compositions on hollow microspheres with SAP solution. Acrylate composition “Renovir-hydrogel” [21] was used as a SAP solution. The SAP solution is obtained by mixing water (W) with the three components of the polymer part ($\Sigma A = A_1 + A_2 + A_3$) and catalyst (B). The component “A_1” is acrylic acid (propenoic acid – $CH_2 = CH - COOH$) or salt (sodium polyacrylate $[–CH_2 – CH(COONa)–]_n$). The component “A_2” is a crosslinking agent in which poly-saturated compounds are widely used. The component “A_3” is an initiator from peroxides, hydroperoxides, hydrogen peroxide, persulfates, azo compounds, or redox systems. Varying the concentrations of each component allows to control the polymerization process and form a different degree of crosslinking and polymerization speed (Table 1).

Table 1. Compositions of the studied concrete.

Variation of the plasticizer			Variation of the SAP			
No	Name	C_{Plast}, % by weight of cement	No	Name	C_{SAP}, % by weight of cement	Ratio W/ΣA
1	P/C-1.0	1.0	6	A/C-0	–	–
2	P/C-1.1	1.1	7	A/C-0.4	0.4	95.0
3	P/C-1.2	1.2	8	A/C-0.8	0.8	47.0
4	P/C-1.3	1.3	9	A/C-1.5	1.5	23.0
5	P/C-1.4	1.4	10	A/C-2.3	2.3	15.0
			11	A/C-3.9	3.9	8.5

Notes: C_{Plast} is concentration of plasticizer; C_{SAP} is the amount of acrylate part of SAP (ΣA); W is the amount of water.

The mobility of the lightweight concrete mix with varying concentration of a plasticizer (1.0...1.4 % of the mass of Portland cement (Table 1)) was determined by the diameter of the cone spread according to EN 1015-3-2007. Retention of volume (buildability) was additionally evaluated. It was evaluated by the change in the volume of the mixture extruded from a metal cylinder with a ratio of diameter to height of 1: 2.

The evaluation of the compatibility of the superabsorbent polymer with the polycarboxylate plasticizer was carried out by changing the surface tension of aqueous solutions using a K100 KRUSS processor tensiometer.

The assessment of the degree of hydration was carried out using the calorimetric method by the total thermal energy [27]. Calorimetric analysis of cement mixtures was carried out for compositions with W/C-ratio 0.5 within 72 hours using an isothermal calorimeter. Cement compositions with SAP were prepared with a polymer content of 0.5...1.5 % of the mass of Portland cement at a constant catalyst B/A_1 = 0.003.

The compressive strength tests were carried using static loading by the servo-hydraulic press “Advantest 9” according to EN 12390-1-2009. The shrinkage deformations were determined by the change in the distance between the reference points during hardening in unfavorable conditions (temperature 25... 27 °C and humidity 50…60 %) using a comparator.

3. Results and Discussion

As shown earlier [28], the mobility of lightweight concrete on hollow microspheres substantially depends on the polycarboxylate plasticizer. Varying its amount is one of the most effective prescription methods for establishing a parity combination of mobility and buildability suitable for 3D printing.

After extrusion from a 3D printer nozzle, the concrete mix changes its original shape under its weight. Ensuring minimal layer deformation is important for such mixtures. In this work, a study was carried out on the preservation of the volume of the mixture after extrusion from the cylinder. Such deformations can be quantified by the value of the vertical settlement of the layer. However, vertical deformation does not fully reflect the volume change, since the layer also changes in the horizontal plane. It is also important for 3D-printing.

Since both the height and the diameter of the cylinder are subject to change than a parameter that takes into account both these changes is taken as the criteria for the preservation of the volume of the concrete mixture. In the initial state, the volume of the mixture takes the shape of a cylinder. In this case, the largest and smallest diameters are $D_1 = D_2$. Therefore, the volume for each of them (at $H = H_0$) is equal to $V_1 = V_2$ (Fig. 3). Then the maximum preservation of the form expressed through the ratio V_1/V_2 will be equal to 1. After deformation, the volumes of the concrete mix specimens calculated with D_1 and D_2 will differ. The V_1/V_2 ratio will also bi changed. Thus, the ratio of the volumes V_1/V_2 and heights $H / H_0 \rightarrow 1$ characterize the best preservation of the concrete mix shape (Fig. 4).

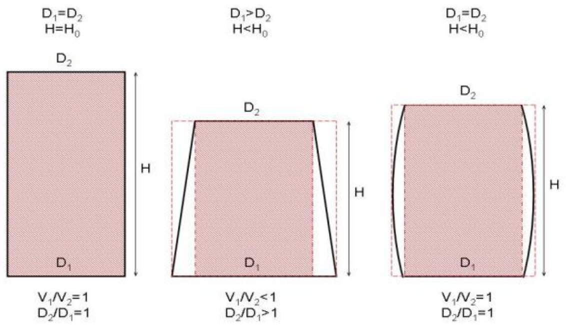

Figure 3. Change in cylinder volume.

Figure 4. The nature of the slump of the concrete mixture after extrusion from the cylinder.

The study of the change in the mobility and buildability of concrete mixtures of lightweight concrete on hollow microspheres on the amount of plasticizer was carried out in this work (Table 2).

Table 2. Rheotechnological properties of concrete mixes for 3D printing.

No	Name	Spread diameter, D_{sp}, mm	Buildability, V_1/V_2	Relative deformation, H/H_0
1	P/C-1.0	129 ± 2	0.97 ± 0.02	0.95 ± 0.02
2	P/C-1.1	135 ± 3	0.94 ± 0.02	0.93 ± 0.02
3	P/C-1.2	160 ± 4	0.88 ± 0.03	0.90 ± 0.03
4	P/C-1.3	165 ± 3	0.83 ± 0.03	0.84 ± 0.01
5	P/C-1.4	182 ± 5	0.62 ± 0.02	0.78 ± 0.02

Table 2 shows that an increase in the spread diameter of the concrete mixture due to the increase in the plasticizer leads to a decrease in buildability. At the same time, more than 90 % of the cylinder shape is retained with a plasticizer content of not more than 1.1 % of the mass of Portland cement. This corresponds to the mobility of the mixture according to the standardized method of 135 mm.

Fig. 5 shows the effect of the rheological properties of the mixture on the geometry of the extruded rectangular layers. It is seen that an increase in the amount of plasticizer, leading to an increase in the mobility of the mixture, contributes to the deterioration of the retention of the shape of the layers.

Figure 5. An example of deformations of extruded lightweight concrete layers in the horizontal (left) and vertical (right) planes.

Thus, it has been established that concrete mixtures on hollow microspheres with an average density of 1400 kg/m^3 can provide a high buildability of more than 90 % with mobility of up to 135 mm along the spread diameter at the varying content of the plasticizing additive. That is, the cross-section of the layer after extrusion will change within 10 %. In practice, it will ensure the stability of the technological process of manufacturing a structure using the 3D printing method (from adjusting the stroke of the printer nozzle to the consumption of materials).

For the studied compositions, the content of the plasticizer in an amount of no more than 1.1 % of the cement mass makes it possible to provide variability in the intensity of liquefaction at the high buildability. Thus, we can conclude that concrete mixes on hollow microspheres are highly suitable for 3D printing in construction.

Also, it can be concluded that it is necessary to develop a universal method for assessing the suitability of concrete mixes for 3D printing by rheological criteria. And the existing standardized test methods require the establishment of boundary ranges of properties for specific types of 3D printers.

Both the mobility of the mixture and its strength after extrusion are important for the development of materials for 3D printing. As is known, an important condition of a controlled increase of design strength values of concrete is the W/C-ratio. However, the large exposed surface of the extruded layers has a significant impact on 3D printing technology. The evaporation of moisture leads to a decrease in the actual value of the W/C-ratio and a deficiency of water for hydration of the binder and also shrinkage. The use of a superabsorbent polymer in the solution form with a controlled polymerization process, in contrast to granular analogs, should allow preserving the mechanical properties of concrete in unfavorable conditions. The results of studying the effect of SAP solution on the properties of compositions for 3D printing are presented in Table 3.

Table 3. Rheological properties of mixtures and physical and mechanical properties of lightweight concrete with SAP solution.

No	Name	D_{sp}, mm	ρ, kg/m^3	R_{fl}, MPa	R_{com}, MPa	ε, mm/m
1	A/C-0	225 ± 2	1370 ± 30	5.52 ± 0.12	45.3 ± 1,1*	1.22 ± 0.05
2	A/C-0.4	212 ± 3	1360 ± 20	5.59 ± 0.09	45.2 ± 0,9	1.16 ± 0.03
3	A/C-0.8	199 ± 2	1360 ± 35	5.81 ± 0.14	47.8 ± 1,0	1.02 ± 0.05
4	A/C-1.5	181 ± 2	1355 ± 30	6.83 ± 0.15	47.6 ± 1,2	1.00 ± 0.04
5	A/C-2.3	180 ± 1	1355 ± 30	6.33 ± 0.14	44.2 ± 1,0	0.95 ± 0.04
6	A/C-3.9	170 ± 1	1325 ± 25	6.02 ± 0.10	37.1 ± 0,8	0.89 ± 0.03

Notes: D_{sp} is spread diameter, ρ is average density, R_{fl} is flexural strength, R_{com} is compressive strength, ε is relative deformation, * is the compressive strength of lightweight concrete hardened under normal conditions is 57.0 ± 1.4 MPa.

It was found that the mobility of lightweight concrete mixes on hollow microspheres decreases after the introduction of SAP in contrast to cement pastes [27]. An increase in the content of polyacrylates to 2.3 % by weight of Portland cement leads to a decrease in the spread diameter of the mixture by 20 %. This pattern can be associated with a significant contribution of the plasticizer to the provision of the rheological properties of such compositions.

One of the possible reasons for the decrease in the mobility of the concrete mix may be the unsatisfactory compatibility of the plasticizer solution and SAP components. However, an assessment of the compatibility of the plasticizer solution and the components of the superabsorbent polymer indicates that this assumption is not valid. The results of the study of changes in the surface tension of the solution of the used plasticizer (0.04 %) from the amount of the acrylate part of SAP are presented in Table 4.

Table 4. Dependence between the surface tension of the plasticizer solution and the content of the acrylate part of SAP.

The physical state	SAP solution concentration, W/ΣA					
	0	95.0	47.0	23.0	15.0	8.5
Before polymerization	47.5 ± 1.4	44.5 ± 1.4	44.4 ± 1.6	43.7 ± 1.3	43.4 ± 1.4	42.5 ± 1.3
After polymerization		45.2 ± 1.3	45.0 ± 1.3	44.6 ± 1.5	44.5 ± 1.2	43.0 ± 1.3

The obtained results show that each of the components of the studied solution (polycarboxylate plasticizer and acrylate SAP) reduces the surface tension regardless of the polymerization degree of SAP. This indicates the compatibility of the plasticizer and SAP. That is, it has been found that the used polycarboxylate plasticizer and polyacrylate SAP can be combined to prepare a solution for producing concrete mixtures and lightweight concrete products.

Thus, it has been shown that each of the concrete compositions under study has sufficient mobility of the mixture to perform technological operations. The mobility of the mixtures D_{sp} > 150 mm ensures sufficient formability during extrusion and buildability after extrusion of the next layer (Fig. 6). The rational concentration of SAP in the developed concrete receipts should not exceed 1.5 % of the mass of Portland cement.

Figure 6. Example of extruded lightweight concrete layers with SAP.

As shown above, the use of granular SAP leads to a decrease in the strength properties of cement composites. This is due to the formation of additional porosity in the structure of the material after desorption of water from the polymer additive. Therefore, the use of SAP in the form of a solution to reduce shrinkage deformations can be justified by the preservation of mechanical characteristics. Table 3 shows the dependence of the flexural strength and compression of lightweight concrete on the number of SAP.

It has been established that the use of SAP solution in the amount of 0.50–1.0 % of the mass of Portland cement provides the smallest decrease in concrete strength. The flexural strength of such concretes varies in the range of 5.5–5.8 MPa, and the compressive strength – 45.3–47.8 MPa at the age of 28 days of hardening in unfavorable conditions. The amount of acrylate part of not more than 2.3 % of the mass of Portland cement in the composition of concrete provides an increase in flexural strength by 17 %. This may be due to the formation of polymer films or fibers that perform the function of a reinforcing additive after desorption. At the same time, an increase in the SAP content of more than 1.5 % of the mass of Portland cement is characterized by a decrease in compressive strength by 8.5 %. Then, the permissible amount of SAP in concrete is limited to 1.0–1.5 % of the mass of Portland cement.

The study of the shrinkage showed the possibility of reducing the deformations of lightweight concrete by 25 % due to the introduction of SAP. The use of SAP solution in small amounts (up to 0.25 % of the mass of Portland cement) leads to a decrease in shrinkage deformation by 26.9 %. The maximum reduction in shrinkage compared to the control composition is achieved with a SAP content of 2.3 %. Taking into account the change in rheological and physical-mechanical properties, varying the SAP content in the range of 0.8–1.5 % of the mass of Portland cement provides the best shrinkage value.

Since the use of SAP is justified by the possibility of providing internal care during the hydration of Portland cement, an important condition for such compositions is the establishment of parity concentrations of the polyacrylate solution, which do not lead to a decrease in the degree of hydration.

The integral thermograms of the total heat release of cement mixtures (Fig. 7) show that the range of SAP concentrations less than 1.5 % provides a heat release level similar to the control composition (without SAP). This indicates a similar degree of binder hydration. That is, the process of SAP polymerization in the indicated concentrations is carried out during the period when the competition between the sorption of polyacrylates and the hydration of Portland cement is the least. At the same time, the presented data of calorimetric studies indicate some inhibition of the process of hydration of Portland cement in the presence of a superabsorbent polymer. But, the effect of SAP is not limited to the first 72 hours of the hydration and hardening process. Assessment of the influence of SAP on the structure formation of cement stone at a later date was carried out by the magnitude of the heat flow in the temperature range of 470 ... 510 °C.

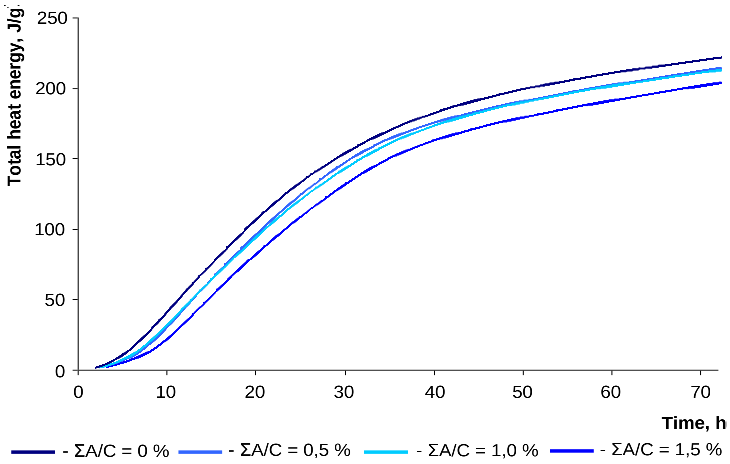

Figure 7. Kinetics of heat energy during hydration of Portland cement with SAP.

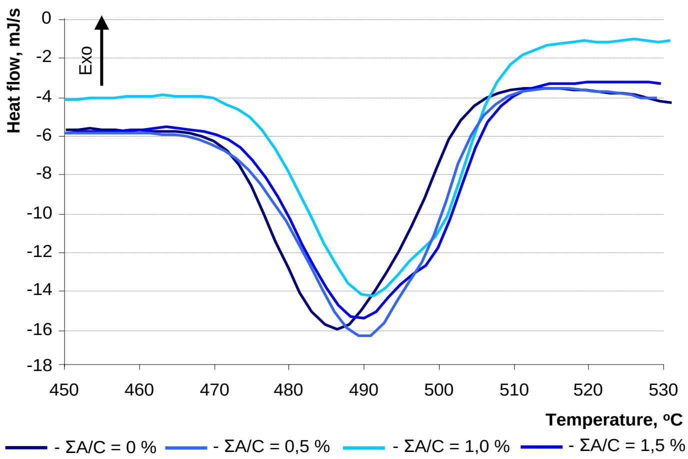

Figure 8. Thermogram of cement stone in the temperature range 470…510 °C.

The total area of the anomaly for the endothermic effect (S) (Fig. 8) of cement stone in the specified temperature range is proportional to the amount of portlandite. This allows to conclude about the number of hydration products or the degree of binder hydration. It is seen that an increase in the SAP content leads to an increase in the area of the anomaly for the endothermic effect. The maximum is achieved when the content of the superabsorbent polymer is 1.0 % by weight of Portland cement (Table 5). A further increase in SAP leads to a decrease in enthalpy. However, the area of the anomaly for the endothermic effect at 1.5 % by weight of Portland cement is more than the S value for the control composition.

Table 5. The total area of the anomaly of the cement stone in the temperature range 470…510 °C.

Index	Ratio A/C, %			
	0	0.5	1.0	1.5
S, mJ·ºC/s	223.0	228.9	252.7	239.7

The study of the structure formation of cement stone samples after hardening for 28 days was carried out. Differential thermal analysis shows an increase in the enthalpy of decomposition of portlandite in cement stone, hardening in the presence of SAP. That is, it can be concluded that the degree of hydration of Portland cement is increased. Thus, the hypothesis about the possibility of using SAP in the form of solutions with controlled polymerization instead of granular additives for the internal curing of Portland cement in the development of concretes for 3D printing technology was confirmed.

The obtained results of the study of lightweight concrete show the high suitability of concrete mixtures on hollow microspheres for extrusion using a forming nozzle of a 3D printer [6]. Also, the implemented solution of using SAP in the form of a solution instead of a granular form is capable of providing the function of internal curing for the cement [18, 21] without loss of concrete strength.

4. Conclusions

Based on this research the following conclusions were made:

1. Concrete mixtures on hollow microspheres with an average density of 1400 kg/m^3 provide buildability after extrusion of more than 90 % and mobility of up to 135 mm at varying content of the plasticizing additive. The content of the plasticizer is not more than 1.2 % by weight of the cement allows to vary the intensity of the dilution for the studied mixtures. The tested concrete mixtures are highly suitable for 3D printing in construction. The tested concrete mixtures have high buildability for 3D printing in construction.

2. The use of SAP solutions with controlled polymerization is an effective solution for providing internal curing for the Portland cement in the production of concrete for 3D printing. The calorimetric analysis shows the positive influence of SAP on the processes of structure formation of cement stone. The SAP in an amount of not more than 1.0 % of the mass of Portland cement corresponds to the maximum amount of Portlandite formed during the hydration of Portland cement.

3. The use of SAP solution in an amount of 0.50...1.0 % of the mass of Portland cement provides the least reduction in the strength of lightweight concrete. The flexural strength varies in the range of 5.5...5.8 MPa and the compressive strength – 45.3...47.8 MPa. An increase in SAP content of more than 1.5 % of the mass of Portland cement is characterized by a decrease in the compressive strength by 8.5 %. The optimal amount of SAP in the concrete composition is limited to the range of 1.0...1.5 % of the mass of Portland cement.

5. Acknowledgement

This work was supported by a grant from the President of the Russian Federation for state support of young Russian scientists - candidates of sciences MK-1394.2020.8.

References

1. Khan, M.S., Sanchez, F., Zhou, H. 3D-printing of concrete: Beyond horizons. Cement and Concrete Research. 2020. 133. 106070. DOI: 10.1016/j.cemconres.2020.106070
2. Buswell, R.A., Leal de Silva, W.R., Jones, S.Z., Dirrenberger, J. 3D printing using concrete extrusion: A roadmap for research. Cement and Concrete Research. 2018. 112. Pp. 37–49. DOI: 10.1016/j.cemconres.2018.05.006
3. Wangler, T., Roussel, N., Bos, F.P., Salet, T.A.M., Flatt, R.J. Digital Concrete: A Review. Cement and Concrete Research. 2019. 123. 105780. DOI: 10.1016/j.cemconres.2019.105780
4. Vatin, N.I., Chumadova, L.I., Goncharov, I.S., Zykova, V.V., Karpenya, A.N., Kim, A.A., Finashenkov, E.A. 3D-pechat' v stroitel'stve [3D printing in construction]. Construction of unique buildings and structures. 2017. 1(52). Pp. 27–46.
5. Lu, B., Weng, Y., Li, M., Qian, Y., Leong, K.F., Tan, M.J., Qian, S. A systematical review of 3D printable cementitious materials. Construction and Building Materials. 2019. 207. Pp. 477–490. DOI: 10.1016/j.conbuildmat.2019.02.144
6. Mechtcherin, V., Nerella, V.N., Will, F., Näther, M., Otto, J., Krause, M. Large-scale digital concrete construction – CONPrint3D concept for on-site, monolithic 3D-printing. Automation in Construction. 2019. 107, 102933. DOI: 10.1016/j.autcon.20-19.102933
7. Buswella, R.A., Leal de Silva, W.R., Jones, S.Z., Dirrenberger, J. 3D printing using concrete extrusion: A roadmap for research. Cement and Concrete Research. 2018. 112. Pp. 37–49. DOI: 10.1016/j.cemconres.2018.05.006
8. Malaeb, Z., AlSakka, F., Hamzeh, F. 3D Concrete Printing: Machine Design, Mix Proportioning, and Mix Comparison Between Different Machine Setups. 3D Concrete Printing Technology. 2019. Pp. 115–136. DOI: 10.1016/B978-0-12-815481-6.00006-3
9. Li, Zh., Wang, L., Ma, G. Method for the Enhancement of Buildability and Bending Resistance of Three-Dimensional-Printable Tailing Mortar. 3D Concrete Printing Technology. 2019. Pp. 161–179. DOI: 10.1186/s40069-018-0269-0
10. Kazemian, A., Yuan, X., Cochran, E., Khoshnevis, B. Cementitious materials for construction-scale 3D printing: Laboratory testing of fresh printing mixture. Construction and Building Materials. 2017. 145, Pp. 639–647. DOI: 10.1016/j.conbuildmat.2017.04.015
11. Suiker, A.S.J., Salet, T.A.M., Lucas, S.M., Wolfs, R.J.M. Elastic buckling and plastic collapse during 3D concrete printing. Cement and Concrete Research. 2020. 135, 106016. DOI: 10.1016/j.cemconres.2020.106016
12. Jayathilakage, R., Rajeev, P., Sanjayan, J.G. Yield stress criteria to assess the buildability of 3D concrete printing. Construction and Building Materials. 2020. 240, 117989. DOI: 10.1016/j.conbuildmat.2019.117989
13. Lesovik, V.S., Elistratkin, M.Yu., Glagolev, E.S., Absimetov, M.V., Shatalova, S.V., Lesnichenko, E.N. Adaptacija tehnologii neavtoklavnogo gazobetona k stroitel'noj 3D pechati [Adaptation of non-autoclaved aerated concrete technology to construction 3D printing]. Vestnik Belgorodskogo Gosudarstvennogo tehnologicheskogo universiteta im. V.G. Shuhova [Bulletin of the Belgorod State Technological University named after V.G. Shukhova]. 2017. No. 8. Pp. 6–11.
14. Slavcheva, G.S., Makarova, T.V. Penobetony dlja teploizoljacionnyh sloev naruzhnyh sten, vozvodimyh metodom 3D-pechati [Foam concrete for thermal insulation layers of external walls, erected by 3D printing]. Stroitel'nye materialy [Building materials]. 2018. No. 10. Pp. 30–35.
15. Inozemtcev, A.S., Duong, T.Q. High-strength lightweight concrete with internal curing for 3D-printing in construction. IOP Conference Series: Materials Science and Engineering. 2020. 869 (3). 032003. DOI: 10.1088/1757-899X/869/3/032003
16. Inozemtcev, A.S. Case Studies of High-strength Lightweight Concrete Using Expanded Siliceous Aggregate. IOP Conference Series: Materials Science and Engineering. 2020. 840 (1). 012017. DOI: 10.1088/1757-899X/840/1/012017
17. Zou, D., Li, K., Li, W., Li, H., Cao, T. Effects of pore structure and water absorption on internal curing efficiency of porous aggregates. Construction and Building Materials. 2018. 163. Pp. 949–959. DOI: 10.1016/j.conbuildmat.2017.12.170

18. Cusson, D., Hoogeveen, T. Internal curing of high-performance concrete with pre-soaked fine lightweight aggregate for prevention of autogenous shrinkage cracking. Cement and Concrete Research. 2008. 38 (6). Pp. 757–765. DOI: 10.1016/j.cemconres.2008.02.001
19. Browning, J., Darwin, D., Reynolds, D., Pendergrass, B. Lightweight aggregate as internal curing agent to limit concrete shrinkage. ACI Materials Journal. 2011. 108 (6). Pp. 638–644.
20. Dang, J., Zhao, J., Du, Z. Effect of Superabsorbent Polymer on the Properties of Concrete. Polymers. 2017. 9 (12). Pp. 672. DOI: 10.3390/polym9120672
21. Shan, J., Guo, Sh. Influence of Super Absorbent Polymer on the Mechanical Property of High Performance Concrete. International Symposium on Material. Energy and Environment Engineering (ISM3E 2015). 2015. Pp. 154–157. DOI: 10.2991/ism3e-15.2015.40
22. Mignon, A., Snoeck, D., Dubruel, P., Vlierberghe, S., Belie, N. Crack Mitigation in Concrete: Superabsorbent Polymers as Key to Success? Materials (Basel). 2017. 10 (3). Pp. 237. DOI: 10.3390/ma10030237
23. Schröfl, Ch., Mechtcherine, V., Gorges, M. Relation between the molecular structure and the efficiency of superabsorbent polymers (SAP) as concrete admixture to mitigate autogenous shrinkage. Cement and Concrete Research. 2012. 42 (6). Pp. 865–873.
24. Senff, L., Modolo, R.C.E., Ascensao, G., Hotza, D., Labrincha, J.A. Development of mortars containing superabsorbent polymer. Construction and Building Materials. 2015. 95. Pp. 575–584.
25. Wang, F., Yang, J., Hu, S., Li, X., Cheng, H. Influence of superabsorbent polymers on the surrounding cement paste. Cement and Concrete Research. 2016. 81. Pp. 112–121.
26. Shan, J., Guo, Sh. Influence of Super Absorbent Polymer on the Mechanical Property of High Performance Concrete. International Symposium on Material. Energy and Environment Engineering (ISM3E 2015), Atlantis Press. Changsha, 2015. Pp. 154–157.
27. Inozemtcev, A.S., Korolev, E.V., Duong, T.Q. Physical and mechanical properties of cement stone with superabsorbent polyacrylate solutions. Magazine of Civil Engineering. 2019. 89 (5). Pp. 179–186. DOI: 10.18720/MCE.89.15
28. Korolev, E.V., Inozemtcev, A.S. Vysokoprochnyj legkij beton [High strength lightweight concrete]. Patent Russia no. 2515450, 2012.
29. Adamcevich, A.O., Pustovgar, A.P. Features of the influence of modifying additives on the kinetics of hardening of cement systems. Dry building mixtures. 2015. 4. Pp. 26–29.
30. Inozemtcev, A., Korolev, E., Duong, T.Q. Study of mineral additives for cement materials for 3D-printing in construction. IOP Conference Series: Materials Science and Engineering. 2018. 365 (3). 032009. DOI: 10.1088/1757-899X/365/3/032009

Contacts:

Aleksandr Inozemtcev, InozemcevAS@mgsu.ru

Evgeniy Korolev, info@nocnt.ru

Thanh Qui Duong, quiduongthanh@gmail.com

**Федеральное государственное автономное образовательное учреждение высшего образования
Санкт-Петербургский политехнический университет Петра Великого**

**Инженерно-строительный институт
Центр дополнительных профессиональных программ**

ПОЛИТЕХ
Санкт-Петербургский политехнический университет Петра Великого

*195251, г. Санкт-Петербург, Политехническая ул., 29,
тел/факс: 552-94-60, www.stroikursi.spbstu.ru,
stroikursi@mail.ru*

**Приглашает специалистов проектных и строительных организаций,
не имеющих базового профильного высшего образования
на курсы профессиональной переподготовки (от 500 часов)
по направлению «Строительство» по программам:**

П-01 «Промышленное и гражданское строительство»
Программа включает учебные разделы:
• *Основы строительного дела* • *Инженерное оборудование зданий и сооружений* • *Технология и контроль качества строительства* • *Основы проектирования зданий и сооружений* • *Автоматизация проектных работ с использованием AutoCAD* • *Автоматизация сметного дела в строительстве* • *Управление строительной организацией* • *Управление инвестиционно-строительными проектами. Выполнение функций технического заказчика*
П-02 «Экономика и управление в строительстве»
Программа включает учебные разделы:
• *Основы строительного дела* • *Инженерное оборудование зданий и сооружений* • *Технология и контроль качества строительства* • *Управление инвестиционно-строительными проектами. Выполнение функций технического заказчика и генерального подрядчика* • *Управление строительной организацией* • *Экономика и ценообразование в строительстве* • *Управление строительной организацией* • *Организация, управление и планирование в строительстве* • *Автоматизация сметного дела в строительстве*
П-03 «Инженерные системы зданий и сооружений»
Программа включает учебные разделы:
• *Основы механики жидкости и газа* • *Инженерное оборудование зданий и сооружений* • *Проектирование, монтаж и эксплуатация систем вентиляции и кондиционирования* • *Проектирование, монтаж и эксплуатация систем отопления и теплоснабжения* • *Проектирование, монтаж и эксплуатация систем водоснабжения и водоотведения* • *Автоматизация проектных работ с использованием AutoCAD* • *Электроснабжение и электрооборудование объектов*
П-04 «Проектирование и конструирование зданий и сооружений»
Программа включает учебные разделы:
• *Основы сопротивления материалов и механики стержневых систем* • *Проектирование и расчет оснований и фундаментов зданий и сооружений* • *Проектирование и расчет железобетонных конструкций* • *Проектирование и расчет металлических конструкций* • *Проектирование зданий и сооружений с использованием AutoCAD* • *Расчет строительных конструкций с использованием SCAD Office*
П-05 «Контроль качества строительства»
Программа включает учебные разделы:
• *Основы строительного дела* • *Инженерное оборудование зданий и сооружений* • *Технология и контроль качества строительства* • *Проектирование и расчет железобетонных конструкций* • *Проектирование и расчет металлических конструкций* • *Обследование строительных конструкций зданий и сооружений* • *Выполнение функций технического заказчика и генерального подрядчика*

По окончании курса слушателю выдается диплом о профессиональной переподготовке установленного образца, дающий право на ведение профессиональной деятельности